Quest for high-performance Mg and Mg-Li/Na ion hybrid batteries

By

Mewin Vincent B.Sc., M.Sc.

Supervised by

Dr. Vinodkumar Etacheri Dr. Maciej Haranczyk

School of Condensed Matter Physics, Nanoscience and Biophysics
Autonomous University of Madrid
July 2021

Abstract

Mg-batteries recently emerged as a promising post-lithium technology due to the abundance (2.3% of earth's crust, ~104 fold > Li), inexpensive nature (~$2/Kg, 10 fold < Li) high volumetric capacities (3833mAh/cm3), dendrite-free redox reactions and environmental benign nature of Mg-metal. However, practical Mg-batteries deliver energy/ power density and cycle-life much lower than the theoretical predictions due to sluggish Mg-ion intercalation kinetics. Mg-hybrid batteries are demonstrated an approach to mitigate these inherent constraints of the pure Mg system without compromising the safety aspects and cost effectiveness of metallic Mg-anodes. However, lack of potential dual-ion compatible cathodes hinder the development of Mg-hybrid battery systems.

This thesis describes different methods for enhancing the Mg and Mg-Li/Na dual-ion storage performance of TiO_2 electrodes through nanoscale material engineering. First chapter describe current developments in the area of Mg and Mg-hybrid battery development and the potential challenges. Second chapter consist of various experimental approaches implemented to synthesize and characterize the cathode materials. Following four chapters details the results and subsequent discussion on the different types of novel cathode materials developed. Final chapter describe the conclusion and possible future work.

Chapter 3 describe high rate, ultralong-life and fast charging Mg-battery based on oxygen-deficient (15%) rutile TiO_2 nanowire cathodes. Oxygen vacancies resulted in the increased disorderness of rutile TiO_2 nanowires. This defective cathode demonstrated exceptional pseudocapacitance (up to 82%), specific capacities (235 mAh/g @ 50 mA/g), rate performance (57 mAh/g @ 1A/g) cycling stability (2000 cycles @ 1A/g, 104% capacity retention) and coulombic efficiency (~100%), outperforming all TiO_2 based cathodes reported earlier. Oxygen vacancies remained unaffected, and rutile crystal structure retained structural integrity

under charge-discharge process. This study demonstrates the significance of crystal defects such as oxygen vacancies in the Mg-ion storage performance of metal oxide based cathodes.

Chapter 4 presents a high-rate and ultralong-life Mg-Li hybrid battery based on a dual-phase hierarchical TiO_2 cathode. Highly pseudocapacitive TiO_2 nanosheets consists of anatase (60%) and bronze (40%) nanocrystallites resulting numerous nanointerfaces due to crystal structure mismatch. This dual-phase hierarchical cathode exhibits excellent pseudocapacitance (up to 92%), specific capacities (235 mAh/g @ 25 mA/g), rate performance (120 mAh/g @ 1A/g) cycling stability (~87% after 3000 cycles @ 1A/g) and coulombic efficiency (~100%). Only minimal structural changes are observed during the charge-discharge of TiO_2 nanosheet cathode. Outstanding electrochemical performance of dual-phase hierarchical TiO_2 nanosheet cathode is attributed to the superior pseudocapacitive Mg/Li-ion diffusion through anatase-bronze nanointerfaces.

Chapter 5 demonstrates a high-performance Mg-Li hybrid battery based on cobalt doped anatase TiO_2 cathode. Extremely pseudocapacitive anatase $Ti_{1-x}Co_xO_{2-y}$ nanosheets consist of an optimum 3.57% Co-atoms. This defective cathode delivered exceptional pseudocapacitance (up to 93%), specific capacities (386 mAh/g @ 25 mA/g), rate performance (191 mAh/g @ 1A/g), cycling stability (3000 cycles @ 1A/g) and coulombic efficiency (~100%). This performance is superior to the TiO_2 based Mg-Li hybrid battery cathodes reported earlier. Mechanistic studies of anatase $Ti_{1-x}Co_xO_{2-y}$ nanosheets revealed dual-ion intercalation pseudocapacitance with negligible structural changes. Excellent electrochemical performance cation doped TiO_2 cathode is attributed to the rapid pseudocapacitive Mg/Li-ion diffusion through the disorderness generated by oxygen vacancies.

Chapter 6 presents a fast charging and ultralong-life Mg-Na hybrid battery based on extremely pseudocapacitive hierarchical TiO_2-B nanosheet cathode. This two-dimensional cathode exhibited outstanding pseudocapacitance (up to 94%), specific capacities (195 mAh/g @ 25

mA/g), rate performance (140 mAh/g @ 1A/g), cycling stability (~76% after 6000 cycles @ 1A/g), and coulombic efficiency (~100%). These performances are vastly superior to the previously reported Mg-Na hybrid batteries based on metal oxide cathodes. Mechanistic investigations revealed Mg/Na-ion intercalation pseudocapacitance without significant structural changes. Exceptional electrochemical performance of the TiO_2-B nanosheet cathode is credited to the dominant pseudocapacitive Mg/Na-ion diffusion through nanointerfaces resulting from the hierarchical microstructure of TiO_2-B nanosheets.

Resumen

Las baterías de magnesio aparecieron como una prometedora tecnología post-litio debido a la abundancia (2.3% de la corteza terrestre, ~104 veces > Li), el bajo coste (~$2/Kg, 10 veces < Li), la alta capacidad volumétrica (3833mAh/cm^3), las reacciones libres de dendritas y la naturaleza ecológica del Mg metálico. Sin embargo, las baterías de Mg ofrecen una capacidad y ciclabilidad específicas mucho más bajas que las predicciones teóricas debido a la lenta cinética de intercalación de iones de Mg^{2+}. Las baterías híbridas de Mg se consideran una adaptación adecuada para mitigar estas limitaciones inherentes al sistema de Mg puro y aprovechar los beneficios de precio y seguridad de los ánodos metálicos de Mg. Sin embargo, la falta de posibles cátodos compatibles con iones duales impide el desarrollo del sistema híbrido de Mg

Esta tesis describe diferentes métodos para mejorar las características de almacenamiento de iones duales de Mg y Mg-Li / Na de los electrodos de TiO_2 a través de la ingeniería de materiales. El primer capítulo describe los avances actuales en el desarrollo de baterías de Mg e híbridas y los potenciales desafíos. El segundo capítulo resume los diversos enfoques experimentales implementados. Los siguientes cuatro capítulos detallan los resultados y la posterior discusión de la tesis. El capítulo final es la conclusión y las perspectivas futuras.

El Capítulo 3 describe una batería de Mg de carga rápida de alta velocidad de vida ultra larga basada en cátodos de nanocables de TiO_2 rutilo, deficientes en oxígeno (15%). Las vacantes de oxígeno resultaron en el aumento del desorden en los nanocables de TiO_2 rutilo. Este cátodo, basado en defectos, demostró una pseudocapacidad excepcional (hasta 82%), capacidades específicas (235 mAh / g @ 50 mA / g), rendimiento de velocidad (57 mAh / g @ 1 A / g) estabilidad de ciclo (2000 ciclos a 1 A / g, 104% de capacidad retención) y eficiencia culómbica (~ 100%) superando a todos las investigaciones previas basadas en TiO_2. Las vacantes de oxígeno no se vieron afectadas y la estructura cristalina mantuvo su integridad durante el

proceso de carga/descarga. Este estudio demuestra la importancia de los defectos en la estructura cristalina, como las vacantes de oxígeno para el almacenamiento de iones de Mg en cátodos basado en óxidos metálicos.

El Capítulo 4 presenta una batería híbrida de Mg-Li de alta velocidad y duración ultra larga, basada en un cátodo de TiO_2 de doble fase. Las nanoláminas de TiO_2, altamente pseudocapacitivas, consisten en nanocristales de anatasa (60%) y bronce (40%) que forman numerosas interfases debido al desajuste de la estructura cristalina. Este cátodo jerárquico de fase dual exhibe una excelente pseudocapacitancia (hasta 92%), capacidad específica (235 mAh / g @ 25 mA / g), capacidad de ciclado (120 mAh / g @ 1A / g), estabilidad de ciclado (~ 87% después de 3000 ciclos @ 1A / g) y eficiencia culómbica (~ 100%). Solo se observan cambios estructurales mínimos durante la carga/descarga del cátodo de nanoláminas de TiO_2. El excelente rendimiento electroquímico del cátodo de nanoláminas de TiO_2 de fase dual se atribuye a la superior difusión pseudocapacitiva de iones Mg / Li a través de nanointerfases entre cristales de bronce y anatasa.

El Capítulo 5 muestra una batería híbrida de Mg-Li de carga rápida y alto rendimiento, basada en un cátodo de anatasa TiO_2 dopado con cobalto. Las nanoláminas de anatasa $Ti_{1-x}Co_xO_{2-y}$, extremadamente pseudocapacitivas, son óptimamente dopadas con átomos de Co (3,57%). Este cátodo basado en defectos mostró una excepcional pseudocapacitancia (hasta 93%), capacidad específica (386 mAh / g @ 25 mA / g), capacidad de ciclado (191 mAh / g @ 1A / g), estabilidad de ciclado (3000 ciclos @ 1A / g), eficiencia culómbica (~100%). El rendimiento es muy superior respecto a los cátodos existentes de baterías híbrida de Mg-Li basadas en TiO_2. Los estudios mecanicistas de las nanoláminas anatasa $Ti_{1-x}Co_xO_{2-y}$ revelan una intercalación pseudocapacitiva dual de iones con cambios estructurales poco significativos. El excelente rendimiento electroquímico del cátodo de TiO_2, dopado con cationes, se atribuye a la rápida cinética de la difusión pseudocapacitiva dual de iones de Mg/Li a través del desorden generado por las vacantes de oxígeno.

El Capítulo 6 presenta una batería híbrida de Mg-Na, de carga rápida y de vida útil ultra larga, basada en un cátodo jerárquico de nanoláminas de TiO_2-B extremadamente pseudocapacitivo. Este cátodo bidimensional exhibió una pseudocapacitancia excepcional (hasta 94%), capacidad específica (195 mAh / g @ 25 mA / g), capacidad de ciclado (140 mAh / g @ 1A / g), estabilidad de ciclado (~ 76% después de 6000 ciclos @ 1A / g), eficiencia culómbica (~ 100%). Estos rendimientos son muy superiores a los cátodos híbridos de baterías de Mg-Na basadas en óxidos metálicos reportados anteriormente. Las investigaciones mecanicistas revelaron una intercalación pseudocapacitiva dual de iones de Mg / Na sin cambios estructurales significativos. El excepcional rendimiento electroquímico del cátodo de nanoláminas de TiO_2-B se atribuye a la dominante difusión pseudocapacitiva dual de iones Mg / Na a través de las nanointerfases que resultan de la microestructura jerárquica de las nanoláminas de TiO_2-B.

Declaration

I hereby certify that this thesis which I now submit for examination for the award of PhD, original and was performed by the candidate in the laboratories in IMDEA Institute of Materials.

This thesis was prepared according to the regulations for postgraduate study by research of The Autonomous University of Madrid and has not been submitted in whole or in part for another award in any Institute.

The University has permission to keep, lend or copy this thesis in whole or in part, on condition that any such use of the material of the thesis be duly acknowledged.

Mewin Vincent

Ad maiorem Dei gloriam

Acknowledgment

I would like to express my sincere gratitude to my supervisor, Dr. Vinodkumar Etacheri, co-supervisor, Dr. Maciej Haranczyk for their academic guidance, financial support and constant encouragement throughout the project. I would also wish to thank my tutor Prof. Jesus Alvarez Alonso and program coordinator Prof. Ruben Perez for being a good bridge to the University for fulfilling the PhD study requirements.

I would like to thank Spanish Ministry of Economy, Industry and Competitiveness (MINECO) for funding, which enable me to finish my study in Spain.

Thanks to IMDEA Materials institute for providing the facilities to successfully execute my research studies.

I am grateful to Mrs. Mary Jacob, Prof. VP Joseph for enlightening a passion for science and research.

It’s a pleasure to thank Dr. N. Raghu, Dr. A. Seema, Dr. M.N Muralidharan, Dr. Libu Manjakkal, Dr. Jobin Varghese Mr. S. Susanth and Dr. Anil for encouraging and directing me to find a PhD position and to do research in battery technology.

I would like to thank my colleagues Rudi, Daniel, Alvaro, Sai and Wenliang, who always help me with my research and studies.

Special thanks to all the technical and administration staff of the IMDEA institute for their constant technical and/or administrative assistance.

Finally, I express my deepest gratitude to my family for their constant support and encouragement.

Table of Contents

Abbreviations used

IPCC	:	Intergovernmental panel on climate change
IEA	:	International energy agency
PHS	:	Pumped hydro storage
LIB	:	Lithium ion battery
SEI	:	Solid electrolyte interface
CE	:	Coulombic efficiency
PAN	:	Polyacrylonitrile
Mg-triflate	:	Magnesium trifluoromethane sulfonate
STEM	:	Scanning transmission electron microscopy
DFT	:	Density functional theory
OCV	:	Open circuit voltage
NASICON	:	NAtrium Super Ionic CONductor
THF	:	Tetrahydrofuran
PAQS	:	Poly (anthraquinonyl sulphide)
APC	:	All phenyl complex
PhMgCl	:	Phenylmagnesium chloride
CNT	:	Carbon nanotube
CNF	:	Carbon nanofiber
PANI	:	Polyaniline
EG	:	Ethylene glycol
R	:	Rutile

A	Anatase
B	Bronze
AB	Anatase bronze hybrid
Diglyme	Bis(2-methoxyethyl) ether
PhMgCl	Phenylmagnesium chloride
XRD	X-ray diffraction
ICDD	International centre for diffraction data
FWHM	Full width at half maximum
BET	Brunauer-Emmet-Teller analysis
BJH	Barret-Joyner-Halenda model
XPS	X-ray photoelectron spectroscopy
EPR	Electron paramagnetic resonance
SEM	Scanning electron microscopy
TEM	Transmission electron microscopy
EIS	Electrochemical impedance spectroscopy
CV	Cyclic voltammetry
SOC	State of charge

List of figures

List of tables

Chapter 1

Introduction

1.1 Background and Motivation

Energy has unique importance in the modern society as it plays a crucial role in economic growth and environmental-social sustainability of the world[1]. Global energy consumption is exhibiting a tremendous increase in the post-industrial revolution era, due to the rapid population growth and consumer habits (Figure 1.1)[2]. It showed an average 1.7% annual growth from the 7160 Million tonnes (Mtoe) consumption in 1985 and reached 13,511 Mtoe in 2017. Studies predict a primary energy demand of 17,487 Mtoe in 2040. Tremendous demand ignited the use of diverse energy sources such as coal, oil, natural gas, nuclear energy, several renewable sources (solar, wind, hydropower) etc[3].

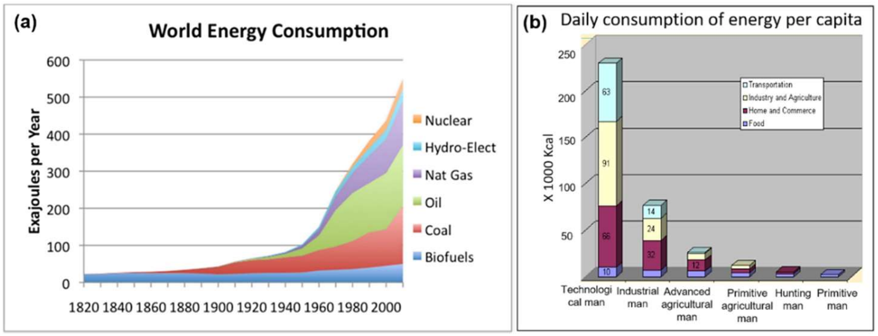

Figure 1.1. (a) Relative contribution of the various energy sources to the total demand. (b) Daily consumption of energy per capita.

Though several energy resources have been identified, at present nearly 80% of demand is backed by coal, oil and natural gas collectively called fossil fuels[3]. Unfortunately, fossil fuel burning produces CO_2 and other dangerous gas emissions that can cause serious environmental impacts such as global warming, ozone layer depletion, atmospheric pollution, climatic changes etc[4]. According to the intergovernmental panel on climate change (IPCC), CO_2 contributes the major share (~78%) to global warming[5]. Hence, there is an urgent call for replacing the high carbon footprint fossil fuel-based energy resources with environmentally benign methods[6]. Renewable resources such as solar, wind, etc. are promising alternatives however, the seasonal, monthly, or daily fluctuations in the supply restrict their extensive uses[7].

However, an intelligent coupling with an energy storage system can resolve the demand-supply incompatibility of renewable sources. The surplus energy produced in the favourable situation can be released when required. According to the international energy agency (IEA), global warming could be reduced by 2 °C by 2050 with a 450 GW energy storage capacity (140GW in 2014)[8]. Owing to its importance, several energy storage techniques have been developed which may be broadly classified as mechanical, electrochemical, chemical and thermal energy storage systems (Figure 1.2)[9].

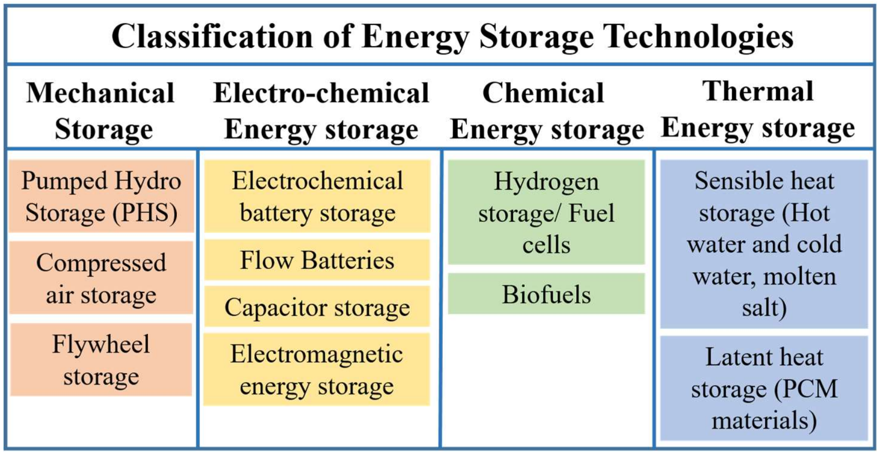

Classification of Energy Storage Technologies

Mechanical Storage	Electro-chemical Energy storage	Chemical Energy storage	Thermal Energy storage
Pumped Hydro Storage (PHS)	Electrochemical battery storage	Hydrogen storage/ Fuel cells	Sensible heat storage (Hot water and cold water, molten salt)
Compressed air storage	Flow Batteries	Biofuels	Latent heat storage (PCM materials)
Flywheel storage	Capacitor storage		
	Electromagnetic energy storage		

Figure 1.2. Classification of energy storage systems based on the form of stored energy.

1.2 Electrochemical energy storage

Though there are many established energy storage technologies, their extensive implementations are restricted due to varying reasons. The geographical constraints of pumped hydro storage (PHS) and compressed air storage, hydrogen storage related safety challenges and low energy density of fuel cells, complexity of durable and low loss bearings of the flywheels, large-scale electrolyte accommodation of the flow batteries, lower efficiency and expensive nature of molten salt storage etc. are some examples for the major challenges[10–15].

Meanwhile, global energy consumption scenarios undergone significant changes. The demand for the electrical energy has rose extensively due to the large control over the production-transmission-consumption of electricity than any other form of energy. In 2018 the final consumption reached 22,315TWh and a 49% demand increase is forecasted by 2040[16]. Additionally, portable electronic devices also gained more prominence in the recent years rather than the grid connected system. They are exceedingly dominating the medical, communication, transportation sectors[17–19]. These situations collectively increased the market demand for reliable, compact, portable, high-energy dense power sources that can facilitate the consumer requirement and carbon neutrality guidelines[20,21]. Electrochemical batteries dominate among the possible methods due to its excellent compatibility with the renewable energy resources and point of applications[22,23]. The high degree of scalability further facilitates the use of single technology for the large scale grid storage and portable applications[24].

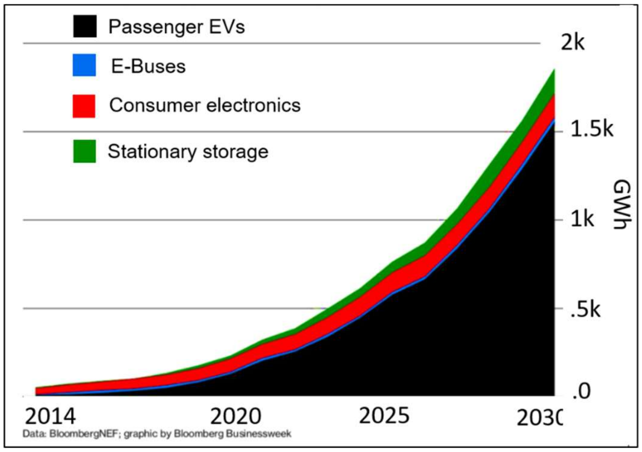

Figure 1.3. Rechargeable battery demand forecast.

The history of modern batteries dating back to the invention of the voltaic pile by Alessandro Volta in 1799[25]. Since then it undergone a continuous evolution resulting in distinct battery chemistries that plays a major role in the electrification requirements ranging from small portable electronics, medical devices and power grids[22]. A tremendous increase in demand is predicted with the proposed transition from internal combustion engines to electric vehicles (Figure 1.3)[26]. Analysts expect an overall 50% growth ($60 billion to $90 billion) of the battery market by 2025 over the 2015 standards[27]. However, the existing technologies are inadequate to unleash their application potential[28]. Hence, a ground-breaking improvement of the battery technologies facilitating performance enhancement and price reduction is crucial to meet the present and future requirements[29].

1.3 Lithium and Sodium-ion Batteries

Current demand for rechargeable batteries is mostly met with Lithium-ion batteries (LIB's) due to the superior characteristics than the prior secondary batteries[30]. It offers 5-6 times power densities and 2-3 times energy densities over the Ni-MH, Ni-Cd or Pb-acid batteries (Table 1.1)[21]. Further, it exhibits good cycle life, better shelf life owing to the limited self-discharge characteristics, wide temperature window and high operating voltage[31,32]. Unlike the Ni-MH or Ni-Cd batteries, it doesn't exhibit any memory effect too[33,34].

Table 1.1. A summary of the performance index of various rechargeable batteries[35].

Battery type	**Cell voltage (V)**	**Specific energy (Wh/kg)**	**Specific power (W/Kg)**	**Cycle life**	**Direct use**	**Technical and cost barriers**
Pb-acid	2.1	30-40	180	500-800	Automotive ignition	Environmental hazard due to Pb
Ni-Cd	1.2	40-60	150	~2000	Power tools and low end electronics	Memory effect and Cd-toxicity
Ni-MH	1.2	60-120	250-1000	500-1000	Portable electronics	High self-discharge, use of rare earth elements in negative electrode
LIB	~2.91	105-128	250-329	~2000	Portable electronics	Initial irreversible capacity loss

Despite of these advantages, lithium-ion batteries cannot be a reliable technology of the future owing to some specific technical drawbacks. Lithium has a very limited availability (0.0017% of earth crust) and an uneven distribution that can cause huge price inflation in the near future (Figure 1.4a)[36]. Lithium metal has an inherent tendency for dendrite growth under electrochemical cycling (Figure 1.4b), which can induce internal short circuit and challenge the safety[37]. Its tendency for violent water reaction requisite specific and hence expensive cell pack manufacturing and disposal conditions (Figure 1.4c)[38]. Further, it exhibits a solid electrolyte interface (SEI) formation due to the electrolyte reduction at low anodic potentials that leads to an initial irreversible capacity loss[39,40]. The dendrite growth issues were addressed by replacing the lithium metal with other compatible materials (Graphite, Silicon, etc) but in exchange for specific capacity[41,42]. Methods like pre-lithiation are implemented to counteract the irreversible capacity loss but lead to complicated cell assembly and elevated prices[43].

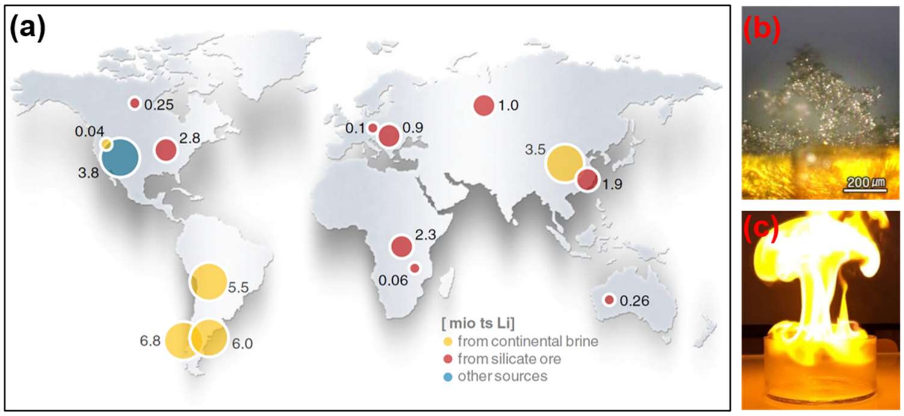

Figure 1.4. (a) Lithium deposition on the earth's crust, (b) Lithium metal dendrite growth and (c) Lithium metal reaction with moisture.

Sodium-ion batteries are a well-developed post lithium technology which is considered as the most competitive, inexpensive ($2.57/kg) and sustainable alternative due to its abundance (2.6% on earth crust) and eco-friendly nature[44]. However, it's Li like dendrite growth, SEI formation and violent reaction with water characteristics restricts the energy capabilities and challenge the safety[45,46]. Moreover, higher Na-ionic size (1.02 Å) than Li-ions (0.76 Å) causes sluggish ion intercalation to the host matrix, resulting in lower specific capacities[47].

Limited energy/power densities of the practical Li and Na-ion batteries and the exponential demand increase triggered a search for high capacity-inexpensive-safe systems. Multivalent ions attracted much attention among the possible alternatives due to their high theoretical volumetric capacity density facilitating higher packing density[48]. It eventually can power the high energy and high power application of the rechargeable batteries such as electric vehicles, avionics, etc. and new application frontiers that are not currently addressed by the Li-ion technology. Figure 1.5 demonstrates the increasing interest in the multivalent post lithium systems as a function of time.

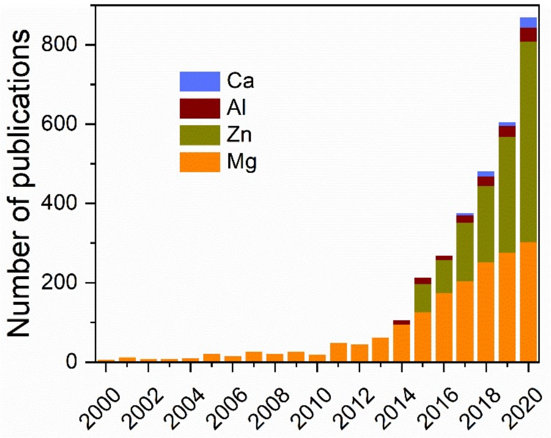

Figure 1.5. The number of publications featuring multivalent electrochemistry.

1.4 Magnesium Batteries

Recently Magnesium batteries attracted much attention as a prospective post lithium candidate due to their predominant electrochemical and sustainability characteristic. Owing to the double charge the Mg-ion possess a very large volumetric capacity of 3832 mAh/cm^3 prevailing both Li (2061 mAh/cm^3) and Na (1128 mAh/cm^3) and proposed multivalent Ca (2073 mAh/cm^3)[49]. It does not exhibit any dendrite growth hence allows metallic magnesium anodes in the battery pack and possible exploitation of complete theoretical specific capacity[33,50]. Nearly 2.3% earth abundance (~1100 times of Li) and homogenous distribution on earth crust ensure a potentially economic (~4USD/kg, 15 times lower to Li pure metal) battery technology for large-scale applications[51,52]. Moreover, Mg is highly resistant to SEI formation and the associated irreversible capacity loss, a property that ensures cheaper battery pack assembly[53]. Finally, environmentally benign characteristics of the Mg entrust easy disposal and recycling hence assure resource sustainability.

Since the prototype demonstration by Aurbach's group in 2000, magnesium battery attracted significant enthusiasm and was widely investigated[54]. Diverse anodes, cathodes, and electrolytes were attempted for elevated practical performance compatible with the commercial requirements. The details on ion-intercalation, electrode-electrolyte interfacial kinetics, changes within the electrolyte, etc. were analyzed using discrete *in-situ* and postmortem techniques for a better understanding of the Mg-ion storage mechanism to improve the electrochemical characteristics.

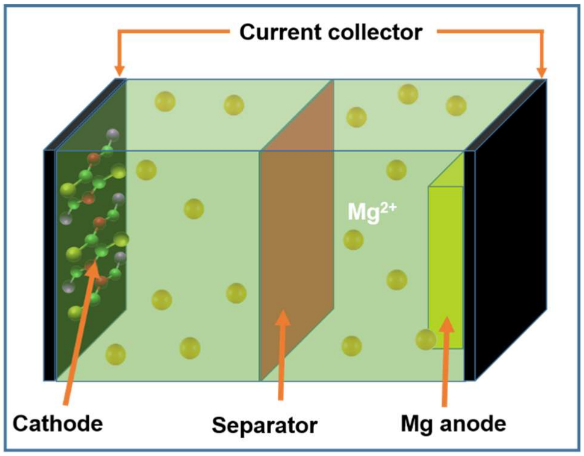

Figure 1.6. Schematic of a Magnesium battery.

1.4.1 Magnesium battery anodes

1.4.1.1 Magnesium metal anode

Owing to the dendrite-free electrochemical plating/stripping characteristics, metallic magnesium was extensively used as the preferred anode in Mg-based rechargeable battery research. Jackle et al. observed the interlayer surface diffusion and barriers of terrace surface diffusion of the magnesium metal, the proposed driving factors enabling a homogenous plating with super high coulombic efficiency (CE >99.5%)[55]. However, many investigations pointed to oxide and/or hydroxide layer formation on the metallic Mg under electrochemical conditions[56]. Surface layer formed by the non-aqueous electrolytes is capable of passivating the metal and causing a sluggish kinetics thereof.

Liang et al. proposed a nanostructured Mg-anode synthesized from the inexpensive $MgCl_2$ salt by the known ion-exchange method as a remedial measure to prevent the passivation layer formation[56]. Nanoparticle morphology effectively diminished the passivation layer intensity and the anode demonstrated dominant ion diffusion characteristics than the bulk magnesium. The introduction of reversible magnesium intercalation enabling artificial organic interface reported by Son et al. is another anode stabilization technique[57]. A polymeric film formed of polyacrylonitrile (PAN), magnesium trifluoromethane sulfonate (Mg-triflate) facilitated high Mg-ion reversibility. Nevertheless, magnesium metal anodes continue to be the most attractive anode for the Mg-battery system.

1.4.1.2 Insertion-type anodes

Following the success of the graphite anode in commercial LIBs, few materials were reported as possible Mg-ion intercalation anodes. Intercalation can be defined as a process in which the gust ion is reversibly inserted into the host lattice (Figure 1.7).

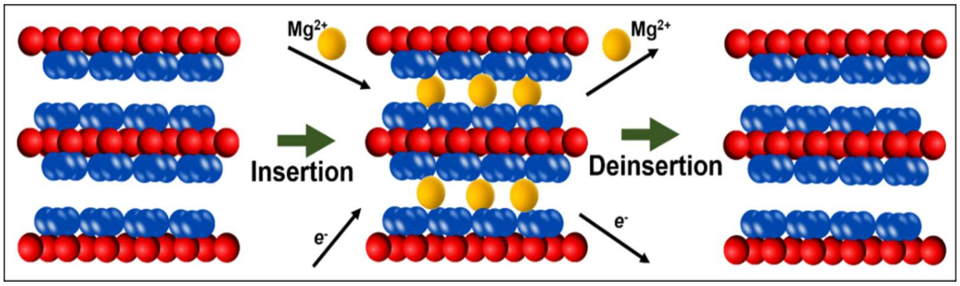

Figure 1.7. Mechanism of Mg-ion insertion/deinsertion to the host lattice.

Na et al. first identified the utility of spinel $Li_4Ti_5O_{12}$ (LTO) as the magnesium intercalation anodes. They reported a stable reversible specific capacity of 175 mAh/g and superior cycling performance up to 500 cycles with a negligible capacity loss (0.01% per cycle)[58]. A combined scanning transmission electron microscopy (STEM) - density functional theory (DFT) studies proposed a Li-ion replacement upon Mg-ion insertion. LTO transformed into $Mg_{2.5}LiTi_5O_{12}$ in the initial step and functioned as a reversible Mg-ion intercalation host thereafter[59]. They further reported LTO nanoparticle size effects, a particle size threshold of

≤40 nm and optimum particle size of 7-8 nm, for electrochemical Mg-ion intercalation. Chen et al. investigated layered $Na_2Ti_3O_7$ (NTO) nanoribbons as compatible Mg-battery insertion anode[60]. Similar to LTO, NTO undergone a structural reorientation into $MgNaTi_3O_7$ (MNTO) upon Mg-ion insertion and continues to be a stable phase enabling reversible intercalation with a specific capacity of 78mAh/g. Luo et al. identified NTO to MNTO conversion as a large capacity consuming process and propose $Na_2Ti_6O_{13}$ instead due to its almost double capacity than MNTO (147 mAh/g)[61]. A mesoporous Li_2VO_4 (LVO)/carbon hollow sphere Mg-ion intercalation anodes were reported by Zeng et al[62]. The specific electrode architecture provides a high initial specific capacity of 318 mAh/g. Good electrochemical performance of the electrode material was attributed to the high surface area and associated shortening of the Mg-ion diffusion path facilitating improved interfacial kinetics.

Theoretical investigations proposed several other materials such as C_2N, arsenene, borophene, graphyne, graphene allotropes, defective graphene, $MnSb_2S_4$, etc. as compatible high-performing Mg-ion intercalation anodes[63–67]. The practical implementations of these materials are underway. Nevertheless, the intercalation anodes are a trade-off between the specific capacity hence displaces the significant advantage (high volumetric capacity) of the Mg-system.

1.4.1.3 Alloying-type anodes

Alloying-type anodes are attractive choices owing to their high theoretical specific capacity and good compatibility with conventional electrolytes[68]. Theoretically, Group IIIA, IVA and VA elements are possible alloying-type anodes for the Mg-system. Their extensive (theoretical) specific capacities similar to the Mg-metal anodes are exceedingly dominant to intercalation type host. However, only limited elements were experimentally verified for Mg-ion compatibility. Usually, the electrochemical charge/discharge profile of an alloying-type anode consists of a low voltage plateau in the range of 0.1-0.4V corresponding to a biphasic transformation leading to alloy formation with Mg[68]. An alloying-type anode charge/discharge mechanism can be represented as shown in figure 1.8.

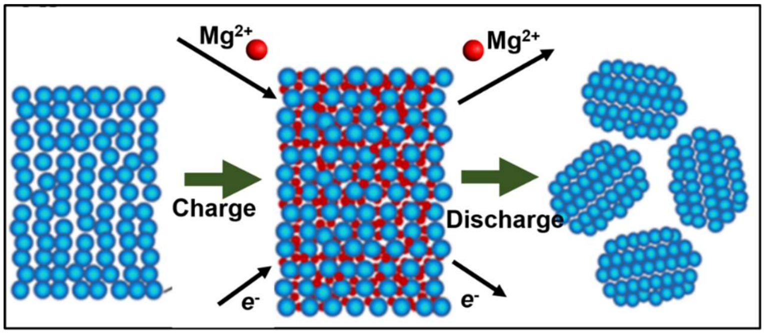

Figure 1.8. Schematic of the Mg-ion alloying-type anode mechanism.

Bismuth (Bi) is widely investigated alloying-type anode for Mg-batteries due to its attractive theoretical volumetric capacity (3783 mAh/cm^3)[69]. It exhibits rapid Mg-ion mobility than other alloying type anodes. Arthur et al. first reported the successful implementation of the Bi anodes having satisfactory cycle-life and capacity retention[70]. The specific nanotube architecture of Shao et al. also demonstrated subtle rate performance (216 mAh/g at 1.92 Ah/g) and cycling stability (303 mAh/g after 200 cycles). Benmayza et al. observed a simultaneous pulverization and amorphization of the Bi anodes under electrochemical cycling, which facilitated faster Mg-ion diffusion kinetics[71]. Several follow-ups work on Bi anodes by various groups point to the dominance of the material as a potential alloying-type anode for Mg-based battery technologies[72,73]. Owing to the successful implementation in Li-battery by Sony corporation, Tin (Sn) gained much attention and both of its allotropes were investigated as possible Mg-battery alloying-type anode. Despite the high volumetric energy density (7.4Wh/cm^3), the use of white (α-Sn) phase is restricted due to its thermal instability[68,74]. Meanwhile, β (Gray-Sn) phase found stable. Singh et al. obtained a maximum specific capacity of ~900 mAh/g for the β-Sn by forming an Mg_2Sn alloy phase[75]. Nguyen et al. increased the active material loading in the composite electrode (80 wt%) for having better performance[76]. Unfortunately, it induced severe side reactions and ultimately to lower performance. Asl et al.

proposed the use of an Mg_2S anode formed of an *in-situ* dealloying inside the Mg-battery[77]. Despite the complex activation step, it delivered a specific capacity of 300 and 150 mAh/g at 180 and 450 mA/g which only one-third of its theoretical limits. Indium (In), Lead (Pb), Antimony (Sb), as Aluminium (Al), Silicon (Si), Germanium (Ge), Phosphorus (P) were also proposed as feasible alloying-type anodes but developments are still in the early stages[70,74,78–81].

Inherent material property of the alloying-type anodes such as the exotic nature of Bi, low melting point of Ge, poor redox activity of Si and Sb, sluggish ion kinetics of Sn and Pb, etc. usually challenges the full exploitation of their theoretical capacities[82]. Multi-element alloying-type anodes are possible solution that can effectively shield the material property interference over the redox performance[68]. A selective combination of multiple elements in optimum ratios helps in ruling out the individual constraints and also brings out additional qualities that the single elemental host cannot provide. Various dual-element alloying-type anodes (Bi-Sb, Bi-Sn, In-Sn, Cu-Sn, Pb-Sn, Sn-Sb, Mg-Sn, Mg-Ga etc.) reported in the literature exhibit substantial improvement in redox chemistry and cycling stability over the corresponding single element anodes[68,82]. Figure 1.9 accumulates all the reported single and multi-element alloying-type anodes together with the specific capacity and cyclability parameters.

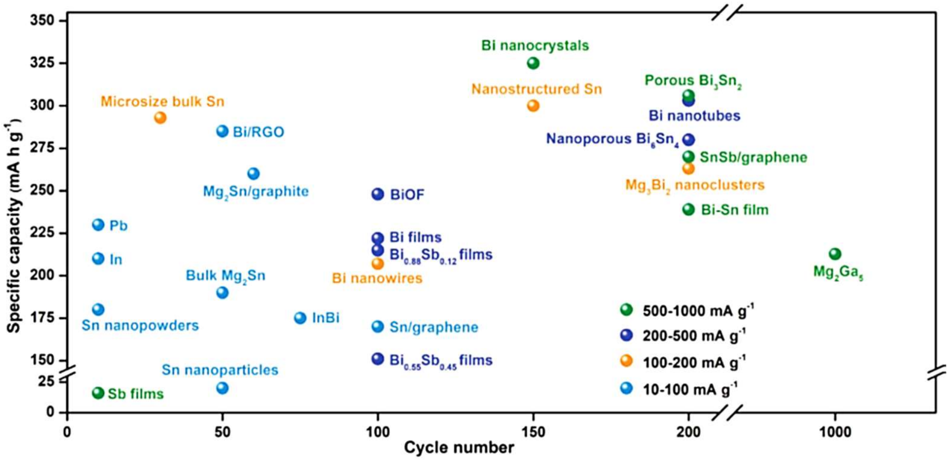

Figure 1.9. Electrochemical performance comparison of the reported alloying-type anodes.

Despite the attractive specific capacities, the practical implementation of alloying- type anodes is still challenging. Extensive stress generation associated with the simultaneous volume expansion with the repeated alloying cycles usually causes electrode pulverization resulting in rapid capacity loss. Though several strategies were predicated to buffer the volume changes, they have not yet successfully met the commercial requirements.

1.4.2 Magnesium battery cathodes

An ideal Magnesium battery cathode is a material capable of reversibly accommodating Mg-ions concurrently with two-electron reduction of the ion host, and provide double the capacity of the existing LIB cathodes[82]. Following the forerunning Li-ion battery technology, various intercalation, conversion and polymer type materials were investigated as feasible Mg-battery cathodes.

1.4.2.1 Insertion-type cathode materials

Transition metal sulfides

Rechargeable battery prototype demonstrated by Aurbach’s team utilizing Chevrel phase (Mo_6S_8) cathode was a breakthrough in the Magnesium battery research that was struggling due to the lack of a reliable cathode[54,83]. The cell provided an initial discharge capacity of ~80 mAh/g at 0.3 mA/cm^2 current density, and the cathode sustained more than 2000 charge/discharge cycles with a significantly larger capacity retention of 85%. The Chevrel phase Mo_6S_8 consist of a three-dimensional open structure having 12 ion storage sites per Mo_6 cluster facilitated rapid Mg-ion diffusion (Figure 1.10)[84]. Despite of its specific crystal properties such as multidirectional diffusion pathways, several cavities, flexible anion backbone etc. facilitating elegant ion storage, several shortcomings challenges its commercial implementation. The lower operating voltage and the low reversible specific capacities caused by the incomplete Mg-ion de-intercalation at the room temperature conditions limits its reliability[85]. Attempts such as nanostructuring, carbon coating, etc. are still underway to mitigate the shortcoming of this benchmark material[86–88]. Structural modification of the Mo_6S_8

by the partial or complete atomic-scale substitution of sulfur with larger chalcogenide such as Selenium (Se) is proposed to increase the electrochemical performance[89–91].

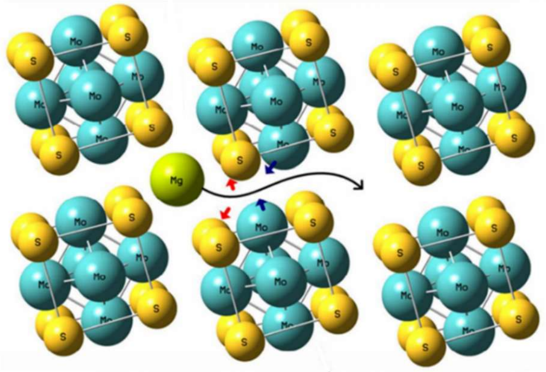

Figure 1.10. Schematic of the Mg-ion diffusion in Chevrel phase electrode.

TiS_2, a two-dimensional layered transition metal sulfide composed of repeatedly stacked sulfur-metal atom sheets is also received ample attention as a feasible Mg-ion insertion cathode[84]. The large interlayer spacing and weak van der Waal's interaction between the layers make TiS_2 an attractive intercalation cathode. TiS_2 nanotube design of Tao et al. provided an initial discharge capacity of 236 mAh/g and 78% capacity retention after 80 cycles[92]. The interlayer expanded designs of Yoo et al. improved both the specific capacity up to 400 mAh/g and cycling stability up to 500 cycles[93]. Studies by Sun et al. revealed a multistep Mg-ion storage mechanism of TiS_2 in which the ions undergo an irreversible initial occupation at the octahedral sites followed by reversible occupation at octahedral and tetrahedral sites[94]. Ion trapping and high Mg-ion migration barrier of TiS_2 cathodes (>1eV) necessitates elevated operational temperatures (~60 ºC) hence limits its room-temperature applications.

MoS_2 is a highly potential graphene-like material that has a long history of energy storage applications enabled Mg-ion insertion/extraction with a theoretical specific capacity of 233.2 mAh/g[95]. MoS_2 surfaces having a reduced activation barrier (0.48 eV) are more active towards Mg-ion storage than the bulk with a higher activation barrier (2.61 eV)[96]. Liang and coworkers demonstrated highly exfoliated MoS_2 cathodes with a specific capacity of 170 mAh/g, nearly 76% of the theoretical value[56]. Several strategies such as MoS_2/Carbon sandwiched microspheres, interlayer expansion, MXene supported MoS_2, etc. were implemented to improve the redox functionality[97–99]. Though it enhanced the specific capacity (~213 mAh/g) close to the theoretical predictions, the operating voltage and the cycle-life still need improvements.

Several other sulfides such as TiS_3, Ti_2S_4, CuS, VS_4, VS_2, Cr_2S_4, Mn_2S_4, Zr_2S_4, etc. have also been studied as Mg-ion battery cathodes[100–106]. Though they exhibited a considerable improvement of specific capacity and capacity retention, the working voltage continues to be at the lower ranges. Moreover, energy densities were also not compatible with the standard requirements.

Transition metal selenides

Transition metal selenides are analogous to the corresponding sulfides in which the Se atom replaces the S in the parent lattice. These materials exhibited elevated Mg-ion storage performance due to the larger diffusion channels with reduced gust ion-host lattice interactions and improved electronic conductivity resulting from weaker migration barrier for Mg-ion diffusion[107].

WSe_2 reported by Shen et al. is currently the most promising selenide cathode for Mg-ion battery. WSe_2 nanowires synthesized through chemical vapor deposition exhibited a stable discharge capacity of ~203 mAh/g at a lower current density of 50 mA/g and retained 70 % (142 mAh/g) at a higher current density of 800 mA/g[108]. Superior performance is believed to be due to the unique nanowire architecture having efficient Mg-ion insertion sites and short diffusion paths. Copper selenides is another attractive material that has a theoretical capacity of 260 mAh/g[82]. Various groups tuned its redox performances by adjusting the cuprous ions concentration. Micrometer-sized β-Cu_2Se cathode reported by Tashiro et al. exhibited a specific capacity of 117 mAh/g (~45% of theoretical capacity)[109]. Meanwhile, nonstoichiometric $Cu_{2-x}Se$ hierarchical designs of Xu et al. provided a much improved specific capacity of 210 mAh/g, excellent rate capability and cycling stability (300 cycles), gifted by the higher electronic conductivity (3000 times) of the nonstoichiometric lattice than the stoichiometric design[110]. $TiSe_2$ electrodes reported by Gu et al. also exhibited elevated performance than the corresponding sulfides[111]. Although the selenides demonstrate improvements in specific capacity and columbic efficiency than the analogous sulfides, operating voltage and the cycle-life are not yet reached satisfactory limits.

Transition metal oxides

Transition metal oxides are promising class of Mg-ion insertion cathodes due to the relatively high insertion voltage and specific capacity facilitated by the specific lattice configuration composed of a stable metal-oxygen bond. Owing to their high iconicity of the metal-oxygen bond and anodic oxidation potentials, they have been extensively investigated as Mg-ion redox hosts[85].

Manganese oxide (MnO_x) is one of the prominent Mg-ion battery insertion cathodes due to its high theoretical energy density, easily tunable redox properties, easy synthesis, environmentally benign nature and abundant polymorphism[85]. The cathode material survey of Gregory et al. first observed Mg-ion compatibility of the Mn_2O_3 and Mn_3O_4[112]. Both allotropes were reported to provide an open circuit voltage (OCV) of 2.4V and were found to accommodate 0.66 mol of Mg per formula unit resulting in a specific capacity of 224 and 154 mAh/g respectively. Nanosized α-MnO_2 electrode designs of Zhang et al. demonstrated a specific capacity of 280 mAh/g with an initial columbic efficiency ~100%. However, the capacity faded drastically in the subsequent cycles[113]. Arthur et al. attempted the electrode stabilization with potassium (K) additives. Specific K-αMnO_2@(Mg, Mn)O core-shell architecture was not much effective in resolving the capacity degradation[114]. A layered δ-MnO_2 electrode demonstrated more stable cyclability with a specific capacity of 230 mAh/g[85]. Mechanistic studies identified trapped water molecules within the crystal layers, which are believed to be advantageous for Mg-ion storage. Studies by Kim et al. identified Mg-ion compatibility of λ-MnO_2 that delivered a specific capacity of 330 mAh/g[115]. Despite the extensive research by several groups including Aurbach’s team, Toyota, etc., the issues of MnO_x electrodes due to the irreversible formation of electrochemically stable MgO during Mg-ion insertion, and the associated capacity degradation remains unsolved[116].

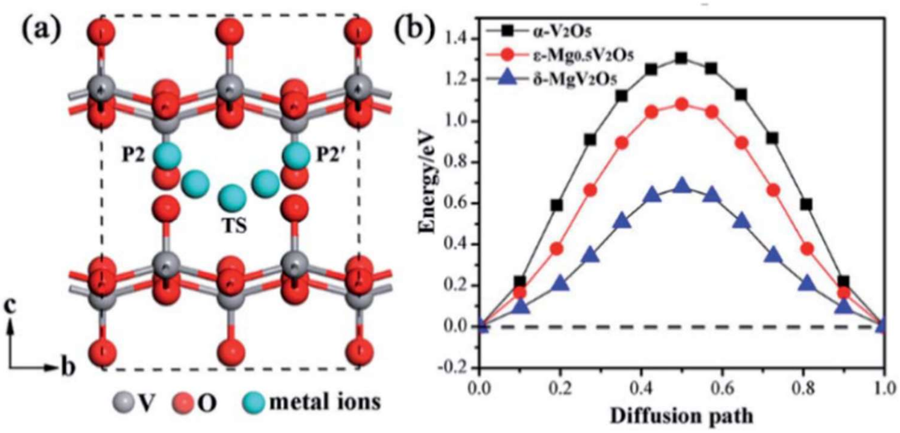

Figure 1.11. (a) Minimum energy diffusion path of Mg in δ-V_2O_5 cathode. (b) Diffusion energy of Mg-ions in different V_2O_5 polymorphs.

V_2O_5 is another widely investigated insertion-type cathode capable of accommodating 0.5 moles of Mg-ion per formula unit[85]. Theoretical explorations of the Mg-ion intercalation into V_2O_5 predicted a structural transformation from α-V_2O_5 to ε-$Mg_{0.5}V_2O_5$ and δ-MgV_2O_5, in which δ-MgV_2O_5 poses the lowest migration barrier energy (Figure 1.11)[117,118]. Several aspects such as nanostructuring, interlayer spacing enhancement, incorporation of water molecules to the lattice, etc. have been attempted for a reliable V_2O_5 based cathode[119,120]. A bilayer V_2O_5 nanoribbon grown on carbon nanofoam electrode architecture reported by Tepavcevic et al. exhibited an initial specific capacity of 240 mAh/g, but failed in capacity retention over extended cycling[121]. Hierarchical designs of a monodisperse spherical V_2O_5 of Mukherjee and coworkers also failed to maintain reliable cycle-life[122]. Novak et al. reported a method of enhancing the redox performances by controlled introduction of water molecules into the V_2O_5 lattice and the partial shielding of Mg-ion polarizations thereof[123]. Perera et al. used PEO as the polarization shielding agent which increased the inter lattice spacing by ~10%[124]. Several other strategies such as porous carbon frameworks hybrids, amorphous V_2O_5-

P_2O_5 hybrid, Mg-ion pre-intercalation, hydrogenation, etc. were also attempted to improve the operating voltage, specific capacity and capacity retention[125–129]. However, V_2O_5 based cathode technology has not yet matured for industrial applications.

TiO_2 is a fascinating cathode material for Mg-based battery electrochemistry due to its unique characteristics such as chemical stability, non-toxicity, low cost, potentially superior specific capacity (~295 mAh/g) and low volume change (<3%) under electrochemical insertion[53,130–134]. However, the poor ion diffusivity and the electronic conductivity cause capacity degradation upon extended cycling, especially at the high current densities[47,135]. Zhang et al. attempted commercial anatase TiO_2 compatibility with the Mg-battery system[136]. Though both capacity and cyclability were far below the required standards, it revealed potential of the material. Ma and co-workers modified anatase lattice with hydroxyl-fluorination and find an improvement in the specific capacity[132]. The cation deficient architecture reported by Koketsu et al. further enhanced specific capacity to 180 mAh/g[130]. Cycling stability also increased to 500 cycles with ~100% coulombic efficiency. Oxygen vacancy-rich black TiO_{2-x} nanoflakes designed by Wang et al. also exhibited similar electrochemical performance[137]. This study further demonstrated a capacitive type storage mechanism for the first time in TiO_2 based Mg-batteries.

Owing to the unique layered structure, orthorhombic MoO_3 is also considered as an attractive cathode material. Spahr et al. first demonstrated the Mg-ion compatibility of the material but structural changes during Mg-ion insertion limit its cyclability[138]. Prendergast et al. modified the MoO_2 lattice with fluorine doping that effectively boosted the electronic conductivity and Mg-ion diffusivity[139,140]. Nanoscale thick film architecture by Gershinsky et al. provided a high specific capacity of 220 mAh/g and a better potential of 1.8 V vs. Mg^{2+}/Mg[141]. Despite of its lattice characteristics favourable to be a good Mg-ion host, studies on MoO_2 are still in the early stages.

Polyanion cathodes

Polyanion compounds are another interesting category of cathode materials. They are more chemically stable than the conventional single anion oxides due to the induction effect of the polyanion group and deeper oxygen *p*-orbital levels. Polyanion materials can be broadly classified into olivine, spinal, NASICON (NAtrium Super Ionic CONductor) and Prussian blue analogous.

Olivine structures are potential cathode materials due to their ability for double electron transfer resulting in high energy density and structural stability during Mg-ion insertion (Figure 1.12a). $Mg_{1.03}Mn_{0.97}SiO_4$ is the first identified Mg-ion compatible olivine type cathode[84]. Nu Li et al. demonstrated Mg-ion storage in $Mg_{1.03}Mn_{0.97}SiO_4$ up to 0.81 mol per formula unit[142,143]. However, redox performances were largely dependent on the electrode morphology and mode of synthesis. Specific capacities of 43.2, 64.5, 100, 200 and 244 mAh/g were obtained for the solid-state synthesized, ball-milled, mesoporous, hierarchical and carbon composite cathodes respectively. Several other olivine materials such as $MgFeSiO_4$, $MgNiSiO_4$, $MgCoSiO_4$ etc. were also reported as Mg-ion compatible cathode materials[144–146].

Prussian blue analogs gained much attention recently due to its unique open cage crystal structures with larger embedded sites facilitating rapid Mg-ion intercalation (Figure 1.12b). They have a generalized $A_xMM'(CN)_6.yH_2O$ formula, in which A stands for the alkaline ions and M and M' are transition metals[147]. $Fe(Fe[CN]_6)$ (iron hexacyanoferrate) is one of the promising Prussian blue analogs with a specific capacity of 200 mAh/g by accommodating 1 mol of Mg-ion per formula[148]. Kim et al. demonstrated Mg-ion storage performance of $Na_{0.69}Fe_2(CN)_6$, which delivered an initial capacity of 70 mAh/g and cyclability up to 35 cycles with good capacity retention[149]. Prussian blue analog cathodes demonstrated excellent specific capacity and cyclability in the aqueous systems. For example, the NiHCF (nickel hexacyanoferrate) reported by Cui et al. exhibited cycling stability of 2000 cycles[150].

$K_{0.1}Cu[Fe(CN)_6]_{0.7}.3.6H_2O$ cathodes also demonstrated such attractive characteristics[151]. However, redox performance of these materials in organic electrolyte system is not attractive enough for real-world applications.

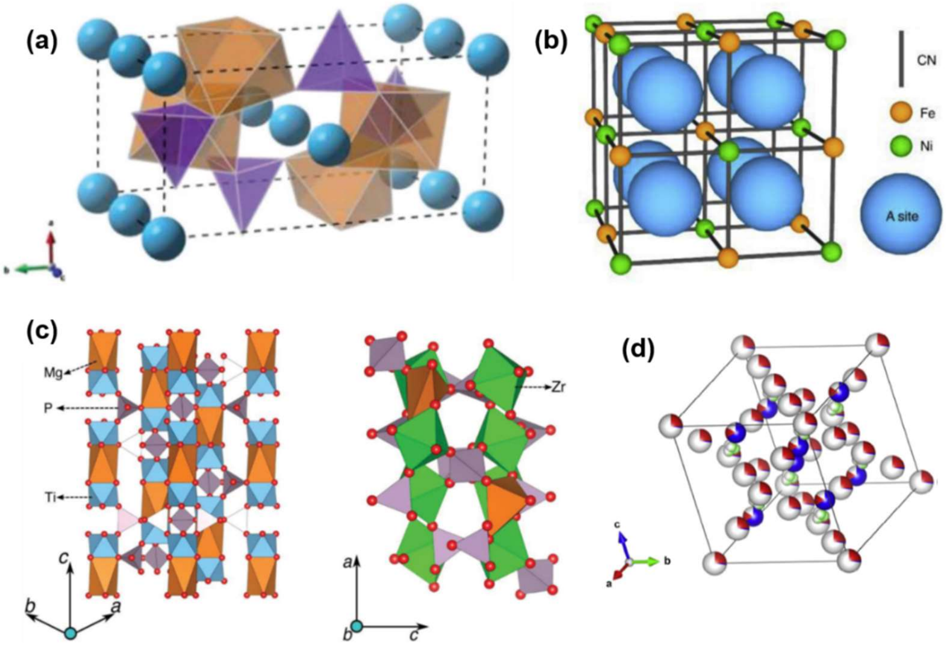

Figure 1.12. (a) Olivine structure of silicates (brown octahedral-transition metal, purple tetrahedral-Si, light blue spheres-Mg), (b) NiCHF Prussian blue analog, (c) Hexagonal and monoclinic NASICON crystal structure and (d) $Mg_{1.5}MnO_3$ cubic defect spinal.

NASICON is a family of inorganic compounds with a general structural formula $Na_{1+x}Zr_2Si_xP_{3-x}O_{12}$ (Figure 1.12c)[147,152]. These isostructural phosphates has high ionic conductivity and lattice spacing capable of accommodating gust ions with minimum structural distortions[152–155]. Hence, these structures were investigated by several groups as possible Mg-battery cathodes. $Mg_{0.5}Ti_2(PO_4)_3$ electrode reported by Makino et al. exhibited reversible intercalation of Mg-ions, but failed to maintain the capacity over long cycling[156]. Takahashi et al. observed an enhanced Mg-ion conductivity of this material gifted from the Ti doping[152]. $Mg_xV_2(PO_4)_3$ reported by Huang and coworkers delivered high average operating potential of 2.9V[157]. A couple of other materials such as $Mg_{0.5}Zr_2(PO_4)$, $CrMo(PO_4)_3$, $Mo_2(PO_4)_3$ were also reported[35,158]. Despite of the structural advantages, NASICON materials have not yet provided a reliable rate performance and cyclability required for practical applications.

Spinels are class of materials with AB_2X_4 crystal structure in which the anion (X) is arranged in the cubic lattice and the cations (A and B) occupying the octahedral and tetrahedral sites (Figure 1.12d)[147]. Sinha et al. successfully demonstrated Mg-ion storage in $MgMn_2O_4$ spinel by replacing Li with Mg in well-known $LiMn_2O_4$ cathode[159]. λ-MnO_2 is another investigated spinel cathode that exhibited a specific capacity of 80 mAh/g[160]. However, the cyclability of the material is limited due to the complex ion exchange between the Mg^{2+} and Mn^{3+} during the charge-discharge process. Okamoto and co-workers attempted $MgCo_2O_4$, Co_3O_4 and $MgMn_2O_4$ as compatible Mg-battery cathodes, but observed poor reversibility of the Mg- ions[161]. Spinel structured transition metal sulfides such as TiS_2, Fe_3S_4 etc. were also studied by various groups[100,162]. Despite of the promising initial capacities, they exhibited fast capacity degradation.

1.4.2.2 Conversion-type cathode materials

Conversion-type cathodes are a breakthrough in the field of Mg-battery as they can effectively bypass the sluggish insertion and slow diffusion of Mg-ions in the crystalline cathodes[85]. Sulfur is the most prominent candidate due to its high theoretical specific energy density (1722 Wh/kg), material availability (0.035%) and inexpensiveness ($55/metric ton). Studies by Robba et al. revealed the Mg-S battery mechanism[163]. According to the study, during the discharge, sulfur electrochemically converts into polysulfides which shuttle between the anode and cathode (Figure 13). Though it is a potential system, Mg-S batteries are in the initial stages of development. Muldoon et al. reported an Mg-S battery using a tetrahydrofuran (THF) based non-nucleophilic electrolytes[164]. It showed an initial discharge capacity of 1200 mAh/g but drastically degraded in the subsequent cycles. Due to the lower thermal stability of THF solvents, some groups investigated the feasibility of Glyme-based electrolytes. Nevertheless, electrolyte replacement dropped the initial specific capacity and facilitated better cyclability. Materials like Selenium, Iodine, etc. are also reported to be potential conversion cathodes for the Mg-battery system[165,166].

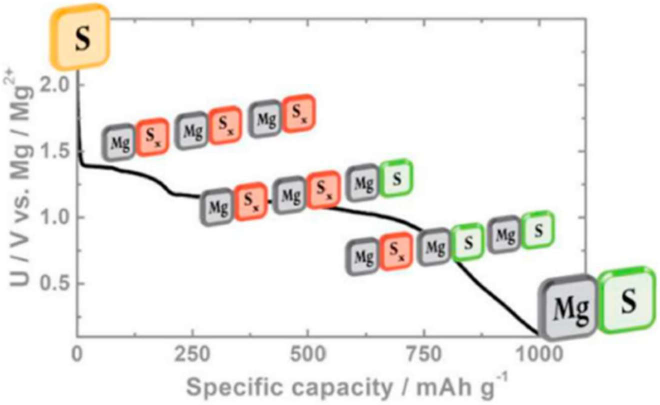

Figure 1.13. Discharge profile of Mg-S battery.

1.4.2.3 Organic polymer cathode materials

Redox-active organic polymer materials are promising cathodes that can mitigate several drawbacks of conventional insertion cathodes due to their open structures facilitating fast Mg-ion diffusion kinetics. Organic cathode materials can be classified into n-type, p-type and bipolar type, which respectively coordinate cations, anions and both respectively[85]. Anthraquinonyl sulphide (PAQS)is the first successful Mg-battery organic cathode reported in the literature[167]. It exhibited compatibility with varying electrolytes and provided a maximum reversible capacity of 200 mAh/g. Quinone-based monomers attracted much interest due to their high energy/ power density and cycling stability. Several imides and radical organic compounds were also proposed and investigated as possible Mg-cathodes. Despite the several attractions of these cathode materials, potential challenges such as excess electrolyte requirement, electrochemical aging, etc. need to be resolved before implementing them for practical applications. Table 1.2 summarizes the various cathode materials and their electrochemical characteristics reported in the literature.

Table 1.2. A summary of Magnesium battery cathodes reported[82,116,147].

Cathode	Initial capacity (mAh/g)	Voltage (V)	Cyclability (Cycles)	Capacity retention %	Columbic efficiency %
Mo_6S_8	80	1.2	>2000	80	-
MoS_2@C porous nanorods	120	1	200	80	90
Graphene like MoS_2	170	1.7	50	80	90
TiS_2	400	0.9	500	74	100
TiS_3	140	1.2	50	57	-
Ti_2S_4	200	1.25	40	70	98
VS_4/rGO	450	1.25	50	66	80
$TiSe_2$	110	1	50	80	-
Nanowire WSe_2	220	1.5	100	100	100
β-$Cu_{2-x}Se$	252	0.9	100	67	100
Cu_3Se_2	310	1	500	80	100
Mo_9Se_{11}	30	1.0	10	60	100
α-MnO_2	280	1.5	3	40	80
α-MnO_2/ Carbon black	310	1.5	10	40	70
Layered MnO_2	109	1.5	10	70	-
λ-MnO_2	330	1.5	5	50	95
Spinal MnO_2	330	2.6	-	-	-
V_2O_5/gel	450	1.5	35	60	70
V_2O_5 thin film	180	2.3	35	83	80
$H_2V_3O_8$	300	2.1	20	83	99
Anatase TiO_2 (Commercial)	80	0.8	50	43	92
$Ti_{0.78}\square_{0.22}O_{1.12}F_{0.4}(OH)_{0.48}$	170	1	500	80	100
TiO_{2-x}	190	1	400	70	100
Co_3O_4	74	1.4	35	60	90
RuO_2	100	3.5	25	80	-
MoO_3	230	1.7	10	95	95
$MgCoSiO_4$	300	1.6	30	80	95
$MgMnSiO_4$	111	2.9	-	-	-
$MgFeSiO_4$	330	2.2	5	100	87
$MgMn_2O_4$	170	1.81	50	23	-
MgV_2O_4	150	1.5	100	99	100
$MgCrMnO_4$	150	0.5	-	-	-
$Na_3V_2(PO_4)_3$	88	1.2	100	70	-
$K_{0.86}Ni[Fe(CN)_6]_{0.954}(H_2O)_{0.766}$	48	0.4	30	62	95

$Mg_{1.03}Mn_{0.97}SiO_4$/ Carbon	300	1.6	20	70	-
$MgFePO_4F$	55	2.2	10	60	140
$Li_3V_2(PO_4)_3$	200	0.4	-	-	-
AgCl	170	2	100	30	110
FeOCl	110	1	20	10	90
S	1200	1.7	20	65	-
I/Activated carbon cloath	240	2.1	120	95	100
1,4-polyanthraquinone	120	1.6	1000	66	100
Aromatic dianhydride-derived polyimides	161	1.6	8000	25	100
3,4,9,10-perylenetetracarboxylic dianhydride	126	1.7	200	63	100
Ethyl viologen	127	1.5	500	62	100
Pyrene-4,5,9,10-tetranone	310	2.2	210	85	110

1.4.3 Magnesium battery electrolytes

Electrolytes are crucial part of an electrochemical energy storage system. It facilitates ion-transfer between the anode and cathode, and hence directly influences battery performance. A reliable Mg-battery electrolyte is expected to exhibit potential stability toward both metallic anode and the cathode over a wide potential window. In the short history of the rechargeable Mg-batteries, several electrolytes were investigated. Starting from the early designs of Li-analogous, several custom-made ionic-liquid based systems, polymer or gel-polymer electrolytes, solid-state Mg-ion conductors, etc. were reported to be compatible with Mg-battery formulations. Figure 1.14 summarizes various types of Mg-battery electrolytes reported in the literature and their features[168]. Among the various types of the Mg-battery electrolytes magnesium complex - Lewis acids type electrolytes attracted huge interest due their better compatibility with the Mg-metal anodes exhibiting good Mg-ion deposition/dissolution characteristics[169]. All phenyl complex (APC) formed of phenyl magnesium chloride and $AlCl_3$ reported by Aurbach and coworkers dominated over the other combinations due to its superior Mg-ion deposition/dissolution characteristics.

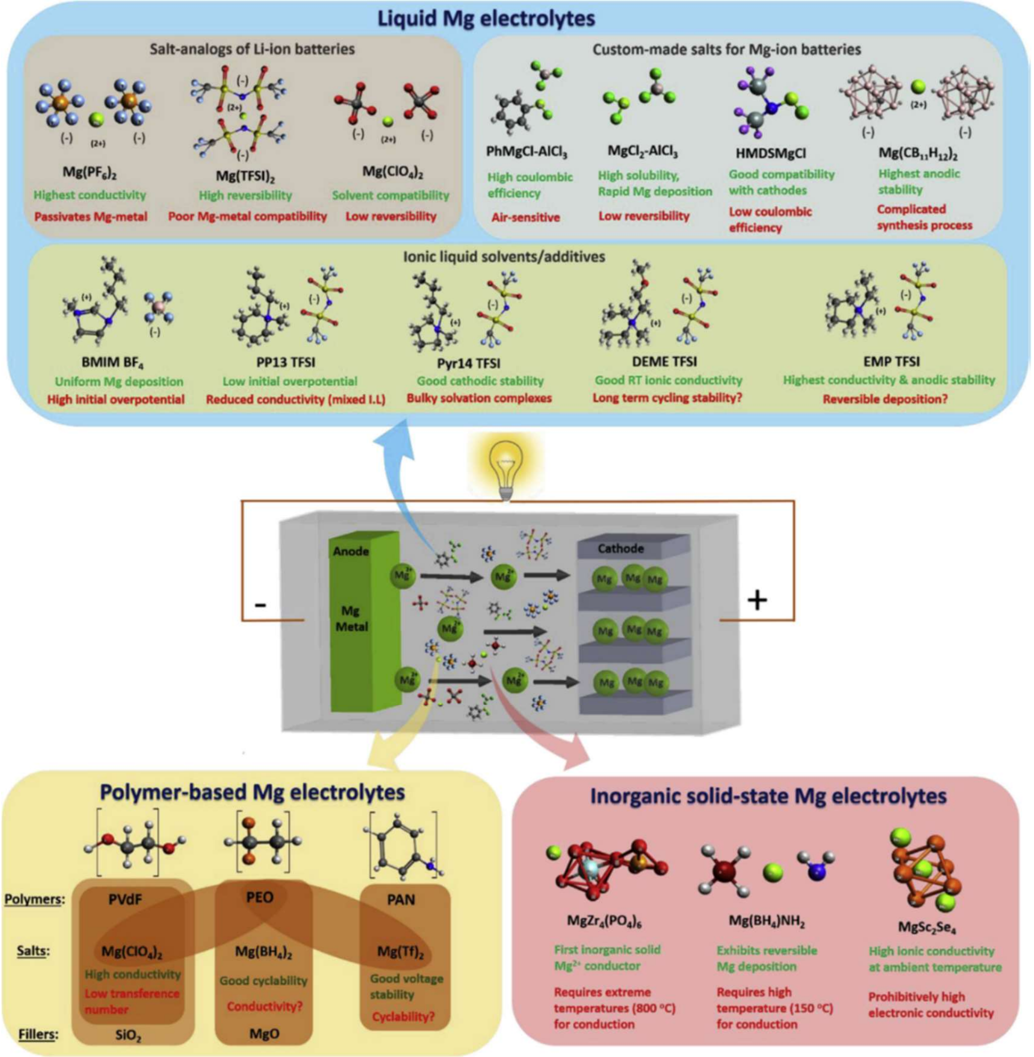

Figure 1.14. Schematic of the Mg-battery electrolytes along with their respective advantages (text in green) and their disadvantages (text in red). Shaded regions in 'polymer-based Mg-electrolytes' indicate the successful combinations.

1.5 Magnesium hybrid batteries

Magnesium hybrid batteries are a revolutionary concept for building practical batteries using metallic magnesium. Mg-electrolyte is modified with a compatible secondary ion such as Li, Na, Zn, etc. (Figure 1.15) in the Mg-hybrid battery design[170]. In addition, a dual-ion compatible material is selected as the cathode and the secondary ion dominates the cathode reaction, which effectively overcome the Mg-ion intercalation constraints[171]. Meanwhile, metallic Mg-anode enables complete exploitation of safety features and inexpensiveness[171]. Moreover, unique charge-discharge characteristics of Mg and secondary-ion dominate anode and cathode reactions respectively[171]. Dual-ion electrolyte in this case must provide sufficient number of the respective ions for the successful functioning of the hybrid battery[172]. Compatible electrochemistry at the anode and cathode facilitates faster ion kinetics and hence provides excellent rate performance, much elevated specific capacities, cyclability and energy/power densities rather than pure Mg-batteries. Presence of secondary-ion further enables the use of a variety of cathodes facilitating a better battery design[172,173].

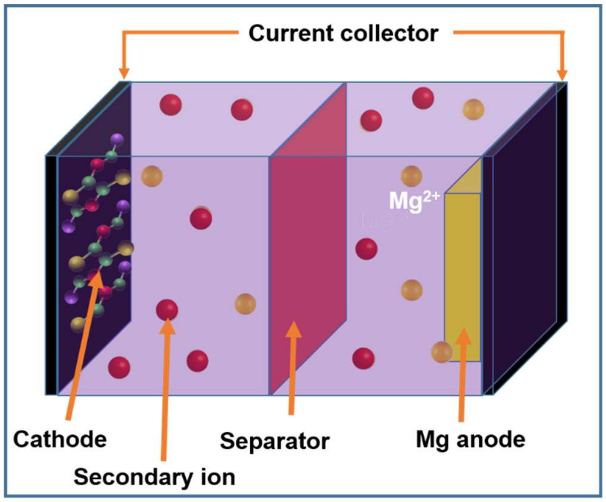

Figure 1.15. Schematic of Mg-hybrid battery.

1.5.1 Magnesium-lithium hybrid battery

Following the extensive literature background on Li-ion batteries, Magnesium-Lithium (Mg-Li) battery is one of the most studied hybrid architecture[174]. This hybrid composed of a metallic Mg-anode, Li-ion redox active cathode, and Mg-Li dual-ion electrolyte. It incorporates the safety features of Mg-anode and excellent reaction kinetics of the Li-ion intercalation cathode. Further, it can deliver higher energy density than both the respective single-ion systems. For example, well-known LTO/LFP battery can theoretically deliver a specific energy density of 143 Wh/kg and conventional Mg/Mo_6S_8 battery can give 134 Wh/kg. Meanwhile, an Mg-Li/LFP can provide a theoretical energy density of 246 Wh/kg, which is far higher than the individual systems[175].

1.5.1.1 Mg-Li hybrid battery cathodes

Theoretically, any Li-cathode materials can function as a potential cathode for the Mg-Li hybrid system. However, experimental studies put forward the Mg-Li dual-ion compatibility of the electrode material as mandatory condition for the proper functioning of the hybrid system[176,177]. In the recent past, several materials including oxides, sulfides, selenides etc. have been reported as Mg-Li hybrid battery cathodes.

Intercalation-type cathodes

Inspired by the chevrel phase based Mg-battery, various metal chalcogenides were investigated as potential Mg-Li hybrid insertion cathodes. Cho et al. examined Mo_6S_8 electrochemistry both theoretically and experimentally in Mg-Li dual-ion presence[178]. It revealed increased lithium occupation in the cathode interstitials compared to Mg-ions, which is also proportional to the Li-ion concentration in the electrolyte. At higher Li-ion concentrations (1M), cathode reactions were dominated by Li-ions, and Mg-ion activity was confined to the anode side. Though the system showed high reversibility and cyclability, specific capacities were limited to 120 mAh/g. Following the results of the Mo_6S_8, various groups without much success also investigated other metal chalcogenides such as MoS_2 and TiS_2[171,173,179,180]. Meanwhile, VS_4 cathodes provided a satisfactory increase of specific capacity over Mo_6S_8 (~650 mAh/g), but in exchange for the cycling stability (200 cycles)[177].

Several metal oxides were also reported as Mg-Li hybrid insertion cathodes. Vanadium-based oxides are one of the most studied groups for this purpose. Various groups investigated the compatibility of modified V_2O_5 lattices due to the Mg-ion incompatibility of the ground stage lattice configuration. Tang et al. reported $H_2V_3O_8$ cathodes composed of interconnected V_3O_7 layers[181]. This material exhibited a strain balancing *via* an inner lattice spacing adjustment simultaneously with the Mg-Li dual-ion insertion-extraction. Despite of the high specific capacity (275 mAh/g), this material encountered large capacity degradation (44% in 50 cycles). Other modifications such as VO_2(B), $NH_4V_4O_{10}$ and LiV_3O_8@GO also showed similar specific capacities, but improved capacity retention up to 500 cycles[182–184]. Meanwhile, $NaV_3O_8 \cdot 1.69H_2O$ nanobelt reported by Rashad et al. demonstrated a substantial improvement in specific capacity up to 450 mAh/g[185]. Despite of several attempts, cycling stability of vanadium-based oxides still needs substantial improvements.

Owing to the Mg and Li-ion compatibility, TiO_2 and its hybrids also gained much attention as Mg-Li hybrid cathodes. Su et al. investigated the Mg-Li dual-ion compatibility of the commercial anatase TiO_2[51]. It provided an initial specific capacity of 160 mAh/g and 86% capacity retention after 90 charge-discharge cycles. Meanwhile, carbon nanotube (CNT) hybrid of anatase TiO_2 exhibited improved specific capacity of 240 mAh/g[186]. Bitenc and coworkers studied the compatibility of well-known $Li_4Ti_5O_{12}$ with the Mg-Li hybrid system[187]. They found a good initial specific capacity (225 mAh/g) and capacity retention (93%). Zhu et al. modified the LTO cathodes with Sr-doping, which provided much enhancement in the cycle-life up to 300 cycles.

Few other materials such as Mn and Mo-oxides, metal phosphates, metal selenides etc. were also reported as possible Mg-Li hybrid cathodes[170,188–191]. However, performance of these materials in terms of specific capacity and cyclability need extensive improvements.

Conversion-type cathodes

Despite of the good cyclability and capacity retention, lower specific capacities limit the application of insertion type cathodes. Meanwhile, conversion type cathodes offer several times higher theoretical capacity. FeS_2 is one of the most known conversion type cathode, which poses a theoretical specific capacity of 894 mAh/g[174]. Zhang et al. probed the real-time performance of this material and obtained an initial reversible specific capacity of 600 mAh/g[192]. However, the system exhibited drastic capacity degradation within 200 cycles. Similarly, FeS cathodes having a theoretical specific capacity of 609 mAh/g provided a capacity of 500 mAh/g but exhibited a similar capacity degradation. Chen et al. modified FeS by hybridizing with carbon nanofiber (CNF) and obtained much-enhanced cycling stability up to 800 cycles[193]. CuS is another conversion cathode that demonstrated Mg-Li dual-ion compatibility. Micro flower architecture of Li et al. provided an initial specific capacity of 325 mAh/g[194]. Meanwhile, the CuS@CNT hybrid prepared by Zhang et al. delivered an improved specific capacity of 475 mAh/g[195]. Nevertheless, capacity degradation during extended cycling is a major challenge that needs appropriate solutions for real-world applications.

Capacitive- type cathodes

In recent years, capacitive type electrodes gained attention beyond conventional intercalation, alloying and conversion electrodes. These materials follow a different surface-controlled diffusion –independent storage mechanism imparting a negligible electrochemical strain. Consequently, they provide higher specific capacities and energy/power densities, fast charging and extended cycling stabilities than conventional electrodes. Owing to the specific attractions, several capacitive type materials were reported as compatible Mg-Li cathodes.

Bronze phase TiO_2 is one of the classic electrodes that follow capacitive type storage. A nanowire design reported by Meng and coworkers exhibited a substantial specific capacity of 300 mAh/g and 93% capacity retention after 200 cycles[196]. A modified nanoflakes design of Su et al. extensively improved the cycling performance (6000 cycles) and capacity retention (100%)[197]. Ti and V doped niobium oxides also exhibited a capacitive type storage characteristic[198]. They provide an initial specific capacity of 250 and 300 mAh/g respectively. However, the cyclability of both materials was not satisfactory. Meanwhile, vanadium-based electrodes $VTi_{2.6}O_{7.2}$ and VS_2 nanosheets exhibited an extensive cyclability of more than 1000 cycles with 80% capacity retention[104,199]. A lithiated V_2C MXene cathode proposed by Liu et al. provided an initial specific capacity of 675 mAh/g and cycling stability up to 500 cycles with an excellent (98%) capacity retention[176]. All these reports demonstrated the potential of capacitive type materials as Mg-Li hybrid battery cathodes, which can provide high specific capacity, cyclability and capacity retention required for their commercialization. Table 1.3 summarizes various Mg-Li hybrid batteries and their electrochemical performances.

Table 1.3. Summary of the performance index of Mg-Li hybrid battery cathode[172,174].

Cathode	Initial capacity (mAh/g)	Voltage (V)	Cyclability (Cycles)	Capacity retention %	Columbic efficiency %
Mo_6S_8	120	1.25	3000	95	100
MoS_2	240	1	250	50	-
MoS_2/Graphene	300	0.9	500	50	100
TiS_2	210	1.4	2250	90	99.9
VS_4	650	1.25	200	87	100
VS_2-GO	250	1.5	10000	60	100
Mn_5O_8	180	3	-	-	-
$(NiCoMn)_3O_4$	550	0.8	100	55	100
$NaV_3O_8.1.69H_2O$	450	1.2	150	44	100
VO_2(B)	275	1.75	500	66	100
$NH_4V_4O_{10}$	230	1.7	100	70	90
$H_2V_3O_8$	275	1.3	50	54	100
LiV_3O_8@GO	278	1.8	500	75	-
TiO_2-A	160	1	90	86	-
CNT@TiO_2-A	240	0.95	100	70	-
$Li_4Ti_5O_{12}$	225	0.9	50	93	-
$LiCrTiO_2$	150	0.75	100	92	100
$SrL_2Ti_6O_{12}$	100	0.6	300	75	100
MoO_2	225	0.8	50	66	-
$Fe_2(MoO_4)_3$	80	3	50	50	100
$Li_3V_2(PO_4)_3$	145	1	200	86	100
$LiFePO_4$	130	2.7	100	70	100
$FeFe(CN)_6$	120	2	50	56	-
VOCl	175	0.75	800	50	100
$FeSe_2$	550	1	100	2	100
$MoSe_2$/C	210	0.8	100	90	100
CuS	350	1.1	100	85	100
CuS/CNT	360	1.2	100	55	-
FeS_2	600	0.9	200	15	-
FeS/CNF	460	1	800	45	98
TiO_2-B nanowire	300	0.6	200	93	100
TiO_2-B nanoflakes	200	0.8	6000	100	100
$TiNb_2O_7$	250	1.5	50	40	100

VNb_9O_{25}	300	1.6	50	66	100
Ni-doped MnO_2/CNT	185	0.8	3000	75	100
$VTi_{2.6}O_{7.2}$	280	1.1	1200	85	100
VS_2 nanosheets	230	1.1	1000	88	100
V_2C MXene	675	1	500	98	100
Co(II)$(OH)_n$@Ti_3C_2	100	-	200	80	-

1.5.1.2 Mg-Li hybrid battery electrolytes

Electrolytes are crucial part of the battery that can directly influence the overall redox performance. Development of Mg-Li dual-ion electrolyte is a challenging process as the Mg-metal is prone to surface passivation film formation upon reaction with most of the common salts (Mg or Li) and aprotic solvents. Hence, only a few Mg-Li hybrid electrolytes are so far reported in the literature.

Owing to the excellent Mg-metal anode compatibility of the APC electrolyte, APC + LiCl in THF solvent is the most investigated Mg-Li hybrid electrolyte. Mg-Li dual-ion electrolyte can be prepared by dissolving an appropriate amount of LiCl in the APC solution[178,200]. It demonstrated a higher anode stability and gradually decreasing Mg-deposition overpotential simultaneously with the LiCl concentration denoting an increased electroactivity of the system.

Shao et al. reported another potential Mg-Li dual-ion hybrid combination composed of $Mg(BH_4)_2$ and $LiBH_4$[201]. Despite the good redox activity, this combination exhibited a relatively narrow stability window (0-2V). Cheng and coworkers recently discovered a new Mg-Li hybrid electrolyte composed of dimagnesiumdichloro dimer [DMDC, $Mg_2(\mu\text{-}Cl)_2(DME)_4$] cation complex prepared by reacting 0.4 M $MgCl_2$ and 0.4 M $AlCl_3$ added with 2.0 M LiTFSI in DME solvent[175]. It exhibited an excellent reversible Mg-ion deposition-dissolution over a wider voltage window of more than 3.4V vs. Mg. Good Mg-ion reversibility and relatively higher voltage window of the electrolyte made them the apt choice for high voltage Mg-Li dual-ion battery system.

1.5.2 Magnesium-sodium hybrid battery

Motivated by the successful realization of Mg-Li system, Mg-Na hybrid batteries were also proposed as an additional potential solution. Due to the inexpensiveness and abundance of both Mg and Na components, Mg-Na hybrid system is believed to be the answer for the search for low-cost, high-capacity and high energy/power density battery technology. In comparison to the Mg or Mg-Li concepts, Mg-Na is a relatively new idea that was first proposed and demonstrated in 2015. Hence, only a few dual-ion electrolytes and compatible cathodes are identified so far.

Walter et al. first reported a Mg-Na dual-ion battery based on FeS_2 cathode and an 0.2M $Mg(BH_4)_2$ + 2M $NaBH_4$ / diglyme hybrid electrolyte[49]. This system exhibited high reversible specific capacity of 225 mAh/g, energy density of 220 Wh/kg, and cyclability up to 40 with nearly 75% capacity retention. As an initial study, these performances were admiring. Bian et.al successfully replaced FeS_2 with TiS_2 without disturbing the specific capacity[202]. However, the design boosted cycling stability up to 20000 cycles even at a higher C-rate (20C). 2D framework of the TiS_2 helped to maintain structural integrity under extended cycling. $NaTi_2(PO_4)_3$@Carbon cathodes of Zeng et al. further extent cycling stability up to 26000 cycles with a 93.7% capacity retention[203]. Despite of the cycling stability, voltages of these designs were limited to ~1V. Li et al. demonstrated a high voltage (~2V) hybrid battery design using $Na_3V_2(PO_4)_3$ cathode and 0.2 M $[Mg_2Cl_2][AlCl_4]_2$/DME electrolyte[204]. $Na_3VCr(PO_4)_3$ cathode proposed by Rubio et al., $FeFe(CN)_6$ cathode proposed by Dong et al. and β-$Na_xV_6O_{15}$ cathode of Cabello et al. also exhibited a similar voltage improvement[205–207]. Kravchyk and coworkers recently demonstrated a unique high-voltage Mg-Na hybrid battery[208]. In addition to the high voltage $Na_{1.5}VPO_{4.8}F_{0.7}$ cathodes, they used β-alumina as an additional Na-ion conducting membrane on the cathode side. 2M $NaBH_4$ + 0.2M $Mg(BH_4)_2$ in tetraglyme and 1M $NaClO_4$ in PC were used as Mg-Na dual-ion and Na-ion electrolytes on the anode and cathode side of the battery (Figure 1.16) respectively. This special configuration provided a cell potential of 3.2 V, which is the highest among all the Mg-based hybrid battery systems reported.

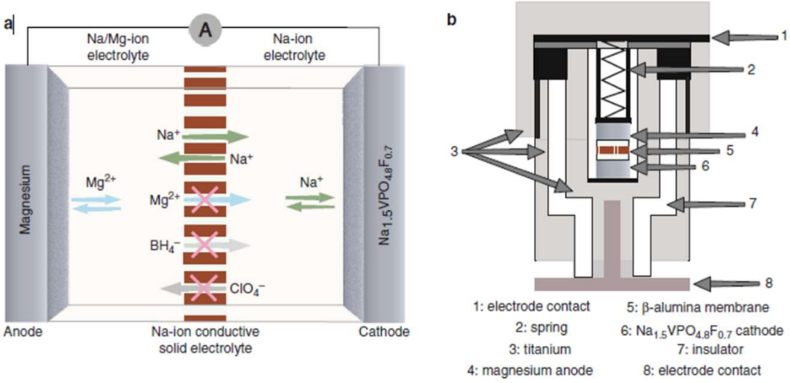

Figure 1.16. Schematic of the (a) charge-discharge processes and (b) cell configuration of a high-voltage Mg-Na dual-ion battery.

1.6 Drawbacks of current generation Mg and Mg-hybrid batteries

1.6.1 Mg-batteries

Magnesium batteries are proposed as a promising solution for the exponentially increasing energy demands beyond the LIB capacity. However, practically the specific capacities are far below the theoretical values mostly due to the sluggish kinetics of ion intercalation. Li and Mg-ions possess a similar ionic radius of 76 and 72 pm respectively[84].

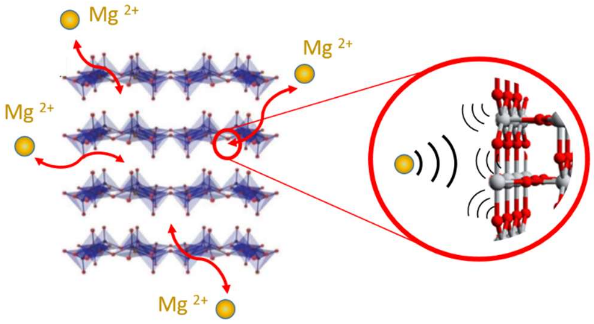

Figure 1.17. Electrostatic repulsion of the electrode host against the Mg-ion insertion.

However, double charge of Mg-ion leads to a high surface charge density of 120 C/mm^3 (Li-52 C/mm^3). Owing to the higher surface charge density, Mg-ions experience much higher electrostatic hindrance from the charge clouds of the host matrix during intercalation (Figure

1.17)[131]. This eventually causes a sluggish ion intercalation, hence poor practical specific capacities and rate performance.

Another bottleneck of the commercialization of the Mg-batteries is the lack of high voltage safe electrolytes compatible with the Metallic Mg-anodes[209]. Mg-analogs of the polar aprotic solvent (carbonates or nitriles) based electrolytes used in the LIB's are found to be incompatible with the Mg-system[153]. Unlike the formation of an SEI layer facilitating improved Li-ion transport in the LIB's, these electrolytes form an electrochemically stable MgO surface passivation film on the Mg-metal surface that is often impermeable to the Mg-ions (Figure 1.18)[52,210]. Elements such as fluorine in the triflate or TFSI based salts could also passivate the Mg- metal blocking reversible Mg-ion plating/stripping.

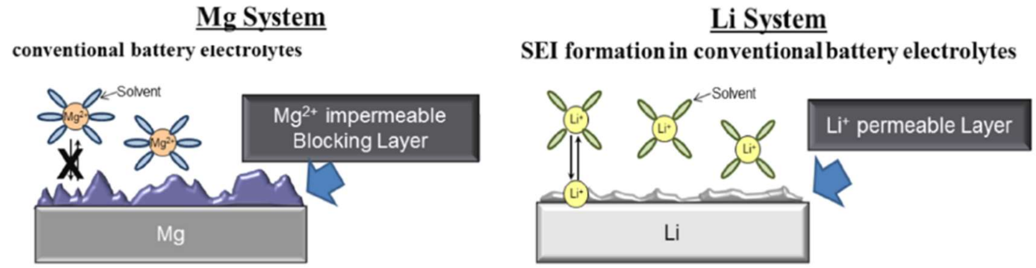

Figure 1.18. Comparison of surface layer formation in Mg and Li-ion battery systems.

In the early days of the Mg-battery development, organo-haloaluminate complexes dissolved in ethereal solvents such as THF or glyme-based solvents were proposed as electrolytes. Some of these electrolytes, specifically the widely used APC in THF electrolytes exhibited good Mg-plating/stripping characteristics. However, lower voltage window (2V) of these electrolytes hamper the use of high-voltage cathodes[209]. Additionally, low flash point of the THF solvents (6 °F) challenges ambient condition applications due to the solvent evaporation and also impart the potential hazard of thermal runaway and fire explosion at an elevated temperature that in effect limits its practical applications.

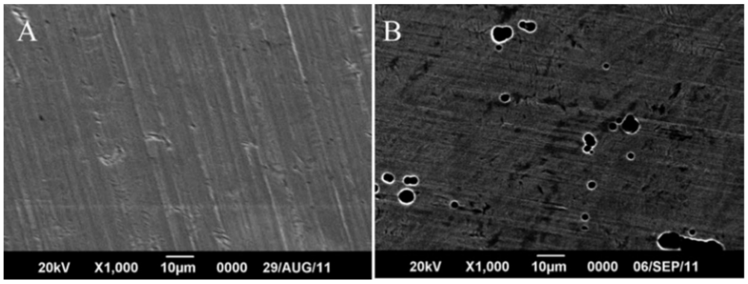

Figure 1.19. SEM images of stainless steel before (a) and after (b) exposure to the magnesium organo-haloaluminate electrolyte.

Most of the Mg-battery electrolytes are highly corrosive due to the presence of halide ions in the anion and/or cation components. These halide ions can cause the corrosion of the battery parts, especially at the higher charging potentials (Figure 1.19). Hence, use of these electrolytes in the coin-cell configuration containing current collectors such as Cu, Al and stainless steel are challenging[131,209].

Figure 1.20. Digital photograph of the dendrites formed from the electrodeposition of Mg-ion from a 0.5M Methyl magnesium chloride solution in THF.

Dendrite-free electrochemical deposition is one of the major advantages of Mg-system over the Li and Na technologies, facilitating the use of metallic Mg-anodes in the battery and complete exploitation of the theoretical specific capacity. However recently Verma et al. observed the Mg-dendrite formation on the metal anodes after reaction with methyl magnesium chloride in THF electrolyte solution (Figure 1.20)[211]. However, it is not yet accepted as a generalized phenomenon, detailed investigations are necessary before commercializing Mg-batteries.

1.6.2 Mg-hybrid batteries

Mg-hybrid batteries are proposed to bypass the setbacks of Mg-battery technology while maintaining its high capacity and safety credentials. However, some critical issues needs to be fixed to fully exploit its proposed advantages.

Theoretically, all Li-compatible cathodes can be implemented in Mg-Li hybrid system. However, dual-ion compatibility of the cathode materials is an essential criterion for a high-performance hybrid system[176,177]. For instance, carbonaceous materials are well-known anodes for Li and Na-batteries. However, due to the incompatibility with the Mg-systems, these electrodes exhibit poor redox performance in the Mg -Li/Na hybrid batteries. Hence, rather than directly replacing the Mg-battery cathodes with Li or Na-compatible electrode materials, dual ion compatible electrodes are mandatory for the hybrid systems. Only limited materials are so far identified for Mg-Li/Na dual-ion system. Performance of these materials reported being gradually improving with continued modifications in the electrode morphology and/or architecture. Nevertheless, they have not yet reached a reliable standard compatible with the commercial demands.

Despite of the electrolyte and cathode modifications, magnesium metal continues to be the anode for Mg-hybrid batteries. Sluggish Mg-ion intercalation at the cathodic side and the associated lower redox performances can be resolved with the introduction of the secondary ion in the electrolyte and the compatible cathode. However, the possibility of Mg-metal passivation and battery component corrosion by the electrolyte persist.

Commonly used Li or Na salts such as $LiPF_6$ or $NaPF_6$ exhibit poor solubility in the ethereal-based solvents. Hence, it is impossible to use in the known ethereal-based Mg-battery electrolyte to formulate electrolyte. Therefore, groundbreaking research starting from the scratch is mandatory to identify high-performing reliable dual ion salt pairs that can meet the requirements of Mg-ion plating at the anode side and easy charge storage at the cathode side.

Investigation of the dual-ion electrolytes is challenging due to a possible mutual interaction of the electrolyte components that can cause unwanted side reactions.

Voltage of the battery is a crucial factor that can directly influence the energy density of the system. The best performing Mg-Li/Na hybrid electrolytes (APC and $Mg(BH_4)_2$+$NaBH_4$ in diglyme respectively) exhibit a lower electrochemical stability window of 0-2V versus Mg-metal anodes[209]. Hence, these electrolytes cannot provide a high energy-density battery formulation. Furthermore, it restricts the use of any high voltage cathodes too. Although some high voltage stable electrolytes have been proposed, they still needs to be optimized to get satisfactory cyclability.

1.7 Concept of pseudocapacitance

Energy storage mechanisms can be broadly classified as faradaic, non-faradaic (capacitive) and pseudocapacitive storages[212]. Faradaic reactions are diffusion-controlled processes in which the ions are inserted into the electrode lattice resulting in a reversible phase transformation causing a sharp peak in CV and flat plateau in the charge-discharge profile[212]. Conventional battery materials are known to follow a faradaic mechanism[213]. On the other hand, non-faradaic or capacitive materials undergo a fast reversible physical double layer formation at the interface with no redox reactions[212]. High power and long cycle-life but low energy mechanism lead to a rectangular CV pattern and triangular charge-discharge profile[214]. Electric double-layer capacitor materials follow a non-faradaic mode of operation. Pseudocapacitance is an intermediate of this two mechanism that follows diffusion independent faradaic mode of operation with no crystallographic changes of the electrode[212].

Conway and Gileadi classified the pseudocapacitance process into underpotential deposition, redox pseudocapacitance and intercalation pseudocapacitance (Figure 1.21a-c)[215].

Monolayer adsorption pseudocapacitance or underpotential deposition is a mechanism mostly observed in metals that originates from a reversible surface electrochemisorption

(Figure 1.21a)[213]. An applied potential induces an adsorbed monolayer formation on the metal surface caused by the reduction of another metal ion, leading to a lower negative potential than the equilibrium potential, which is nothing but the underpotential deposition. Pb atom deposition on the Au surface is one of the typical examples of the mechanism. Pb preferentially deposits on the Au surfaces than on the Pb surface owing to an increased Pb-Au interaction dominant to the Pb-Pb interaction.

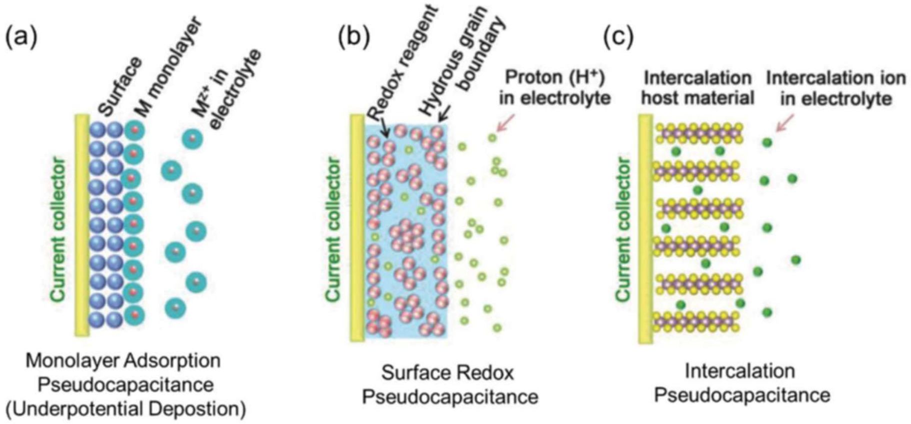

Figure 1.21. Different types of reversible redox mechanisms involved in pseudocapacitance.

Surface redox pseudocapacitance is a mode of ion-storage mechanism in which alkali ions are adsorbed onto the surface or near-surface of the electrode *via* a charge-transfer process (Figure 1.21b)[216]. This mode of storage was first observed in the hydrated RuO_2 electrodes. Later MnO_2, conducting polymers such as polyaniline (PANI), polypyrrole and poly(3,4-ethylenedioxythiophene) were also found to exhibit similar mechanisms. These materials follow a general strategy in which the charge storage is taking place by a fast redox reaction due to the intercalation of an alkali metal cation or a proton. However, the charge storage does not lead to any chemical transformation of the material but forms a functionalized molecular layer due to the faradaic reactions.

Intercalation pseudocapacitance is a diffusion-independent faradaic storage mechanism in which the ions undergo a rapid intercalation/deintercalation to the storage locations (conducting channels or layers) of the electrode material bulk rather than the surface or near-surface locations (Figure 1.21c)[217]. It is different from conventional intercalation due to the absence of any significant crystallographic phase changes simultaneous to the ion storage[212]. TiO_2-B, T-Nb_2O_5 are two prominent inherent intercalation pseudocapacitance materials (intrinsic pseudocapacitive)[218,219]. Several other materials such as MoO_x, MoS_2, TiS_2, MXenes, etc also found to exhibit tunable intercalation pseudocapacitance characteristics by various strategies namely size reduction, doping, lattice spacing modification, etc. (extrinsic pseudocapacitive)[217,220–222].

Despite faradaic characteristics, pseudocapacitive materials exhibit a phenomenological behavior similar to capacitors. Hence the fractional extent of the charge (X) storage and the potential (E) can be related as

$$E = E^0 + \frac{RT}{nF}\ln\frac{X}{1-X} \text{ ----- } (1.1)$$

Where R = ideal gas constant, T = temperature, n = number of electrons and F = faraday's constant. Further, the relative potential can be related to the extent of charge as

$$Q = C\Delta E \text{ ----- } (1.2)$$

Where Q = charge passed, C = pseudocapacitance and ΔE = potential change. This typical behavior of the capacitive storage hence resulting in pseudocapacitance[213].

Current (i_c) and the voltage (v) during CV measurements can be related as

$$i_c = \frac{dQ}{dt} = \frac{CdU}{dt} = Cv \text{----- } (1.3)$$

As both the capacitance and the capacitive currents are potential independent, CV patterns of normal capacitors follow a rectangular nature. Owing to the surface-controlled electrochemical processes, underpotential deposition and the surface redox pseudocapacitance also follow the same strategy (Figure 1.22a). Meanwhile, in the case of intercalation pseudocapacitance, the charge storage is taking place in the bulk but the kinetics is diffusion-independent, and hence result in overall capacitive behavior. Pseudocapacitive current contribution can be quantified by analyzing the CV patterns. The current response ($i(V)$) at a fixed potential usually is a combination of capacitance (i_c) and diffusion (i_d) current components. ie.

$$i(V) = i_c + i_d \text{ ----- } (1.4)$$

Meanwhile, capacitance current is proportional to the sweep rate v (eq. 1.3)[216]. On the other hand, according to the Rendle-Sewik equation, the diffusion current is proportional to the square root of the sweep rate. Hence, the eq. 1.4 can be modified as

$$i(V) = k_1 v + k_2 v^{1/2} \text{ ----- } (1.5)$$

The proportionality constants k_1 and k_2 describe the capacitive and diffusion-controlled processes. These constants can be obtained from $i(V)/v^{1/2}$ - $v^{1/2}$ plot as the slope and intercepts respectively[223].

Capacitive and diffusion contribution to the peak current (i_p) at any sweep rate can further be expressed with the power-law equation as

$$i_p = av^b \text{ ----- } (1.6)$$

Where a and b are two arbitrary variables[224].

Value of b that can be obtained as the slope of the linear scale log plot between current (i) and sweep rate (v) interpret the nature of the storage mechanism. A b value of 1 and 0.5 signifies a complete capacitive (electric double layer capacitor) and diffusion (conventional battery electrodes) mechanisms respectively (Figure 1.22d)[47]. The range between 0.5 to 1 can be considered as a transition region in which fractions of both capacitive and diffusion currents are existing. The b value also exhibits large dependence on the sweep rate voltage. Several materials that follow diffusion-dependent storage at the lower sweep rate exhibit a gradual transition to diffusion-independent mechanism with an increase of sweep rates. For example, graphene-coupled titanium oxide electrode reported by Chen et al. demonstrated nearly 50% diffusion-dependent storage at a lower scan rate of 0.2 mV/s. However, more than 90% of pseudocapacitive capacity contribution was observed at a higher scan rate of 10 mV/s.

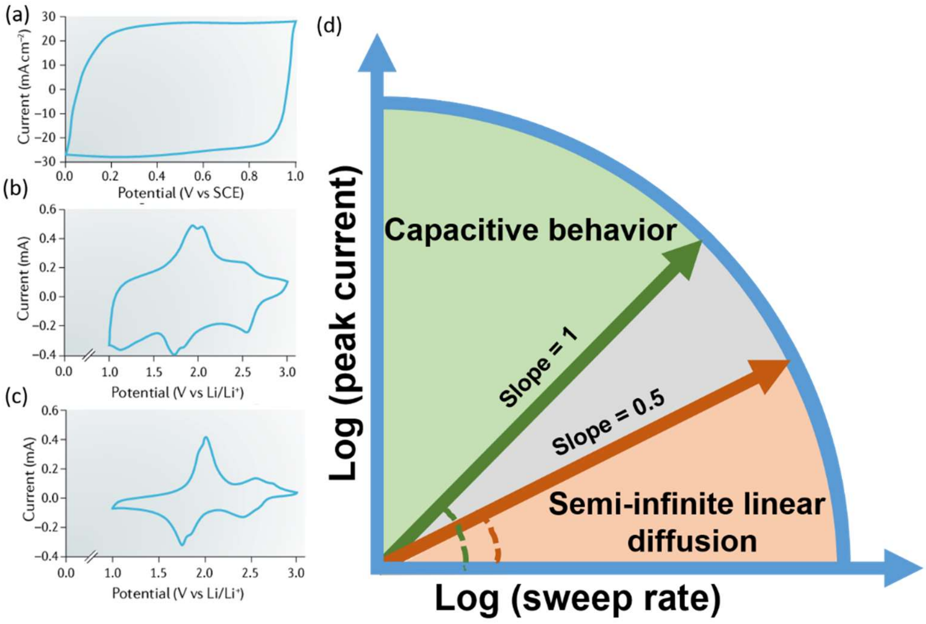

Figure 1.22. CV patterns of (a) surface redox pseudocapacitance, (b) intercalation pseudocapacitance and (c) conventional battery material.

1.8 Overview of the thesis

Despite of its numerous theoretical advantages, development of magnesium and magnesium-based hybrid batteries are facing several challenges. Sluggish ion-intercalation and associated low specific capacities, fast capacity degradation and limited cycling stabilities are the main drawbacks of magnesium system. Meanwhile, cathode incompatibility of dual-ion electrolyte is the major constraint for Mg-Li/ Mg-Na hybrid systems. Hence, this thesis focus on the development of reliable, high rate, high capacity and long-lasting cathode materials for Mg and Mg-Li/ Mg-Na hybrid batteries. This objective is tackled by designing and fabrication of pseudocapacitive electrodes that can store ions through multiple mechanisms. Integration of diffusion-independent pseudocapacitive ion-storage in electrodes enabled high specific capacity, rate performance and cycling stability compared to conventional Mg, Mg-Li/ Mg-Na battery systems. Different strategies such as nanostructuring, defect and interface engineering are implemented for the development of advanced high-performance electrodes[84,85,225–227]. This thesis is arranged in seven chapters as briefed below.

Chapter 1 describe literature background of Mg and Mg-Li/Na hybrid batteries. It details various types of anode and cathode materials, electrode engineering, existing electrolyte formulations, comparison of specific capacity, capacity retention, etc. and the practical challenges of the technology. It also includes a brief discussion of the concept of pseudocapacitance.

Chapter 2 narrates synthesis strategies used for cathode and electrolyte preparation for both Mg and Mg-hybrid system. It also discusses the details of various material and electrochemical characterization techniques used in this study.

Chapter 3 details oxygen vacancy induced pseudocapacitive Mg-ion storage in rutile TiO_2 nanowires. It reveals strong dependence of crystal structure defects and electrochemical performance of metal oxide cathodes.

Chapter 4 investigates the application of anatase-bronze hybrid nanosheets as cathodes for Mg-Li hybrid batteries. A detailed investigation of the effect of nanointerfaces between different polymorphs of TiO_2 is presented in this study.

Chapter 5 explains the effect of cobalt doping on the Mg/Li-ion storage performance and mechanism of TiO_2-A nanosheets. Doped nanosheets are implemented as cathodes for Mg-Li hybrid batteries, and detailed mechanistic studies are performed.

Chapter 6 demonstrates a long-lasting Mg-Na hybrid battery based on bronze TiO_2 cathode. This study demonstrated TiO_2-B nanosheet as potential pseudocapacitive cathodes, and investigated Mg/ Na-ion mechanisms in detail.

Chapter 7 includes possible future extensions of the present study in the field of Mg and Mg-Li/Na hybrid batteries

Chapter 2

Experimental Section

2.1 Synthesis of Electrode Materials

TiO_2 based nanostructured cathode materials were synthesized through solvothermal approach. This bottom-up synthetic method is chosen due to its specific characteristics such as the production of high-quality crystals, easy experimental setup, high yield and precise control over the morphology and/or phase by varying temperature, vapor pressure, time and reaction medium. Table 2.1 shows the chemicals (with technical specifications) used for synthesis.

Table 2.1. Chemicals used for the TiO_2 based nanomaterials synthesis

Chemical	Chemical formula	Supplier	Purity
Titanium (iv) chloride (20% solution in 2N solution in HCl)	$TiCl_4$	Acros Organics	99.99%
Titanium (iii) chloride (0.09M solution in 20% HCl)	$TiCl_3$	Acros Organics	99.99%
Ethylene glycol	$C_2H_6O_2$	Fisher Scientific	99.99%,
Cobalt acetate tetrahydrate	$Co(CH_3CO_2)_2.4H_2O$	Alfa Aesar	99.999%
Ammonia solution	NH_3	ITW reagents	30%
Absolute ethanol	C_2H_5OH	ITW reagents	99.5%

2.1.1 Synthesis of oxygen deficient rutile TiO_{2-x} nanowires

Oxygen-deficient rutile TiO_{2-x} nanowires were synthesized as described below (figure 2.1). In a typical synthesis, 4 mL of 20% $TiCl_4$ in HCl was uniformly mixed with 50 mL ethylene glycol and 4 mL of deionized water under constant stirring. Resulting mixture was then transferred to a 100 mL Teflon lined stainless steel autoclave and heated to 180 °C for 6 h (heating rate of 10 ºC/min). Product formed was collected and washed (centrifugal method) several times with a deionized water-ethanol mixture (1:1 Vol%) followed by drying at 80 °C under vacuum for 6 h. Control samples containing higher and lower amount of oxygen vacancies were also prepared by calcining the final powder at 400 ºC (Ar + 5% H_2), 600 ºC (air) and 1000 ºC (air) at a heating rate of 10 ºC/minutes.

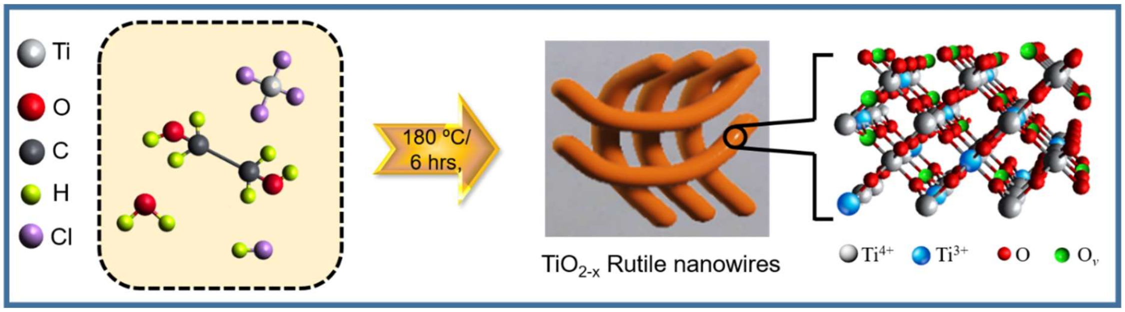

Figure 2.1. Schematic of the synthesis of rutile TiO$_{2-x}$ nanowires

2.1.2 Synthesis of hierarchical anatase-bronze hybrid TiO$_2$ nanosheets

Ultrathin hierarchical TiO$_2$ nanosheets were synthesized through a solvothermal method followed by heat treatment (Figure 2.2).

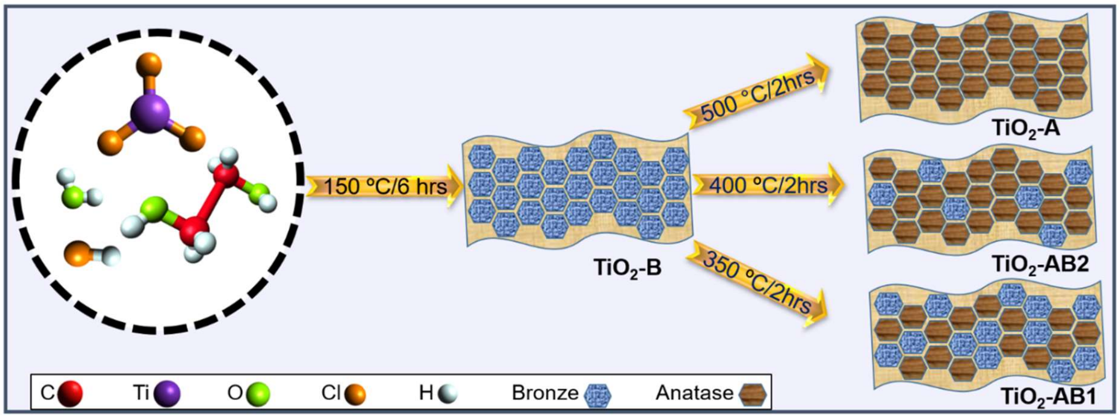

Figure 2.2. Schematic of the synthesis of single and dual-phase hierarchical TiO$_2$ nanosheets

In a typical synthesis, 4 mL of 20% TiCl$_3$ in HCl was uniformly mixed with 50 mL ethylene glycol and 4 mL of deionized water under constant stirring. Resulting mixture was then transferred to a 100 mL Teflon lined stainless steel autoclave and heated to 150 °C for 6 h. Precipitate obtained after cooling the autoclave to room temperature was several times washed with deionized water and ethanol followed by overnight drying at 80 °C under vacuum to form bronze TiO$_2$ (TiO$_2$-B) nanosheets. Calcination of TiO$_2$-B nanosheets at 350 °C, 400 °C for 2 h under air flow resulted in the formation of anatase-bronze dual phase TiO$_2$ nanosheets

(TiO_2-AB1 and TiO_2-AB2) with different anatase: bronze ratio. Phase-pure anatase TiO_2 (TiO_2-A) nanosheets are obtained at a higher calcination temperature of 500 °C.

2.1.3 Synthesis of $Ti_{1-x}Co_xO_{2-y}$ nanosheets

$Ti_{1-x}Co_xO_{2-y}$ nanosheets were synthesized through a two-step solvothermal reaction. In the first step, $TiCl_3$ was dissolved in hydrochloric acid, ethylene glycol and deionized water were taken in a relative volume ratio of 1:12.5:1 and made into a uniform solution under magnetic stirring (10 minutes). The homogenous solution was then heated to 150 °C for 6 hours in a half-filled Teflon-lined stainless steel autoclave. The product was collected and washed with deionized water and dried at 80 °C under vacuum.

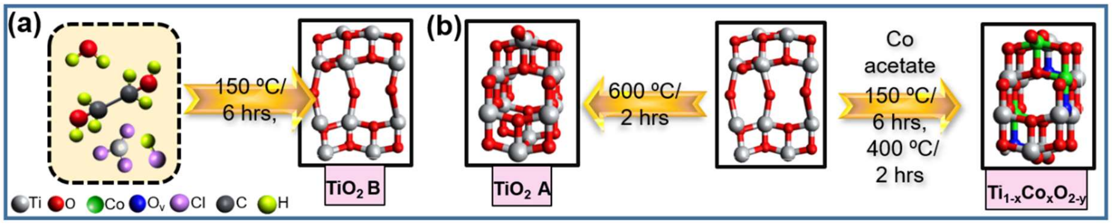

Figure 2.3. Schematic of the synthesis (a) TiO_2-B nanosheets and (b) cobalt doped TiO_2-A nanosheets

In the second step, 25 mg of the obtained powder and Cobalt acetate was further dispersed in 28 mL absolute ethanol under ultrasonication (10 minutes). Ammonia solution was added under continuous stirring to adjust the pH to 10. Final solution obtained was subjected to solvothermal reaction in a Teflon-lined stainless steel autoclave at 150 °C for 6 h. The precipitate obtained was collected, washed with ethanol and dried under similar conditions used in the first step. Powder obtained was calcined at 400 °C for 2 h under air-flow to form $Ti_{1-x}Co_xO_{2-y}$ nanosheets. 6 mg, 8 mg and 10 mg of cobalt acetate and 2.4 mL, 3.2mL and 4mL of ammonia solution was used to form $Ti_{0.92}Co_{0.08}O_{1.91}$, $Ti_{0.89}Co_{0.11}O_{1.98}$ and $Ti_{0.87}Co_{0.13}O_{1.87}$ nanosheets respectively. TiO_2-B nanosheets were calcined at 400 °C for 2 h under air-flow to form TiO_2-A nanosheets for comparing electrochemical performance.

2.2 Electrolyte preparation

Electrolytes were prepared by magnetic stirring inside an argon (99.999%) filled glove box with moisture and oxygen concentration less than 1ppm. Salts used were dried under vacuum at a constant temperature of 80 ºC for 12 h before the electrolyte preparation. Solvents were also dried subsequently with 5Å and 3Å molecular sieves (Honeywell Fluka) for one week. Chemicals used for various electrolytes are given in table 2.2.

Table 2.2. Chemicals used for Mg and Mg hybrid battery electrolytes

Chemical	Chemical formula	Supplier	Purity
Tetrahydrofuran (THF)	C_4H_8O	Acros Organics	99.9%
Bis(2-methoxyethyl) ether	$C_6H_{14}O_3$	Sigma Aldrich	99.5%
Phenylmagnesium chloride (2M solution in THF)	C_6H_5ClMg	Sigma Aldrich	99%
Aluminum chloride	$AlCl_3$	Alfa Aesar	99%
Lithium chloride	LiCl	Alfa Aesar	99.95%
Magnesium borohydride	$Mg(BH_4)_2$	Sigma Aldrich	95%
Sodium tetrahydridoborate	$NaBH_4$	Alfa Aesar	98%

2.2.1 Preparation of Mg battery electrolyte

All phenyl complex (APC) was used as Mg-battery electrolyte (0.4M). Dual-component electrolyte was prepared by dissolving Phenylmagnesium chloride (PhMgCl) and $AlCl_3$ in THF in an optimized 2:1 mole ratio. As $AlCl_3$ dissolution is exothermic, salt addition was maintained at a constant nominal speed to overcome unwanted side reactions. Mixture was allowed to stir for 4 h to ensure complete dissolution.

2.2.2 Preparation of Mg-Li hybrid battery electrolyte

Mg-Li hybrid electrolytes were prepared in a two-step process. In the first step APC electrolyte was obtained by mixing the required amounts of PhMgCl and $AlCl_3$ in THF. Required amount of LiCl is further added to the APC electrolyte to form the Mg-Li hybrid electrolyte. Mixture was allowed to stir for 12 h to ensure complete dissolution of the components.

2.2.3 Preparation of Mg-Na hybrid battery electrolyte

Mg-Na hybrid electrolyte was prepared by dissolving required amounts of $Mg(BH_4)_2$ and $NaBH_4$ in diglyme. As $NaBH_4$ solubility especially at higher concentrations is lower, electrolyte was prepared at its slightly elevated highest solubility temperature of 40 ºC. Mixture was allowed to stir for at least 12 h to ensure complete dissolution of salt.

2.3 Composite electrode preparation and battery fabrication

One of the main drawbacks of oxide-type battery electrode materials is its poor electronic/ionic conductivity. To overcome this limitation, a conductive agent was usually added to the active material. Acetylene black serves as the conductive agent in this study. Further, a binding additive - polyvinylidene fluoride (PVDF), was also used to ensure the inter-connectivity of electrode matrix and proper adhesion to the current collector. Ingredients were mixed into a uniform slurry in a volatile solvent *N*-Methyl-2-pyrrolidone (NMP) using a THINKY SR-500 slurry mixer at a speed of 800 rpm for 10 minutes. A typical electrode slurry composition is given in table 2.3.

Table 2.3. Typical composition of electrode slurries.

Component	Material	Content	supplier
Active material	TiO_2	70 wt%	Synthesized
Conducting additive	acetylene black	20 wt%	Alfa Aesar
Binder	PVDF	10 wt%	MTI Chemicals
Solvent	NMP	200 wt%	Aladdin Chemicals

Resulting uniform dispersion was coated on stainless steel foil current collector using doctor blade technique. This electrode fabrication technique is adequate to form uniform thin films of well-defined thickness. Obtained laminate was dried for 6 h at 80 ºC under vacuum to ensure complete solvent removal. Slurry composition, mixing time, coating standards and the drying environment were optimized to obtain a uniform laminate without cracks. Dried laminate supported on stainless steel current collector was cut in to a 1cm diameter disc using a hole puncher.

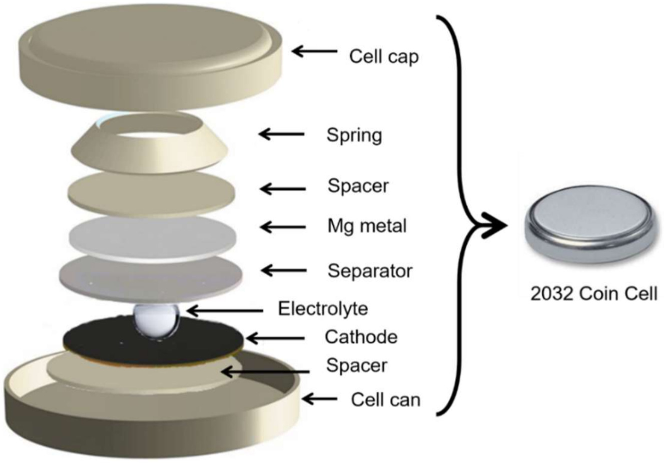

Figure 2.4. Coin cell parts and coin cell.

CR2032 type coin cells (Figure 2.4) were fabricated in argon (99.999%) filled glove box. Oxygen and moisture sensors/ absorbers aided to maintain high purity (H_2O, O_2 < 1ppm) atmosphere. Two-electrode cell consists of the composite working electrode (2-3 mg active material), polished Mg-metal anode (Alfa Aesar), glass fiber separator (Whatman, GF/B type-150mm) and the respective electrolyte.

2.4 Characterization Techniques

Various characterization methods were employed to effectively analyze material properties of the synthesized metal oxide powders and their specific electrochemical behavior as compatible Mg and Mg-Li/Na hybrid battery cathodes.

2.4.1 Materials Characterization

Following sections describe the characterization techniques employed to investigate physical, chemical and morphological properties of synthesized nanomaterials. Working principles and specifications of these instruments are also detailed.

2.4.1.1 X-ray Diffraction (XRD) Analysis

X-radiations are electromagnetic radiation having wavelength in the range of 0.01-10nm and energies in between 120 eV and 120 keV. It can effectively reveal the crystallographic structure, phase purity and physical properties of both powdered materials and thin films in a non-destructive fashion. The unique diffraction pattern generated by the interaction between the X-rays and atoms and electrons of the crystal is fingerprint of the materials. Hence it can be used to identify unknown materials by comparing with the diffraction pattern database of the international center for diffraction data (ICDD).

As the wavelength of X-rays and crystal lattice spacing of the materials are of similar ranges, diffracted signals from different layers of the material undergo a constructive interference when Bragg's law is fulfilled. Bragg's law of diffraction may be stated as

$$n\lambda = 2dSin\theta \text{ ----- } (2.1)$$

where n is an integer representing the orders of reflection, λ is the wavelength of the X-ray beam, d is the interplanar spacing between the atomic planes and θ is the angle made by the atomic plane and incident or reflected X-ray beam. Crystallinity of the samples was analyzed with PANalytical Empyrean high-resolution diffractometer equipped with a Cu-Kα X-ray source (λ=1.5406 Å) and Lynx detector.

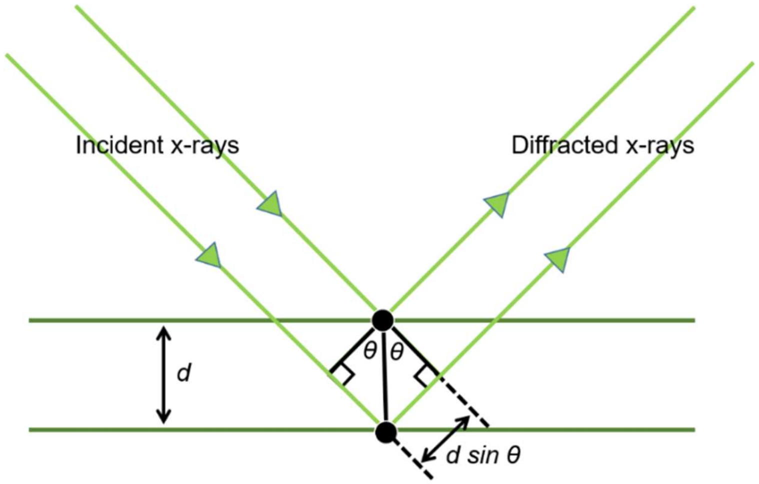

Figure 2.5. Bragg’s diffraction.

Average crystallite size of the samples was calculated using the Debye Scherrer equation

$$D = K\lambda/\beta Cos\theta \text{ ----- (2.2)}$$

where D is the crystallite size, K is the shape factor (=0.9), λ is the X-ray wavelength and β is full width at half maximum (FWHM) of the most prominent intensity peak.

Crystal structure variations with the stoichiometric changes and nanostructuring were evaluated in terms of the lattice parameter changes extracted from the X-ray diffractograms. The lattice constants may be evaluated as

$$\frac{1}{d^2} = \frac{h^2}{a^2} + \frac{k^2}{b^2} + \frac{l^2}{c^2} \text{ ----- (2.3)}$$

where h, k, l are the miller indices, a, b, c are the lattice constants and d is the inter-lattice spacing calculated from Bragg's law corresponding to the 2θ angles.

2.4.1.2 Raman Spectroscopy

Raman spectroscopy is a non-destructive technique to investigate the chemical structure, phase and polymorphism, crystallinity and molecular interactions. It relies on the interaction between a monochromatic light beam and the chemical bonds within the material.

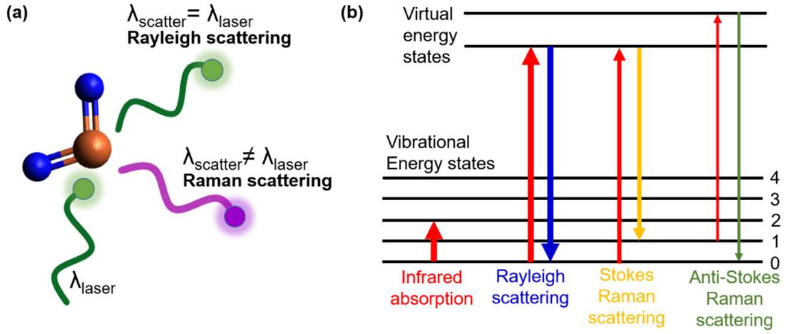

Figure 2.6. (a) Scattering of light by molecule (b) Different types of Raman scattering.

Molecular characteristics are analyzed from the light scattering by the target material. A laser source is used to initially excite the target. Most of the scattered light would be of the same wavelength as the incident light which is called the Rayleigh scattering (Figure 2.6 a). Equal wavelength scattering usually does not provide any useful information about the molecular structure. The small fraction of nearly 0.0000001% scattering at different wavelengths is called Raman Scattering. Phonon of the incident light excites the molecule above its ground state to an unstable virtual energy state. Under molecular relaxation, it returns to different rotational or vibrational stats simultaneously with a photon emission corresponding to the energy release (Figure 2.6 b). The new occupational energy state may be identified by comparing the difference between the emitted photon and incident light frequencies. An increase in the ground state energy level causes a shifting of the emitted photon frequency to the lower side to follow the energy conservation, designated as Stocks shift. Lowering of the ground stage energy leads to shifting to a higher frequency, designated as Anti-Stocks shift. The relative change in the energy spectrum corresponds to the phonon modes in the system. As the position and intensity of the bands in the Raman spectrum is a fingerprint of specific molecular bond vibration, a complete spectrum analysis reveals the crystallinity and stoichiometry variations despite their concentrations. In this study, a Renishaw PLC Raman spectrometer fitted with a 532 nm Nd: YAG laser was used for collecting the Raman spectra of electrode active materials. Laser power was limited to 5 mW to reduce sample damage.

2.4.1.3 Brunauer-Emmet-Teller (BET) Analysis

Brunauer– Emmett–Teller (BET) method is the most accepted approach to inspect the surface area of solid materials. Usually, the surface area is extracted from the nitrogen adsorption isotherms formed by the surface gas adsorption at its boiling point. According to BET theory, a multilayer gas adsorption is allowed and the layers are in equilibrium condition with no mutual interactions. Further, each adsorbed layer act as the adsorption site for the consecutive upper layers. The BET equation may be defined as

$$\frac{1}{n\left(\left({P_0}/{P}\right)-1\right)} = \frac{1}{n_m C} + \frac{C-1}{n_m C}\left(\frac{P}{P_0}\right) \text{ ---- (2.4)}$$

where P_0 = Saturation pressure, n = Specific amount of gas adsorbed at the instant of P/P_0, n_m = Monolayer capacity of the adsorbed gas and C= BET constant that exponentially related to the monolayer adsorption energy. BET constant provides the shape of the adsorption isotherm in the BET range. There can be six types of adsorption isotherms that correspond to the changes in the porosity and surface area (appendix-1).

BET equation requires a liner plot between the $1/[n(P/P_0)-1]$ and P/P_0. A typical multipoint BET plot is presented in figure 2.7. A minimum of three points is mandatory in the relative pressure range to meet the multipoint BET standard.

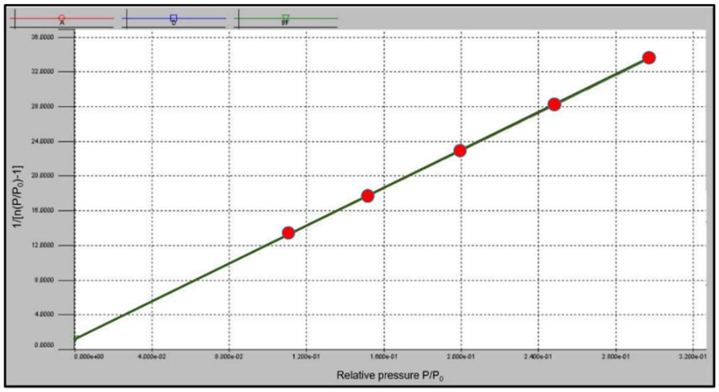

Figure 2.7. Multipoint BET plot.

Monolayer capacity n_m of the adsorbed gas may be calculated as

$$n_m = \frac{1}{s+i} \text{ ---- (2.5)}$$

where $s = \frac{C-1}{n_m}$ ---- (2.6)

and $i = \frac{1}{n_m C}$ ---- (2.7)

are respectively the slope and intercept of the multipoint BET plot. Further, total surface area (S_t) can be calculated as

$$S_t = \frac{n_m N A_{cs}}{M} \text{ ---- (2.8)}$$

where N is the Avogadro's number, M is the molecular weight of the adsorbate and A_{cs} is the adsorbate cross-sectional area (16.2Å for Nitrogen). Specific surface (S) is then calculated as

$S = \frac{S_t}{n}$ ---- (2.9)

Nitrogen adsorption and desorption isotherms of the materials were collected with a Quantachrome Quadrasorb surface analyzer at liquid nitrogen temperature. Before the analysis, the samples were degassed under a vacuum at 300 °C. Pore diameter and volume of the materials were evaluated from the desorption branch of the Barret-Joyner-Halenda (BJH) model.

2.4.1.4 X-ray photoelectron spectroscopy (XPS)

X-ray photoelectron spectroscopy is a surface analytical non-destructive technique often used for the quantitative investigation of the chemical composition and the electronic structure of a material. The technique works based on the famous photoelectric effect invented by Heinrich Rudolf Hertz and explained by Albert Einstein.

In short, the material surface is initially bombarded with a monochromatic X-ray beam. Electrons of the inner shells (K or L electrons) absorb the energy of the incident beam and ejected. Obtained ejected electron number or the power of electrons are plotting as a function of binding or kinetic energy. The plot is further evaluated for the qualitative characterization of the electronic and chemical properties of the material. Kinetic energy (E_k) of the ejected electron can be defined as

$E_k = h\upsilon - E_b - \Phi$ ---- (2.10)

Where $h\upsilon$ is the energy of the incident photon (h = Plank's constant, υ = frequency of the signal), E_b is the binding energy of the ejected electron and Φ is the work function of the instrument. A schematic of a typical XPS spectrometer is presented in figure 2.8.

XPS analysis was carried out with a Thermo Scientific Mutilab 2000 spectrometer fitted with an Mg-K_α and Al-K_α dual-anode X-Ray source with photon energies 1253.6 and 1486.7 eV respectively and a 110mm hemispherical sector analyzer. The core-level spectra were fitted using the PONER NOMBRE software package. Spectrum calibration was carried out with respect to the 285 eV C 1s binding energy.

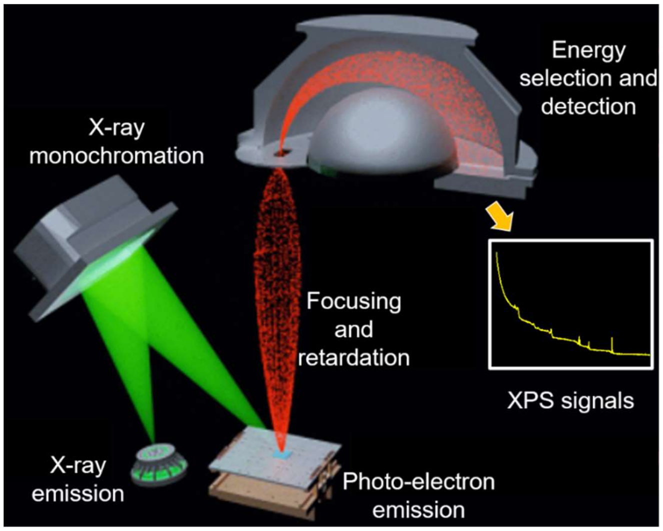

Figure 2.8. Schematic of an X-ray photoelectron spectrometer.

2.4.1.5 Electron paramagnetic resonance spectroscopy (EPR)

Electron paramagnetic resonance spectroscopy (EPR) is a non-destructive technique that is a branch of magnetic resonance spectroscopy that utilizing microwave radiation to inspect the chemical species with unpaired electrons in the presence of an externally applied static magnetic field.

An electron has two kinds of motion such as (a) spinning around the nucleus causing orbital magnetic moment and (b) spinning around its axis causing spin magnetic moment. The total spin angular momentum M_s can be expressed as

$$M_s = \sqrt{S(S+1)}\,\frac{h}{2\pi} \text{ ---- } (2.11)$$

Where S is the spin quantum number and *h* is the Plank's constant. The z component of a single unpaired electron can have only two possible values corresponds to the $\pm 1/2$ values of M_s. the magnetic moment μ_e can be expressed as

$$\mu_e = -g_e\,\mu_B M_s \text{ ---- } (2.12)$$

Where $g_e\mu_B$ is the gyromagnetic ratio and μ_B is the Bohr magneton which may be express as

$$\mu_B = \frac{eh}{4\pi m_e} \text{ ---- } (2.13)$$

in which e and m_e are respectively the charge and mass of electron and g_e is the free electron g-factor. The magnetic moment and the magnetic field (B) interaction can be express as

$$E = -\mu \cdot B \text{ ---- } (2.14)$$

Hence the two possible energy states of an unpaired electron are

$$E_{+1/2} = \frac{1}{2} g\mu_B B \text{ ---- } (2.15) \quad \text{and} \quad E_{-1/2} = -\frac{1}{2} g\mu_B B \text{ ---- } (2.16)$$

In the presence of an external magnetic field (B) the difference between these energy states is

$$\Delta E = h\upsilon = g\mu_B B \text{ ---- } (2.17)$$

Energy difference gradually increases with increasing the applied magnetic field intensity. Once the energy difference and the incident microwave radiation matches a phonon will be absorbed which will appear as an EPR signal.

An absorption signal will appear as shown in figure 2.9 (a.i). however, usually, the EPR spectrum is presented as the first derivatives (Figure 2.9 (a.ii)). The instrumental setting for EPR measurements is given in figure 2.9 b.

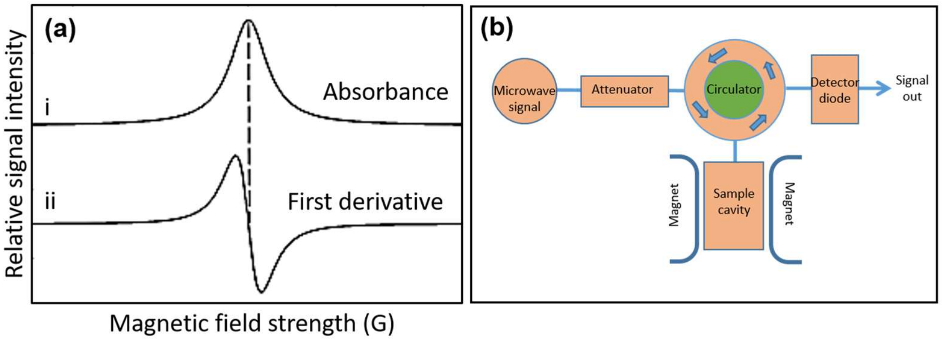

Figure 2.9. (a) Absorbance and first derivative spectrum. (b) Schematic of an EPR spectrometer.

In this study, a Bruker EMX spectrometer is used. The measurements were carried out in three different temperatures (120K, 200K and 300K).

2.4.1.6 Scanning Electron Microscopy (SEM)

Scanning electron microscopy (SEM) is one of the most frequently used methods for collecting high-resolution images of the surfaces. Electrons emitted by a high potential source (20kV) use to scan over the samples and the images are generating by successive capturing and amplification of the emitted signals from the sample surface.

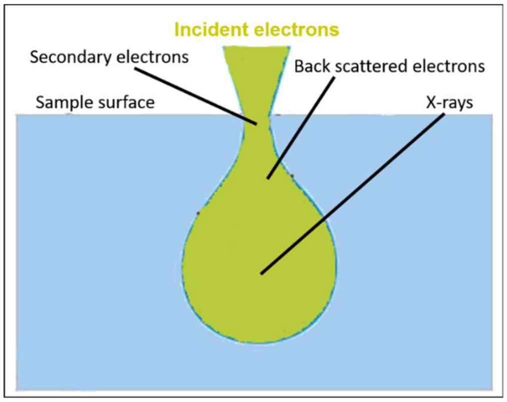

Figure 2.10. Signals generated from the SEM sample.

Incident high-energy electrons induce the generation of various signals from the sample (figure 2.10). Backscattered electrons are the high-energy electrons that originate from much deeper in the sample. It interacts more strongly with the sample and hence provides compositional information. Secondary electrons have much less energy than the backscattered electrons usually originate from few nanometers from the surface and provides the topographic information. In this study, a FEI Helios NanoLab 600i microscope scanning electron microscope operating at 20 kV was employed to investigate the morphology of synthesized TiO_2 nanomaterials.

2.4.1.7 Transmission Electron Microscopy (TEM)

Transmission electron microscopy (TEM) is working similarly to that of an optical microscope however, instead of visible light the electron beam is allowed to pass through the sample. Images are formed of the interaction between the electron beam and the target sample. Method is suitable to produce significantly higher resolution images owing to the small de

Broglie wavelength of electrons. In this study, Powder samples were dispersed in absolute ethanol with ultrasonication and spread over the carbon coated copper grids. An FEI Talos F200X FEG microscope working at an acceleration voltage of 200 kV was used to record the high-resolution transmission electron microscopy (HR-TEM) images and selected area electron diffraction (SAED) patterns.

2.4.2 Electrochemical Characterization

2.4.2.1 Electrochemical Impedance Spectroscopy (EIS)

Electrochemical impedance spectroscopy (EIS) is a technique to investigate the electrical response such as intercalation processes, electron transport, reaction rates and mass transport mechanisms of chemical systems. Quantitative outputs obtain from the measurements enable the precise evaluation of chemical mechanisms at the electrode-electrolyte interface and within the electrolytic solution. Analysis of Nyquist plot differentiates various internal resistance elements such as solid electrolyte interface (SEI) resistance, interfacial charge transfer, and electrolyte resistance for ion diffusion.

EIS tests were conducted with a ZIVE-SP1 electrochemical workstation at the open-circuit voltage (OCV) in the frequency range of 0.01 Hz to 1.0 MHz. Ion diffusion coefficients (*D*) were calculated with the formula.

$$D = \frac{1}{2}\left(\frac{R\,T}{AF^2\,\sigma_\omega\,C}\right)^2 \quad \text{---- (2.18)}$$

Where, R= universal gas constant, T= absolute temperature in Kelvin, A= electrode area, F= Faraday's constant, σ_W= Warburg impedance coefficient - determined from the slope of the linear plot between Z′ and $\omega^{-1/2}$ and C= ion concentration. ω and Z′ stand for the frequency and the corresponding impedance respectively.

2.4.2.2 Cyclic Voltammetry (CV)

Cyclic voltammetry (CV) is a dynamic technique for qualitative and quantitative investigation of redox processes occurring in the electrochemical system. It records current as a function of potential of the working electrode scanned between two boundary voltages at a certain scan rate. CV tests at various scan rates in the range of 0.1 mV/s to 1000 mV/s were conducted on an electrochemical workstation (ZIVE-SP1). Power-law equation was used to segregate the diffusion and capacitance contribution of the total storage at different scan rates as stated below.

$$i = a\, v^{b} \quad \text{---- (2.19)}$$

Where i and v stand for current and the scan rate, a and b are adjustable parameters in which b can be calculated as the slope of the log(i) vs log (v) plot. Fraction of the diffusion and capacitance contributions were quantified using the following relation.

$$i(v) = k_1\, v + k_2\, v^{1/2} \quad \text{---- (2.20)}$$

Where i is the total current, $k_1 v$ and $k_2 v^{1/2}$ are the current contributions from pseudocapacitance and diffusion process respectively. k_1 and k_2 are arbitrary constants that can be calculated from $i/v^{½}$ $vs.$ $v^{½}$ plot.

2.4.2.3 Galvanostatic Measurements

Galvanostatic charge-discharge studies are aimed to investigate the electrochemical Mg^{2+} or Mg^{2+}-Li^{+}/Na^{+} dual ion storage performance of the composite electrodes. Cells were subjected to a constant current and execute discharge-charge cycles with simultaneous voltage response monitoring. Usually, the study involves constant-current (CC) and/or constant-voltage (CV) charging and discharge. A CC charge is applied initially to increase the voltage up to CV for stabilizing the system. It avoids high currents that can lead to excessive temperatures and battery damage. Charge-discharge curves represent the voltage changes with respect to time under the applied constant positive (charge) and negative (discharge) currents. Currents (i) values are calculated using current density (A g^{-1}) in which g is the electrodes active material weight in grams. Thus, the resultant specific capacity (Ah g^{-1}) is the product of current density (A/g) and charging time (in hours).

In this study, galvanostatic measurements were performed using a Neware BTS-4000 battery cell tester under various current densities (25mA/g-1A/g). All electrochemical measurements were performed in the voltage window of 0-2V and 25 °C constant temperature conditions.

2.4.3 *In-Situ* XRD measurements

In-situ X-ray diffraction technique is a powerful tool for investigating the crystallinity, phase change and chemical composition variation of the electrode materials simultaneously with the electrochemical charging/discharging. Results are usually more detailed in comparison to the ex-situ measurements, which help to potentially improve the electrode material architecture for better battery performances. Significant advantages are (1) instant probing provides more reliable and precise data, (2) observation of non-equilibrium or fast-transient process during the redox cycles, and (3) avoid the possible contamination, relaxation or irreversible change happening with the ex-situ measurements.

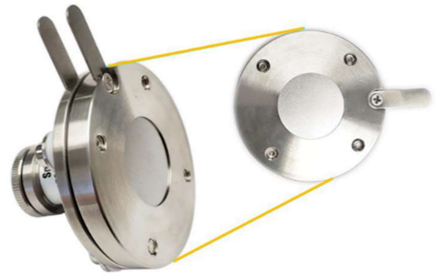

Figure 2.11. The split cell configuration used for in-situ XRD measurements.

Split-cell configuration (MTI Corporation) was used for the in-situ XRD measurements. However, Beryllium (Be) window was replaced with battery-grade Aluminum foil (Sigma Aldrich) for better investigation of the electrode materials with low crystallinity. XRD patterns were collected in each 0.1V interval maintaining a constant state of charge (SOC) at each voltage step.

Chapter 3

Realizing ultralong life, fast-charging magnesium batteries through oxygen vacancy induced pseudocapacitance of TiO_2 nanowires

3.1 Introduction

Despite of its several advantages including high theoretical capacities and dendrite-free electrochemistry, commercialization of Mg-batteries is hampered due to its mediocre electrochemical performance resulting from kinetically sluggish ion-insertion. Mg-metal (anode) surface passivation by electrolyte components and electrochemically stable MgO formation also inevitably deteriorate its redox performances. In the past two decades of Mg battery development, diverse materials, including metal oxides/sulfides, spinals, carbon hybrids, etc. were investigated as reversible intercalation host[153,228,229]. However, high current instability and cycling inefficiency still need substantial solutions. TiO_2 has been investigated as a versatile Mg battery cathode owing to its good theoretical capacity (294.5 mAh/g or 0.5 moles of Mg), exceptional thermal/chemical stability, nontoxicity, low cost and minimal volumetric change (~5%)during charge-discharge process[53,130–132,134,136,196]. However, its poor electronic conductivity together with the Mg-ion's inherent insertion constraints severely deteriorates its practical application[47,135]. Performances are further lowered with the c-axis intercalation constrain of the rutile TiO_2 polymorph. Oxygen vacancy defect engineering is a viable route employed to enhance the metal oxide redox functionality[137,217]. Defect-induced bond relaxations lead to surface reconstructions and ultimately to disordered lattices[230]. Further, it enriches the carrier concentration hence nourish electrical conductivity altogether elevates overall electrochemistry[137,231]. Pseudocapacitance is another recently demonstrated technique to enhance ion-storage capacity[224,232]. Unlike conventional Mg-ion storage mechanisms, diffusion independent pseudocapacitance facilitates surface and/or near-surface storage independent of bulk electronic-ionic conductivity[212,213]. Hence, it imparts minimal volume changes, which resulted in electrode robustness and thereby substantial cycling stabilities even at higher current rates. Though both approaches are demonstrated for the Li and Na-ion systems, they are seldom investigated to improve the Mg-ion intercalation.

Herein we demonstrated an oxygen vacancy induced pseudocapacitance of rutile TiO_2 nanowires for next generation fast charging ultralong life magnesium batteries. Rational design and synthesis of the defective TiO_2 cathode is based on the following aspects. (1) One-dimensional nanowire is selected as the preferred morphology due to its superior charge transfer kinetics, improved ionic and electronic conductivity. (2) Oxygen vacancies provide additional Mg-ion diffusion pathways by generating disorderness in the crystal structure, promoting pseudocapacitive storage. Exceptional Mg-ion storage performance of oxygen deficient rutile TiO_2 nanowires makes it a suitable cathode material for high rate and ultralong life fast charging magnesium batteries.

3.2 Results and discussion

3.2.1 Synthesis and characterization of rutile TiO_{2-x} nanowires

Oxygen deficient rutile TiO_{2-x} nanowires are synthesized through a solvothermal method. Reaction environment played a significant role in the highly disordered-one dimensional nanostructure formation. Abundance of H^+ and Cl^- (released by HCl dissociation and $TiCl_4$ hydrolysis) ions slow down the hydrolysis rate and the available growth units thereof. Besides, higher ethylene glycol (EG) volume (~86%) increases the solution viscosity hence diminishes ion diffusivity. Consequently, under constrained circumstances, crystallites preferentially grew in the thermodynamically favorable (lowest Gibbs energy) nanowire structure. Partial EG burning in corollary to reaction temperature (180 °C) close to the boiling point (~197 °C) creates an oxygen-deficient medium similar to the carbothermal reaction. This promotes the formation of oxygen vacancies in the resulting rutile TiO_2 nanowires. Oxygen vacancies of rutile TiO_2 nanowires are further controlled by heat treating under oxidizing (air) or reducing (Ar+H) atmosphere.

Morphological and the structural characteristics of TiO_2 nanowires are investigated in detail both qualitatively and quantitatively. Major reflections in the X-ray diffraction patterns

(Figure 3.1b) can be indexed with a P42/mnm space group corresponding to rutile TiO_2 (JCPDS no. 88-1172). Minor shift in the diffraction peaks, reduced FHWM (increased crystallite size), and reduced lattice spacing are observed (Table 3.1) with a decrease in oxygen vacancies (increase in calcination temperature).

Table 3.1 Crystallite size and d spacing variation of the various TiO_{2-x} nanowires extracted from the XRD.

	Crystallite size (nm)	**d (Å)**
$TiO_{1.6}$	7.79	3.249
$TiO_{1.7}$	5.87	3.244
$Ti_{1.89}$	18.75	3.229
TiO_2	40.45	3.228

Raman analysis provided further details of the degree of oxygen vacancies present in rutile TiO_2 nanowires (Figure 3.1c). Spectra of rutile TiO_2 samples exhibited characteristic B_{1g} (141.35 cm^{-1}), E_g (445.93 cm^{-1}), A_{1g} (608.02 cm^{-1}) Raman bands, a number of second overtones (232.77 cm^{-1}, 357.56 cm^{-1}, 547.51 cm^{-1}, 698.71 cm^{-1}) and a nanosize activated surface vibrational mode (115 cm^{-1}). These vibration modes experience a band broadening with an increase in the non-stoichiometry caused by oxygen vacancies (Table 3.2). Widening of low frequency bands and E_g band redshifting are also observed in proportion to 3D phonon confinement effects occurring with the crystallite size reduction.

Table 3.2 Band position and FHWM changes of Raman active bands of the various TiO_{2-x} nanowires

	E_g		**A_{1g}**	
	Raman shift (cm^{-1})	**FHWM (cm^{-1})**	**Raman shift (cm^{-1})**	**FHWM (cm^{-1})**
$TiO_{1.6}$	433.6	60.1	606.0	66.0
$TiO_{1.7}$	455.3	39.9	607.8	43.4
$Ti_{1.89}$	446.1	38.1	608.5	39.6
TiO_2	446.6	33.9	609.0	37.1

Existence of oxygen vacancies was qualitatively probed with Electron Paramagnetic Resonance spectroscopy (EPR) (Figure 3.1d). Resonance signal at g = 2.014 of rutile $TiO_{1.7}$ nanowires indicates substantial amount of superoxide radicals (O_2^-) trapped at the oxygen vacancies. Rutile $TiO_{1.6}$ nanowires exhibited a signal at g = 2.003 representing trapped electrons (F-center) exposed after oxygen radical release. Meanwhile, EPR signal intensities reduced considerably with a decrease in oxygen vacancies.

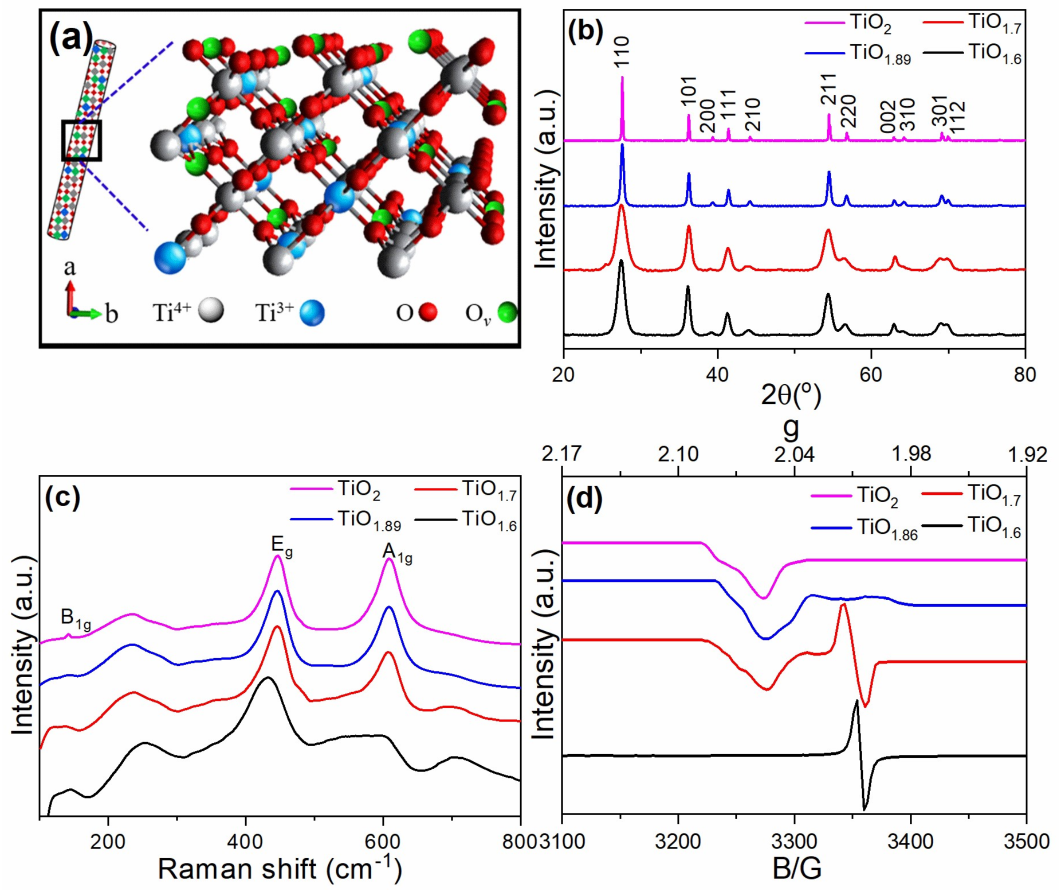

Figure 3.1 (a) Schematic of the crystal structure of an oxygen-deficient rutile TiO_{2-x} nanowire. (b), XRD patterns, (c) Raman spectra and (d) EPR spectra of rutile TiO_{2-x} nanowires

X-ray photoelectron spectroscopy (XPS) of the TiO_{2-x} nanowires provided oxygen vacancy quantification by comparing the chemical bonding characteristics. Both the O 1s and

Ti 2p spectrums experience a lowering of binding energies (with increasing disorderliness) representing Ti^{4+} to Ti^{3+} conversions demonstrating the existence of oxygen vacancies (Figure 2)[233].

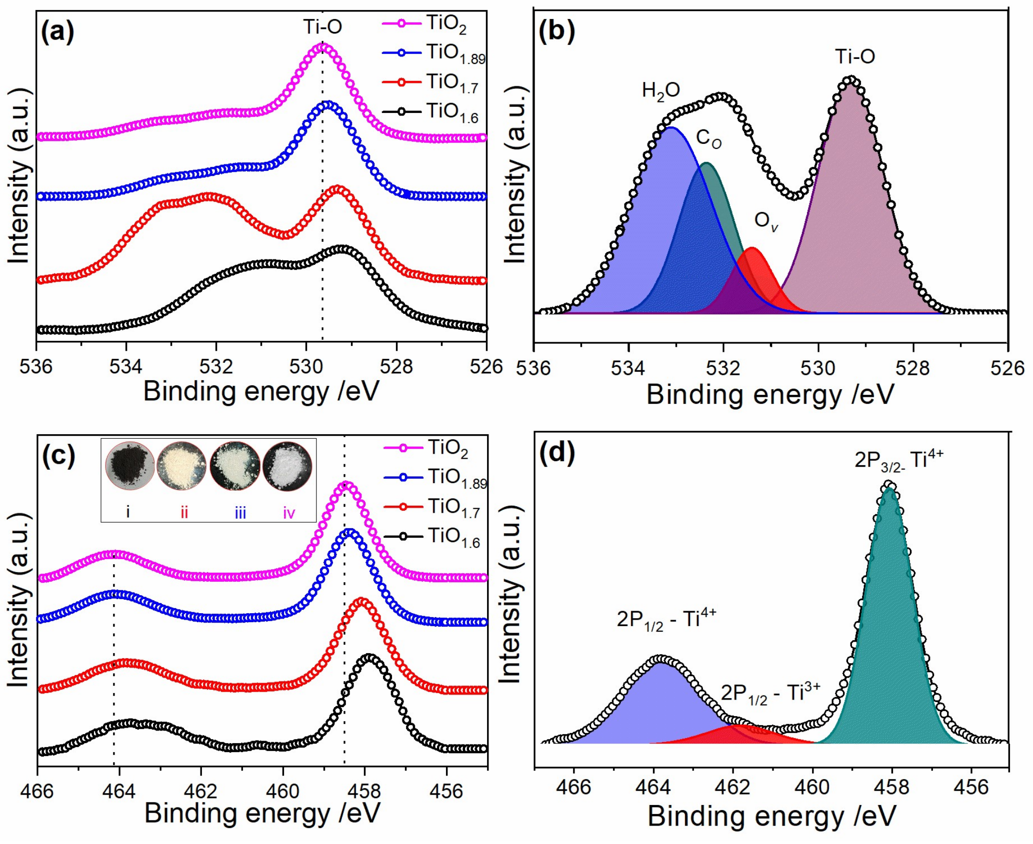

Figure 3.2 (a) High-resolution O 1s XPS patterns of TiO_{2-x} nanowires. (b) Deconvolutions of $TiO_{1.7}$ nanowire O 1s spectra. (c) High-resolution Ti 2p XPS patterns of TiO_{2-x} nanowires. (d) deconvolutions of $TiO_{1.7}$ nanowire Ti 2p spectra.

High-resolution O 1s spectra of rutile $TiO_{1.7}$ nanowire can be deconvoluted lattice oxygen (O^{2-}-529.27 eV), oxygen vacancies (O_v-531.4 eV), chemisorbed oxygen (C_o-532.4 eV) and adsorbed moisture (H_2O-533.4 eV) components (Figure 3.2b)[234]. Comparison of the area under O^{2-} and O_v bands (excluding peak overlaps) confirmed the presence of ~15% of oxygen vacancies. Similar quantification of TiO_2 nanowires treated under Ar + H-400 ºC atmosphere, air-600 ºC and air-1000 ºC exhibited ~20%, ~5% and 0% oxygen vacancies. Meanwhile Ti 2p spectra of oxygen deficient nanowires experienced minor shift in the binding energy in addition to the appearance of an intermediate energy satellite band (2P 1/2 band of Ti^{3+}) (Figure 3.2d)[235]. Oxygen vacancies in the result in a pair of unpaired electrons which are later shared between the unoccupied 3d orbitals of the two adjacent Ti^{4+} ions, and hence reduced to Ti^{3+}. Comparison of the area under Ti^{3+} to Ti^{4+} (2p 1/2) bands in the high-resolution spectrum of rutile $TiO_{1.7}$ nanowires exhibited ~14.5% oxygen vacancy, which is in agreement with O1s spectrum based calculations. Color of rutile TiO_2 nanowires varied significantly with an increase in oxygen vacancy concentration (Figure 3.2c inset).

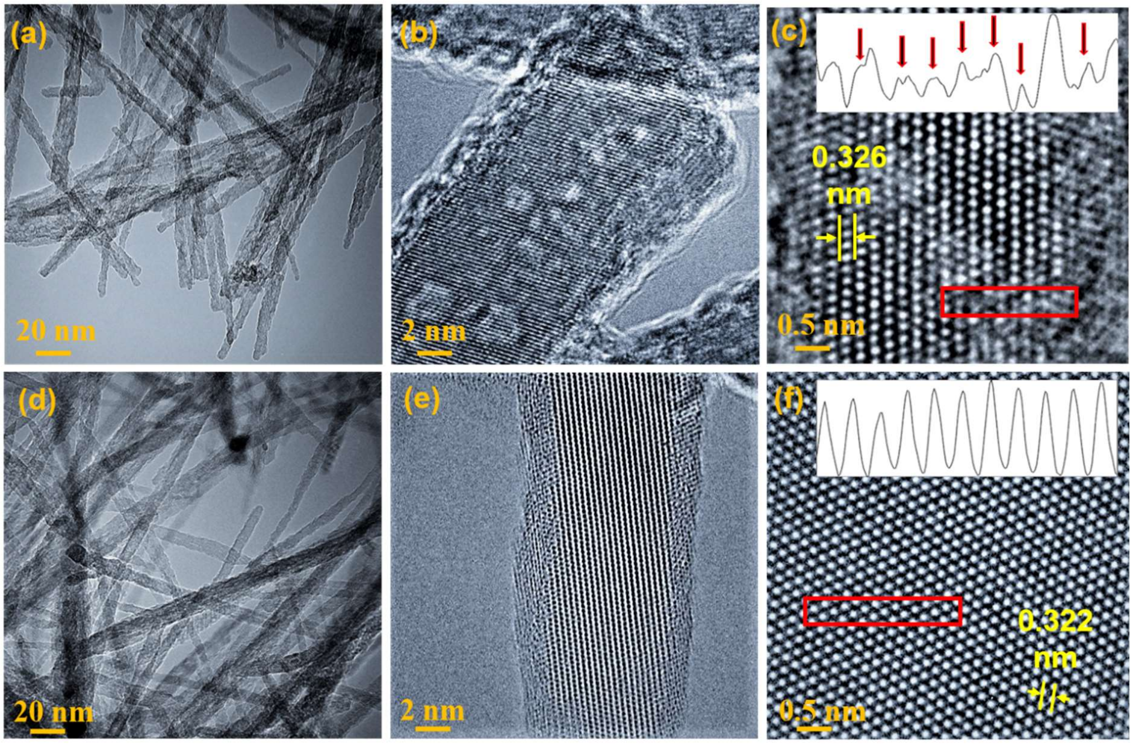

Figure 3.3 Low and intermediate resolution TEM images of (a-b) $TiO_{1.7}$ and (d-e) TiO_2nanowire. Atomic column mapping of HRTEM images of (c) $TiO_{1.7}$ and (f) TiO_2 nanowires.

Microstructural characteristics of stoichiometric and oxygen deficient TiO_{2-x} nanowires are further investigated through transmission electron microscopy (TEM). Independent of the calcination temperatures, nanowires retain ultrafine dimensions of 6±1 nm diameter and 100±5 nm length (Figure 3.3a, d). However, lattice spacing reduced (0.326 for $TiO_{1.7}$, and 0.322 for TiO_2) on decreasing the oxygen vacancy concentration (Figure 3.3c, f). Increased crystal structure disorderness in the case of $TiO_{1.7}$ nanowires is clearly visible in the high resolution images (Figure 3.3c, f). Atomic column mapping of the HRTEM images further verified the periodic arrangement of oxygen atoms in stoichiometric TiO_2 and irregular distribution in the case of $TiO_{1.7}$ nanowires (Figure 3.3c, f inset).

3.2.2 Electrochemical performance of rutile TiO_{2-x} nanowires

Mg-ion storage performance of rutile TiO_{2-x} nanowires are evaluated in coin-cell configurations. Highly defective $TiO_{1.7}$ cathode delivered an initial reversible capacity of 235 mAh/g at a low current density of 50 mA/g. This performance is nearly 4, 6 and 40 times higher than$TiO_{1.6}$, $TiO_{1.89}$ and TiO_2 capacities (Figure 3.4a). Further, in addition to its superior rate performance, $TiO_{1.7}$ retained a specific capacity of 55 mAh/g at 1A/g, and regained 210 mAh/g on decreasing the current density to 50 mA/g. Galvanostatic voltage profiles of stoichiometric and oxygen deficient rutile TiO_2 nanowires are presented in Figure 3.4b & c. Though both profiles exhibited sloping characteristic representing capacitive ion-storage, $TiO_{1.7}$ accommodated 0.352 moles (70.5% of theoretical limit) of Mg^{2+}, but only 0.008 moles (1.72%) by TiO_2. Cyclic voltammograms of rutile $TiO_{1.7}$ nanowires in the range of 0-2.1V (Figure 3.4d) are collected to investigate the Mg-ion storage process. First cathodic signal (at 0.1 mV/s) consists of three distinct regions denoting distinguishable electrochemical processes (Figure 3.4e). The sloping region between 2.1-0.65 V denote diffusion-independent Mg-ion intercalation[53]. Cathodic response in the 0.65-0.37V represent diffusion-limited Mg-ion intercalation[47]. Cathodic signal in the 0.37-0V region correspond to SEI layer formation related to electrolyte decomposition, which gradually disappeared during the subsequent cycles[134].

Stoichiometric TiO_2 is also exhibits similar CV patterns (Figure 3.4f) with a significantly lower current density, which is expected due to its limited Mg-ion storage capacity.

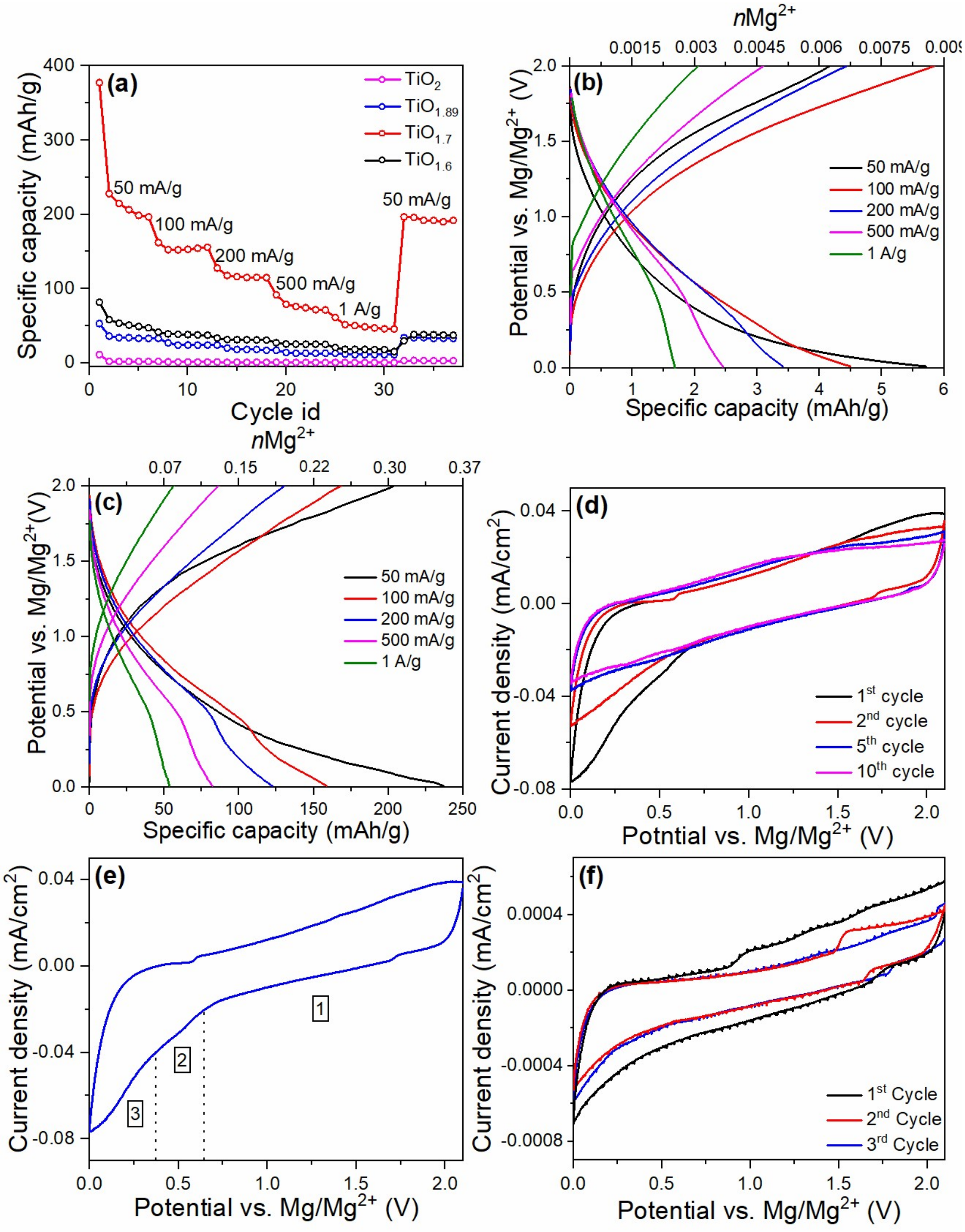

Figure 3.4 (a) Galvanostatic rate performance of rutile TiO_{2-x} nanowires in the voltage of 0-2V. (b-c) Galvanostatic charge-discharge voltage profiles at different current densities for TiO_2 and $TiO_{1.7}$ cathodes (d) CV curves from 1st to 10th cycle for $TiO_{1.7}$ at 0.1mV/s. (e) Initial cyclic voltammetric curve of the $TiO_{1.7}$ nanowire electrode at 0.1 mV/s scan rate marked with different regions (f) **.** Initial Cyclic voltametric curve of TiO_2 nanowire electrode at 0.1 mV/s scan rate.

Cyclic voltammograms of rutile $TiO_{1.7}$ nanowires at various scan rates (Figure 3.5a) are collected for the further investigation of Mg-ion storage process. Anodic and cathodic signals exhibited broad patterns, which depends linearly with the scan rate, signifying a pseudocapacitive behavior. The power law relationship $i = av^b$ correlates the anodic and cathodic current (i) to the scan rate (v), where a and b are adjustable parameters. Generally, b-value represents the nature of the storage mechanism. Diffusion controlled and independent process are characterized by b-values of 0.5 and 1.0 respectively. Calculated cathodic and anodic b-values of rutile $TiO_{1.7}$ nanowires are 0.76 and 0.77 respectively in the scan rate range of 0.1 to 30 mV/s (Figure 3.5b), representing dominant pseudocapacitive Mg-ion storage. These b-values decreased to 0.5 on increasing the scan rates beyond 30 mV/s, representing diffusion-dependent nature of Mg-ion diffusion at higher san rates. Such response is quite normal for pseudocapacitive electrode materials.

Pseudocapacitive Mg-ion storage process are further quantified by implementing the extended power law equation. At very low scan rates (0.1-0.3 mV/s), rutile $TiO_{1.7}$ nanowires followed a diffusion-controlled intercalation process with low fraction of pseudocapacitance. At a scan rate of 1 mV/s, pseudocapacitance contribution increased to 66% (Figure 3.5c) and attained a maximum of 82% at 10 mV/s (Figure 3.5d). Meanwhile, stoichiometric TiO_2 exhibited an extremely low pseudocapacitance of 1.9% at a scan rate of 1 mV/s, justifying its diffusion-dependent Mg-ion intercalation mechanism. These pseudocapacitance contributions are in good agreement with the high specific capacity and rate performance of rutile $TiO_{1.7}$ nanowires in comparison to stoichiometric rutile TiO_2 nanowires.

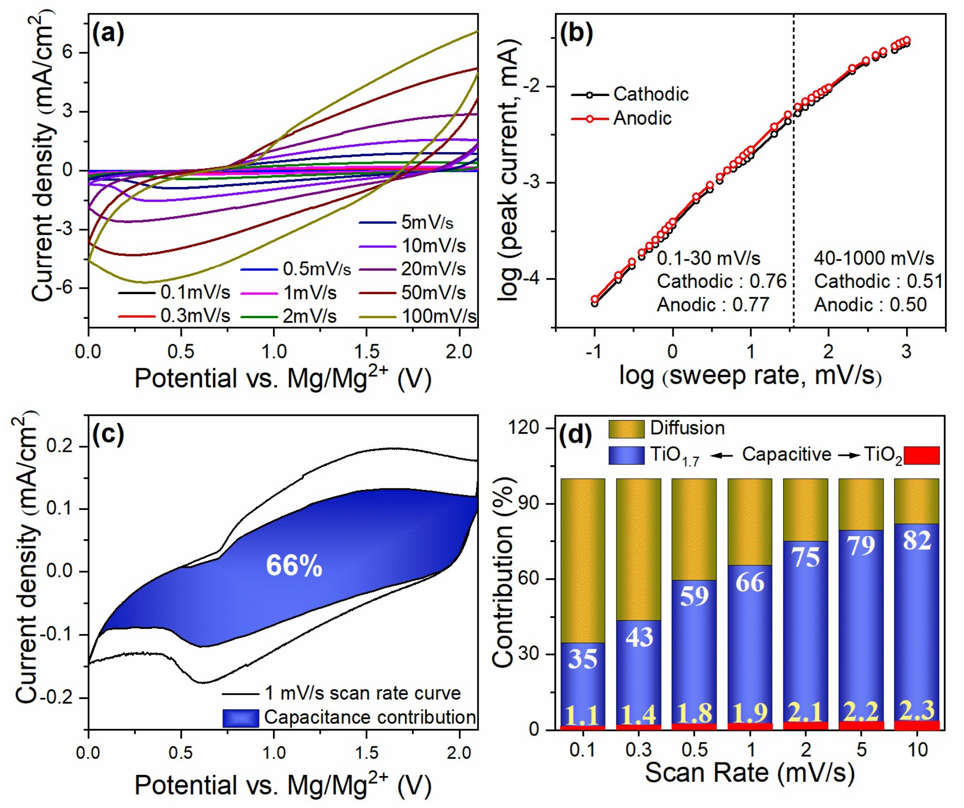

Figure 3.5 (a) CV curves of rutile TiO_{2-x} nanowires at various scan rates ranging from 0.1mV/s to 100mV/s. (b) log(i) Vs log (v) plot for anodic and cathodic currents. (c) Cyclic voltammograms of rutile $TiO_{1.7}$nanowire at a scan rate of 1mV/s. Pseudocapacitive current contribution is shown in the shaded region. (d) Pseudocapacitive capacity contribution of rutile $TiO_{1.7}$ and TiO_2 nanowire at various scan rates ranging from 0.1 mV/s to 10 mV/s.

Long cycling stability is one of the crucial factor of a rechargeable battery that decides its practical applications. Rutile $TiO_{1.7}$ nanowires exhibited stable cycling up to 2000 times at a high current density of 1A/g (Figure 3.6a) with ~100% coulombic efficiency and 104% capacity retention. Identical voltage profiles throughout the entire cycling (Figure 3.6b) demonstrate structural integrity of the cathode and reversibility of the storage mechanism. Electrode robustness together with extreme pseudocapacitance further facilitated fast-charging characteristics (100% in 4.3 minutes).

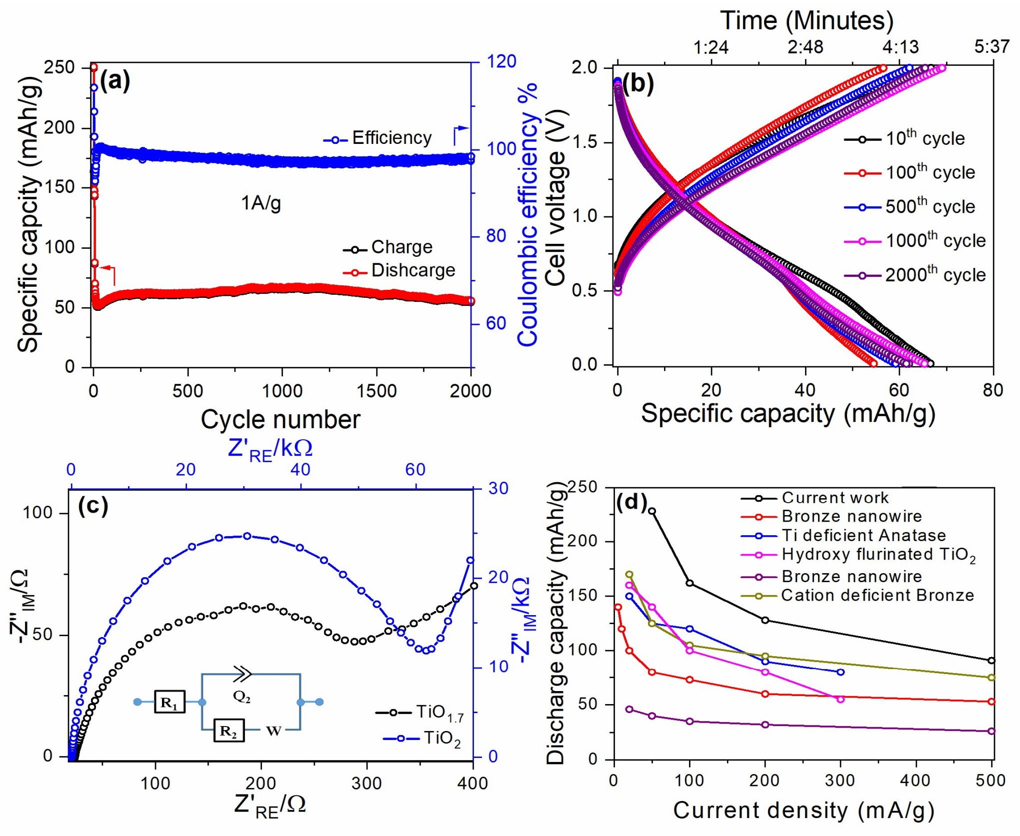

Figure 3.6 (a) Galvanostatic long cycling performance of the $TiO_{1.7}$ nanowires at a current density of 1A/g. (b) Corresponding charge-discharge curves at different instants of long cycling. (c) EIS plots of the $TiO_{1.7}$ and TiO_2 nanowires. (d) Comparative study of the galvanostatic rate performance of $TiO_{1.7}$ cathodes with reported TiO_2 based cathodes.

Mg-ion diffusion kinetics to the TiO_{2-x} electrodes are further characterized with electrochemical impedance spectroscopy (EIS) (Figure 3.6c). Nyquist plots of the electrode comprise a high-frequency semicircle corresponds to the charge transfer resistance (R_{ct}) and low-frequency slopping line representing the solid-state diffusion (Z_w) of Mg-ion respectively. Equivalent circuit fitting reviled R_{ct} of 287.7 Ω ($TiO_{1.7}$) and 61.912 kΩ (TiO_2) and Z_w of 3.943E-14 ($TiO_{1.7}$) and 1.726E-15 (TiO_2). Lower impedance and higher diffusion coefficient of the defective $TiO_{1.7}$- electrode over TiO_2 validated the influence of oxygen vacancies on the Mg-ion diffusion kinetics and pseudocapacitance. Specific capacity, rate performance and cycling stability of rutile $TiO_{1.7}$ nanowires presented here is superior to numerous TiO_2 based cathodes reported in the literature (Figure 3.6d)[51,53,130,134].

3.2.3 Detailed analysis of pseudocapacitive Mg-ion storage

Mg-ion storage mechanism of rutile $TiO_{1.7}$ nanowires are further investigated using different spectroscopic and microscopic techniques. *In-situ* XRD patterns of $TiO_{1.7}$ at different state of charge demonstrated only negligible changes in the crystal structure during charge-discharge process (Figure 3.7a-b).

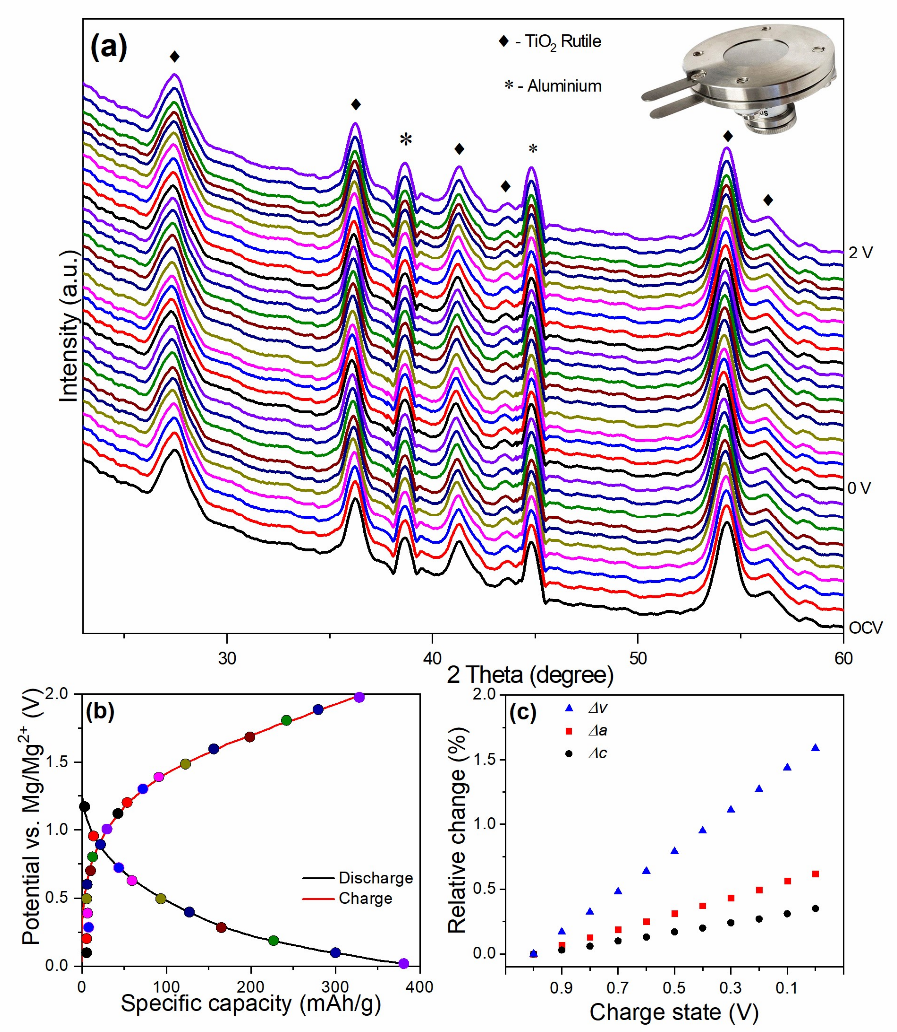

Figure 3.7 (a) In-situ X-ray diffraction patterns of rutile $TiO_{1.7}$ electrode at different states of charge. (b) Galvanostatic voltage profile of rutile $TiO_{1.7}$ cathode at a current density of

25mA/g. States of charge corresponding to the *In-Situ* XRD are marked (c) Relative change of the lattice constants a,c and unit cell volume with respect to the state of charge.

Major peak characteristic of rutile phase experienced only minor shift during the Mg-ion intercalation process. Such an ion-storage mechanism indicated intercalation pseudocapacitance rather than surface storage. Lattice constant changes are further calculated from the XRD spectrum corresponding to different state of charge. This confirmed only a negligible (~1.5%) change in volume during charge-discharge process (Figure 3.7c) , which is lower than during Li-ion intercalation (~10%) [236]. Vacancy-mediated pseudocapacitive Mg-ion storage associated with zero strain is beneficial to achieve ultralong cycling stability.

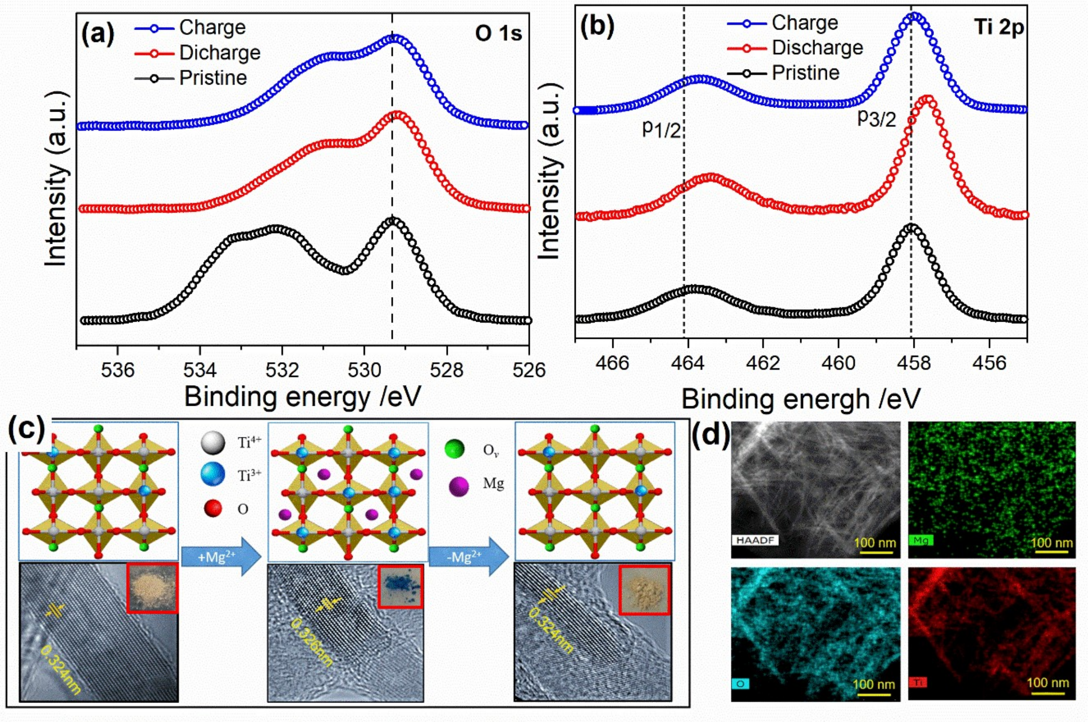

Figure 3.8 Ex-situ post cycling (a) O 1s and (b) Ti 2p XPS patterns of $TiO_{1.7}$ electrode at discharge and charge states with respect to the uncycled electrode. (c) Schematic of the Mg-ion storage mechanism and corresponding lattice spacing changes of $TiO_{1.7}$. (d) Post-cycling EDX elemental mapping of the $TiO_{1.7}$ electrode.

Ex-situ XPS analysis of rutile $TiO_{1.7}$ nanowire electrode at different state of charge (Figure 3.8a-b) confirmed reversible reduction of Ti^{4+} to Ti^{3+} ($Ti^{4+}\leftrightarrow Ti^{3+}$) associated with Mg-ion intercalation. High-resolution Ti 2p spectrum experienced slight shift towards lower binding energy due to Mg-ion intercalation, which represent the reduction of Ti^{4+} to Ti^{3+}. However, binding energy of this spectrum increased to the original position after charging to 2V. No significant changes are observed in the case of high resolution O 1s spectra. This is a clear indication of the oxygen vacancy retention during charge discharge process. Disappearance of the signals characteristic of oxygen containing functional groups can be credited to their reaction with the electrolyte solution during SEI formation.

High resolution TEM images of pristine, discharged and charged rutile $TiO_{1.7}$ nanowires are collected (Figure 3.8c) to investigate the structural charges at the atomic scale. Preservation of the nanowire morphology during charge-discharge process can be clearly visible from these images. Lattice spacing increased from 0.324 nm to 0.326 nm during discharging, and decreased to 0.324 nm upon charging. Hence it is clear that Mg-ion intercalation doesn't cause any significant changes in the crystal structure of rutile $TiO_{1.7}$ nanowires.

Based on these results, Mg-ion storage mechanism consists of intercalation pseudocapacitance, which can be represented as

$$Ti^{iv}O_{1.7} + xMg^{2+}\ 2xe^{-} \quad \rightarrow \quad Ti^{iv}_{1-2x}\,Ti^{iii}_{2x}\,O_{1.7}\,Mg_{x}$$

TEM analysis and EDX mapping of the cycled electrode (Fig3.8d) further verified the nanowire morphology retention and homogenous distribution of Mg. Such a high mechanical stability is crucial to achieve long cycling stability as observed in the present case.

Exceptional Mg-ion storage performance of oxygen deficient rutile TiO_2 nanowires anode can be credited to its oxygen vacancies, and one-dimensional morphology. Crystal structure disorderness caused by oxygen vacancies provided additional pathways for ultrafast pseudocapacitive Mg-ion intercalation. Diffusion independent pseudocapacitive Mg-ion intercalation into oxygen deficient rutile TiO_2 lattice caused high-rate performance and ultra-long cycling stability. Mg-ion intercalation without crystal structure change ensure ultralong cycling stability. Moreover, one-dimensional microstructure, mesoporosity, and high-aspect-ratio nanowire acts as secondary factors for improving the electrochemical performance. In conclusion, oxygen vacancy-induced pseudocapacitive Mg-ion storage of rutile $TiO_{1.7}$ nanowires make it an excellent cathode material for next-generation high energy density ultralong-life fast charging magnesium batteries.

3.3 Conclusions

In summary, we have demonstrated fast charging and ultralong life magnesium batteries based on highly pseudocapacitive oxygen deficient rutile TiO_2 nanowire cathodes. This electrode exhibited outstanding specific capacities, cycling stability, and rate performance compared to conventional TiO_2 based cathodes reported earlier. Exceptional Mg-ion storage performance of rutile $TiO_{1.7}$ nanowires is credited to the extreme Mg-ion intercalation pseudocapacitance. Crystal structure disorderness caused by oxygen vacancies provided additional pathways for ultrafast pseudocapacitive Mg-ion intercalation. Hence, tremendous pseudocapacitance enhanced electrochemical performance of oxygen deficient rutile TiO_2 nanowires makes it a potential candidate for the next-generation high energy density, fast-charging and ultra-long-life magnesium-batteries.

Chapter4

High-rate and ultralong-life Mg-Li hybrid batteries based on highly pseudocapacitive dual-phase TiO_2 nanosheet cathodes

4.1 Introduction

Despite of numerous advantages such as high theoretical volumetric capacity, dendrite free redox reaction, low cost, ecofriendly nature, etc. the commercialization of Mg batteries is hindered by the limited practical specific capacity, rate performance and cycling stability due to the sluggish Mg-ion diffusion. Mg-Li hybrid batteries have been proposed with the hope to overcome the drawbacks of conventional Mg-batteries while maintaining superior cost-effectiveness and safety credentials. Energy storage mechanism of this dual ion system composed of hybrid electrolyte and Mg-metal anode involves both Mg and Li-ion insertion in to the cathode. Only a limited number of materials such as metal sulfides (MoS_2, VS_2, TiS_2, FeS_2, Mo_6S_8), metal oxides (MoO_2, $Li_4Ti_5O_{12}$, TiO_2, VO_2), and MXene has been investigated as cathodes for Mg-Li hybrid batteries. Unfortunately, these electrodes were either prone to poor electrochemical characteristics at high current densities or require complex synthesis procedures, both of which hinder their real-world application. As in the case of pure Mg-battery described in the previous chapter, TiO_2 is considered as an attractive cathode material for Mg-Li hybrid due to its compatibility with both Mg and Li-ions. However, the TiO_2 cathode in Mg-Li hybrid system also faces several constraints due to its poor electronic conductivity and low Mg-ion diffusivity. These shortcomings cause low specific capacity and inhibit capacity retention during extended cycling, especially at the higher current densities. Nanostructuring of electrode materials in the form of nanoparticles, nanosheets, nanowires, nanorods, etc. has been one of the widely used methods to tackle these shortcomings. Mesoporous structures were also found to improve the performance due to enhanced contact with the electrolyte solution. These approaches are however inadequate due to nominal increase in electrochemical performance. Hence, new strategies are necessary for the substantial increase of specific capacity, rate performance and cycle-life that are crucial for the real-world application of TiO_2 based Mg-Li hybrid batteries. Pseudocapacitive Mg and Li-ion storage, a recently reported mechanism is superior to conventional process due to its diffusion independent nature. As discussed in the previous sections, pseudocapacitive type electrode materials exhibit minimal volume changes due to the bulk electronic-ionic conductivity independent surface/ near surface storage characteristics. Although several electrode materials including TiO_2 demonstrated pseudocapacitive Li-ion storage, their application in Mg-Li hybrid batteries are limited due to the above mentioned sluggish Mg-ion diffusion.

Dual-phase TiO_2 is a well-known concept that is widely used for various application areas such as catalysis, CO_2 reduction, solar cells, sensor applications, etc due to the structural and electronic property modification over the single-phase architecture facilitating better performance in the respective areas[237,238]. The dual-phase TiO_2 was also reported as a potential cathode design for electrochemical batteries. The interfaces generated at the grain boundaries function as additional storage locations and/or fast diffusion channels hence provided better storage capacities than the single-phase electrodes having the inherent surface or interstitial storage locations. The idea was successfully implemented both in the Li and Na batteries but not yet investigated for high performance Mg-Li hybrid designs.

Herein, we present a high rate and ultra-long life Mg-Li hybrid battery based on dual-phase hierarchical TiO_2 nanosheet cathode. Following aspects are accounted while designing the high-performance cathode. (i) Two-dimensional morphology is selected for promoting superior electrode-electrolyte contact and ion diffusion. (ii) Ultrathin nature, high surface area and mesoporosity are intended for enhanced ion diffusion kinetics. (iii) Hierarchical microstructure composed of TiO_2 nanocrystallites is aimed at the generation of numerous interfaces that can possibly act as ion-diffusion pathways. (iv) Moreover, crystal mismatch between the anatase-bronze polymorphs results in additional ion diffusion pathways, promoting pseudocapacitive storage. Fast kinetics of the diffusion independent pseudocapacitive Mg-Li ion diffusion also minimizes structural changes and provides electrode robustness. Morphological and microstructural uniqueness of the hierarchical dual-phase TiO_2 nanosheets made it an excellent cathode for high rate and ultralong life Mg-Li hybrid batteries.

4.2 Results and discussion

4.2.1 Synthesis and characterization of hierarchical TiO_2 nanosheets

Single and dual-phase TiO_2 nanosheets are synthesized through a solvothermal process and subsequent calcination. Selection of less reactive precursor $TiCl_3$ in this case instead of other more reactive chemicals such as Ti{OCH(CH3)2}4 and $TiCl_4$ is aimed at the slow crystallization and bottom-up growth of TiO_2 nanosheets without agglomeration. Ethylene glycol solvent played multiple roles in the formation of hierarchical 2D microstructure of TiO_2 nanosheets. Reaction between $TiCl_3$ and ethylene glycol results in the formation of a less reactive Ti-glycolate intermediate, which undergo slow hydrolysis and condensation during solvothermal reaction to form bronze TiO_2 nanosheets. OH groups of ethylene glycol also interact with Ti-OH groups during the hydrolysis and condensation process. This results in the free energy change of TiO_2 crystal planes and facilitate anisotropic crystal growth necessary for 2D morphology formation. Its high viscosity slow down the crystal growth by reducing the diffusivity of the precursor molecules [239]. Presence of H^+ ions in the reaction medium reduces the hydrolysis rate, and hence control the co-crystallization of TiO_2 nanocrystallites [240]. Hydrochloric acid used for stabilizing $TiCl_3$ also provides sufficient Cl^- ions that promote the crystallization and growth of 2D microstructure [240]. Excessive crystal growth is also forbidden by the limited availability of the $TiCl_3$ precursor, facilitating the formation of 2D morphology [241,242]. Hence, hydrolysis and condensation of Ti-glycolate complex in the presence of ethylene glycol and Cl^- ions result in the formation of hierarchical bronze TiO_2 nanosheets. Crystallization of thermodynamically more stable anatase phase occurs during the heat treatment, resulting in the formation of anatase-bronze hybrid nanosheets.

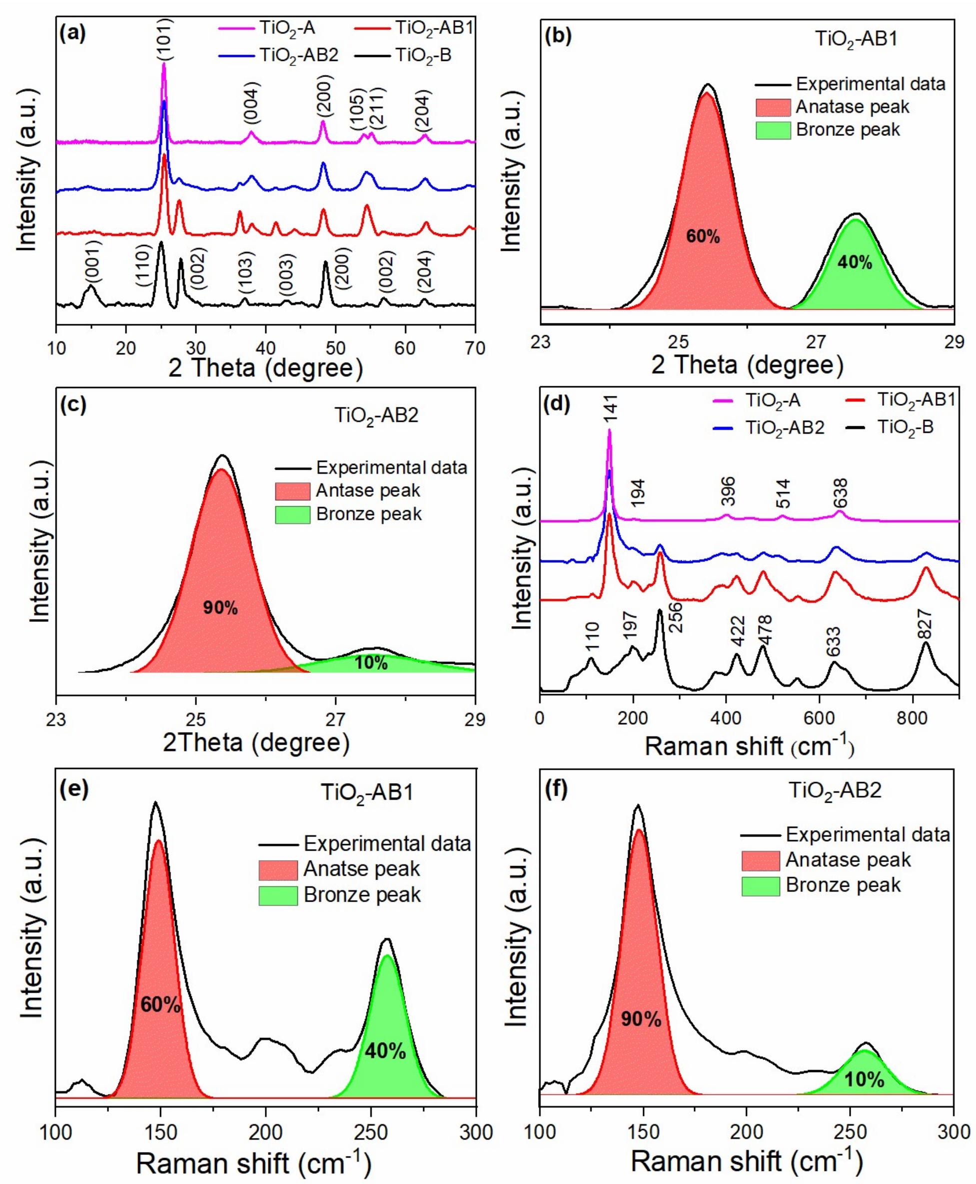

Figure 4.1 (a) X-ray diffraction patterns and (d) Raman spectra, of single and dual-phase hierarchical TiO_2 nanosheets. XRD (b-c) and Raman spectral (e-f) quantification of anatase and bronze polymorphs present in dual-phase TiO_2-AB1 and TiO_2-AB2 hierarchical nanosheets.

X-ray diffraction patterns of single and dual-phase TiO_2 nanosheets (Figure 4.1a) showed distinct diffraction peaks corresponds to anatase and bronze polymorphs of TiO_2. Sample obtained after solvothermal reaction exhibited distinct peaks corresponding to metastable monoclinic bronze TiO_2 (JCPDS no. 46-1237) [243]. Whereas, TiO_2 nanosheets calcined at 500 °C distinct signals characteristic of tetragonal anatase TiO_2 (JCPDS no. 21-1272)[244]. XRD patterns verified the presence of both anatase and bronze polymorphs in samples heat-treated at 350 °C and 400 °C. Quantification of anatase and bronze polymorphs from the relative area of anatase (101) peak at 25.37° and bronze (002) peak at 27.5° (Figure 4.1b-c) are found to be 60:40 and 90:10 for 350 °C and 400 °C treated samples respectively. Average crystallite size calculations using Debye Scherrer equation with respect to the prominent diffraction peaks ($2\theta=25.36$ for anatase, $2\theta=27.62$ for bronze) revealed 13±2, 17±2, 20±2 and 24±2nm crystallites for TiO_2-B, TiO_2-AB1, TiO_2-AB2 and TiO_2-A samples respectively. As expected, crystallite size increased because of the higher calcination temperatures. TiO_2 nanosheets were further subjected to Raman spectral analysis (Figure. 4.1d), which is a surface sensitive technique compared to XRD. The results obtained are in good agreement with the XRD measurements. Raman spectrum of bronze TiO_2 nanosheets exhibited active modes at 110, 197, 256, 422, 478, 633 and 827 cm^{-1} [245246]. Whereas, spectrum of anatase TiO_2 consist of signals at 141, 194, 396, 514 and 638 cm^{-1}. Dual-phase nanosheets spectra composed of both anatase and bronze Raman modes. These observations also confirmed the phase purity of TiO_2 nanosheets. Anatase: bronze ratios present in the dual-phase TiO_2 nanosheets calculated from Raman spectra (Figure 4.1e-f) are also in good agreement with the XRD results.

Textural characteristics of TiO_2 nanosheets are investigated using the N_2 adsorption-desorption analysis. Type IV isotherms having H3 type hysteresis and large steepness at the high relative pressure (Figure 4.2a) revealed the presence of mesopores. Pore diameter of both single and dual phase nanosheets lies in the 3-5nm range (Figure 4.2b) denoting the mesoporosity independent of calcination temperatures. The Brunauer- Emmett-Teller (BET) surface area of the nanosheets (Table 4.1) decreased gradually with an increase of the calcination temperature. Barret-Joyner-Halenda (BJH) analysis further confirmed mesoporosity of both single and dual-phase TiO_2 nanosheets (Figure 4.2b). Pore size increased with an increase of calcination temperature due to the crystallite growth. Mesoporosity and large surface area of TiO_2 nanosheets are advantageous in reducing the Li and Mg-ion diffusion length by improved contact with the electrolyte solution. Mesopores can additionally serve as reservoirs for the surface storage of Mg/Li-ions and thereby delivering superior electrochemical performance.

Table 4.1. Textural properties of single and dual-phase hierarchical TiO_2 nanosheets.

	BET Surface area (m^2/g)	**Pore volume (cm^3/g)**	**Pore diameter (nm)**
TiO_2-B	123	0.21	3.61
TiO_2-AB1	115	0.30	3.67
TiO_2-AB2	106	0.28	3.69
TiO_2-A	80	0.25	4.17

Surface chemical characteristics of electrochemically most active dual phase TiO_2 nanosheets are further investigated with X-ray photoelectron spectroscopy (XPS). High-resolution Ti 2p spectrum (Figure 4.2c) exhibited typical Ti^{4+} oxidation state with a pair of signals at 458.52 eV and 464.25 eV that corresponds to $2p_{3/2}$ and $2p_{1/2}$ components. Low intensity deconvoluted signal at 461.9 eV represent Ti^{3+} oxidation state, indicating oxygen non-stoichiometry (~3%). The relative areal comparison between Ti^{3+} and Ti^{4+} bands showed a maximum of 1.5% oxygen deficiency. Slightly higher spin orbit splitting value (5.9 eV) compared to previous reports can be related to the presence of oxygen vacancies and 2D morphology. High-resolution O1s spectrum (Figure 4.2d) consists of a low binding energy band and a broad shoulder extending to the higher binding energies. Deconvoluted signal located at 529.8 eV denotes the lattice oxygen (O^{2-}) of the TiO_2 crystal structure [47]. Presence of water molecules adsorbed at oxygen vacancies are evident from the low intensity signal centered at 531.9 eV. Non-stoichiometry of TiO_2 is beneficial for improved electronic conductivity and surface storage of Mg/Li-ions [137]. Peak at 533 eV represent loosely bonded chemisorbed carbonate groups formed during the *in-situ* decomposition of the Ti-glycolate complex [247].

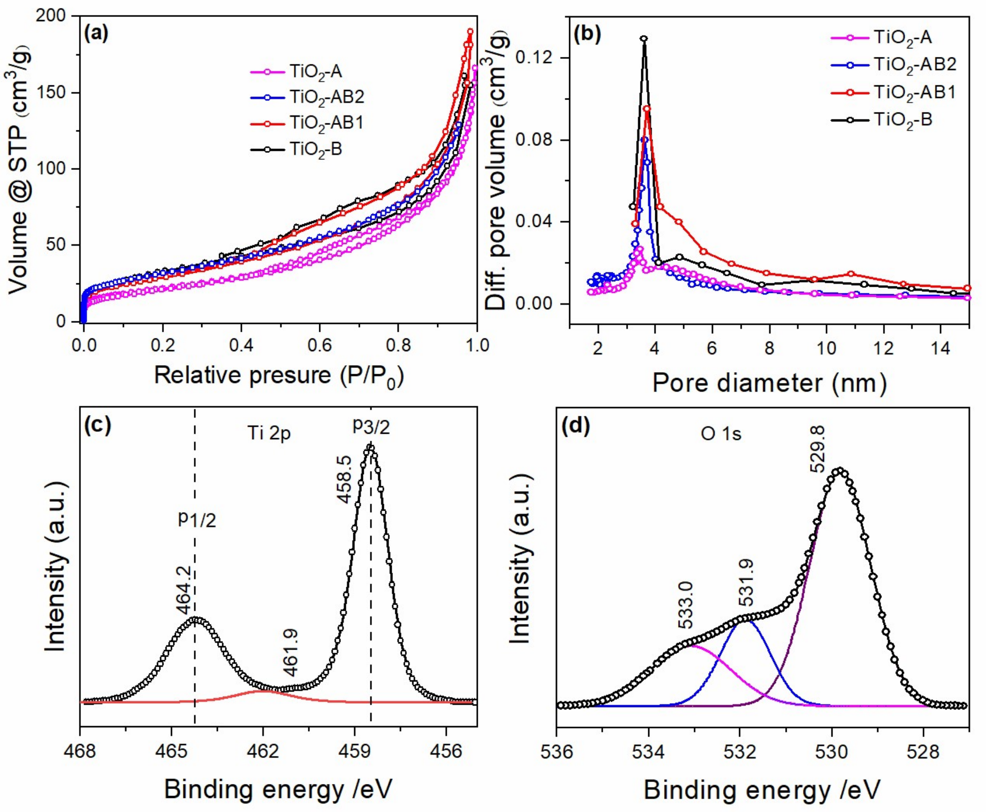

Figure 4.2. (a) N_2 adsorption-desorption isotherms and (b) pore-size distributions of single and dual-phase hierarchical TiO_2 nanosheets. High-resolution (c) Ti 2p and (d) O 1s XPS spectra of dual-phase hierarchical TiO_2 nanosheets.

Transmission electron microscopy (TEM) images (Figure 4.3) revealed the hierarchical microstructure of TiO_2 nanosheets. It is clear that the flower like microstructure composed of interconnected nanosheets are independent of the calcination temperature. Bronze and anatase nanocrystallites can be distinguished from 0.62 nm and 0.35 nm lattice spacings corresponding to (001) and (101) crystal planes (Figure 4.3.c,f,i) of the respective polymorphs [241,248]. Presence of well-defined interfaces between anatase and bronze nanocrystallites are clearly visible in these TEM images. These nanointerfaces are formed due to the crystal mismatch between the two polymorphs. Unique physiochemical properties are often observed in metal oxides containing such nanointerfaces[135,249,250]. Electrode architecture containing numerous nanointerfaces are attractive due to the possibility of additional surface ion storage. Hence, it can be concluded that solvothermal hydrolysis and condensation reaction of $TiCl_3$ in ethylene glycol followed by controlled heat treatment resulted in the formation of hierarchical TiO_2 nanosheets composed of bronze and/ or anatase nanocrystallites.

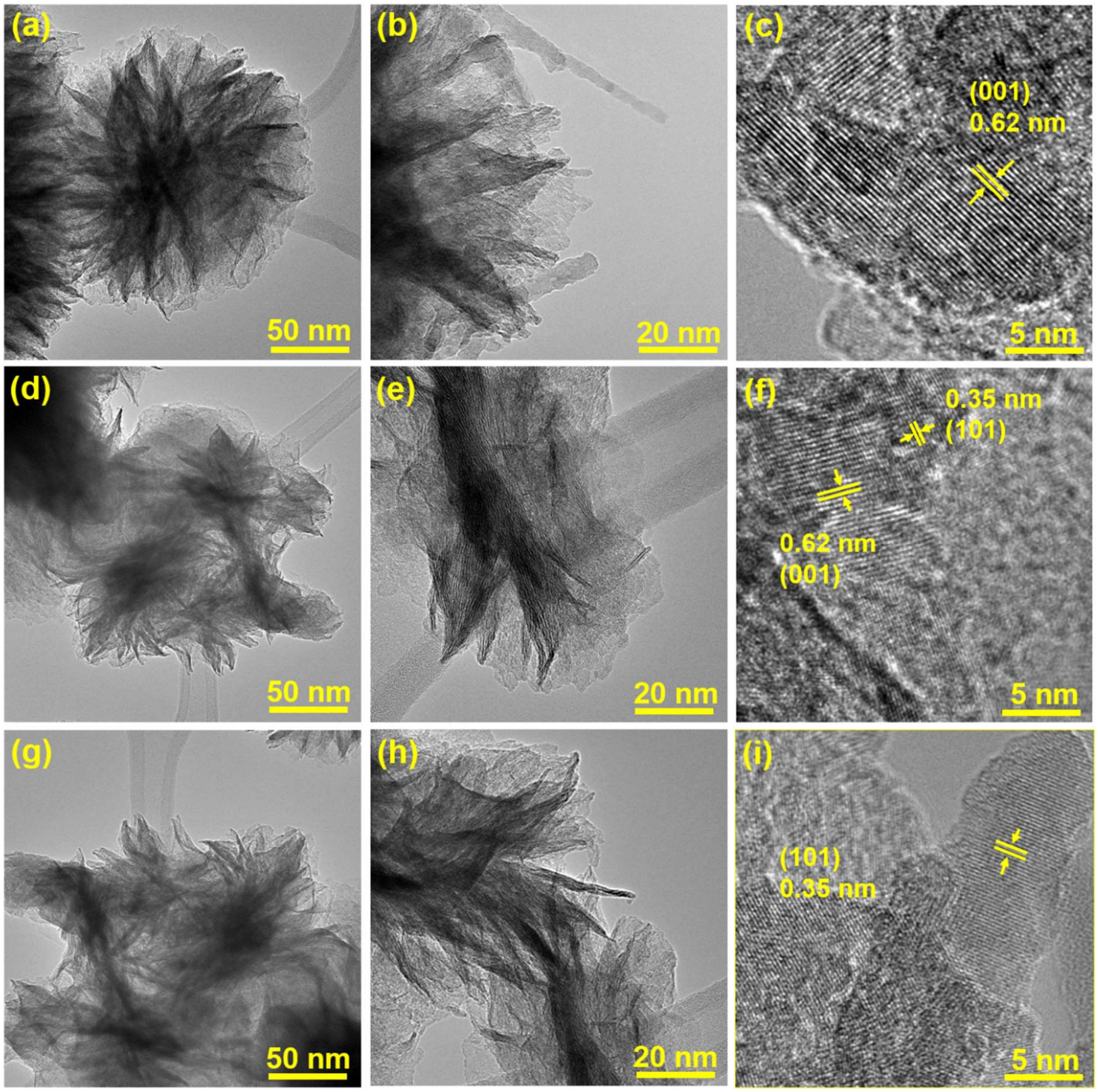

Figure 4.3 TEM images of hierarchical (a-c) bronze TiO_2 nanosheets, (d-f) dual-phase TiO_2 nanosheets, and (g-i) anatase TiO_2-nanosheets.

4.2.2 Electrochemical performance of hierarchical TiO2 nanosheets

Electrochemical performance of hierarchical dual-phase TiO_2 nanosheets are initially tested as Mg-battery cathodes (Figure 4.4a). Poor electrochemical performances are observed irrespective of the electrode composition. Reversible capacities are limited to a maximum of 42 mAh/g, which is in line with the previous reports of TiO_2 based cathodes [136,251]. Galvanostatic charge-discharge studies of these electrodes in the Mg-Li hybrid configuration exhibited significant increase in the specific capacities, indicating their dual-ion compatibility. High specific capacity in Li-ion half-cells (Figure 4.4b) confirmed that Li-ion intercalation process contributes a major role in the excellent electrochemical performance of dual-phase TiO_2 nanosheets.

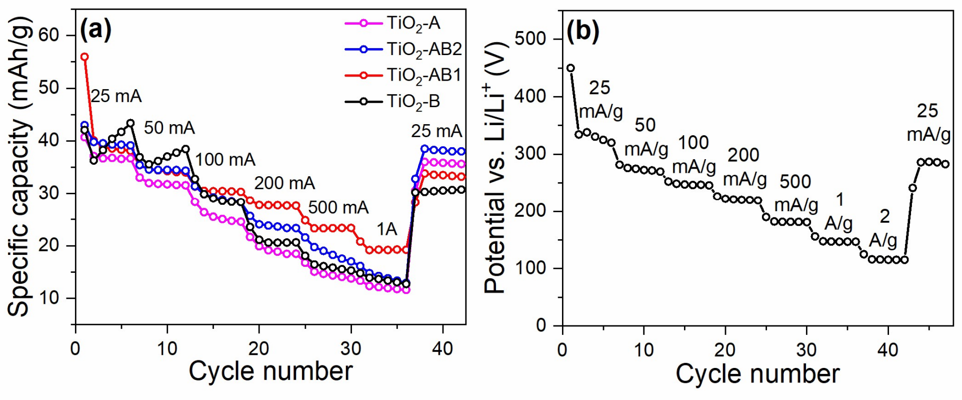

Figure 4.4 (a) Galvanostatic rate performance of single and dual-phase hierarchical TiO_2 nanosheets as pure Mg-battery cathodes, (b) Galvanostatic rate performance of the TiO_2-AB1 hybrid nanosheet Li-ion half-cell configuration.

Electrochemically most active sample TiO_2-AB1 (60:40 - Anatase: Bronze) demonstrated considerably higher specific capacities compared to other compositions containing different anatase: bronze ratio (Figure 4a). Initial discharge capacity of this cathode reached 328 mAh/g in Mg-Li hybrid configuration at a current density of 25 mA/g, and retained ~70% (235 mAh/g) in the consecutive cycle (Figure 4.5a). Unlike the Mg-battery system, all TiO_2 nanosheet electrodes experienced irreversible first cycle capacity loss in the Mg-Li hybrid system due to solid electrolyte interface (SEI) formation [252]. Strategies such as prelithiation or use of electrolyte additives are required to reduce the irreversible capacity loss of these electrodes [253].

Second charge-discharge voltage profiles of TiO_2-AB1 nanosheets as Mg-Li hybrid battery cathode is presented in Figure 4.5b. Slopping voltage profile of this dual-phase TiO_2 cathode indicate diffusion-independent pseudocapacitive type Mg/Li-ion storage [224]. Voltage profiles remain identical at various current densities, indicating similar Mg/Li-ion storage process irrespective of the diffusion rates [47]. Voltage profiles of other electrode compositions are also collected (Figure 4.5c-e) for comparing the electrochemical processes. Phase pure TiO_2-B exhibited an ideal sloping curve characteristic of pseudocapacitive intercalation [254]. TiO_2-A electrode demonstrated an entirely different profile, which consisted of a plateau followed by a slopping region representing the diffusion limited intercalation and interfacial storage, respectively [249]. It is thus clear that voltage profile of TiO_2-AB1 signifies the coexistence of the pseudocapacitive intercalation and interfacial storage process. Increased slope of the voltage profiles at higher current densities denoted an increased pseudocapacitive Mg/Li-ion storage. Electrochemical response of single and dual-phase TiO_2 nanosheets are further evaluated through cyclic voltammetric studies. In the case of TiO_2-AB1 nanosheet electrode (Figure 4.5f), broad cathodic peak centered at 0.75V indicate SEI formation resulting from electrolyte decomposition and Mg/Li-ion intercalation [251]. Two distinct anodic signals located at 0.85 and 1.3 V correspond to Mg/Li-ion deintercalation from bronze and anatase polymorphs respectively [251]. Similar cathodic and anodic responses at slightly different potentials are also observed in the case of anatase (Figure 4.5g) and bronze TiO_2 nanosheet (Figure 4.5h) electrodes. Although cathodic and anodic signals of TiO_2-B, and cathodic signal of TiO_2-A match well with the electrochemical response of TiO_2-AB1, anodic signal of TiO_2-A appeared at a lower voltage of 1.3V.

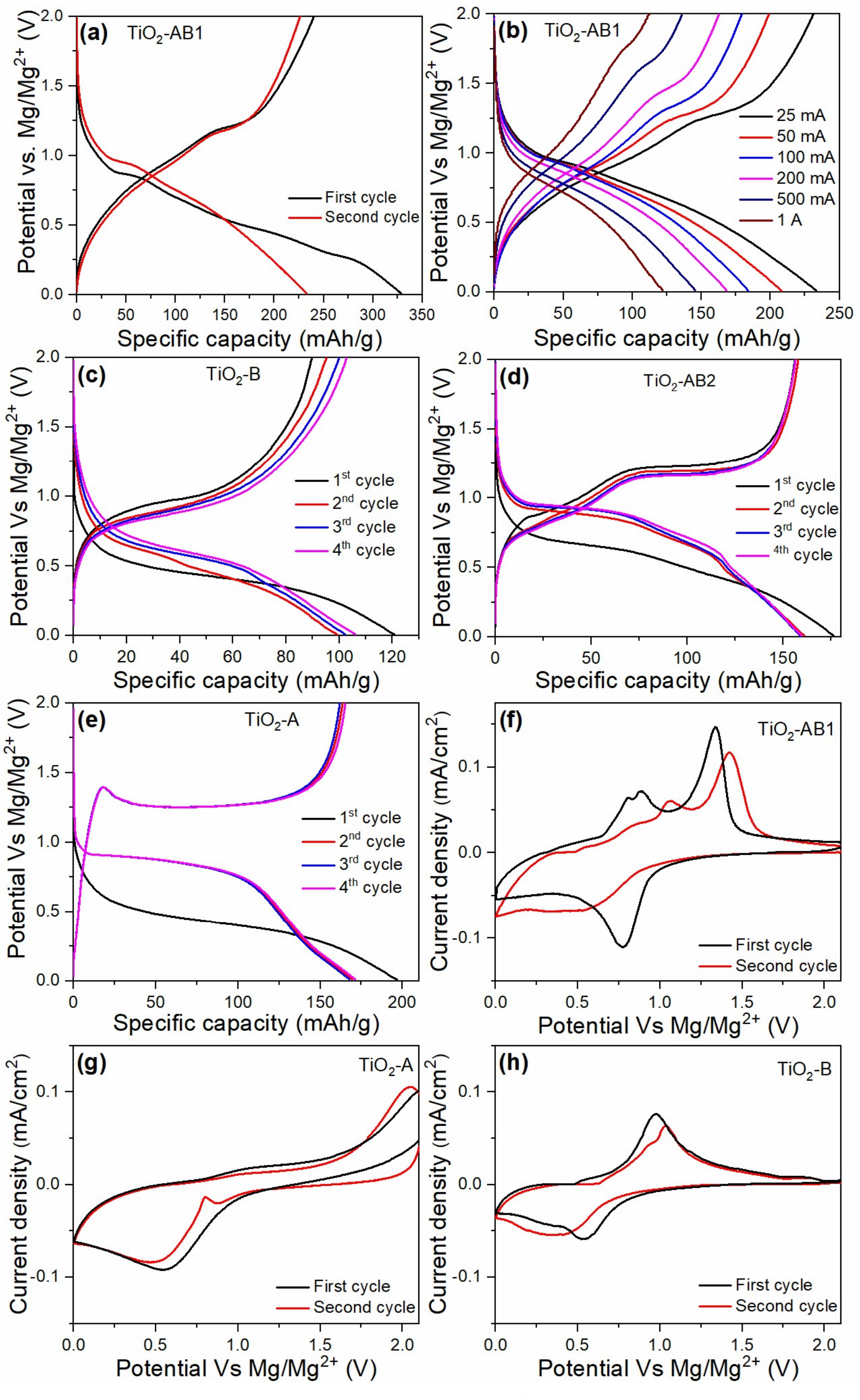

Figure 4.5 (a) Galvanostatic voltage profiles of dual-phase hierarchical TiO_2 nanosheets at different current densities. (b) First and second galvanostatic voltage profiles of dual-phase TiO_2 nanosheet cathode at a current density of 25mA/g in Mg-Li hybrid battery configuration. (c-e) First three galvanostatic voltage profiles of single and dual-phase hierarchical TiO_2 nanosheets at 0.025A/g current density. (f-h) Cyclic voltammograms of dual and single-phase hierarchical TiO_2 nanosheets at a scan rate of 0.1 mV/s.

This indicated different Mg/Li-ion intercalation mechanism, possibly due to the presence of a bronze polymorphs that result in the formation of anatase-bronze nanointerfaces. Cathodic and anodic responses are shifted to slightly lower and higher potentials, respectively, during the second step due to the SEI formation [255]. Reduced intensity of the second cycle voltammogram of all three electrodes verified complete SEI formation in the first cycle, and in good agreement with the first cycle irreversible capacity loss observed from galvanostatic studies. Increased reactivity of the dual-phase TiO_2 nanosheets during the first and second charge-discharge cycles compared to phase-pure counterparts are also evident from these voltammograms. Shape of these cyclic voltammograms are in good agreement with the galvanostatic voltage profiles observed for single and dual-phase TiO_2 nanosheets.

Galvanostatic rate performance of TiO_2 nanosheet cathodes are investigated at varying current densities (25 mA/g –1 A/g) in the voltage window of 0-2V (Figure 4.6a). Dual-phase TiO_2 nanosheet containing 60% anatase and 40% bronze (TiO_2-AB1) exhibited considerably improved electrochemical performance compared to single phase bronze (TiO_2-B), anatase (TiO_2-A) and dual phase sample containing 90% anatase and 10% bronze (TiO_2-AB2). Maximum reversible specific capacity of 235 mAh/g is observed at a current density of 25 mA/g, which is ~2.3, 1.4 and ~1.3 fold higher compared to TiO_2-B, TiO_2-AB1 and TiO_2-A respectively. This electrode also retained a high reversible capacity of 120 mAh/g even at a high current density of 1 A/g, which is seldom observed for Mg-Li hybrid battery cathodes. Unlike the previous reports, electrochemical performance of bronze phase TiO_2 nanosheets are inferior to the other anatase and anatase-bronze hybrid nanosheets. It should be noted that specific capacity and rate performance of TiO_2-AB1 electrode is superior to various metal oxide cathodes reported earlier [174]. At a current density of 1 A/g, this dual-phase TiO_2 cathode achieved a reversible specific capacity of 150 mAh/g and retained ~87% of initial- after 3000 charge-discharge cycles (Figure 4.6b) The corresponding charge-discharge voltage profiles

(Figure 46c) remain identical throughout the cycling, further justifying the excellent reversibility of the electrochemical process. Specific capacity, rate performance and cycling stability of the dual-phase TiO_2 nanosheets are superior to the previously reported Mg-Li hybrid battery cathodes[174,251,256]. Outstanding ion-diffusion kinetics of TiO_2-AB1 cathode enabled fast charging of the Mg-Li hybrid battery (Figure 4.6d). For instance, at a current density of 1A/g, hybrid battery is able to achieve complete charge/ discharge in 5.5 minutes.

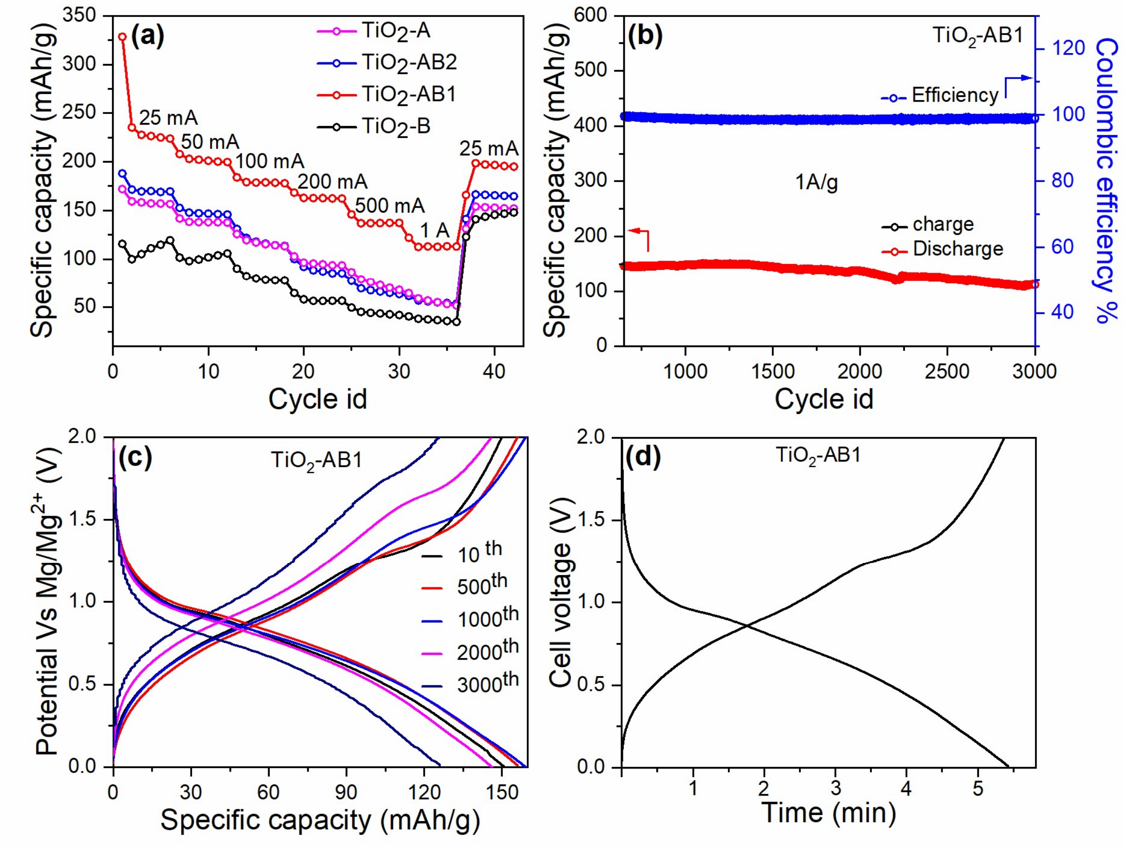

Figure 4.6 (a) Galvanostatic rate performances of single and dual-phase hierarchical TiO_2 nanosheets. (b) Galvanostatic cycling performance of dual-phase hierarchical TiO_2 nanosheets at a current density of 1A/g, and (c) corresponding voltage profiles at different cycle numbers. (d) Time-voltage profile of the TiO_2-AB1 nanosheet.

Driving factors behind the superior electrochemical behavior of dual-phase TiO_2-AB1 cathode is further investigated through cyclic voltammetry measurements at different scan rates (Figure 4.7a). Linear dependence of the peak current densities in this case is a clear indication of the dominant pseudocapacitive type charge storage [224]. Qualitative evaluation of pseudocapacitive and diffusion-limited charge storage is obtained from the log(i) *vs* log (v) plot for the anodic and cathodic peak currents (Figure 4.7b). According to power law equation, b value (slope of the line) of 1 represent complete pseudocapacitance, and 0.5 represent diffusion-limited process. During the scan rate of 0.1 -100 mV/s, TiO_2-AB1 nanosheets exhibited b value of ~0.75 for cathodic and anodic peaks that represent dominant pseudocapacitive charge storage[213,216]. However, b value reduced to ~0.5 beyond scan rate of 100mV/s, representing diffusion-controlled charge storage [224]. This change in the charge storage mechanism can be attributed to the increased diffusion constraints and Ohmic resistance at faster charge rates, which is similar to pseudocapacitive Li and Na battery electrode [47,224]. Pseudocapacitive contributions of single and dual-phase TiO_2 nanosheet cathodes at a scan rate of 1 mV/s are presented in figure 4.7c-f. Shapes of the voltammograms are distinct, representing different Mg/Li-ion storage mechanisms in these electrodes. Bronze and anatase TiO_2 nanosheet cathodes exhibited sharp cathodic and anodic signals. However, broad cathodic signal and two anodic signals are identified in the case of TiO_2-AB1 cathode. Mg/Li-ion intercalation over a wide voltage range in this case confirmed the participation of both anatase and bronze phase in the ion-storage mechanism. Broad anodic and cathodic peaks are also indication of the diffusion-independent pseudocapacitive process [213]. Regardless of the presence of open channels in the crystal structure of bronze-TiO_2 consist of open channels, only a pseudocapacitance contribution of 38% is observed (Figure 4.7c). This can be mainly credited to the sluggish diffusion of Mg-ion resulting from electrostatic repulsion with Ti^{4+} ions [257]. Fast Li-ion diffusion should be expected in this case similar to the previous reports of bronze-TiO_2 based electrode [196,251]. Anatase TiO_2 exhibited slightly higher pseudocapacitance contribution of 49% (Figure 4.7d). Electrochemically most active TiO_2-AB1 cathode (60% anatase + 40% bronze) exhibited the highest pseudocapacitance of 77% (Figure 4.7e), which is 2-fold higher compared to those of bronze TiO_2 nanosheets. Lower pseudocapacitance contribution of 50% is identified for TiO_2-AB2 containing 90% anatase and 10% bronze polymorphs (Figure 4.7f). These results confirmed the strong dependence of anatase bronze ratio on the Mg/Li-ion storage mechanism.

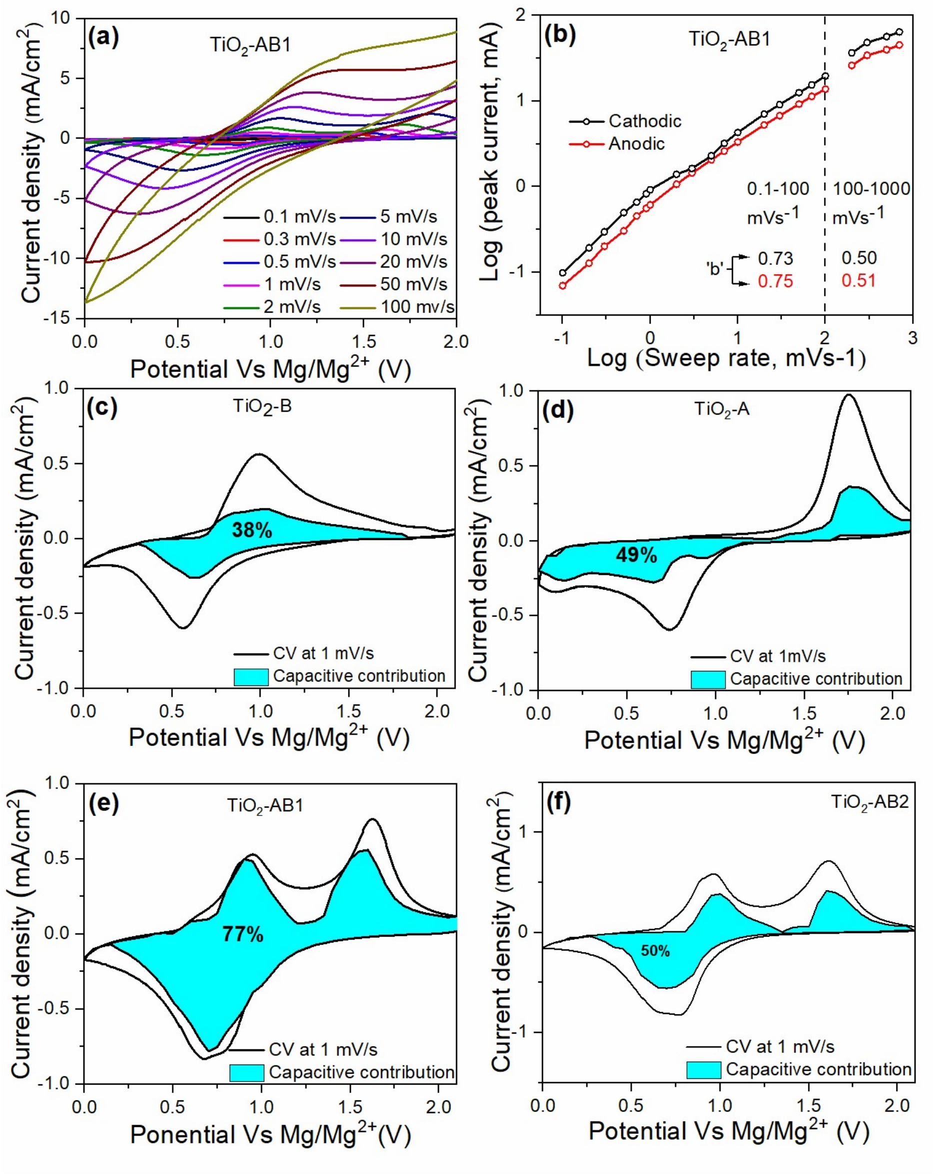

Figure 4.7 (a) Cyclic voltammograms of dual-phase hierarchical TiO_2 nanosheets at various scan rates (b) peak current dependence of scan rates in a Mg-Li hybrid battery. (c-f) Cyclic voltammograms of single and dual-phase hierarchical TiO_2 nanosheets at a scan rate of 1mV/s.

Diffusion-independent (Figure 4.8a-d) pseudocapacitive contribution increased with an increase of scan rate. For instance, TiO_2-AB1 delivered extreme pseudocapacitance of 92% at a scan rate of 10 mV/s (Figure 5f). This is in good agreement with the slopping voltage profiles at higher current densities. Pseudocapacitance contribution in this case is substantially higher than the values previously reported for Mg and Mg-Li hybrid batteries [196,258].

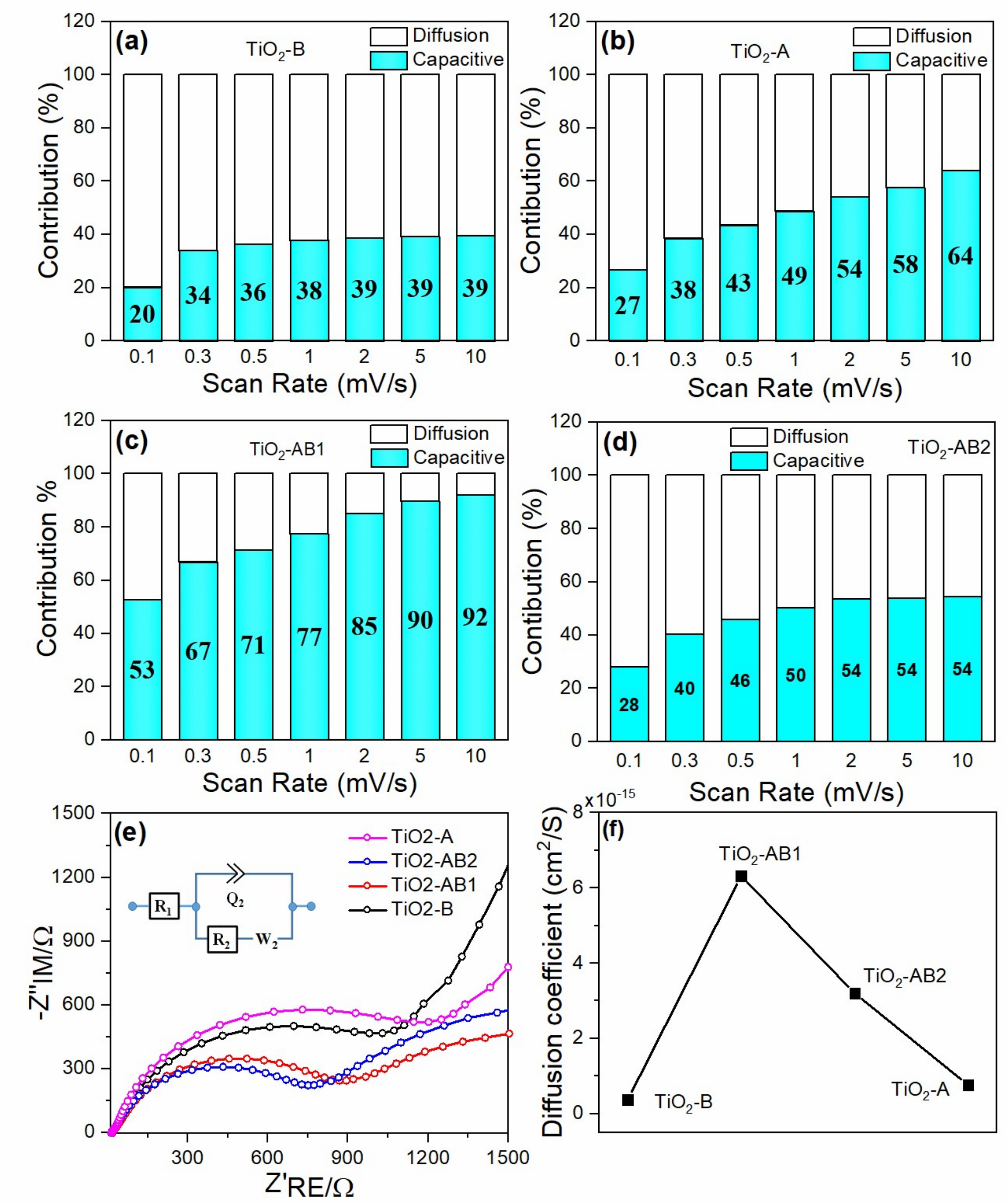

Figure 4.8 (a-d) Pseudocapacitive capacity contribution of single and dual-phase hierarchical TiO_2 nanosheets at various scan rates. (e) Nyquist plot and Randles equivalent circuit (inset) of TiO_2 nanosheets. (f) Diffusion coefficients of TiO_2 nanosheet samples.

Ion diffusion kinetics of single and dual-phase TiO_2 nanosheet cathodes are further investigated through electrochemical impedance spectroscopy (EIS). Nyquist plots of these electrodes (Figure 4.8e) composed of a low frequency slopping line and high frequency semicircle corresponding to solid-state diffusion (Z_w) and charge-transfer resistance (R_{ct}) respectively. Charge transfer resistances of 1031 Ω (TiO_2-B), 865 Ω (TiO_2-AB1), 764 Ω (TiO_2-AB2), and 1204 Ω (TiO_2-A) are obtained by fitting the Nyquist plot to the equivalent circuit (Figure 4.8e inset). Reduced charge transfer resistance of the dual-phase TiO_2 samples can be endorsed to their optimum surface area and pore size that ensure superior contact with the electrolyte solution. Calculated diffusion coefficients of 0.3695×10^{-15} (TiO_2-B), 6.319×10^{-15} (TiO_2-AB1), 3.201×10^{-15} (TiO_2-AB2), and 0.7597×10^{-15} (TiO_2-A) followed a different trend (Figure 4.8f). Highest diffusion coefficient of TiO_2-AB1 cathode justifies its outstanding electrochemical performance as Mg-Li hybrid battery cathode. Strong dependence of the anatase-bronze nanointerfaces, Mg/Li-ion diffusion coefficients and pseudocapacitance is also evident from these results.

Finally, Mg/Li-ion storage mechanism of the electrochemically most active dual-phase nanosheets (TiO_2-AB1) during charge-discharge process are investigated through post cycling *ex-situ* XRD and XPS techniques. XRD patterns of pristine and electrodes at different states of charge corresponding to galvanostatic voltage profile are presented in figure 4.9a. The main intensity peak at $2\theta = 25.4^{\circ}$ corresponding to anatase phase remains unaffected throughout the charge/discharge process. Meanwhile, the bronze signal at $2\theta = 27.4^{\circ}$ gradually disappeared upon initial discharge to 0 V and reappears during charging to 2V. Anatase signal only experienced negligible shifting after initial discharge. High-resolution Ti 2p XPS spectra of discharged and charged electrode (Figure 4.9b) also confirmed reversible formation of Ti^{3+} ($Ti^{4+} \leftrightarrow Ti^{3+}$) during Mg/Li-ion intercalation-deintercalation. High-resolution O1s spectrum of discharged and charged cathodes doesn't undergo significant binding energy shift (Figure

4.9c). Additional broad signal centered at 531.5 eV correspond to the oxygen containing components of the solid electrolyte interface resulting from electrolyte decomposition.

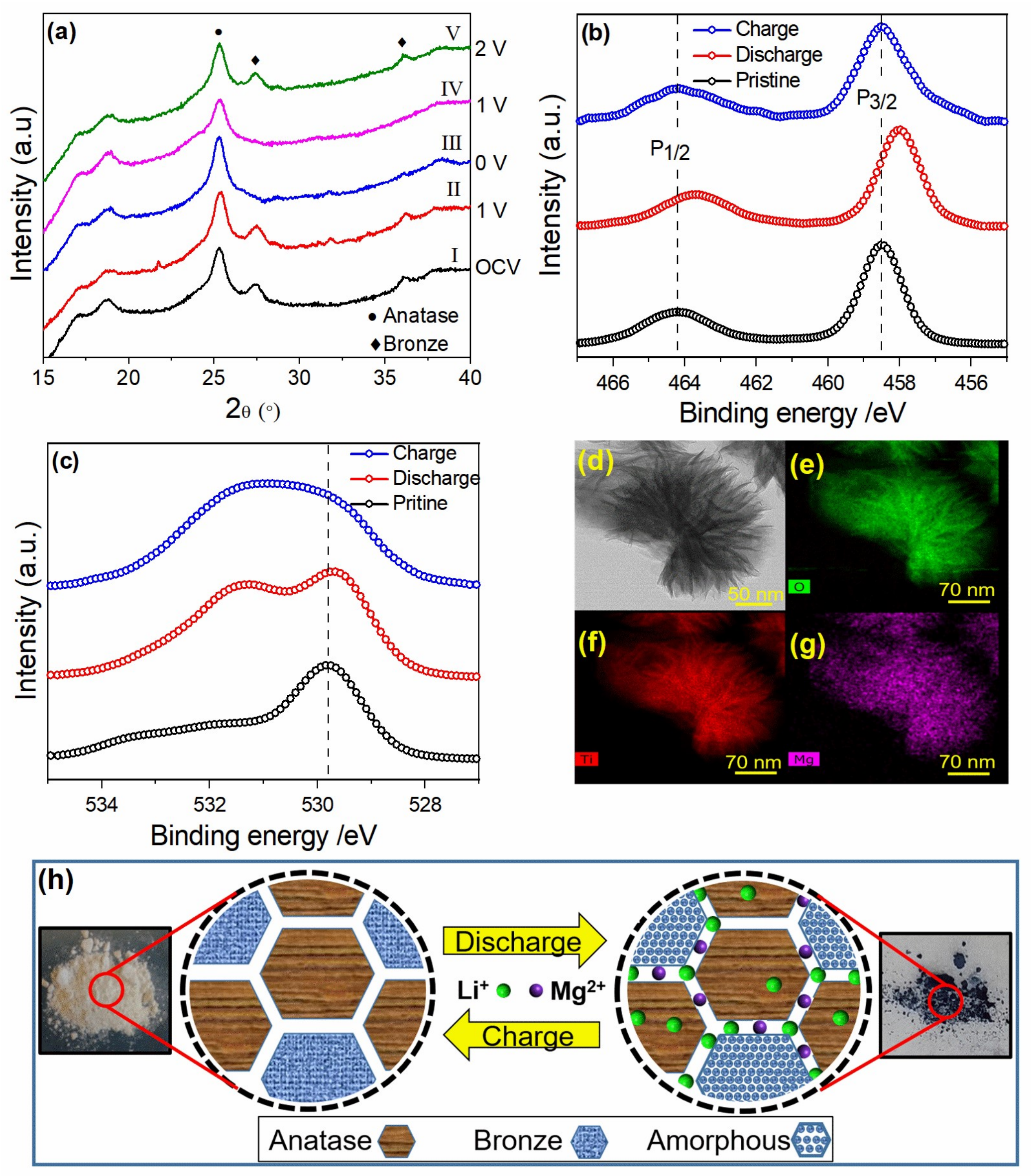

Figure 4.9 (a) Ex-Situ XRD patterns of dual-phase hierarchical TiO_2 nanosheets at various states of charge. (b) Ex-Situ Ti 2p and (c) O 1s high-resolution XPS spectra of dual-phase hierarchical TiO_2 nanosheet cathodes at different state of charge. (d) HAADF image of TiO_2-AB1 electrode and corresponding (e-g) EDX elemental mapping after first discharge. (h) Schematic illustration of ion storage mechanism in dual-phase hierarchical TiO_2 nanosheets and photographs of the completely charged/ discharged powder samples.

Post-cycling TEM image (Figure 4.9d) further verified the structural stability of dual-phase TiO_2 nanosheets during charge-discharge process, which is one of the key reasons for its outstanding cycling stability. EDX elemental mapping (Figure 4.9e-g) confirmed uniform distribution of Ti, O and Mg, which demonstrate homogeneous Mg-intercalation and SEI formation associated with electrolyte decomposition. Dual-phase TiO_2 nanosheets also exhibited reversible color change during charge-discharge process (Figure 4.9h). Blue color of the TiO_2 powder discharged to 0V indicated the distinctive formation of Ti^{3+} ions. Only negligible variations in the anatase lattice parameters are identified during Mg/Li-ion intercalation (Table 4.2).

Table 4.2 Anatase phase lattice parameters of TiO_2-AB1 nanosheet at various states of charge

Charge state	**a**	**c**
OCV	3.5226	9.5131
0V	3.5057	9.4329
2V	3.5180	9.4912

These findings confirmed pseudocapacitive Mg/Li-ion intercalation rather than diffusion limited process and capacitive surface storage [259,260]. This is additionally confirmed by the poor electrochemical performance of high surface area single-phase bronze TiO_2 nanosheets. Pseudocapacitive intercalation through nanointerfaces, an energetically favorable process over diffusion-controlled insertion through crystal planes should be expected in this case [135]. Hence, it is clear that nanointerfaces resulting from anatase-bronze crystal mismatch play a key role in the outstanding electrochemical performance of dual-phase TiO_2 nanosheets. Mg/Li-ion storage in dual-phase TiO_2 nanosheets thus involves reversible amorphization of bronze TiO_2 and pseudocapacitive ion intercalation into anatase crystal structure. This mechanism is totally different from the surface Mg and Li-ion storage reported earlier[51,251]. It is also worth noting that the mechanism demonstrated here is unique in contrast to other intercalation type Mg-Li hybrid battery cathodes[199,258,261]. Pseudocapacitive Mg/Li-on storage without significant structural change of the electrode is often beneficial for obtaining excellent rate performance and cycling stability[259].

Outstanding electrochemical performance of the hierarchical dual-phase TiO_2 nanosheet cathodes can be credited to the anatase-bronze nanointerfaces. High specific capacity, rate performance and cycling stability are caused by the dominant pseudocapacitive type Mg/Li-ion storage. Nanointerfaces between anatase and bronze crystallites in this case act as additional pathways for the intercalation of Mg and Li-ions without considerably affecting the crystal structure of the electrode (Figure 4.9h). Such diffusion-independent ion storage imparts reduced strain to the electrode, and avoids pulverization during extended charge-discharge cycles. Crucial role of well-defined anatase-bronze nanointerfaces is further confirmed by the poor electrochemical performance of physically mixed anatase-bronze hybrid nanosheets (Figure S8). Secondary factors such as 2D morphology, mesoporosity and high surface area improve electrochemical performance by facilitating superior contact with the electrolyte solution. In conclusion, extreme pseudocapacitance caused by rapid ion intercalation through nanointerfaces of dual-phase hierarchical TiO_2 nanosheets make it an excellent cathode for Mg-Li hybrid batteries. The concept of nanointerfaces induced pseudocapacitive ion intercalation can be implemented for the designing of numerous electrode materials for next generation rechargeable batteries.

4.3 Conclusions

In summary, we have demonstrated a high rate and ultra-long life Mg-Li hybrid batteries based on highly pseudocapacitive dual-phase hierarchical TiO_2 nanosheet cathodes. Two-dimensional hierarchical electrode consists of anatase and bronze nanocrystallites and exhibited electrochemical performance superior to the TiO_2 based cathodes reported earlier.

Outstanding Mg-Li dual- ion compatibility is credited to the enhanced pseudocapacitive charge storage facilitated by the rapid ion diffusion through nanointerfaces between anatase and bronze crystallites. Additional factors such as high surface area, mesoporosity and ultrathin nature played only secondary role for the improved electrochemical performance. The dual-phase cathode presented herein also facilitated Mg/Li-ion storage without significant structural change and strain, resulting in excellent cycling stability. The demonstrated approach of nanointerfaces induced pseudocapacitive Mg and Li-ion intercalation can be extended for the designing of numerous cathodes for next-generation Mg-Li hybrid batteries.

Chapter 5

Anatase $Ti_{1-x}Co_xO_{2-y}$ nanosheets as high performance cathodes for Mg-Li hybrid batteries

5.1 Introduction

Mg-Li hybrid battery technology facilitate the selective combination of the low cost-safety features of the Mg-system and high redox activity of the Li-ion system while mitigating the individual shortcomings (slow diffusion kinetics and dendrite growth respectively). Regardless of the attractive characteristics, Mg-Li hybrid battery performances are inadequate to introduce the technology at the commercial level. As described in the previous chapter, among the various intercalation (Mo_6S_8, TiS_2, VS_4, $H_2V_3O_8$, VO_2(B), Mn_5O_8, $Li_4Ti_5O_{12}$, $NH_4V_4O_{10}$, LiV_3O_8@GO), conversion (FeS_2, FeS, CuS), alloying (Bi) and capacitive (TiO_2-B, $VTi_{2.6}O_{7.2}$, VS_2, V_2C MXene) type Mg-Li hybrid cathodes, TiO_2 is highly promising to its unique chemical-thermal stability, low volume fluctuations (<3%) during charge-discharge process, and good redox capacities[51,53,172,174,262].

Among the various polymorphs, metastable bronze TiO_2 (TiO_2-B) is the most attractive due to its superior redox activity[133,197]. However, the difficulty in the large-scale synthesis restricts its commercial implementation[263]. Meanwhile, anatase TiO_2 (TiO_2-A) is more desirable owing to the relatively easy synthesis and good thermal stability. Low specific capacity and other shortcomings of the TiO_2-A has been addressed with various strategies such as nanostructuring, porosity engineering for improved electrolyte contact and electrochemical volume expansion buffering, hybridizing with other polymorphs (TiO_2-B) or carbonaceous materials (CNT), etc. [174,186,223]. Despite of these advances only nominal improvement in the electrochemical performances were achieved, which is inadequate for commercial applications. Hence, further improvement of the TiO_2-A electrodes (capacity, rate and cyclability) is necessary to implement in high performance Mg-Li hybrid battery systems.

This study demonstrates high-performance Mg-Li hybrid battery system based on Co-doped anatase TiO_2 ($Ti_{1-x}Co_xO_{2-y}$) nanosheets. Anatase is chosen as the preferred polymorph due to its high thermal stability and low-cost. Nanosheet morphology is selected to enable improved contact with the electrolyte solution. Mesoporosity and large surface area are intended for enhanced diffusion kinetics. Cation doping is implemented to increase the oxygen vacancies of the anatase TiO_2 crystal structure. Cobalt (Co) is chosen as the dopant owing to its capability of improving the conductivity, thermal stability and redox activity of the active material. Simultaneous oxygen vacancy formation facilitates ion-electron transport contributing to the overall conductivity. Lattice distortions caused by cation doping are also beneficial to improve the number of interfaces between the individual nanocrystallites of the hierarchical nanosheets. Such nanointerfaces can potentially act as ion-diffusion pathways for improved pseudocapacitance. Rapid kinetics of diffusion-independent pseudocapacitive Mg-Li dual-ion storage ensures structural integrity and electrode robustness over extended charge/discharge cycles. The unique cathode architecture having specific morphological and microstructural characteristics made it an excellent Mg-Li hybrid battery cathode.

5.2 Results and discussion

5.2.1 Ssynthesis and characterization of anatase $Ti_{1-x}Co_xO_{2-y}$ nanosheets

Anatase $Ti_{1-x}Co_xO_{2-y}$ nanosheets are synthesized through a two-step solvothermal reaction followed by calcination as depicted in experimental section (Figure 2.3). In the first solvothermal step, hydrolysis and condensation of $TiCl_3$ in viscous ethylene glycol (EG) lead to the formation of hierarchical TiO_2-B nanosheets. Low reactivity of the Ti precursor in this case facilitated a slow crystallization of ultrafine nanosheets with negligible agglomeration[255]. Meanwhile, high viscosity of EG restricted precursor molecule diffusivity, and hence the rate of crystal growth[223]. Less reactive titanium glycolate intermediate formed by reaction between $TiCl_3$ and EG ensures slow hydrolysis and condensation facilitating the formation of uniform ultrathin TiO_2-B nanosheets[47]. Additionally, interaction between the OH groups of EG and titanium glycolate facilitate anisotropic crystal growth crucial for the nanosheet formation[135]. Presence of H^+ and Cl^- ions in the reaction medium also influence the rate of crystallization and hence contribute to 2D morphology formation[240]. Co-doping of the TiO_2 nanosheets are achieved in the subsequent solvothermal reaction. During this step, ammonia reacts with cobalt acetate to form cobalt-ammonia complex capable of incorporating cobalt ions to the TiO_2 crystal structure[264,265]. Owing to the similar ionic radii (Co^{2+}-74.5 pm, Co^{3+}-61 pm, Ti^{4+}-60.5 pm), Co-ions can easily replace Ti-ions until an equilibrium condition which is collectively controlled by the relative concentrations of the Co and Ti ions and the specific solvothermal environment[266]. Metastable bronze structure is transformed to a thermodynamically more stable anatase polymorph upon final calcination. In short, controlled hydrolysis and condensation of titanium precursor formed ultrathin hierarchical TiO_2 nanosheets, and further interaction with cobalt-ammonia complex followed by calcination leads to the formation of anatase $Ti_{1-x}Co_xO_{2-y}$ nanosheets.

Transmission electron microscopy (TEM) images revealed a flower-like architecture of the first solvothermal step product (Figure 5.1a-c) composed of radially grown nanosheets. Such a hierarchical nanosheet morphology is favourable for the Mg/Li-ion storage rather than the individual nanosheets due to the superior contact with electrolyte solution without agglomeration, and ion- diffusion kinetics improvement. Flower-like morphology of these nanosheets remains unaffected irrespective of the second solvothermal reaction with cobalt acetate and/or calcination step (Figure 5.1d-e, g-h). High-resolution images of anatase TiO_2 and $Ti_{0.89}Co_{0.11}O_{1.89}$ nanosheets displayed lattice spacings of 0.36 and 0.34 nm corresponding to the (101) crystal planes of anatase polymorph (Figure 5.1 f, i)[267]. Reduced lattice spacings as a result of Co-doping is in good agreement with the previous reports[265,268]. Moreover, crystallinity also reduced largely upon Co-doping. This can be credited to the formation of disordered areas in the crystal structure due to the oxygen vacancy generation as a result of Co-doping. EDX elemental mapping (Figure 5.2) of anatase $Ti_{0.89}Co_{0.11}O_{1.89}$ nanosheets further revealed a homogenous distribution of co-ions. Corresponding spectral analysis revealed Co-atom percentages of 2.76, 3.57 and 4.35 for anatase $Ti_{0.92}Co_{0.08}O_{1.91}$, $Ti_{0.89}Co_{0.11}O_{1.89}$ and $Ti_{0.87}Co_{0.13}O_{1.87}$ nanosheets respectively. Oxygen vacancies of these anatase TiO_2 nanosheets formed by the replacement of Ti-ions by Co-ions are calculated to be 4.5, 5.5 and 6.5% respectively.

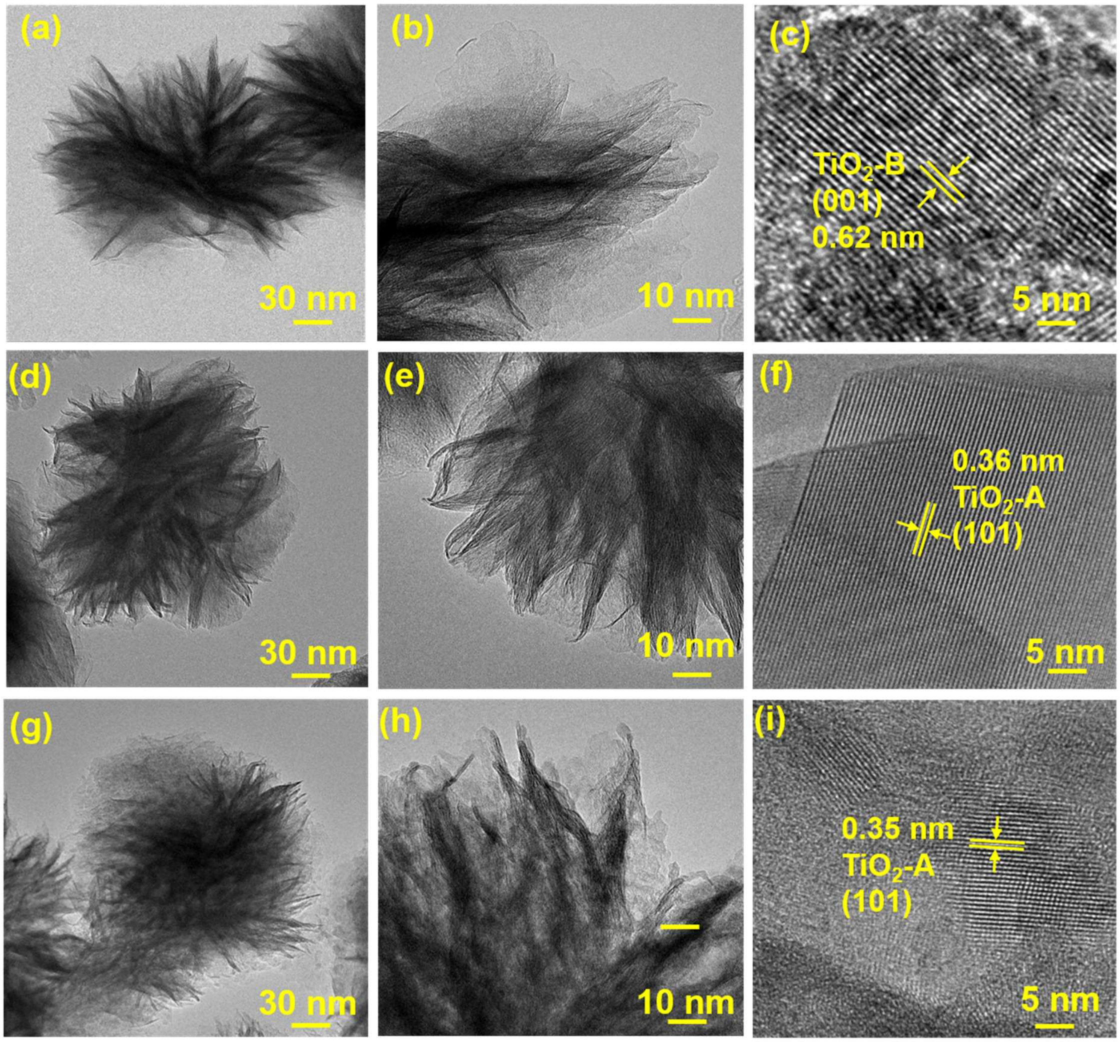

Figure 5.1 TEM images of (a-c) bronze TiO_2 (d-f) anatase TiO_2 and (g-i) anatase $Ti_{1-x}Co_xO_{2-y}$ nanosheets.

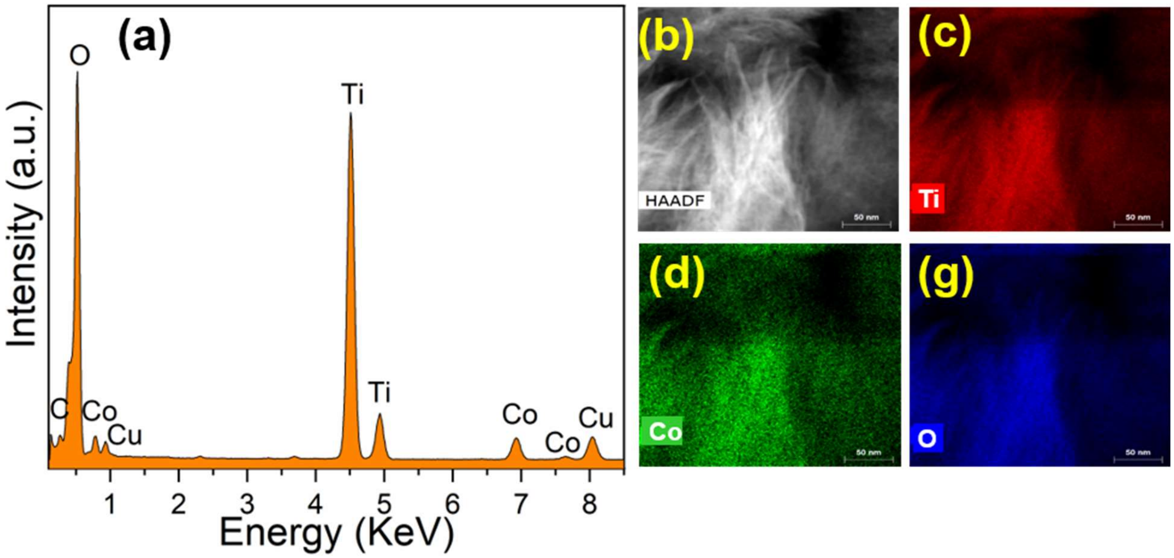

Figure 5.2 (a) EDX spectra, (b) HAADF image and elemental mapping of anatase $Ti_{0.89}Co_{0.11}O_{1.89}$ nanosheets.

X-ray diffraction patterns of the anatase TiO_2 nanosheets (figure 5.3a) confirmed tetragonal anatase TiO_2 phase (JCPDS no. 78-2486, $I4_1$/amd space group)[243,244]. Despite the Co doping, $Ti_{1-x}Co_xO_{2-y}$ nanosheets preserved anatase phase with no significant traces of other TiO_2 polymorphs or CoO_x phases denoting efficient doping of Co atoms within the host lattice. However, XRD patterns of Co-doped compositions exhibited a slight shift to the higher angles signifying a perturbation in the TiO_2 base lattice with the partial replacement of the Ti with Co ions[269,270]. Simultaneous peaks broadening and lower intensity of diffraction peaks further indicates the crystallite size reduction and long-range order disruption due to Co-doping[269–271]. Upon high-temperature calcination, dopant ions exert a drag force in the crystal opposing the driving force of the grain growth and causes crystallite size reduction[271]. Difference in the ionic charges of Ti (4+) and Co (2+ or 3+) results in the formation of oxygen vacancies to satisfy charge neutrality of the lattice[271,272]. Cation replacement and associated oxygen deficiency together collapse the periodicity and crystallite size of the lattice and impart more amorphisity. Table 5.1 summarizes the relative changes in the lattice parameters and hence the cell volume. It shows a decrease in the lattice parameters and hence the unit cell volume with the Co doping with the lowest volume for for $Ti_{0.89}Co_{0.11}O_{1.89}$ nanosheets[269]. Scherrer equation analysis using the most prominent (101) peak provided average crystallite sizes of 17.5±2, 11.7±2, 8.4±2, 8.9±2 nm respectively for TiO_2, $Ti_{0.92}Co_{0.08}O_{1.91}$, $Ti_{0.89}Co_{0.11}O_{1.89}$ and $Ti_{0.87}Co_{0.13}O_{1.87}$.

Table 5.1 Lattice parameters and unit cell volume of anatase TiO_2 and $Ti_{1-x}Co_xO_{2-y}$ nanosheets

	a	c	v
TiO_2	3.7669	9.445	134.0201
$Ti_{0.92}Co_{0.08}O_{1.91}$	3.7442	9.4132	131.9569
$Ti_{0.89}Co_{0.11}O_{1.89}$	3.7323	9.4012	130.9593
$Ti_{0.87}Co_{0.13}O_{1.87}$	3.7382	9.4072	131.461

Structural modifications because of Co-doping were further investigated with Raman spectroscopy (Figure 5.3b). Similar to the XRD results, TiO_2 and $Ti_{1-x}Co_xO_{2-y}$ nanosheets exhibits characteristics E_g (141, 197 and 639 cm^{-1}), B_{1g} (395cm^{-1}) and A_{1g}+B_{1g} (515cm^{-1}) bands of anatase TiO_2[47]. However, 140 cm^{-1} band experienced a gradual broadening and redshift due to the increasing oxygen vacancy concentration and the decreasing grain size resulting from cation doping[268,270]. Furthermore, Raman analysis identified two additional low-intensity bands at 273 and 701 cm^{-1} indicating traces amounts of rutile TiO_2[273]. This could be credited to the Ti-O-Ti bond weakening associated with Co doping, which facilitated minor anatase to rutile transition[274]. Concentration of rutile phases is extremely low, which cannot be detected with the XRD technique. However, intensity of these additional peaks are stronger for the $Ti_{0.89}Co_{0.11}O_{1.89}$ rather than other $Ti_{1-x}Co_xO_{2-y}$ nanosheets having lower and higher Co concentrations.

Textural properties of pure and Co-doped TiO_2 nanosheets were probed with N_2 adsorption/desorption analysis. Type IV isotherm and H3 type hysteresis, and the higher steepness at the high relative pressure signifies the mesoporosity of the nanosheets (Figure

5.3c). Pore diameter and differential pore volume increased significantly for the $Ti_{1-x}Co_xO_{2-y}$ compared to TiO_2 nanosheets (Figure 5.3d).

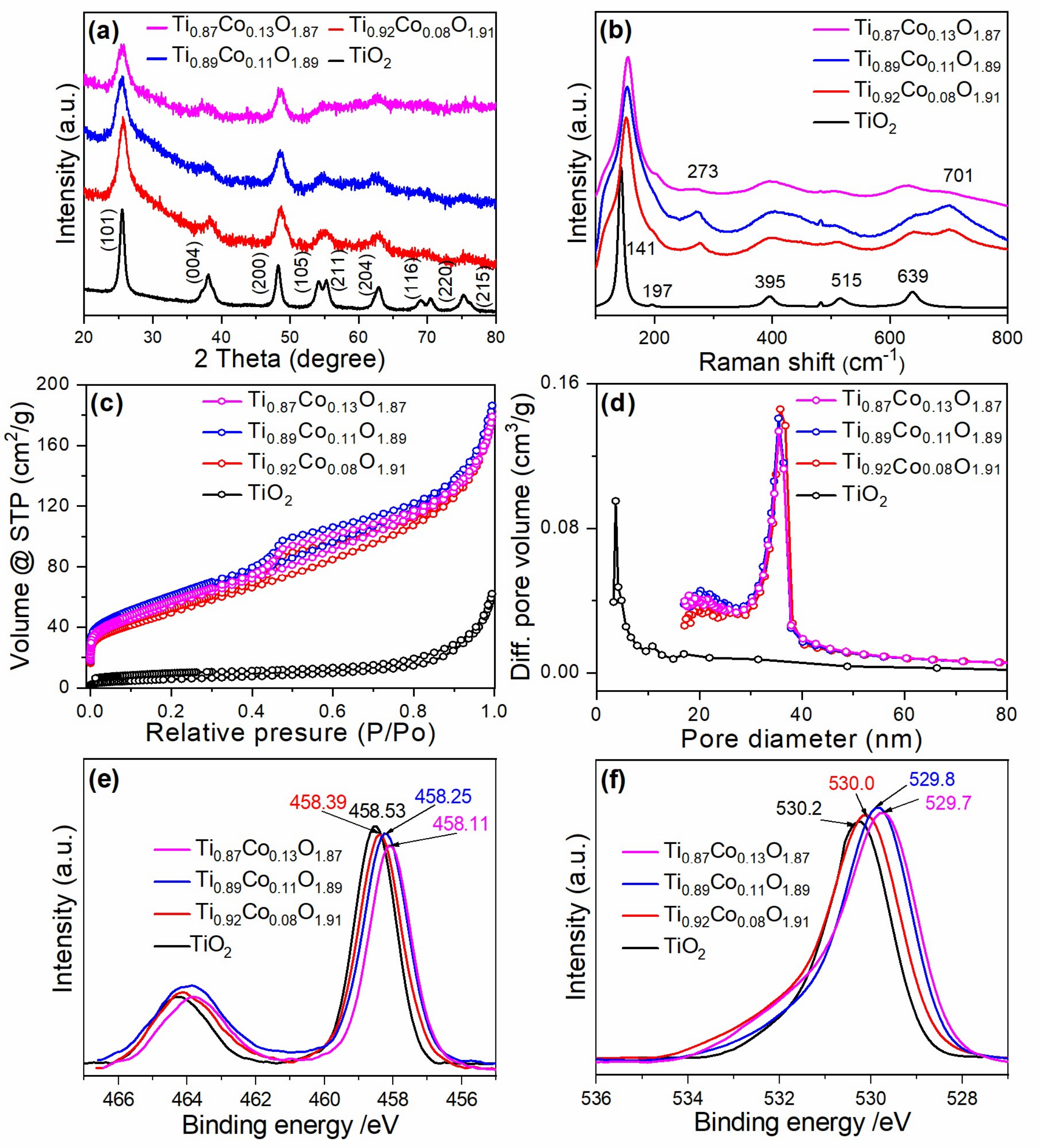

Figure 5.3 (a) X-ray diffraction patterns, (b) Raman spectra, (c) N_2 adsorption-desorption isotherms and (d) pore-size distributions and high-resolution (e) Ti 2p and (f) O 1s XPS spectra of anatase TiO_2 and $Ti_{1-x}Co_xO_{2-y}$ nanosheets

It indicates high dependency of the mesoporosity to the Co-doping. Brunauer- Emmett-Teller (BET) surface area and Barret-Joyner-Halenda (BJH) pore volume also exhibited a considerable enhancement after Co-doping (Table 5.2) with the highest values for anatase

$Ti_{0.89}Co_{0.11}O_{1.89}$ nanosheets. Meanwhile, average pore diameter decreased with an increase of Co-content. This can be related to the increased disorderness resulting from Co-doping, which can eventually reads to the disruption of long-range order and porosity[271]. Increased surface area and mesoporosity of anatase $Ti_{1-x}Co_xO_{2-y}$ nanosheets are advantageous to facilitate superior contact with the electrolyte solutions, and thereby improving the charge transfer kinetics. In short, 3.57 at% Co-doping of anatase $Ti_{0.89}Co_{0.11}O_{1.89}$ nanosheets resulted in enhanced surface area, mesoporosity, reduced crystallite size and highest electrochemical performance.

Table 5.2 Textural properties of anatase TiO_2 and $Ti_{1-x}Co_xO_{2-y}$ nanosheets.

	BET Surface area (m^2/g)	**Pore volume (cm^3/g)**	**Pore diameter (nm)**
TiO_2	80	0.025	4.17
$Ti_{0.92}Co_{0.08}O_{1.91}$	180	0.19	4.08
$Ti_{0.89}Co_{0.11}O_{1.89}$	211	0.20	3.89
$Ti_{0.87}Co_{0.13}O_{1.87}$	200	0.19	3.93

Crystal structure changes resulting from Co-doping are further investigated using X-ray photoelectron spectroscopy (XPS). Despite Co-doping, signals corresponding to CoO_x are absent in the spectra, denoting efficient incorporation of Co-ions into the TiO_2 lattice. High-resolution Ti 2P spectra of TiO_2 nanosheets composed of spin-orbit splitting $p_{3/2}$ (458.53 eV) and $p_{1/2}$ (464.26 eV) doublets (Figure 5.3e). Binding energy difference of 5.73 eV in this case signifies Ti^{4+} oxidation state[223]. This spectrum exhibits a gradual shift to lower binding energies proportional to the Co doping, denoting a reduction in the stoichiometry of TiO_2[233]. Co-ions partially substitute Ti –ions of the TiO_2 crystal structure resulting in the formation of Ti-O-Co bonds, causing Ti-O-Ti bond weakening and lowering of Ti 2P binding energy. High-resolution O 1s spectra also experienced a lowering of binding energy (Figure 5.3f) associated with Co-doping, confirming the substitution of Ti-ions in the crystal structure. This is a clear indication of the oxygen vacancy formation and weakening of the Ti-O-Ti bond strength. Additionally, O 1s spectra also broadened with an increase of Co-doping concentration, which is caused by the oxygen vacancy induced electron delocalization.

5.2.2 Electrochemical performance of anatase $Ti_{1-x}Co_xO_{2-y}$ nanosheets

Mg-Li dual-ion compatibility of anatase $Ti_{1-x}Co_xO_{2-y}$ nanosheets are investigated using various electrochemical techniques. Figure 5.4a depicts galvanostatic rate performance of TiO_2 nanosheet cathodes at current densities ranging from 25 mA/g to 1A/g in the 0-2V voltage window. TiO_2 nanosheets exhibited an initial specific capacity of 185 and 85 mAh/g at 0.25 and 1A/g current density respectively, which is in agreement with the previous reports[51,223,251].

Meanwhile, anatase $Ti_{0.92}Co_{0.08}O_{1.91}$, $Ti_{0.89}Co_{0.11}O_{1.89}$ and $Ti_{0.87}Co_{0.13}O_{1.87}$ nanosheets respectively exhibited a specific capacity of 358, 386 and 352 mAh/g at a lower current density of 25 mA/g. These electrodes also retained a high reversible specific capacity of 165, 191 and 152 mAh/g respectively at a higher current density of 1A/g. Co-doping tremendously enhanced (nearly twice) the specific capacity, and 3.57 at% dopant concentration ($Ti_{0.89}Co_{0.11}O_{1.89}$) found to be the optimum condition for the highest redox activity. Best electrochemical performance of anatase $Ti_{0.89}Co_{0.11}O_{1.89}$ nanosheets can be attributed to the optimum amount of oxygen vacancies and disorderness resulting from Co-doping. Despite its superior performance, Co-doped TiO_2 nanosheets encountered irreversible capacity loss (~13%) associated with solid electrolyte interface (SEI) formation (Figure 5.4b), probably due to the increased reactivity of the generated oxygen vacancies[252]. Additional techniques such as prelithiation and/or introduction of electrolyte additive are needed to minimize the first-cycle capacity loss[253]. Anatase $Ti_{0.89}Co_{0.11}O_{1.89}$ nanosheets are further studied as Mg and Li-battery cathodes (Figure 5.4c-d) to compare the electrochemical performances. It delivered extremely low performance in the Mg (40 mAh/g at 25 mA/g) system. Whereas, Li-ion half-cells delivered a high specific capacity (400 mAh/g at 25 mA/g). It denotes the potential role of Li$^+$ secondary ions in the Mg-Li hybrid system.

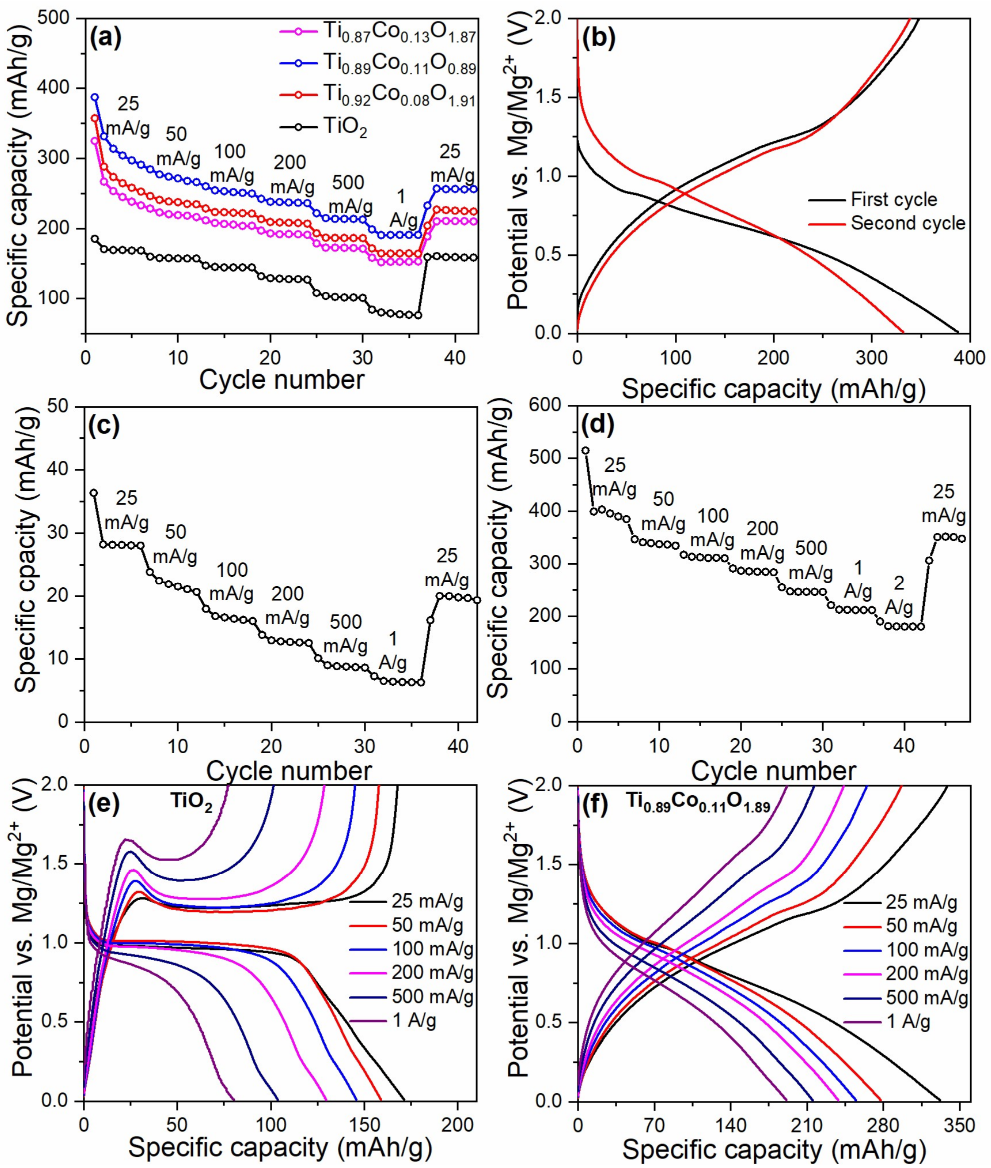

Figure 5.4 (a) Galvanostatic rate performances of anatase TiO$_2$ and Ti$_{1-x}$Co$_x$O$_{2-y}$ nanosheets in Mg-Li hybrid configuration. (b) First and second galvanostatic voltage profiles of anatase Ti$_{0.89}$Co$_{0.11}$O$_{1.89}$ nanosheet cathode at a current density of 25mA/g. Galvanostatic rate performance of anatase Ti$_{0.89}$Co$_{0.11}$O$_{1.89}$ nanosheet in (c) Mg and (d) Li-ion cell configuration. Galvanostatic voltage profiles of (e) anatase TiO$_2$ and (f) Ti$_{0.89}$Co$_{0.11}$O$_{1.89}$ nanosheets at different current densities in Mg-Li hybrid configuration.

Second cycle galvanostatic charge-discharge voltage profiles of anatase TiO_2 and $Ti_{0.89}Co_{0.11}O_{1.89}$ nanosheets as Mg-Li dual-ion battery cathode is presented in Figure 5.4e-f. TiO_2 electrodes demonstrated a typical pattern composed of a plateau and slopping region respectively representing diffusion-controlled intercalation and interfacial storage[249]. This performance is very similar that to Li-ion half cells[275]. Meanwhile, anatase $Ti_{0.89}Co_{0.11}O_{1.89}$ nanosheets exhibited an entirely different slopping voltage profile indicating diffusion independent pseudocapacitive Mg-Li dual -ion storage[224,249]. Stability of the voltage profiles of both electrodes at various current densities signifies the dependability of the respective storage mechanisms to the electrode architecture rather than the current density variations.

Electrochemical characteristics of pure and Co-doped TiO_2 nanosheet cathodes are further analyzed through cyclic voltammetry (CV) technique. TiO_2 nanosheet electrodes exhibited a CV pattern composed of sharp cathodic and anodic signals at 0.79V and 1.54V respectively (Figure 5.5a)[251]. This is typical for the diffusion-controlled intercalation-type battery material. Meanwhile, anatase $Ti_{0.89}Co_{0.11}O_{1.89}$ nanosheet cathodes exhibited an entirely different profile indicating a pseudocapacitive storage mechanism (Figure 5.5b). Broad cathodic peak centered at 0.33V denote the Mg-Li dual- ion intercalation and SEI formation. Anodic signal centered at 1.19 represents dual-ion deintercalation from anatase TiO_2 nanosheet lattice. Sharp peak at 1.33V can be attributed to the diffusion-controlled process, disappeared at higher scan rates simultaneously with considerable increase in pseudocapacitance. Anodic/cathodic peaks of both systems exhibited a slightly different potentials for the second cycle due to the SEI formation[255]. Relative area and the intensity of cyclic voltammograms also experienced a reduction in the second cycle, representing irreversible capacity loss. However, changes are more prominent in the case of anatase $Ti_{0.88}Co_{0.12}O_{2-\delta}$ nanosheets due to its increased redox activity. These observations are also in line with the galvanostatic studies. Anatase $Ti_{0.89}Co_{0.11}O_{1.89}$ nanosheets are further tested in Mg and Li-ion half-cells (Figure 5.5c-

d) to confirm the role of Li-ions in the superior electrochemical performance of Mg-Li hybrid battery system.

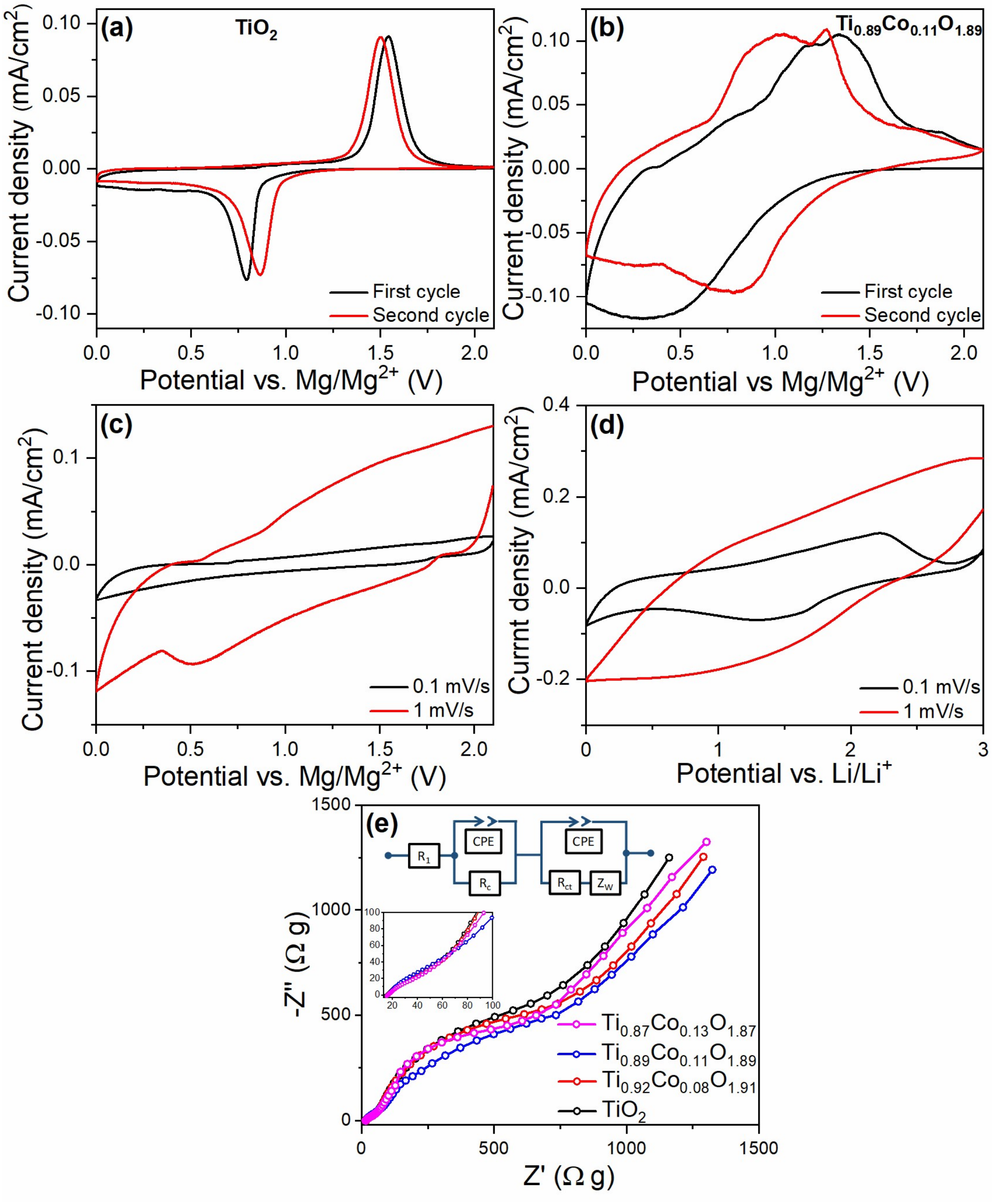

Figure 5.5 Cyclic voltammograms of (a) anatase TiO_2 and (b) $Ti_{0.89}Co_{0.11}O_{1.89}$ nanosheets at a scan rate of 0.1 mV/s. Cyclic volatmmograms of the anatase $Ti_{0.89}Co_{0.11}O_{1.89}$ nanosheet in (c) Mg and (d) Li-ion cell configuration. (e) Nyquist plot and equivalent circuit (inset) of anatase TiO_2 and $Ti_{1-x}Co_xO_{2-y}$ nanosheets.

Ion-diffusion kinetics of anatase TiO_2 nanosheet cathodes are further analysed with electrochemical impedance spectroscopy (EIS) (Figure 5.5e). Nyquist plots of these electrodes are composed of high (Figure 3f inset) and middle-frequency semicircles and a low-frequency slopping line denoting contact impedance (R_c) due to either the passivation layer, particle-to-particle or particle-current collector interaction, charge transfer impedance (R_{ct}) and solid-state diffusion (Warburg element-Z_w) respectively[276]. Equivalent circuit fitting of the Nyquist plot (Figure 5.5e inset) resulted R_c of 52 Ω, 58 Ω, 61 Ω and 56 Ω, R_{ct} of 760 Ω, 740 Ω, 725 Ω and 734 Ω and diffusion coefficients of 7.59×10^{-16}, 8.67×10^{-16}, 10.5×10^{-16} and 8.15×10^{-16} for anatase TiO_2, $Ti_{0.92}Co_{0.08}O_{1.91}$, $Ti_{0.89}Co_{0.11}O_{1.89}$ and $Ti_{0.87}Co_{0.13}O_{1.87}$ nanosheet cathodes respectively. Increase in the contact impedance observed with the Co-doping can be attributed to excess SEI layer formation. Decrease in the charge transfer resistance and increased diffusion coefficients can be attributed to the enhanced electrode-electrolyte interface due to the surface area and porosity enrichment. The highest R_c and lowest R_{ct}-diffusion coefficients of anatase $Ti_{0.89}Co_{0.11}O_{1.89}$ cathodes are consistent with the galvanostatic and CV results. Most distorted TiO_2 lattice having the highest surface area and porosity demonstrated superior redox activity. These results validate the strong dependence between the Co-doping induced lattice distortions, Mg-Li dual- ion diffusion kinetics and pseudocapacitance.

Driving factors behind the dual-ion storage performance of anatase TiO_2 and $Ti_{0.89}Co_{0.11}O_{1.89}$ nanosheets are further investigated by collecting cyclic voltammograms at various scan rates (Figure 5.6a-b). As expected from the galvanostatic results, TiO_2 nanosheet anodes exhibited considerably lower peak current densities compared to $Ti_{0.89}Co_{0.11}O_{1.89}$ cathodes. Different shapes of the voltammograms further indicate different storage mechanisms. Relative variation of cathodic and anodic current response (i) in the voltammograms at different scan rates (v) is depicted in Figure 5.6c. Kinetic responses and charge storage mechanisms can be deconvoluted by relating these log scale plots with power-law equation[213]

$$i(v) = a\, v^b \quad \text{----------} \quad (1)$$

Where *i* is current, *v* is the scan rate, *a* is arbitrary constant and *b* is the power-law exponent, which can be obtained as the slope of log(*i*) *vs* log (*v*) plot.

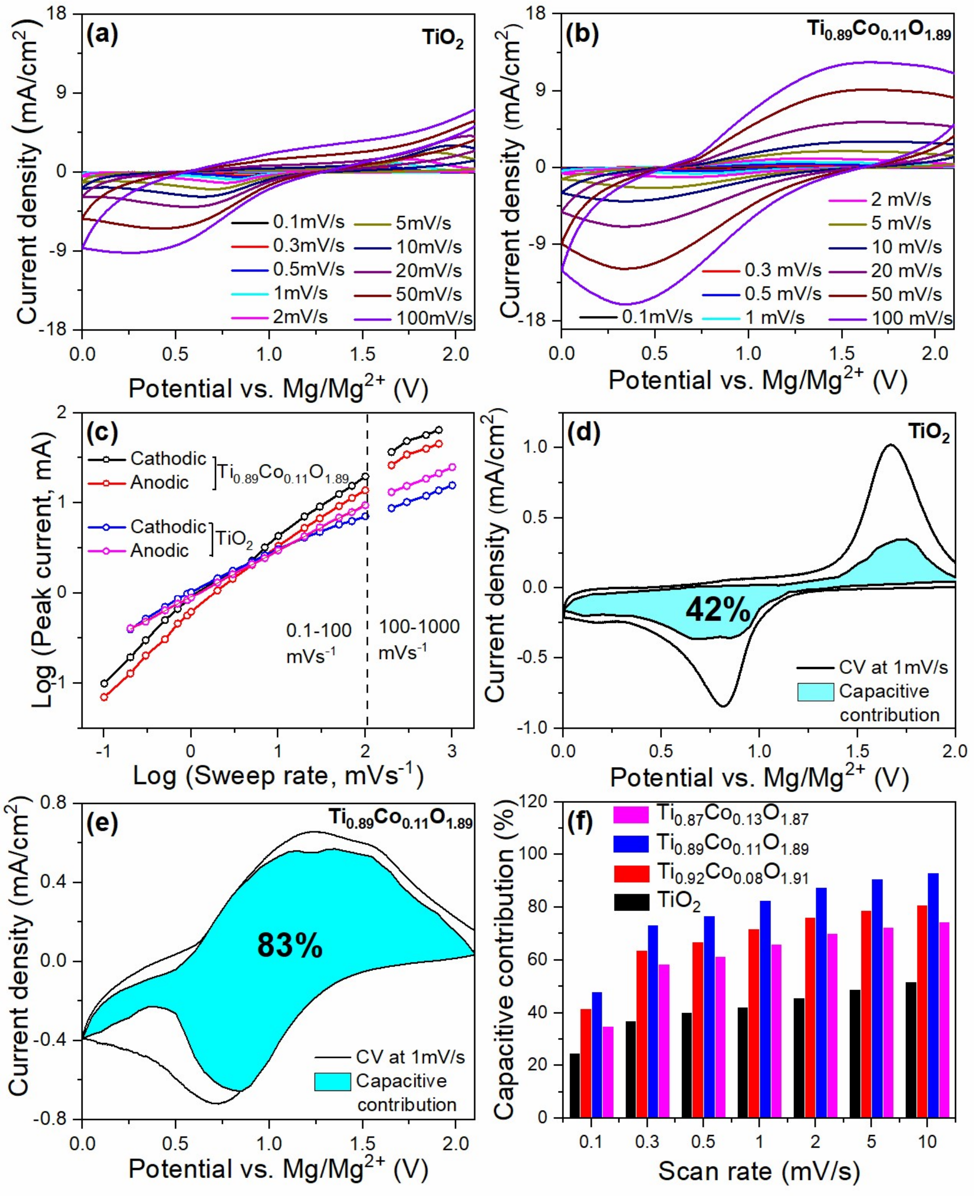

Figure 5.6 (a, b) Cyclic voltammograms at various scan rates and (c) peak current dependence of scan rates of anatase TiO_2 and $Ti_{0.89}Co_{0.11}O_{1.89}$ nanosheets in a Mg-Li hybrid battery configuration. Cyclic voltammograms of (d) anatase TiO_2 and (e) $Ti_{0.89}Co_{0.11}O_{1.89}$ nanosheets at a scan rate of 1mV/s. Pseudocapacitive current contribution is shown in the shaded region. (f) Pseudocapacitive capacity contribution of anatase TiO_2 and $Ti_{1-x}Co_xO_{2-y}$ nanosheets at various scan rates.

For currents obeying the power-law equation, a b-value of 0.5 and 1 is an indication of semi-infinite linear diffusion and surface controlled pseudocapacitance respectively. Anodic and cathodic power-law exponent for the $Ti_{0.89}Co_{0.11}O_{1.89}$ cathodes are 0.73 and 0.75 in the scan rate range of 0.1-100 mV/s, denoting superior pseudocapacitive storage[137]. These values reduced to ~0.5 above 100 mV/s scan rate, suggesting a complete transition to the diffusion-controlled storage due to elevated diffusion constraints and Ohmic resistance[213]. Meanwhile, anatase TiO_2 cathode exhibited a b value of 0.55 and 0.53 in the scan rate rage of 0.1-100 mV/s, pointing to predominant diffusion-limited intercalation process.

Diffusion-controlled intercalation and pseudocapacitance fractions can be quantified as a function of potential using the following equation.

$$i(v) = k_1\, v + k_2\, v^{1/2} \quad \text{----------} \quad (2)$$

Where i is total current, k_1v and $k_2v^{1/2}$ are current contributions from pseudocapacitance and diffusion-controlled process respectively[137]. Pseudocapacitive fractions to the total storage of TiO_2 and $Ti_{0.89}Co_{0.11}O_{1.89}$ nanosheet cathodes at 1mV/s are depicted in figure 5.6d-e. Co-doped cathode exhibited almost double pseudocapacitive contribution (83%) than the stoichiometric TiO_2 electrode. Distinct profiles of the voltammograms indicate different Mg-Li dual-ion storage mechanisms. Limited intercalation of Mg/Li -ions into the anatase crystal lattice resulted in the reduced specific capacity and pseudocapacitance. Pseudocapacitance contribution of anatase $Ti_{0.89}Co_{0.11}O_{1.89}$ nanosheets extend all over the voltage range with a minimum contribution in the 0.75-0V. Significant pseudocapacitance at the peak current densities also indicate the diffusion independent nature of Mg/Li-ion intercalation reaction, which is usually a diffusion-dependent process in the case of TiO_2 anodes [53,277]. Pseudocapacitive fraction of the total storage capacity of TiO_2 is limited to a maximum of 51% (Figure 5.6f), which is in good agreement with its inferior electrochemical performance. However, pseudocapacitance contributions increased with an increase of Co-loading, and highest percentage is identified for the electrochemically most active anatase $Ti_{0.89}Co_{0.11}O_{1.89}$ nanosheets. This sample delivered 48% and 93% pseudocapacitance at scan rates of 0.1 and 10 mV/s respectively. Slightly lower to the best performing cathode, anatase $Ti_{0.92}Co_{0.08}O_{1.91}$ and $Ti_{0.87}Co_{0.13}O_{1.87}$ nanosheets attained fractions of 80% and 74% at 10 mV/s scan rate, which is much above the undoped TiO_2 nanosheet performance. These observations are consistent with the galvanostatic voltage profiles, specific capacities and rate performances. These outcomes also validate the strong correlation between the crystal structure of $Ti_{1-x}Co_xO_{2-y}$ nanosheets and Mg-Li dual-ion storage mechanism.

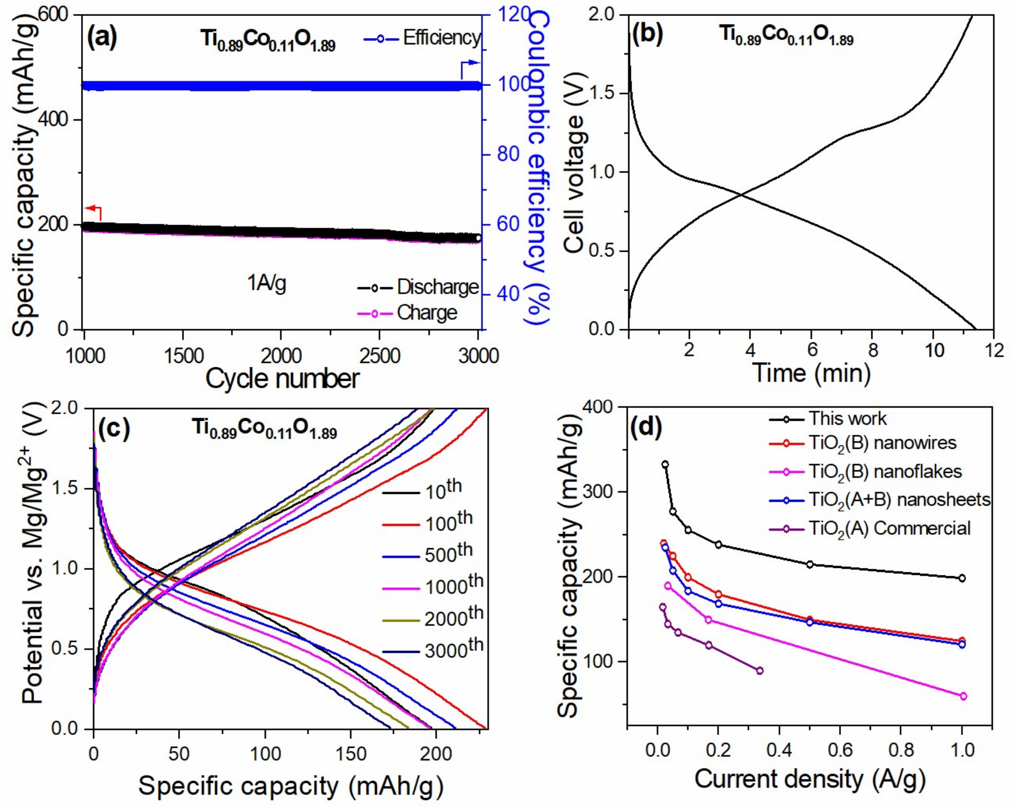

Figure 5.7 (a) Galvanostatic cycling performance of anatase $Ti_{0.89}Co_{0.11}O_{1.89}$ nanosheets at a current density of 1A/g, (b) time *vs* voltage graph of Mg-Li hybrid battery, (c) Galvanostatic voltage profiles at different cycle numbers. (d) Specific capacity and rate performance comparison of anatase $Ti_{0.89}Co_{0.11}O_{1.89}$ nanosheets cathodes with TiO_2 based Mg-Li hybrid cathodes reported earlier

Anatase $Ti_{0.89}Co_{0.11}O_{1.89}$ nanosheet cathodes demonstrated remarkable cyclability as Mg-Li dual -ion hybrid battery cathode (Figure 5.7a). At 1A/g current density, it achieved a high reversible specific capacity of 200 mAh/g and demonstrated 87% capacity retention after 3000 cycles with coulombic efficiency of ~100%. Defective nature of TiO_2 nanosheets further imparted fast-charging characteristics (Figure 5.7b), enabling complete charge of Mg-Li hybrid battery in 11.2 minutes. Identical charge-discharge voltage profiles (Figure 5.7c) throughout the cycling demonstrate the excellent reversibility of the redox process. Discharge capacities of anatase $Ti_{0.89}Co_{0.11}O_{1.89}$ nanosheets outperformed existing TiO_2 based Mg-Li hybrid battery cathodes (Figure 5.7d).

5.2.3 Oxygen vacancy induced Mg-Li dual-ion storage mechanism.

Mg-Li dual-ion storage mechanism of the best performing $Ti_{0.89}Co_{0.11}O_{1.89}$ nanosheet cathode is investigated through various techniques unveiling the crystal structure and microstructural changes. Figure 5.8a depicts the *in-situ* XRD patterns of $Ti_{0.89}Co_{0.11}O_{1.89}$ cathode collected at different charge-discharge states. Irrespective of the states of charge, these electrodes exhibited XRD profiles of anatase-phase TiO_2 with no noticeable crystallinity changes. However, the most prominent (101) diffraction peak undergone a slight reversible shift to the lower angles. This behavior is typical for intercalation pseudocapacitance. E*x-situ* XRD patterns of $Ti_{0.89}Co_{0.11}O_{1.89}$ cathode in Mg and Li-ion-half cells at different state of charge (Figure 5.8b-c) also demonstrates a similar characteristic. High-resolution Ti 2p spectra of the $Ti_{0.89}Co_{0.11}O_{1.89}$ electrode exhibited a reversible shift (0.37 eV) to the lower binding energy (Figure 5.9a). It indicates a reversible Ti^{3+} ($Ti^{4+} \leftrightarrow Ti^{3+}$) formation associated with Mg-Li dual-ion intercalation. This also confirms the ion-intercalation into the crystal structure rather than the defect assisted surface storage. High-resolution O1s spectra of charged and discharged samples does not experience significant change in the binding energy (Figure 5.9b). However, band broadening towards the higher binding energy region, signifying the formation of SEI composed of various oxygen containing species [223].

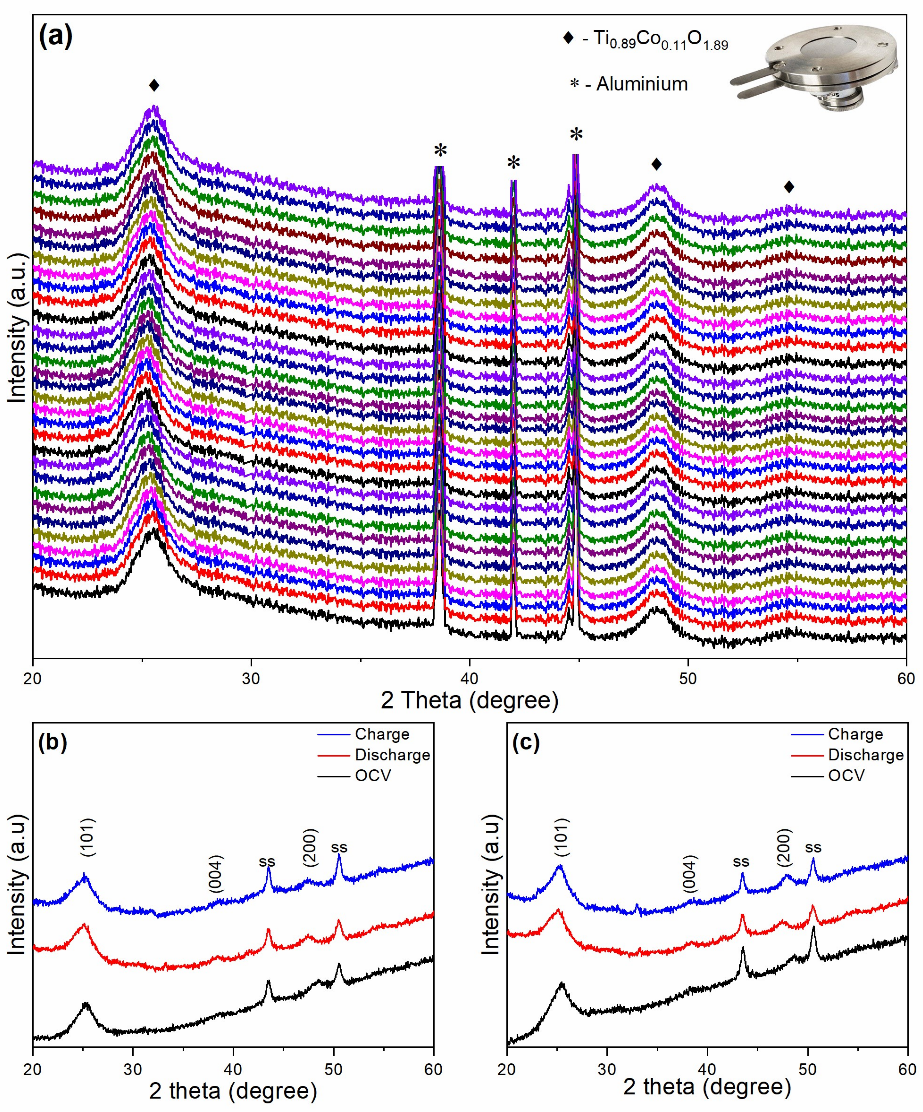

Figure 5.8 (a) In-situ XRD patterns of anatase $Ti_{0.89}Co_{0.11}O_{1.89}$ nanosheets at different states of charge in Mg-Li hybrid configuration. Ex-situ XRD patterns of anatase $Ti_{0.89}Co_{0.11}O_{1.89}$ nanosheet cathode at various states of charge in (b) Mg and (c) Li-ion half cells.

Durability of $Ti_{0.89}Co_{0.11}O_{1.89}$ cathodes during charge-discharge process is further verified through post cycling TEM analysis. TiO_2 nanosheets collected after 1st discharge and 3000 discharge-charge cycles (Figure 5.9c-d) exhibited similar morphology signifying their structural integrity.

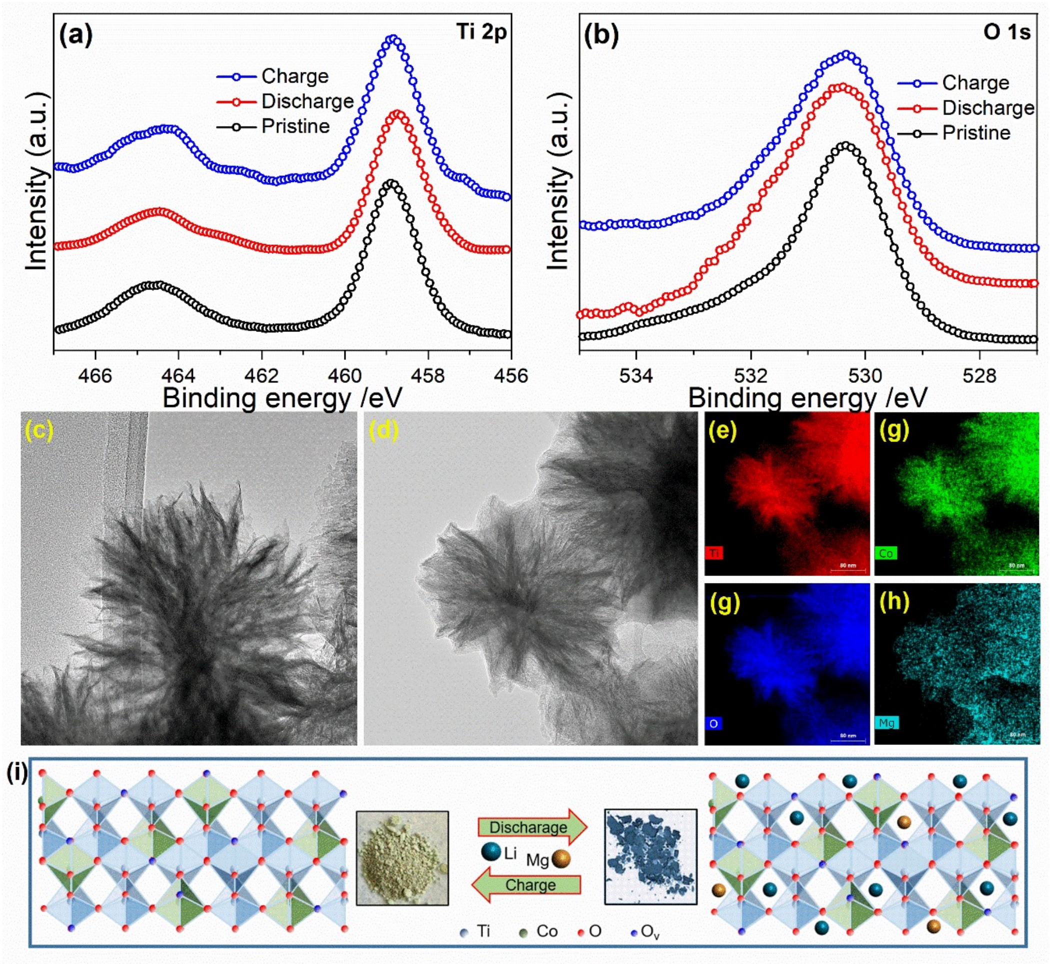

Figure 5.9 *Ex-Situ* high-resolution (a) Ti 2p and (b) O 1s XPS spectra of anatase $Ti_{0.89}Co_{0.11}O_{1.89}$ nanosheets at various states of charge. (c) TEM image of anatase $Ti_{0.89}Co_{0.11}O_{1.89}$ nanosheets after first discharge, (d) 3000 discharge-charge cycles, and (e-h) the corresponding EDX elemental mapping. (i) Schematic illustration of dual-ion storage mechanism in anatase $Ti_{0.89}Co_{0.11}O_{1.89}$ nanosheets, and photographs of the completely charged and discharged powder samples.

Uniform Ti, Co and O distribution obtained from the EDX elemental mapping once again confirms the crystal structure stability during charge-discharge process (Figure 5.9e-h). Homogenous distribution of Mg further revealed the uniform Mg-ion intercalation and SEI formation related to the *in-situ* electrolyte decomposition. Reversible color change (light green ↔ blue) of the $Ti_{0.89}Co_{0.11}O_{1.89}$ nanosheets under dual-ion intercalation/deintercalation also evidenced $Ti^{4+}\leftrightarrow Ti^{3+}$ conversion (Figure 5.9i). Mg-Li dual-ion storage associated with minor lattice parameter changes and $Ti^{4+} \rightarrow Ti^{3+}$ oxidation change is different from the reported surface and/or diffusion limited intercalation type Mg and Li-ion storage in anatase TiO_2 electrodes. Dual-ion intercalation in this case does not induce any crystallinity changes, instead causes a slight change in the lattice parameters to compensate the ion-intercalation strain. Charge balancing simultaneously induce $Ti4^{+} \rightarrow Ti^{3+}$ reduction. These findings signify a pseudocapacitive Mg-Li dual-ion intercalation rather than a surface ion-storage and/or diffusion limited process[259,260]

Remarkable Mg-Li dual-ion storage performance of defective anatase TiO_2 nanosheet cathodes can be attributed to its unique physiochemical properties resulting from Co-doping, two-dimensional morphology, hierarchical microstructure high surface area and mesoporosity. Crystal structure disorderness of anatase $Ti_{0.89}Co_{0.11}O_{1.89}$ nanosheets generated by lattice distortions and oxygen vacancies resulting from Co-doping act as additional channels for pseudocapacitive Mg/Li ion intercalation. Such pseudocapacitive Mg-Li dual-ion storage without negligible structural changes is highly desirable for obtaining superior rate performance and ultralong cycling stability[223]. Hierarchical microstructure of $Ti_{0.89}Co_{0.11}O_{1.89}$ nanosheets results in the formation of numerous interfaces that can also act as additional sites for Mg/Li ion intercalation. Two dimensional morphology, high surface area act as additional factors to achieve superior contact with the electrolyte solution, and thereby improving the charge transfer kinetics.

In conclusion, extreme Mg/Li ion intercalation pseudocapacitance of anatase $Ti_{0.89}Co_{0.11}O_{1.89}$ nanosheets make it an attractive cathode for thigh capacity, fast charging and ultralong life Mg-Li hybrid batteries. Strategy of oxygen vacancy induced pseudocapacitance presented here can also be extended for the designing of other electrode materials and Mg-Li hybrid batteries.

5.3 Conclusions

In summary, we demonstrated anatase $Ti_{1-x}Co_xO_{2-y}$ nanosheets as high-performance pseudocapacitive cathodes for fast-charging and ultralong life Mg-Li hybrid batteries. This defective two-dimensional cathode exhibited outstanding specific capacity, rate performance and cycling stability compared to any of the TiO_2 cathodes reported to date. Exceptional Mg-Li dual-ion storage performance of $Ti_{1-x}Co_xO_{2-y}$ nanosheets is attributed to the rapid pseudocapacitive dual-ion diffusion through the crystal structure disorderness caused by lattice distortions and oxygen vacancies resulting from Co-doping. Pseudocapacitive dual-ion diffusion without phase change of the anatase crystal structure ensured ultralong cycling stability and rate performance. Secondary factors such as ultrathin nature, high surface area, 2D morphology and mesoporosity of the nanosheets also contributed to the electrochemical characteristics by improving contact with the electrolyte solution. The demonstrated strategy of improving the electrochemical performances through oxygen vacancy induced disorderness can be further extended for the designing of other electrode materials and hybrid battery systems.

Chapter 6

Fast-charging and long-lasting Mg-Na hybrid batteries based on extremely pseudocapacitive bronze TiO_2 nanosheet cathodes

6.1 Introduction

Mg-hybrid batteries are recently proposed as an alternative system to fully exploit the advantages of metallic Mg-anode[49]. A secondary ion added to the Mg-battery electrolyte often results in dominant charge storage at the cathode and circumvents the intercalation constraint. Mg-Na hybrid battery is desirable over the Mg-Li system due to its cost-effectiveness[251]. However, increased size of Na-ions is one of the main challenge in developing high performance Mg-Na hybrid batteries[47]. Only limited cathode materials such as ($Na_3V_2(PO_4)_3$, $FeFe(CN)_6$, $NaTi_2(PO_4)_3$, β-NaV_6O_{15}, $Na_{1.5}VPO_{4.8}F_{0.7}$), TiS_2, $Na_3VCr(PO_4)_3$, and $NaCrO_2$ are reported for the Mg-Na hybrid system[202,204,278–280]. These electrode materials are either toxic or exhibited mediocre electrochemical performance. TiO_2 is a widely investigated electrode for rechargeable batteries due to its chemical stability, non-toxicity, low cost, and low volume-change (<3%) during ion-insertion[51,281]. Amorphous are crystalline polymorphs of TiO_2 such as anatase and bronze were investigated for Li, Na and Mg-ion batteries. Among these different phases, bronze-TiO_2 exhibited superior specific capacities due to the presence of open channels in the crystal structure[282]. Nevertheless, electronic conductivity and ion-diffusivity of different TiO_2 polymorphs are not sufficient to facilitate high specific capacity, rate performance and cycling stability[47,53]. Different strategies such as nanostructuring, increasing surface area, porosity control and hybrid formation with carbonaceous materials were investigated for improving the electrochemical performance of TiO_2 electrodes[283–285].

Pseudocapacitive Mg and Na-ion storage gained much attention recently as an alternative to conventional insertion, alloying and conversion reactions[47,137]. This surface and/or near-surface redox reaction follows diffusion-independent kinetics irrespective of the bulk ionic and electronic conductivity of the electrode material[224]. Despite being a faradaic reaction, it does not cause any crystallographic phase changes and hence imparts only minimal volume changes during charge-discharge process[224]. Ion-storage characteristics also ensure faster charge-discharge cycles than conventional battery electrodes. Moreover, excellent crystal structure stability during ion-insertion and extraction ensure extended cycling stability[47]. Though TiO_2-B known to demonstrate pseudocapacitive Li-ion intercalation, Na and Mg-ion storage has not yet exploited successfully due to their inherent intercalation constraints resulting from sluggish diffusion and charge density[286].

Herein, we demonstrate for the first time a high capacity, fast charging and ultra-long life Mg-Na hybrid battery based on extremely pseudocapacitive TiO_2-B nanosheet cathode. High-performance cathode material was designed based on the following aspects. (i) Bronze polymorph (TiO_2-B) is chosen owing to its crystal structure enabling pseudocapacitive ion-storage. (ii) Nanosheet morphology is intended for ensuring substantial contact with the hybrid electrolyte solution. (iii) Mesoporosity, larger surface area and ultrathin nature are selected for enhanced ion-diffusion kinetics. (iv) Hierarchical microstructure of TiO_2-B nanosheets composed of nanocrystallites is preferred for maximizing the density of interfaces that can function as effective ion-diffusion channels. Rapid kinetics of the diffusion-independent pseudocapacitive Mg-Na dual-ion storage further ensures structural integrity and electrode stability. The unique morphology and microstructure of the TiO_2-B nanosheets made it an outstanding Mg-Na hybrid battery cathode.

6.2 Results and discussion

6.2.1 Synthesis and characterization of hierarchical TiO_2-B nanosheets

Hierarchical TiO_2-B nanosheets are synthesized using a solvothermal reaction as depicted in figure 2.2. $TiCl_3$ is chosen as the Ti precursor instead of more reactive $TiCl_4$ or $Ti\{OCH(CH_3)_2\}_4$ to ensure a slow crystallization facilitating the bottom-up growth of TiO_2-B nanosheets with low degree of agglomeration and hierarchical microstructure[17,34]. Multiple roles of ethylene glycol are also crucial in this synthetic method. Firstly, formation of a less reactive glycolate complex by the reaction between ethylene glycol and $TiCl_3$ reduced the hydrolysis/ condensation rate, facilitating the bronze phase formation. High viscosity of ethylene glycol also reduce the crystal growth rate by reducing diffusion of precursor molecules[35]. Finally, 2D morphology formation is facilitated by the free energy change and anisotropic crystal growth associated with the interaction of Ti-OH groups with OH groups of ethylene glycol during the hydrolysis and condensation process[32]. Limited availability of $TiCl_3$ precursor also control the excessive crystal growth and 2D morphology formation[36,37].

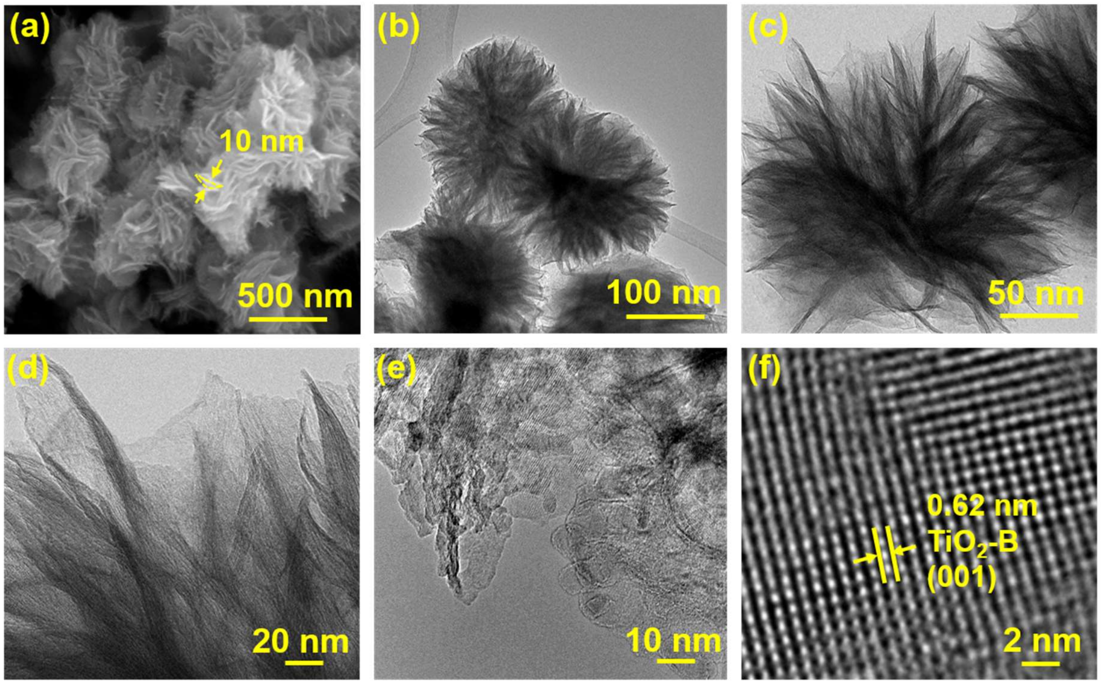

Figure 6.1. (a) SEM and (b-f) TEM images of the hierarchical TiO_2-B nanosheets at various magnifications.

Scanning Electron Microscope (SEM) images demonstrate flower shaped TiO_2-B with an average diameter of ~0.3 µm (Figure 6.1a). TEM images confirmed that flower shaped clusters are composed of radially grown bundles of ultrathin nanosheets of ~10 nm thickness imparting a distinctive hierarchical morphology (Figure 6.1b). Interconnected nature of ultrathin nanosheets are clearly visible from these images (Figure 6.1c, d). HRTEM image (Figure 6.1e) demonstrated individual nanosheets are composed of numerous nanocrystallites with well-defined nanointerfaces between them. Such interfaces often resulted in the unique physicochemical properties of metal oxide nanostructures reported earlier[223,224,255]. In the present case, interfaces between bronze TiO_2

nanocrystallites can act as sites for surface Mg/Na-ion storage, and/or act as intercalation pathways for dual-ion intercalation. HRTEM image (Figure 1g) also verified the exposed (001) crystal planes of the bronze phase TiO_2 associated with a lattice spacing of 0.62 nm[241].

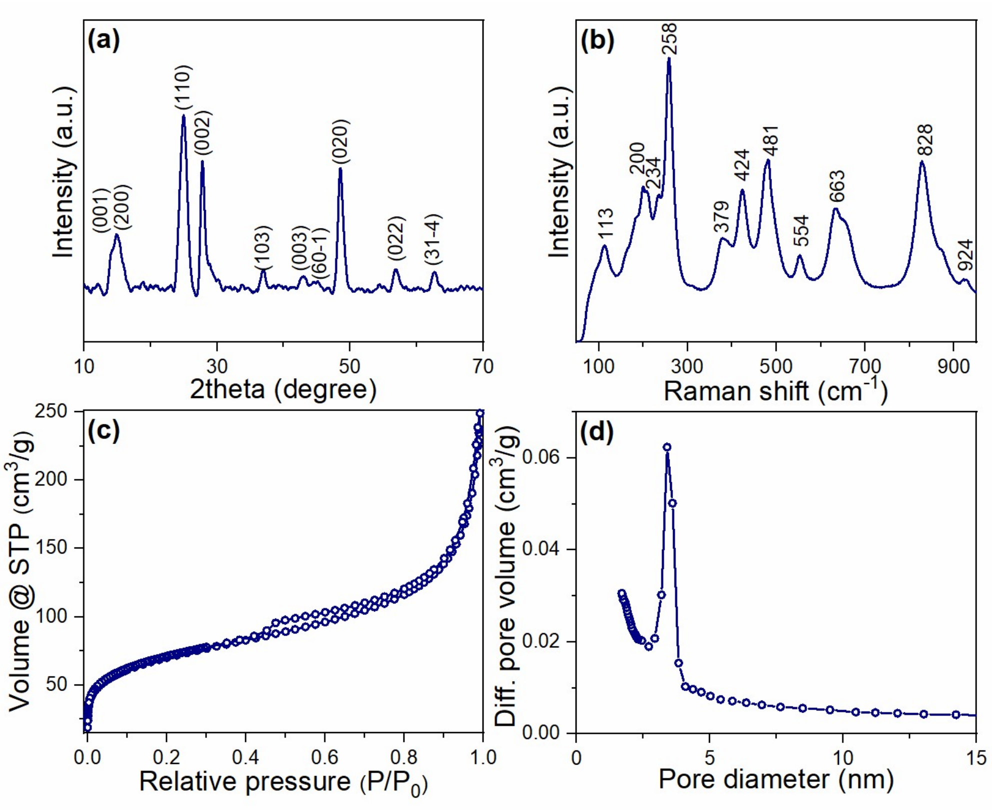

Figure 6.2. (a) X-ray diffraction patterns, (b) Raman spectra, (c) N_2 adsorption-desorption isotherms, (d) pore-size distributions and high-resolution of hierarchical TiO_2-B nanosheets.

X-ray diffraction pattern of TiO_2-B nanosheets (Figure 6.2a) exhibited peaks characteristics of metastable monoclinic bronze polymorph (JCPDS no. 46-1237, C2/m space group) with no traces of other crystal phases[286]. Average crystallite size calculated from the FHWM of most prominent (110) peak using the Debye Scherrer equation revealed the existence of 13±2 nm sized bronze nanocrystallites, which is in good agreement with the TEM results. Phase purity of bronze TiO_2 nanosheets are further confirmed by a more surface sensitive Raman spectral analysis (Figure 6.2b) capable of precisely detecting nanocrystalline phases even at extremely low concentrations. TiO_2 nanosheets exhibited A_g (113, 379, 424, 481, 828 cm^{-1}) and B_g (200, 234, 258, 554, 663 cm^{-}

^{1}) Raman active modes, signifying the formation of phase-pure bronze polymorph, which is in line with the XRD results[287]. High intensity signal at 258 cm^{-1} B_g band and 828 cm^{-1} A_g band point towards the nanosheet morphology of bronze TiO_2 [288]. Textural properties of TiO_2-B nanosheets are analyzed using N_2-adsorption-desorption technique. It exhibited type IV isotherm with H4 type hysteresis (Figure 6.2c), and an increased slope in the 0.4-0.95 relative pressure range signifying the presence of mesopores. Brunauer- Emmett-Teller (BET) and the Barret-Joyner-Halenda (BJH) analysis revealed specific surface area, cumulative pore volume and average pore diameter of 249 m^{2}g^{-1}, 0.15 cm^{3}g^{-1} and 3.39 nm respectively (Figure 6.2d). Such a high surface area and mesoporosity are advantageous to reduce Mg and Na-ion diffusion length by improving contact with the electrolyte solution. Mesopores can further contributes to elevated electrochemical performance by functioning as reservoirs for Mg-Na dual-ion storage.

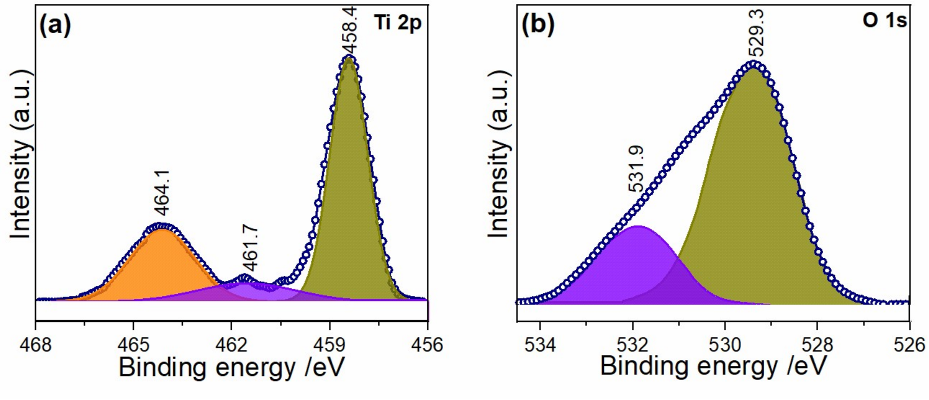

Figure 6.3. (a) Ti 2p and (b) O 1s XPS spectra of hierarchical TiO_2-B nanosheets.

Additional surface chemical characteristics of hierarchical TiO_2-B nanosheets are probed with X-ray photoelectron spectroscopy (XPS) analysis. High-resolution Ti 2P spectrum (Figure 6.3a) consists of a pair of Ti^{4+} energy bands at 458.3 eV and 464.2 eV corresponds to $2p_{3/2}$ and $2p_{1/2}$ components. An intermediate low energy band at 461.7 eV is also visible in the deconvoluted spectra, denoting the presence of Ti^{3+} $2p_{1/2}$ component, which is a clear indication of oxygen nonstoichiometry. Comparison of the relative surface area of Ti^{3+} and Ti^{4+} $2p_{1/2}$ bands confirmed ~10% oxygen deficiency in the crystal lattice. Slight increase in the spin energy separation (5.9 eV) than previous literature can be attributed to oxygen nonstoichiometry and two-dimensional morphology. Deconvolution of the high-resolution O 1s spectra resulted a dominant peak at 529.3 eV denoting the lattice oxygen (O^{2-}) bonded to the Ti atoms in the crystal lattice (Figure 6.3b)[47]. Additional low-intensity signal at 531.9 eV originates from the adsorbed oxygen and/or moisture at the oxygen vacancies. Existence of oxygen vacancies and adsorbed moisture is a common phenomenon in low temperature treated TiO_2 samples, especially in the case of TiO_2-B[47,286]. Oxygen deficiency, and resulting lattice distortions are advantageous for superior electronic conductivity and possible surface ion storage[137]. In summary, controlled hydrolysis and condensation of $TiCl_3$ in ethylene glycol-water mixture results in the formation of hierarchical oxygen deficient TiO_2 nanosheets composed of numerous bronze nanocrystallites[223,255].

6.2.2 Electrochemical performance of TiO_2-B nanosheets

Electrochemical performances of hierarchical TiO_2-B nanosheet cathodes are initially investigated in Mg-battery system (Figure 6.4a). This composite electrode exhibited extremely lower reversible specific capacities (~20 mAh/g at 25 mA/g current density) due to the inherent Mg-ion intercalation constraints. These observations are in good agreement with the previous reports of TiO_2 based Mg-battery cathodes[251]. Meanwhile, the same cathode exhibited tremendous specific capacity improvement in Mg-Na hybrid system, signifying its dual ion compatibility (Figure 6.4b). Galvanostatic charge-discharge measurements of TiO_2-B cathode in Mg-Na hybrid configuration showed an initial discharge capacity of 202 mAh/g at a current density of 25 mA/g (Figure 6.4c). Unlike the previously reported Mg-Na battery hybrid cathodes, it showed low first-cycle irreversible capacity loss, and retained a specific capacity of 197 mAh/g in the consecutive cycle. It represents the complete formation of a SEI during the first cycle with minimum Mg/ Na-ion consumption, which is highly beneficial for the fabrication of a full-cell low-cost battery pack[289]. This cathode also exhibited excellent rate performance, and capacity retention at various current densities. Specific capacity of 140 mAh/g obtained at 1A/g is ~70% of the initial capacity at 25 mA/g current density, a highly desirable but seldom observed characteristic of Mg-hybrid battery cathodes. Additionally, it regained a specific capacity of 205 mAh/g while reducing the current density to 25 mA/g, denoting the high stability of Mg-Na hybrid system. Effect of crystal structure and morphology on the dual- ion storage performance is compared with nanoparticles and nanosheets of anatase and bronze polymorphs (Figure 6.4b).

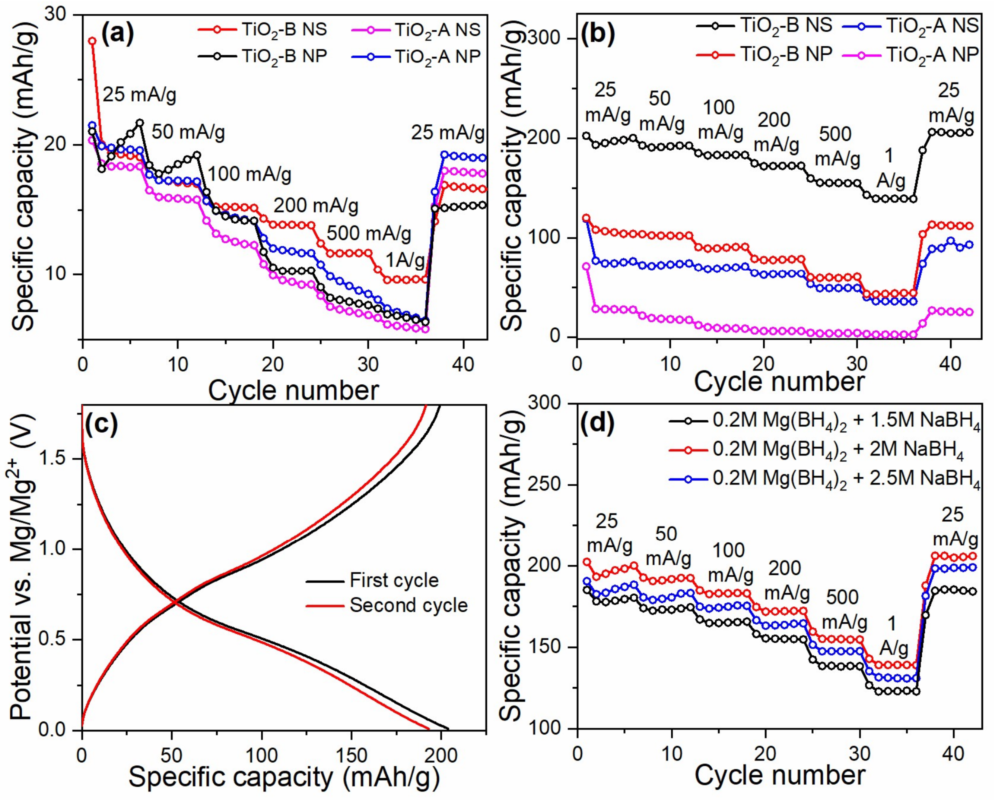

Figure 6.4. Galvanostatic rate performances of various TiO_2 nanosheets and nanoparticles as (a) Mg and (b) Mg-Na hybrid battery cathode. (c) First and second galvanostatic voltage profiles of TiO_2-B nanosheet cathode at a current density of 25mA/g in Mg-Na hybrid battery configuration (d) Galvanostatic rate performances TiO_2-B nanosheets in different Mg-Na hybrid electrolyte solutions.

Maximum reversible capacity of TiO_2-B nanoparticle, TiO_2-A nanosheet and TiO_2-A nanoparticles are only 56%, 40% and 14% of the TiO_2-B nanosheet performance. More tightly-packed crystal structure with fewer diffusion channels leads to lower performance of anatase phase[290]. Meanwhile, substantial drop in the interfacial kinetics resulting from lower exposed surface area caused inferior electrochemical performance of nanoparticles[286]. Specific capacities, rate performance and cycling stability observed in the case of TiO_2-B nanosheet cathode is vastly superior to numerous metal oxide cathodes reported earlier for Mg-Na hybrid[149,204,208,291,292].

Influence of Na-ion concentration on the overall performance of TiO_2-B nanosheet cathodes are investigated by varying the $NaBH_4$ percentage in the dual ion electrolyte (Figure 6.4d). Reversible specific capacities obtained are178, 195 and 182 mAh/g corresponding to 1.5, 2 and 2.5 M of $NaBH_4$ concentrations respectively at a current density of 25 mA/g. Specific capacities increased linearly with $NaBH_4$ concentration up to 2M, but reduced after 2.5M. Hence, electrolyte concentration has a distinct effect on the overall electrochemical performance due to variations in solution viscosity, ion mobility and electrolyte conductivity[261].Galvanostatic charge-discharge profiles of TiO_2-B nanosheets in Mg-Na dual-ion battery configuration is depicted in figure 6.5a. It displayed a slopping pattern pointing to diffusion-independent limited pseudocapacitive Mg-Na dual-ion storage[224]. Identical voltage profiles independent of the current densities (25-1000 mA/g) represents similar ion- storage mechanism at all charge-discharge rates. Increasing slope of the voltage profiles proportional to the current density increment verified a corresponding rise in pseudocapacitive dual-ion storage[47].

Cyclic voltammetric studies provided further insight into the electrochemical response of TiO_2-B nanosheet cathodes towards Mg-Na dual-ion intercalation. Figure 6.5b represents initial three cycles at a scan rate of 0.1mV/s. In general, patterns follow a rectangular-like behavior denoting a predominant pseudocapacitive storage mechanism[213]. Low irreversible capacity observed in the galvanostatic rate performance is also evident from these voltammograms. Cathodic signal in the 1.52-0V voltage window of the first cathodic scan correspond to Mg/Na-ion intercalation and irreversible capacity loss due to SEI formation[53]. Stabilization of the voltammograms after first cycle is a clear indication of the complete SEI formation in the first charge-discharge process[47]. Cathodic scan of the CV curve consist of two distinct regions (1.8-0.7V and 0.7-0V) corresponding distinct electrochemical reactions. According to the DFT reports, high voltage sloping current reflection and the following broad peak at 0.47V respectively represent pseudocapacitive cation adsorption at A2 and C sites of TiO_2-B lattice associated with $Ti^{4+}\rightarrow Ti^{3+}$ conversion[53]. Broad anodic signal located at 0.75V corresponds to the Mg-Na dual-ion deintercalation from the TiO_2-B storage locations with $Ti^{3+}\rightarrow Ti^{4+}$ reversal. Identical anodic/cathodic responses in the subsequent cycles without any noticeable changes represent extreme reversibility of the Mg/Na-ion storage[255]. Cyclic voltammograms of TiO_2-B nanosheets in Mg and Na-ion battery half-cell configurations (Figure 6.5c-d) confirmed negligible contribution of Mg-ions towards specific capacity. Hence, higher performance of Mg-Na hybrid system can be attributed to dominant Na-ion intercalation in to TiO_2-B nanosheet cathodes.

Detailed Mg-Na dual-ion storage process mechanism is further investigated by collecting CV patterns of TiO_2-B nanosheets at different scan rates (Figure 6.5e). Linear dependence of peak anodic/cathodic current densities and scan rates evidence predominant pseudocapacitive charge storage[224]. Quantification of pseudocapacitance and diffusion-controlled ion- storage is carried out using log scale plot between the peak current i (anodic and cathodic) and the scan rate voltage v (Figure 6.5f). As per power law equation, b value (slope of the $\log(i)$ *vs* $\log(v)$ plot) of 1 and 0.5 respectively represents a diffusion-independent diffusion-dependent process. In the case of TiO_2-B nanosheet cathode, anodic and cathodic b value can be quantified as 0.71 and 0.7 in the scan rate of 0.1-100 mV/s, suggesting a dominant capacitive response with a certain diffusion contribution[213,216]. However, slops and hence the *b* value decreased on increasing the scan rate above 100 mV/s corresponding to the shifting to diffusion-dependent ion-storage kinetics[224]

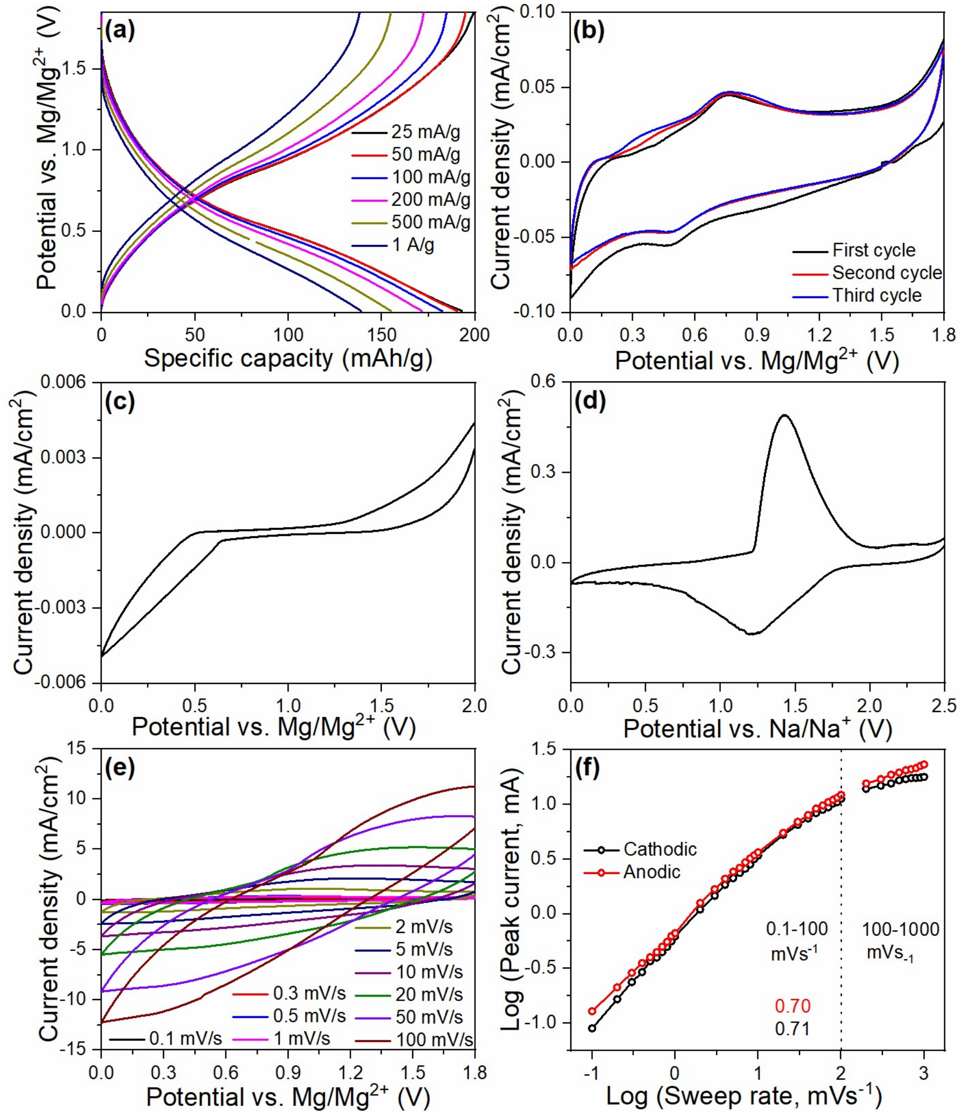

Figure 6.5. (a) Galvanostatic voltage profiles. Cyclic voltammograms at a scan rate of 0.1 mV/s TiO_2-B nanosheets as (b) Mg-Na, (c) Mg and (d) Na battery cathode. (e) Cyclic voltammograms at various scan rate and (f) Peak current dependence of TiO_2-B nanosheets at different scan rates in Mg-Na hybrid battery configuration.

This behavior can be attributed to the increased diffusion constraints and ohmic resistance at faster sweep rates. A similar phenomenon has been previously observed for pseudocapacitive Li, Na and Mg-Li hybrid battery cathodes[47,224]. Above-mentioned fractions of capacitive and diffusion controlled contributions can be quantified by separating the specific contribution using extended form of power law equation as described in previous chapters.

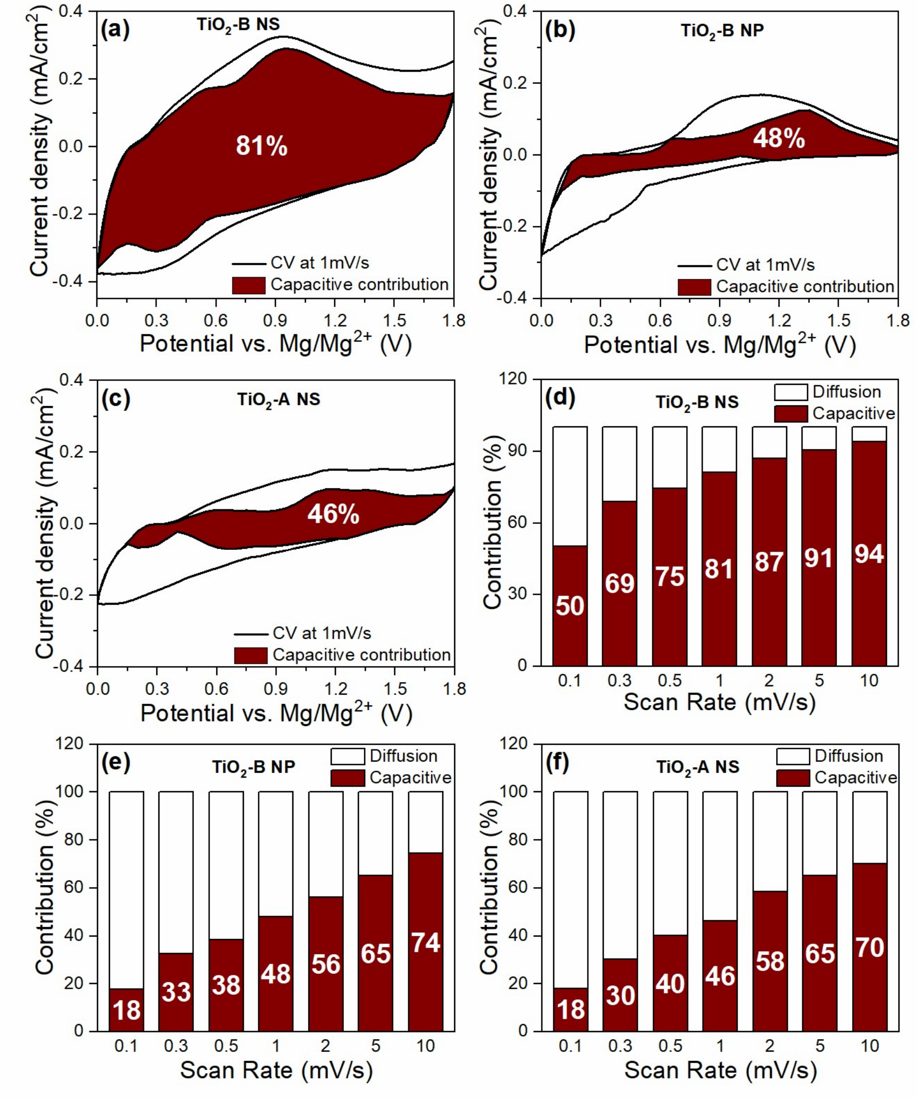

Figure 6.6. Cyclic voltammograms of (a) TiO_2-B nanosheets, (b) TiO_2-B nanoparticles and (c) TiO_2-A nanosheets at a scan rate of 1mV/s. Pseudocapacitive current contribution is shown in the shaded region. Pseudocapacitance contribution of (d) TiO_2-B nanosheets, (e) TiO_2-B nanoparticles and (f) TiO_2-A nanosheets at various scan rates.

As presented in figure 6.6a pseudocapacitive charge storage dominate most of the voltage range in the case of TiO_2-B cathode[133,277]. Though CV curves of TiO_2-B nanoparticles consist of pseudocapacitive process, contribution is limited to only 48% (Figure 6.6b). Mg/Na-ion intercalation in this case is mostly diffusion-limited at lower voltage ranges, which can be credited to the lack of nanointerfaces and 2D morphology. TiO_2-A nanosheets also demonstrated 46% pseudocapacitive contribution (Figure 6.6c) due to intercalation constraints. These pseudocapacitive contributions are significantly lower considering the specific capacity values are much lower than TiO_2-B nanosheet cathodes. Pseudocapacitance contributions of all TiO_2 cathodes increased at higher scan rates (Figure 6.6e-f), and TiO_2-B nanosheets exhibited a maximum of 94% at the 10mV/s (Figure 6.6d). These results are in line with the slopping voltage profiles at higher current densities. These values are considerably superior to the previously reported pseudocapacitance of Mg and Mg hybrid battery cathodes[133,223]. Strong dependence of morphology and crystal structure on the Mg/Na-ion storage mechanism is evident from these results.

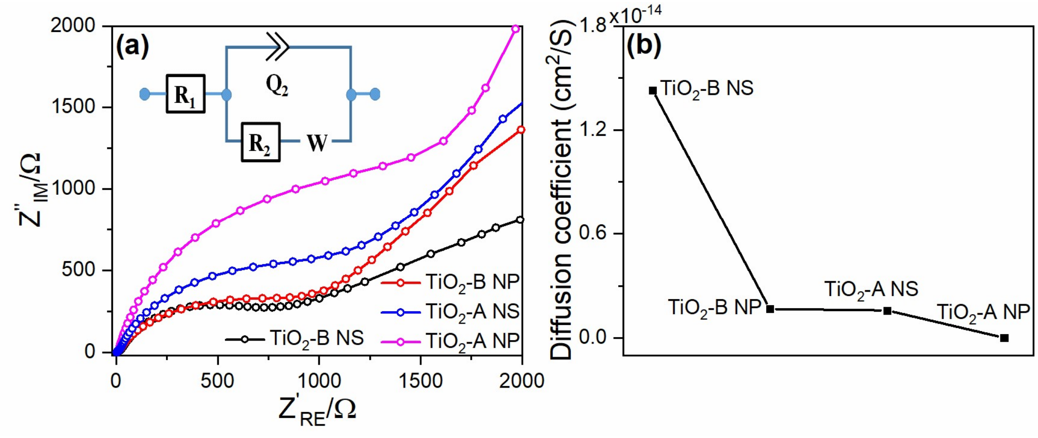

Figure 6.7 (a). Nyquist plot, inset: Randles equivalent circuit, and (b) diffusion coefficients of TiO_2 nanosheets nanoparticles based electrodes.

Electrochemical impedance spectroscopy (EIS) further revealed dual-ion diffusion kinetics of TiO_2 electrodes (Figure 6.7a). Nyquist plots comprised of a high-frequency semi-circle and a low-frequency slopping line respectively representing the charge transfer resistance (R_{ct}) and solid-state diffusion coefficient (Z_w). Equivalent circuit fitting (Figure 6.7a inset) of the Nyquist plots revealed R_{ct} of 775Ω (TiO_2-B NS), 996 Ω (TiO_2-B NP), 1139 Ω (TiO_2-A NS) and 1452 Ω (TiO_2-A NP). Lowest R_{ct} of TiO_2-B nanosheets compared to the other electrodes can be endorsed to hierarchical microstructure, and nanosheet morphology that facilitate improved electrode-electrolyte contact. Despite of its lower surface area than TiO_2-A NS (106 m^2g^{-1}), TiO_2-B NP (80 m^2g^{-1}) exhibited slightly lower R_{ct} suggesting the possible influence of crystal structure in the dual-ion storage performance. Diffusion coefficients calculated from the Warburg impedance (Eq. 3) are 1.43 x 10^{-14} (TiO_2-B NS), 1.67 x 10^{-15} (TiO_2-B NP), 1.59 x 10^{-15} (TiO_2-A NS) and 1.95 x 10^{-16} (TiO_2-A NP), which are also in line with the R_{ct} variations (Figure 6.7b). Highest diffusion coefficient of TiO_2-B NS validates the strong correlation between Mg/Na dual-ion diffusion kinetics, pseudocapacitance and excellent electrochemical performance.

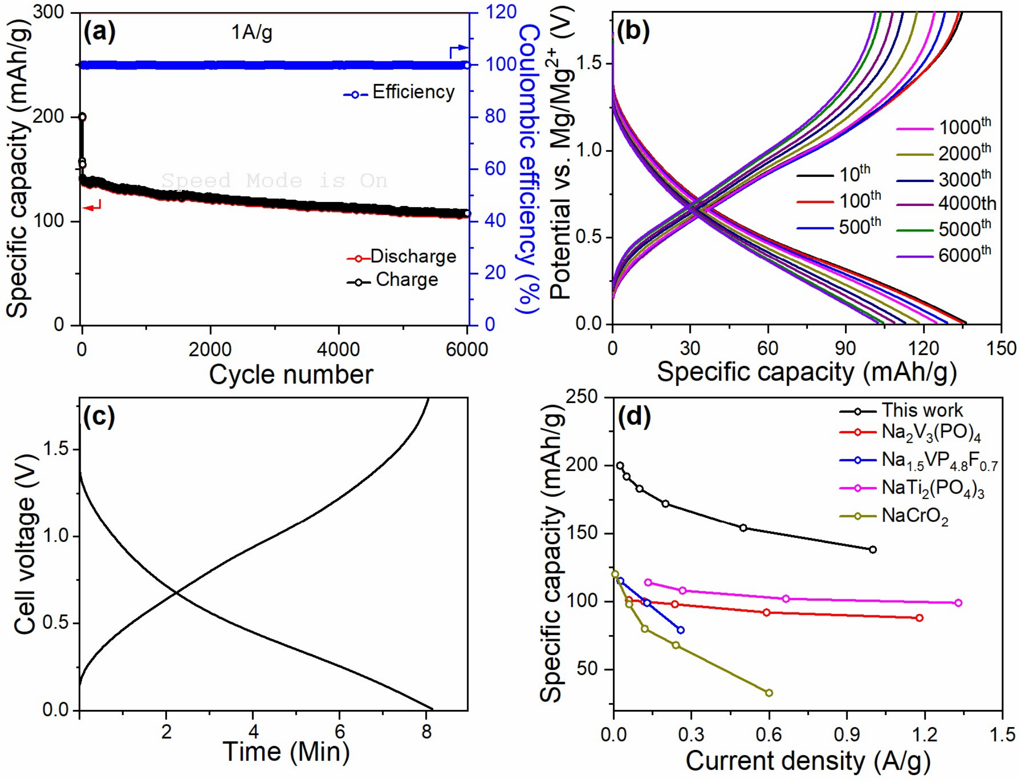

Figure 6.8 (a) Galvanostatic cycling performance of TiO_2-B nanosheets at a current density of 1A/g and (b) corresponding voltage profiles at different cycle numbers. (c) Charge-discharge speed of TiO_2-B nanosheet cathode at 1A/g current density in Mg-Na hybrid battery configuration (d) Specific capacity and rate performance comparison of TiO_2-B nanosheets cathodes with oxide type Mg-Na hybrid cathodes reported earlier.

TiO_2-B nanosheets exhibited exceptional cycling stability as Mg-Na hybrid battery cathode (Figure 6.8a). At a higher current density of 1A/g, it delivered a reversible specific capacity of 140 mAh/g, and retained ~76% capacity after 6000 charge-discharge cycles ~100% coulombic efficiency. This outstanding cycling stability is considerably superior to any of the metal oxide based cathodes reported earlier[149,204,208,291,292]. Identical voltage profiles (Figure 6.8b) at different instants of the cycling signify a stable electrochemical system with excellent reversibly. It further exhibited fast charging characteristics, which require only 8.1 minutes for complete charge (Figure 6.8c). Specific capacities and rate performance of TiO_2-B nanosheet electrodes are substantially superior to the performance of the previously reported metal oxide type Mg-Na hybrid battery cathodes (Figure 6.8d).

6.2.3 Detailed evaluation of Mg-Na dual-ion storage mechanism

Finally, Mg-Na dual-ion storage mechanisms of TiO_2-B nanosheet cathodes are investigated using XRD, Raman, XPS and TEM techniques. *In-situ* XRD patterns collected at different states of charge are presented in figure 6.9a. These patterns exhibited no significant crystal structure changes during Mg-Na dual-ion intercalation and deintercalation. *Ex-situ* Raman spectra of composite electrode at OCV and different states of charge are depicted in Figure 6.9b. Similar to the XRD patterns, it showed no significant variations in the characteristic spectra. These nominal changes reflect minor lattice parameter changes during charge-discharge process. High-resolution XPS spectra of the discharged TiO_2-B nanosheet electrode exhibited a lowering of Ti 2p binding energy by 0.37 eV compared to the pristine sample (Figure 6.9c). This confirms the reversible $Ti^{4+} \leftrightarrow Ti^{3+}$ oxidation state change during the Mg-Na dual-ion intercalation-deintercalation process. Structural robustness of TiO_2-B nanosheets during charge-discharge process is revealed from the post cycling *ex-situ* TEM image after first discharge (Figure 6.10a) and 6000 cycles (Figure 6.10b). A uniform distribution of Ti, O, Mg and Na observed in the EDX elemental mapping further confirmed homogeneous Mg-Na dual-ion intercalation into the stable TiO_2 matrix (Figure 6.10c-f) and uniform SEI formation. Reversible color change from off-white to blue observed during the discharge process once again indicates $Ti^{4+} \leftrightarrow Ti^{3+}$ switching (Figure 6.10g) during charge-discharge process.

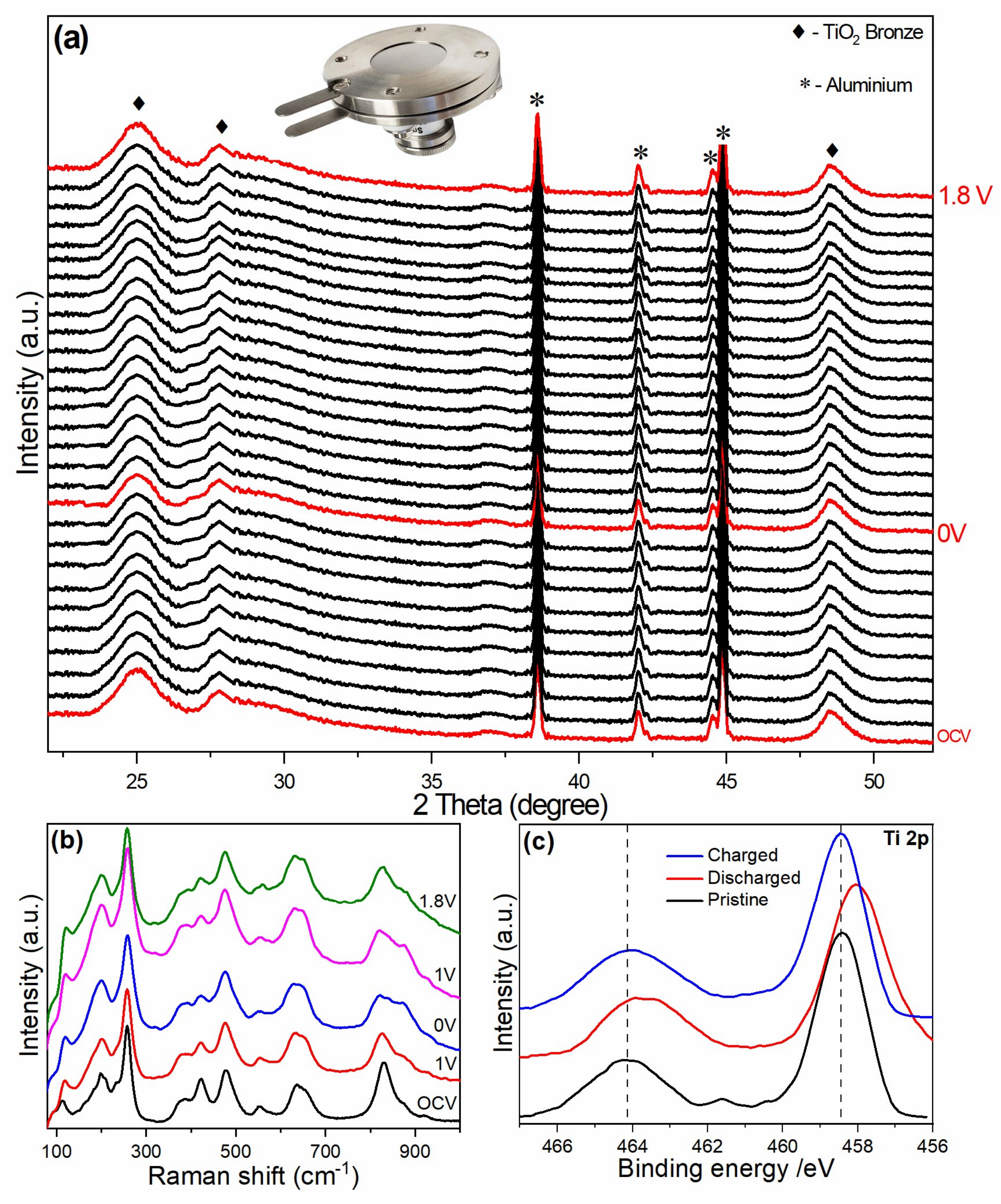

Figure 6.9 (a) *In-situ* XRD patterns of the TiO_2-B nanosheets at different states of charge. Inset: *In-situ* electrochemical cell used for collecting the XRD patterns. (b) *Ex-Situ* Raman spectra and (c) high-resolution Ti 2p XPS spectra of TiO_2-B nanosheets at various states of charge.

These results verified pseudocapacitive Mg/Na-ion intercalation pseudocapacitance rather than diffusion limited intercalation and surface storage[223,255]. This should be expected due to the energetically more favorable nature of pseudocapacitive intercalation through nanointerfaces compared to diffusion-controlled insertion through crystal planes. Crucial role of nanointerfaces is also verified by the poor electrochemical performance of TiO_2-B nanoparticles lacking such hierarchical structure (Figure 6.4b). Observed Mg-Na dual-ion storage accompanied by $Ti^{4+} \rightarrow Ti^{3+}$ conversion is entirely different from the previously reported surface Mg and Na-ion storage in TiO_2-B cathodes[197,293,294]. It is also worth noting that the mechanism demonstrated here is unique compared to other intercalation type Mg-Na hybrid battery cathodes [202,204,278–280]. Such pseudocapacitive Mg/Na dual-ion storage with no significant crystal structure change is highly desirable for enhanced rate capability and prolonged cycle life[259].

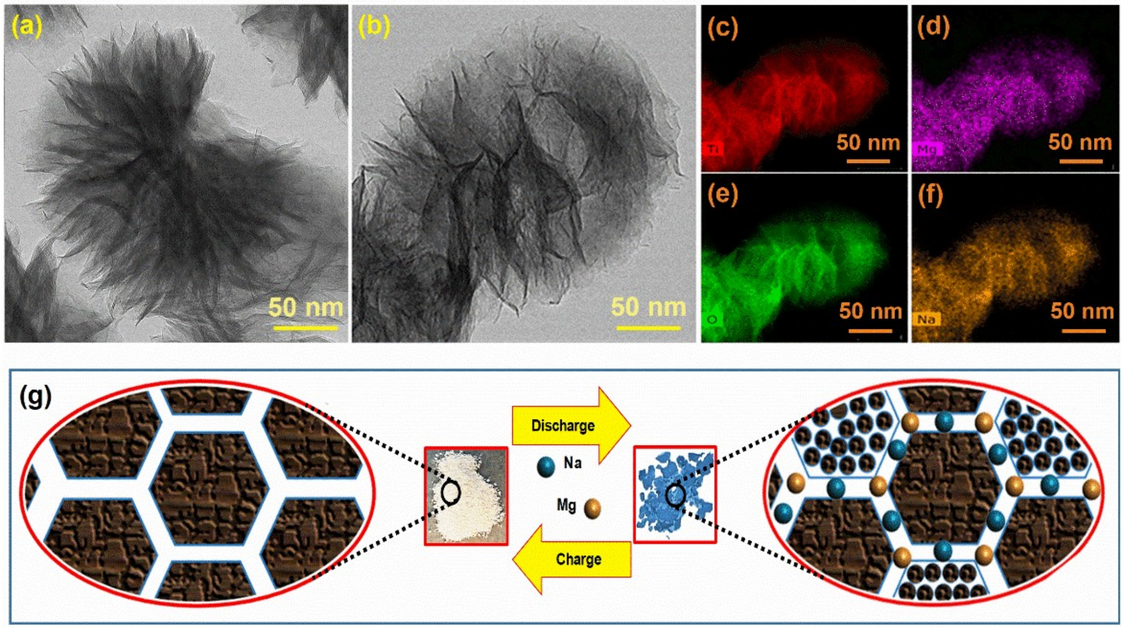

Figure 6.10 (a) TEM image of TiO_2-B nanosheet after first discharge, (e) 6000 cycles, and (f-i) the corresponding EDX elemental mapping. (j) Schematic illustration of dual ion storage mechanism in TiO_2-B nanosheets, and photographs of the completely charged and discharged powder samples.

Remarkable Mg-Na dual-ion storage performance of TiO_2-B nanosheet cathode can be ascribed to its unique physiochemical properties resulting from hierarchical microstructure and two-dimensional morphology. Extreme pseudocapacitive ion-storage resulted in the high specific capacity, rate performance and cycling stability. Numerous nanointerfaces between bronze crystallites of the hierarchical microstructure can act as additional pathways for Mg/Na-ion intercalation without affecting the crystal structure (Figure 6.10g). Such diffusion independent mechanism enhanced electrode robustness by minimizing the strain associated with ion insertion. It eventually resulted in the outstanding rate performance and cycling stability of TiO_2-B nanosheet cathode. High surface area, 2D morphology and mesoporosity act as secondary factors to improve the electrochemical performance by increasing contact with the electrolyte solution. Additionally, oxygen vacancies present in the sample is beneficial for improved electronic conductivity. Crucial role of nanointerfaces and two-dimensional morphology in the electrochemical performance of TiO_2 cathodes are further verified from the control experiments (Figure 6.4b). In conclusion, exceptional pseudocapacitive Mg-Na dual-ion storage is caused by the rapid ion-diffusion aided by numerous nanointerfaces present in the hierarchical TiO_2-B nanosheets. Unique physiochemical properties of TiO_2-B nanosheets make it an excellent cathode material for high performance Mg-Na hybrid batteries. Demonstrated strategy of nanointerfaces driven Mg-Na dual-ion insertion pseudocapacitance can be extended for the designing of high performance electrodes for advanced Mg-Na hybrid batteries.

6.3 Conclusions

In summary, we presented the implementation of highly pseudocapacitive hierarchical TiO_2-B nanosheets as compatible cathodes for high rate and ultra-long life Mg-Na hybrid batteries. The two-dimensional hierarchical mesoporous cathode comprising immense nanograins and oxygen nonstoichiometry exhibited superior electrochemical characteristics dominating all the previously reported metal oxide cathodes. Potentially higher Mg-Na dual-ion storage characteristics are attributed to the higher intercalation pseudocapacitance established by the fast ion diffusion through the nanograin interfaces and defect locations. The minimum lattice strain ensured electrode robustness upon extended cycling. The high surface area, ultrathin nature and mesoporous structure also contributed to adequate electrode-electrolyte contact and facile interfacial kinetics. The demonstrated approach of enriching the electrochemical characteristics by additional intercalation pseudocapacitance can potentially be extended for designing the next generation battery electrodes.

Chapter 7

Summary and Future work

7.1 Summary

This doctoral thesis is focused on the designing of environmentally benign inexpensive TiO_2 based high performance Mg and Mg-Li/Na hybrid battery cathodes. Defect engineering of nanostructured electrode materials is the key strategy implemented to induce pseudocapacitive type ion storage in these electrodes. Defects such as oxygen vacancies, cation doping, and interfaces between crystalline polymorphs are explored in this case. Mechanistic studies including in-situ XRD, HRTEM, and XPS were used to investigate the Mg/Na/Li-ion storage mechanism of the defect-engineered electrodes. Oxygen deficient rutile TiO_{2-x} nanowires exhibited Mg^{2+}-ion intercalation pseudocapacitance enhancement and hence the overall specific capacity improvement in the least redox-active rutile TiO_2 polymorph. Nanointerfaces present in the anatase-bronze dual-phase TiO_2 nanosheets facilitated Mg^{2+}-Li^+ pseudocapacitive dual -ion intercalation. Selective doping of the Co-atoms further enhanced the lattice distortions and the pseudocapacitive Mg^{2+}-Li^+ dual ion storage of anatase TiO_2 polymorph. Hierarchical TiO_2-B nanosheet cathodes demonstrated excellent Mg^{2+}-Na^+ pseudocapacitive storage capacity and cycling stability. The industrial application of the demonstrated methods would facilitate inexpensive, safe, fast-charging, long-lasting and high energy/ power density Mg-based post-lithium batteries.

7.2 Future work

Absence of SEI layer on anode surface and the lack of associated irreversible capacity loss are the major proposed advantages of the Mg-based batteries (in addition to the electrochemical performance) over the Li/Na-ion systems. However, despite its high reversible specific capacity close to the theoretical limit of TiO_2 electrodes, oxygen-deficient rutile TiO_{2-x} cathode-based Mg battery (chapter 3) experienced a severe (nearly 40%) initial irreversible capacity loss. High density of defects (oxygen vacancies) may influence the reactivity of the material towards electrolyte solutions, and hence promote SEI formation and initial cycle capacity loss. Elevated electrode-electrolyte interaction due to the ultrafine nature of the rutile TiO_{2-x} nanowires may also functioned as additional factors. Nevertheless, it is crucial to avoid the irreversible capacity loss for the successful transfer of the technology to the industry. Additional studies (theoretical and/or experimental) may require understanding the reason/s behind and to fix the irreversible capacity loss.

This study demonstrated a method of converting the least electrochemically active rutile phase of TiO_2 into a high-performance cathode for Mg-ion storage. Oxygen vacancy engineering facilitated diffusion-independent intercalation pseudocapacitance rather than the diffusion-controlled conventional storage mechanism. This method can be extended to other materials to enhance the Mg-ion storage capacities. Demonstrated approach can also be useful in the search for potential cathodes for other multivalent battery technologies (Al^{2+}, Ca^{2+}, $Zn^{2+,}$ etc.).

High-performance oxygen-deficient rutile TiO_{2-x} nanowires in this study was synthesized via a solvothermal method. This method was chosen due to its potential control over the material property such as morphology, stoichiometry, etc. However, yield of the reaction is found to be small due to the specific reaction condition having limited Ti precursor concentration. Several hydrothermal cycles are needed to produce the required amount (~1 g) of cathode material. This limitation of synthetic method may adversely affect the real world application of the technology. Hence, synthesis method needs to be modified or new strategies such as continuous flow solvothermal process etc. need to be implemented to enhance the product yield.

Mg-hybrid batteries are a revolutionary design that combines the safety/ low-cost advantage of the Mg and good redox activity of a secondary (for instance Li/Na) ion. Mg-Li hybrid batteries based on anatase-bronze dual-phase TiO_2 (chapter 4) and Co-doped anatase TiO_2 nanosheet cathode (Chapter 5) demonstrated irreversible capacity loss. For the Co-doped

TiO_2 cathodes, capacity degradation is not only confined to the initial cycle but extended to few consecutive cycles. This observation is reasonable due to the large concentration of Li-ions which usually leads to SEI formation associated with electrolyte decomposition. Methods such as prelithiation and/or use of electrolyte additives are found to be effective in LIBs. Similar strategies need to be implemented to fix the irreversible capacity loss observed in Mg-Li hybrid batteries.

Despite of the high specific capacity of pseudocapacitive Co-doped anatase TiO_2 nanosheets as Mg-Li hybrid battery cathode, use of Co-ions in the cathode matrix is challenging the environmental benign nature of TiO_2. Presence of hazardous Co in the system will require specific strategies for disposal and recycling to limit the environmental impacts. Hence, Co-doping could be replaced with other element/s without affecting the redox capacities to ensure the guidelines for sustainable future technologies. Additionally, various anion doping can also be attempted in addition to cation doping to facilitate improved electrochemical performances.

Use of APC-based electrolytes involve the use of highly flammable THF solvent and highly reactive PhMgCl. This is challenging the safety of Mg and Mg-Li hybrid batteries. This sensitive electrolyte combination can cause fire explosions under elevated operating temperatures. Similarly, borohydride-based electrolytes used in the Mg-Na hybrids are also challenging the safety standards due to their high-temperature hydrogen release characteristics. Hence, specific strategies such as the development of safer electrolyte compositions, or the use of fire retardant electrolyte additives need to be implemented to ensure the safe operation of the batteries.

Despite of the good specific capacity and cyclability demonstrated, Mg and Mg-Li/Na hybrid batteries are largely inferior to the LIBs and NIBs in terms of the operating voltage. These Mg-based batteries were limited to the voltage window of 0-2V due to the lower voltage stability of the electrolytes. It restricts their extensive implementation in the area of high energy applications. Though these electrolytes are the best among available combinations, it is necessary to develop high-voltage stable electrolyte combinations to develop high-performance Mg-based batteries.

7.1 Summario

Esta tesis doctoral está centrada en el diseño de cátodos para baterías híbridas Mg y Mg-Li/Na de alto rendimiento, basados en TiO_2 ecológico y de bajo coste. El diseño de defectos en materiales para electrodos nanoestructurados es la estrategia clave empleada para inducir un almacenamiento de iones, de tipo pseudocapacitivo, en estos electrodos. Defectos como las vacantes de oxígeno, dopaje con cationes, e interfases entre cristales polimorfos son explorados en este caso. Estudios mecanicistas, que incluyen in-situ XRD, HRTEM y XPS, fueron utilizados para investigar el mecanismo de almacenamiento de los iones de Mg/Na/Li en los defectos de los electrodos diseñados. Nanocables de TiO_{2-x} rutilo, con deficiencia de oxígeno, exhibieron un incremento de intercalación pseudocapacitativa de iones Mg^{2+} y, por ello, una mejora general en la capacidad específica en el polimorfo de TiO_2 rutile menos activo por redox. Las nanointerfases presentes en las nanoláminas de TiO_2 , de fase dual anatasa-bronce, facilitaron la intercalación pseudocapacitativa dual de iones Mg^{2+}-Li^{+}. El dopaje selectivo con átomos de Co incrementó las distorsiones de red y el almacenamiento pseudocapacitivo dual de iones Mg^{2+}-Li^{+} en el polimorfo de TiO_2 anatasa. Los cátodos de nanoláminas jerarquizadas de TiO_2-B demostraron una excelente capacidad de almacenamiento pseudocapacitativo de iones Mg^{2+}-Na^{+} and y estabilidad de ciclado. La aplicación industrial de los métodos demostrados facilitaría el desarrollo de baterías de Mg duraderas, seguras, de bajo coste, de carga rápida y con altas densidad de energía y potencia.

7.2 Trabajo future

La ausencia de la capa SEI en la superficie del ánodo y la falta de pérdida irreversible de capacidad son las mejores ventajas propuestas en las baterías de Mg, añadido a su rendimiento electroquímico, frente a los sistemas de iones de Li/Na. Sin embargo, a pesar de su reversible alta capacidad específica, cercana al límite teórico de los electrodos de TiO_2, la batería de Mg basada en el cátodo de TiO_{2-x} rutilo (capítulo 3), con deficiencia de oxígeno, experimentó una severa e irreversible pérdida de capacidad inicial (alrededor del 40%). La alta densidad de defectos (vacantes de oxígeno) podría influir en la reactividad del material hacia el electrolito y, por ello, promover la formación de la capa y la pérdida de capacidad del ciclo inicial. La elevada interacción electrodo-electrolito, debido a la naturaleza ultrafina de los nanocables de TiO_{2-x} rutilo, podrían también funcionar como factores adicionales. Sin embargo, es crucial evitar la irreversible pérdida de capacidad para la exitosa transferencia de tecnología hacia la industria. Estudios adicionales (teóricos y/o experimentales) podrían requerir entender las razones que lo motivan y solucionar la irreversible pérdida de capacidad. Este estudio demostró un método para convertir la fase menos electroquímicamente activa de TiO_2 rutilo en un cátodo de alto rendimiento para el almacenamiento de iones de Mg. El diseño de vacantes de oxígeno facilitó la intercalación pseudocapacitativa, no dependiente de la difusión, en lugar de convencional mecanismo de almacenamiento controlado por la difusión. Este método puede ser extendido a otros materiales para mejorar la capacidad de almacenamiento de iones de Mg. La aproximación demostrada puede También resultar útil en la búsqueda de potenciales cátodo para otras tecnologías de iones multivalentes (Al^{2+}, Ca^{2+}, $Zn^{2+,}$ etc.)

Los nanocables de TiO_{2-x} rutilo, deficientes en oxígeno, de alto rendimiento presentados en este estudio fueron sintetizados mediante el método solvotermal. Este método fue elegido por su potencial control sobre las propiedades del material, como la morfología, la estequiometría, etc. Sin embargo, el rendimiento de la reacción es reducido, debido a las específicas condiciones de reacción por la limitación de concentración de la concentración de Ti en el reactivo precursor. Varios ciclos hidrotermales son necesarios para producir las cantidades requeridas (~1 g) del material catódico. Esta limitación del método de síntesis podría afectar a la aplicación de esta tecnología en el mundo real. Por ello, el método de síntesis debe ser modificado o deben ser implementadas nuevas estrategias, como el proceso hidrotermal de proceso continuo, para mejorar el rendimiento del producto final.

Las baterías híbridas de Mg son un diseño revolucionario que combina la seguridad y el bajo coste del Mg y la buena actividad redox de iones secundarios (por ejemplo, iones de Li/Na). Las baterías híbridas de Mg están basadas en una fase dual de TiO_2 anatasa-bronce (capítulo 4) y cátodos de nanoláminas de TiO_2 anatasa dopados con Co (capítulo 5) demostraron una irreversible pérdida de capacidad. Para los cátodos de TiO_2 dopados con Co, la degradación de capacidad no solo se produce solo en el ciclo inicial, sino que se extiende a los siguientes ciclos. Esta observación es razonable por la alta concentración de iones de Li que, comúnmente, conduce a la formación de una capa SEI asociada a la descomposición del electrolito. Métodos como la prelitiación y/o el empleo de aditivos en el electrolito parece que son efectivos en baterías Li-ion. Estrategias similares necesitan ser implementadas para solucionar la irreversible pérdida de capacidad observada en las baterías híbridas de Mg-Li.

A pesar de la alta capacidad específica pseudocapacitativa en las nanoláminas TiO_2 anatasa, dopadas con Co, como cátodos para baterías híbridas de Mg-Li, el uso de iones de Co en la matriz del cátodo es un reto para ecológica naturaleza del TiO_2. La presencia del nocivo Co en el sistema requerirá estrategias específicas para su deshecho y reciclaje, con el fin de limitar su impacto medioambiental. Por ello, el dopaje con Co podría ser reemplazado por otros elementos que no afecten la capacidad redox para asegurar las directrices necesarias para las tecnologías sostenibles del futuro. Además, el dopaje con aniones alternativos puede ser utilizado junto con el dopaje catiónico para facilitar la mejora del rendimiento electroquímico. La utilización de electrolitos basados en APC implica el uso de THF, un disolvente altamente inflamable, y de PhMgCl, un compuesto altamente reactivo. Esto supone un reto para la seguridad de las baterías híbridas de Mg y de Mg-Li. Esta complicada combinación de electrolito puede provocar explosiones si la temperatura de operación es elevada. Similarmente, los electrolitos basados en borohidruros que se emplean en baterías híbridas de Mg-Na suponen también un reto para los estándares de seguridad debido al característico gran desprendimiento de hidrógeno a alta temperatura. Por ello, estrategias específicas, como el Desarrollo de electrolitos de composición segura o el empleo de aditivos para el electrolito que retrasen la ignición, necesitan ser implementados para asegurar la seguridad de operación de las baterías. A pesar de la buena capacidad específica y la ciclabilidad demostradas, las baterías híbridas de Mg y Mg-Li/Na son ampliamente inferiores a las baterías de Li-ion y Na-ion en términos de voltaje de operación. Estas baterías basadas en Mg tuvieron una Ventana de voltaje limitada de 0-2V debido a la baja estabilidad del electrolito. Esto restringe su implementación efectiva para aplicaciones de alto requerimiento energético. A pesar de que estos electrolitos representan la mayor combinación posible, es necesario desarrollar combinaciones de electrolitos estables a cualquier voltaje que permitan desarrollar baterías de Mg de alto rendimiento

---

Publications by the author

Patents

1. A method for the large scale synthesis of metal oxide nanosheets, and their uses
   M. Vicnent and V. Etacheri
   European patent filing **2020**, EP20383049.2
2. Electrode comprising oxygen-deficient rutile TiO_2 nanowires and uses thereof
   M. Vicnent, V.S. Avvaru and V. Etacheri
   European patent filing **2020**, EP20382542.7

Journal publications

1. High-rate and ultralong-life Mg-Li hybrid batteries based on highly pseudocapacitive dual phase TiO_2 nanosheet cathodes
   M. Vincent, V.S. Avvaru, M.C. Rodríguez, M. Haranczyk, V. Etacheri
   Journal of power sources 506 (**2021**) 230118
2. Lithium-ion Batteries for electric vehicle applications
   V.S. Avvaru, M. Vincent, V. Etacheri
   Ann Chem Sci Res. 2(2). ACSR. 000532. **2020**

Publications under preparation

1. Realizing, ultralong life, fast charging Magnesium batteries through oxygen vacancy induced pseudocapacitance of titanium dioxide nanowire
   M. Vincent, V.S. Avvaru, Rajkumar, A. Datta, M. Haranczyk, V. Etacheri
2. $Ti_{1-x}Co_xO_{2-y}$ nanosheets as high performance cathode for Mg-Li hybrid batteries
   M. Vincent, M. Haranczyk, V. Etacheri
3. A long cycle life Mg-Na dual ion battery based on highly pseudocapacitance TiO_2 Bronze nanosheet cathodes
   M. Vincent, M. Haranczyk, V. Etacheri
4. A high performance Mg-Li hybrid battery based on pseudocapacitance TiO2 Bronze nanosheet cathodes

M. Vincent, M. Haranczyk, V. Etacheri

Book contribution

1. Rechargeable Lithium-ion batteries, Trends and progress in electric vehicles
   Advanced lithium-ion batteries for electric vehicles: Trends and Progress in Electric Vehicles
   V.S Avvaru, M. Vincent, V. Etacheri, CRC press; Editors: T. Maiyalagan and P. Elumalai.
   ISBN 9781138484092 (**2020)**
2. Carbon Based Nanomaterials for Advanced Thermal and Electrochemical Energy Storage and Conversion
   Carbon nanotubes, graphene, porous carbon, and hybrid carbon-based materials: synthesis, properties, and functionalization for efficient energy storage
   R. Paul, M. Vincent, V. Etacheri, A.K. Roy, Elsevier; Editors: R. Paul, V. Etacheri, Y. Wang, C. Lin
   ISBN 9780128140833 (**2019)**

Presentations by the author

Oral presentations

1. Long lasting and fast charging Mg-Na hybrid battery based on TiO_2-B nanoshee cathode
   M. Vincent, M. Haranczyk, V. Etacheri
   World nano congress on advanced science and technology (WNCST-2021), Vellore institute of technology, India, **2021**, March 8-13
2. Long lasting and fast charging Mg-Li hybrid batteries based bronze TiO2 nanosheet cathodes
   M. Vincent, M. Haranczyk, V. Etacheri
   I Congreso Anual de Estudiantes de Doctorado (I-CAED) 2021, Miguel Hernandez University, Spain, **2021**, February 2
3. Investigation of dual-phase TiO_2 nanosheet as pseudocapacitive cathodes for long lasting Mg-Li hybrid batteries
   M. Vincent, V.S Avvaru, M. Haranczyk, V. Etacheri

4th Erwin Schrodinger Symposium 2021, Erwin Schrodinger society for nanoscience, Austria, **2021**, January 11-12

4. Long-lasting Mg-Li hybrid batteries based on pseudocapacitive TiO_2 nanosheet cathodes
   M. Vincent, V.S Avvaru, M. Haranczyk, V. Etacheri
   14th International Conference on Surfaces, Coatings and Nanostructured Materials (NANOSMAT) 2020, Virtual Conference, **2020**, September 8-10
5. Pseudocapacitive hybrid TiO_2 cathode for long-lasting Mg-Li dual ion batteries
   M. Vincent, V.S Avvaru, M. Haranczyk, V. Etacheri
   Virtual international transdisciplinary conference (VITC) 2020, Vellore institute of technology, India, **2020**, August 26-28
6. Co_3O_4 decorated TiO_2 nanosheets as highly pseudocapacitive cathodes for long-lasting rechargeable Mg-Li hybrid batteries
   M. Vincent, M. Haranczyk, V. Etacheri
   3rd International Conference on Nanomaterials Science and Mechanical Engineering 2020, University of Aveiro, Portugal, **2020**, July 7-10
7. Ultralong-life Mg-Li hybrid batteries based of pseudocapacitive Co_3O_4-TiO_2 hybrid nanosheet cathodes
   M. Vincent, M. Haranczyk, V. Etacheri
   International virtual conference: Electric mobility 2020", Vellore institute of technology, India, **2020**, June 25
8. Pseudocapacitance driven ultralong life Mg-Li hybrid batteries based on TiO_2 nanosheet cathodes
   M. Vincent, M. Haranczyk,V. Etacheri
   National seminar on current trends in chemistry (CTriC2020), Cochin University of science and technology, India, **2020**, February 6-7

Poster presentations

1. Influence of polymorphic interfaces in the pseudocapacitive Mg-Li dual ion storage on TiO_2 cathodes
   M. Vincent, V.S Avvaru, M. Haranczyk, V. Etacheri

International Conference on Multifunctional electronic materials and processing (MEMP-2021), Centre for materials for electronics technology (C-MET), India, **2021**, March 8-10

2. Fast charging Mg-Na hybrid batteries based on TiO_2 Bronze nanosheet cathodes

   M. Vincent, M. Haranczyk, V. Etacheri

   The Netherlands catalysis and chemistry conference 2021, University of Leiden, Netherlands, **2021**, March 1

3. Investigation of Bronze TiO_2 nanosheets as long-lasting, fast-charging Mg-Na hybrid battery cathode

   M. Vincent, M. Haranczyk, V. Etacheri

   Swiss Battery days 2020/21, Paul Scherrer Institute, Switzerland, **2021**, February 15-17

4. Nano interface enhanced pseudocapacitive Mg^{2+}/Li^{+} storage in dual phase TiO_2 cathodes

   M. Vincent, V.S Avvaru, M. Haranczyk, V. Etacheri

   Material science: Characterization and applications of advanced nanophotonic materials and structures (virtual event) 2021, OXFORD instruments, **2021**, February 9-10

5. Effect of oxygen vacancies on the electrochemical performance of Anatase TiO_2 as Mg-Li hybrid battery cathode

   M. Vincent, M. Haranczyk, V. Etacheri

   9th Symposium on Electrochemistry in Nanoscience (ELECNANO9) 2020, Société chimique de France, Paris, France, **2020**, November 23-34

References

1 D. I. Stern, *Ann. N. Y. Acad. Sci.*, 2011, **1219**, 26–51.

2 World Energy Consumption Since 1820 in Charts | Our Finite World, https://ourfiniteworld.com/2012/03/12/world-energy-consumption-since-1820-in-charts/, (accessed 28 June 2021).

3 B. Dudley, *Stat. Rev. World Energy*, 2018, **67**, 40.

4 M. Höök and X. Tang, *Energy Policy*, 2013, **52**, 797–809.

5 J. Tollefson, *Nature*, 2018, **562**, 172–173.

6 W. Rowley and A. Westwood, *Energy*, 2012, **2**, 16–18.

7 A. Azarpour, S. Suhaimi, G. Zahedi and A. Bahadori, *Arab. J. Sci. Eng.*, 2013, **38**, 317–328.

8 N. Khan, S. Dilshad, R. Khalid, A. R. Kalair and N. Abas, *Energy Storage*, 2019, **1**, 1–49.

9 H. Chen, T. N. Cong, W. Yang, C. Tan, Y. Li and Y. Ding, *Prog. Nat. Sci.*, 2009, **19**, 291–312.

10 A. Benato and A. Stoppato, *Therm. Sci. Eng. Prog.*, 2018, **6**, 301–315.

11 M. Antonelli, S. Barsali, U. Desideri, R. Giglioli, F. Paganucci and G. Pasini, *Appl. Energy*, 2017, **194**, 522–529.

12 D. Mori and K. Hirose, *Int. J. Hydrogen Energy*, 2009, **34**, 4569–4574.

13 A. Mohd, E. Ortjohann, A. Schmelter, N. Hamsic and D. Morton, *IEEE Int. Symp. Ind. Electron.*, 2008, 1627–1632.

14 C. W. Forsberg, *Proc. 2006 Int. Congr. Adv. Nucl. Power Plants, ICAPP'06*, 2006, **2006**, 699–705.

15 T. Nguyen and R. F. Savinell, *Electrochem. Soc. Interface*, 2010, **19**, 54–56.

16 L. Rivera-González, D. Bolonio, L. F. Mazadiego and R. Valencia-Chapi, *Sustain.*, 2019, **11**, 5316.

17 J. Paulo and P. D. Gaspar, *WCE 2010 - World Congr. Eng. 2010*, 2010, **2**, 909–914.

18 P. Somavat and V. Namboodiri, *J. Green Eng.*, 2011, **1**, 447–475.

19 X. Sun, Z. Li, X. Wang and C. Li, *Energies*, 2019, **13**, 1–29.

20 J. Li and S. Passerini, *J. Power Sources*, 2021, **484**, 2–3.

21 V. Etacheri, R. Marom, R. Elazari, G. Salitra and D. Aurbach, *Energy Environ. Sci.*, 2011, **4**, 3243–3262.

22 M. Armand and J. M. Tarascon, *Mech. Eng.*, 2017, **139**, 10–11.

23 B. Dunn, H. Kamath and J. Tarascon, *Science (80-.).*, 2011, **334**, 928–936.

24 S. Maddukuri, D. Malka, M. S. Chae, Y. Elias, S. Luski and D. Aurbach, *Electrochim. Acta*, 2020, **354**, 136771.

25 P. A. Abetti, *Electr. Eng.*, 2013, **71**, 773–776.

26 A. Beaudet, F. Larouche, K. Amouzegar, P. Bouchard and K. Zaghib, *Sustainability*, 2020, **12**, 1–12.

27 P. Pacheco, E. Garcia and C. Gonzalez-Aquino, *Proc. 33rd Annu. Int. Batter. Semin. Exhib.*, 2017, **20**, 1–98.

28 K. Baes, F. Carlot, Y. Ito, M. Kolk and A. Merhaba, *Arthyr D Little*, 2018, 1–24.

29 D. Malka, N. Shpigel, R. Attias and D. Aurbach, *J. Solid State Electrochem.*, 2020, **24**, 2027–2029.

30 M. Li, J. Lu, Z. Chen and K. Amine, *Adv. Mater.*, 2018, **30**, 1–24.

31 K. Zaghib, M. Dontigny, A. Guerfi, P. Charest, I. Rodrigues, A. Mauger and C. M. Julien, *J. Power Sources*, 2011, **196**, 3949–3954.

32 G. E. Blomgren, *J. Power Sources*, 2003, **119–121**, 326–329.

33 H. D. Yoo, I. Shterenberg, Y. Gofer, G. Gershinsky, N. Pour and D. Aurbach, *Energy Environ. Sci.*, 2013, **6**, 2245–2550.

34 N. Watanabe, T. Arakawa, Y. Sasaki, T. Yamashita and I. Koiwa, *J. Electrochem. Soc.*, 2012, **159**, A1949–A1953.

35 P. Saha, M. K. Datta, O. I. Velikokhatnyi, A. Manivannan, D. Alman and P. N. Kumta, *Prog. Mater. Sci.*, 2014, **66**, 1–86.

36 A. G. Mamalis, K. N. Spentzas and A. A. Mamali, *Eur. Transp. Res. Rev.*, 2013, **5**, 1–10.

37 M. S. Park, S. B. Ma, D. J. Lee, D. Im, S. G. Doo and O. Yamamoto, *Sci. Rep.*, 2014, **4**, 1–8.

38 R. A. Rhein, 1990, 1–63.

39 Q. Zhang and R. E. White, *J. Power Sources*, 2008, **179**, 793–798.

40 G. Liu and W. Lu, *J. Electrochem. Soc.*, 2017, **164**, A1826–A1833.

41 F. Wu, Y. X. Yuan, X. B. Cheng, Y. Bai, Y. Li, C. Wu and Q. Zhang, *Energy Storage Mater.*, 2018, **15**, 148–170.

42 D. Deng, *Energy Sci. Eng.*, 2015, **3**, 385–418.

43 F. Holtstiege, P. Bärmann, R. Nölle, M. Winter and T. Placke, *Batteries*, 2018, **4**, 1–39.

44 M. Chen, Q. Liu, S. W. Wang, E. Wang, X. Guo and S. L. Chou, *Adv. Energy Mater.*, 2019, **9**, 1803609.

45 B. Lee, E. Paek, D. Mitlin and S. W. Lee, *Chem. Rev.*, 2019, **119**, 5416–5420.

46 C. Bommier and X. Ji, *Small*, 2018, **14**, 1703576.

47 R. R. Maça, Daniel Cintora Juarez, M. C. Rodríguez and V. Etacheri, *Chem. Eng. J.*, 2019, **391**, 123598.

48 Y. Liang, H. Dong, D. Aurbach and Y. Yao, *Nat. Energy*, 2020, **5**, 646–656.

49 M. Walter, K. V. Kravchyk, M. Ibáñez and M. V. Kovalenko, *Chem. Mater.*, 2015, **27**, 7452–7458.

50 C. Kim, P. J. Phillips, B. Key, T. Yi, D. Nordlund, Y. S. Yu, R. D. Bayliss, S. D. Han, M. He, Z. Zhang, A. K. Burrell, R. F. Klie and J. Cabana, *Adv. Mater.*, 2015, **27**, 3377–3384.

51 S. Su, Z. Huang, Y. Nuli, F. Tuerxun, J. Yang and J. Wang, *Chem. Commun.*, 2015, **51**, 2641–2644.

52 P. Earis, N. Nugent, M. Martinez-fresno, S. Wilkes, S. Spring, J. Dean, N. Lewis, U. C. Berkeley and H. Bolt, *Energy*, 2009, 3–10.

53 Y. Meng, D. Wang, Y. Zhao, R. Lian, Y. Wei, X. Bian, Y. Gao, F. Du, B. Liu and G. Chen, *Nanoscale*, 2017, **9**, 12934–12940.

54 D. Aurbach, Z. Lu, A. Schechter, Y. Gofer, H. Gizbar, R. Turgeman, Y. Cohen, M. Moshkovich and E. Levi, *Nature*, 2000, **407**, 724–727.

55 M. Jäckle, K. Helmbrecht, M. Smits, D. Stottmeister and A. Groß, *Energy Environ. Sci.*, 2018, **11**, 3400–3407.

56 Y. Liang, R. Feng, S. Yang, H. Ma, J. Liang and J. Chen, *Adv. Mater.*, 2011, **23**, 640–643.

57 S. B. Son, T. Gao, S. P. Harvey, K. X. Steirer, A. Stokes, A. Norman, C. Wang, A. Cresce, K. Xu and C. Ban, *Nat. Chem.*, 2018, **10**, 532–539.

58 N. Wu, Y. C. Lyu, R. J. Xiao, X. Yu, Y. X. Yin, X. Q. Yang, H. Li, L. Gu and Y. G. Guo,

NPG Asia Mater., 2014, **6**, 1–7.

59 N. Wu, Y. X. Yin and Y. G. Guo, *Chem. - An Asian J.*, 2014, **9**, 2099–2102.

60 C. Chen, J. Wang, Q. Zhao, Y. Wang and J. Chen, *ACS Energy Lett.*, 2016, **1**, 1165–1172.

61 L. Luo, Y. Zhen, Y. Lu, K. Zhou, J. Huang, Z. Huang, S. Mathur and Z. Hong, *Nanoscale*, 2020, **12**, 230–238.

62 J. Zeng, Y. Yang, C. Li, J. Li, J. Huang, J. Wang and J. Zhao, *Electrochim. Acta*, 2017, **247**, 265–270.

63 Y. Mao and H. Soleymanabadi, *J. Mol. Liq.*, 2020, **308**, 113009.

64 B. Mortazavi, A. Dianat, O. Rahaman, G. Cuniberti and T. Rabczuk, *J. Power Sources*, 2016, **329**, 456–461.

65 X. J. Ye, G. L. Zhu, J. Liu, C. S. Liu and X. H. Yan, *J. Phys. Chem. C*, 2019, **123**, 15777–15786.

66 D. Wu, B. Yang, H. Chen and E. Ruckenstein, *Nanoscale*, 2019, **11**, 15472–15478.

67 D. Er, E. Detsi, H. Kumar and V. B. Shenoy, *ACS Energy Lett.*, 2016, **1**, 638–645.

68 J. Niu, Z. Zhang and D. Aurbach, *Adv. Energy Mater.*, 2020, **10**, 1–33.

69 K. V. Kravchyk, L. Piveteau, R. Caputo, M. He, N. P. Stadie, M. I. Bodnarchuk, R. T. Lechner and M. V. Kovalenko, *ACS Nano*, 2018, **12**, 8297–8307.

70 T. S. Arthur, N. Singh and M. Matsui, *Electrochem. commun.*, 2012, **16**, 103–106.

71 A. Benmayza, M. Ramanathan, N. Singh, F. Mizuno and J. Prakash, *J. Electrochem. Soc.*, 2015, **162**, A1630–A1635.

72 W. Jin and Z. Wang, *Mater. Chem. Phys.*, 2018, **217**, 388–392.

73 T. R. Penki, G. Valurouthu, S. Shivakumara, V. A. Sethuraman and N. Munichandraiah, *New J. Chem.*, 2018, **42**, 5996–6004.

74 O. I. Malyi, T. L. Tan and S. Manzhos, *J. Power Sources*, 2013, **233**, 341–345.

75 N. Singh, T. S. Arthur, C. Ling, M. Matsui and F. Mizuno, *Chem. Commun.*, 2013, **49**, 149–151.

76 D. T. Nguyen, X. M. Tran, J. Kang and S. W. Song, *ChemElectroChem*, 2016, **3**, 1813–1819.

77 H. Yaghoobnejad Asl, J. Fu, H. Kumar, S. S. Welborn, V. B. Shenoy and E. Detsi, *Chem. Mater.*, 2018, **30**, 1815–1824.

78 M. A. Long, P. B. Stretesky, G. Harms, R. Sollund, P. Macmillan and B. Chapter, *J. Mater. Sci.*, 2016, **51**, 7355–7360.

79 F. Murgia, E. T. Weldekidan, L. Stievano, L. Monconduit and R. Berthelot, *Electrochem. commun.*, 2015, **60**, 56–59.

80 K. Periyapperuma, T. T. Tran, M. I. Purcell and M. N. Obrovac, *Electrochim. Acta*, 2015, **165**, 162–165.

81 T. T. Tran and M. N. Obrovac, *J. Electrochem. Soc.*, 2011, **158**, A1411.

82 C. You, X. Wu, X. Yuan, Y. Chen, L. Liu, Y. Zhu, L. Fu, Y. Wu, Y. G. Guo and T. Van Ree, *J. Mater. Chem. A*, 2020, **8**, 25601–25625.

83 M. D. Levi, H. Gizbar, E. Lancry, Y. Gofer, E. Levi and D. Aurbach, *J. Electroanal. Chem.*, 2004, **569**, 211–223.

84 Z. Guo, S. Zhao, T. Li, D. Su, S. Guo and G. Wang, *Adv. Energy Mater.*, 2020, **10**, 1–17.

85 R. Dominko, J. Bitenc, R. Berthelot, M. Gauthier, G. Pagot and V. Di Noto, *J. Power Sources*, , DOI:10.1016/j.jpowsour.2020.229027.

86 E. Levi, Y. Gofer, Y. Vestfreed, E. Lancry and D. Aurbach, *Chem. Mater.*, 2002, **14**, 2767–2773.

87 E. Lancry, E. Levi, Y. Gofer, M. D. Levi and D. Aurbach, *J. Solid State Electrochem.*, 2005, **9**, 259–266.

88 M. Mao, Z. Lin, Y. Tong, J. Yue, C. Zhao, J. Lu, Q. Zhang, L. Gu, L. Suo, Y. S. Hu, H. Li, X. Huang and L. Chen, *ACS Nano*, 2020, **14**, 1102–1110.

89 E. Levi, A. Mitelman, O. Isnard, M. Brunelli and D. Aurbach, *Inorg. Chem.*, 2008, **47**, 1975–1983.

90 A. Mitelman, E. Levi, E. Lancry and D. Aurbach, *ECS Trans.*, 2007, **3**, 109–115.

91 M. D. Levi, E. Lancri, E. Levi, H. Gizbar, Y. Gofer and D. Aurbach, *Solid State Ionics*, 2005, **176**, 1695–1699.

92 J. Chen, X.-L. Gou, H.-T. Yuan, Z.-L. Tao and L.-N. Xu, *Chem. Commun.*, 2004, 2080.

93 H. D. Yoo, Y. Liang, H. Dong, J. Lin, H. Wang, Y. Liu, L. Ma, T. Wu, Y. Li, Q. Ru, Y. Jing, Q. An, W. Zhou, J. Guo, J. Lu, S. T. Pantelides, X. Qian and Y. Yao, *Nat. Commun.*, 2017, **8**, 1–10.

94 X. Sun, P. Bonnick and L. F. Nazar, *ACS Energy Lett.*, 2016, **1**, 297–301.

95 L. Li, Y. Lu, Q. Zhang, S. Zhao, Z. Hu and S. L. Chou, *Small*, , DOI:10.1002/smll.201902767.

96 S. Yang, D. Li, T. Zhang, Z. Tao and J. Chen, *J. Phys. Chem. C*, 2012, **116**, 1307–1312.

97 Y. Liu, L. Jiao, Q. Wu, J. Du, Y. Zhao, Y. Si, Y. Wang and H. Yuan, *J. Mater. Chem. A*, 2013, **1**, 5822–5826.

98 J. Shuai, H. D. Yoo, Y. Liang, Y. Li, Y. Yao and L. C. Grabow, *Mater. Res. Express*, 2016, **3**, 1–8.

99 M. Xu, N. Bai, H. X. Li, C. Hu, J. Qi and X. Bin Yan, *Chinese Chem. Lett.*, 2018, **29**, 1313–1316.

100 M. Arsentev, A. Missyul, A. V. Petrov and M. Hammouri, *J. Phys. Chem. C*, 2017, **121**, 15509–15515.

101 P. Bonnick, X. Sun, K. C. Lau, C. Liao and L. F. Nazar, *J. Phys. Chem. Lett.*, 2017, **8**, 2253–2257.

102 F. Xiong, Y. Fan, S. Tan, L. Zhou, Y. Xu, C. Pei, Q. An and L. Mai, *Nano Energy*, 2018, **47**, 210–216.

103 C. Pei, Y. Yin, R. Sun, F. Xiong, X. Liao, H. Tang, S. Tan, Y. Zhao, Q. An and L. Mai, *ACS Appl. Mater. Interfaces*, 2019, **11**, 31954–31961.

104 R. Sun, C. Pei, J. Sheng, D. Wang, L. Wu, S. Liu, Q. An and L. Mai, *Energy Storage Mater.*, 2018, **12**, 61–68.

105 B. J. Smith, G. M. Phillip and M. E. Sweeney, *Energy Environ. Sci. Sci.*, 2016, **9**, 3201–3209.

106 D. D. S. M. Laser, M. E. Doroshenko, M. Jelínek, J. Šulc, H. Jelínková, N. Č. Michal, V. V Osiko, V. V Badikov and D. V Badikov, *Chem.*, 2018, **30**, 4683–4693.

107 M. Mao, X. Ji, S. Hou, T. Gao, F. Wang, L. Chen, X. Fan, J. Chen, J. Ma and C. Wang, *Chem. Mater.*, 2019, **31**, 3183–3191.

108 B. Liu, T. Luo, G. Mu, X. Wang, D. Chen and G. Shen, *ACS Nano*, 2013, **7**, 8051–8058.

109 Y. Tashiro, K. Taniguchi and H. Miyasaka, *Electrochim. Acta*, 2016, **210**, 655–661.

110 D. Chen, Y. Zhang, X. Li, J. Shen, Z. Chen, S. an Cao, T. Li and F. Xu, *Chem. Eng. J.*, 2020, **384**, 123235.

111 Y. Gu, Y. Katsura, T. Yoshino, H. Takagi and K. Taniguchi, *Sci. Rep.*, 2015, **5**, 1–9.

112 T. D. Gregory, R. J. Hoffman and R. C. Winterton, *J. Electrochem. Soc.*, 1990, **137**, 775–780.

113 R. Zhang, X. Yu, K. W. Nam, C. Ling, T. S. Arthur, W. Song, A. M. Knapp, S. N. Ehrlich, X. Q. Yang and M. Matsui, *Electrochem. commun.*, 2012, **23**, 110–113.

114 T. S. Arthur, R. Zhang, C. Ling, P. A. Glans, X. Fan, J. Guo and F. Mizuno, *ACS Appl. Mater. Interfaces*, 2014, **6**, 7004–7008.

115 J. S. Kim, W. S. Chang, R. H. Kim, D. Y. Kim, D. W. Han, K. H. Lee, S. S. Lee and S. G. Doo, *J. Power Sources*, 2015, **273**, 210–215.

116 R. Zhang and C. Ling, *MRS Energy Sustain.*, 2016, **3**, 1–19.

117 R. Xiao, J. Xie, T. Luo, L. Huang, Y. Zhou, D. Yu, C. Chen and Y. Liu, *J. Phys. Chem. C*, 2018, **122**, 1513–1521.

118 B. Zhou, H. Shi, R. Cao, X. Zhang and Z. Jiang, *Phys. Chem. Chem. Phys.*, 2014, **16**, 18578–18585.

119 G. Pagot, K. Vezzù, A. Nale, M. Fauri, A. Migliori, V. Morandi, E. Negro and V. Di Noto, *J. Electrochem. Soc.*, 2020, **167**, 070547.

120 G. Sai Gautam, P. Canepa, W. D. Richards, R. Malik and G. Ceder, *Nano Lett.*, 2016, **16**, 2426–2431.

121 S. Tepavcevic, Y. Liu, D. Zhou, B. Lai, J. Maser, X. Zuo, H. Chan, P. Král, C. S. Johnson, V. Stamenkovic, N. M. Markovic and T. Rajh, *ACS Nano*, 2015, **9**, 8194–8205.

122 A. Mukherjee, S. Taragin, H. Aviv, I. Perelshtein and M. Noked, *Adv. Funct. Mater.*, 2020, **30**, 1–9.

123 P. Novák and J. Desilvestro, *J. Electrochem. Soc.*, 1993, **140**, 140–144.

124 S. D. Perera, R. B. Archer, C. A. Damin, R. Mendoza-Cruz and C. P. Rhodes, *J. Power Sources*, 2017, **343**, 580–591.

125 Q. An, Y. Li, H. Deog Yoo, S. Chen, Q. Ru, L. Mai and Y. Yao, *Nano Energy*, 2015, **18**, 265–272.

126 Y. Cheng, Y. Shao, V. Raju, X. Ji, B. L. Mehdi, K. S. Han, M. H. Engelhard, G. Li, N. D. Browning, K. T. Mueller and J. Liu, *Adv. Funct. Mater.*, 2016, **26**, 3446–3453.

127 T. S. Arthur, K. Kato, J. Germain, J. Guo, P. A. Glans, Y. S. Liu, D. Holmes, X. Fan and F. Mizuno, *Chem. Commun.*, 2015, **51**, 15657–15660.

128 Y. Xu, X. Deng, Q. Li, G. Zhang, F. Xiong, S. Tan, Q. Wei, J. Lu, J. Li, Q. An and L. Mai, *Chem*, 2019, **5**, 1194–1209.

129 D. Ni, J. Shi, W. Xiong, S. Zhong, B. Xu and C. Ouyang, *Phys. Chem. Chem. Phys.*, 2019, **21**, 7406–7411.

130 T. Koketsu, J. Ma, B. J. Morgan, M. Body, C. Legein, W. Dachraoui, M. Giannini, A. Demortière, M. Salanne, F. Dardoize, H. Groult, O. J. Borkiewicz, K. W. Chapman, P. Strasser and D. Dambournet, *Nat. Mater.*, 2017, **16**, 1142–1148.

131 K. McColl and F. Cor`, *J. Mater. Chem. A*, 2019, **7**, 3704–3713.

132 J. Ma, T. Koketsu, B. J. Morgan, C. Legeinf, M. Body, P. Strasserc and D. Dambournet, *Chem. Commun.*, 2018, **54**, 10080–10083.

133 Y. Meng, D. Wang, Y. Wei, K. Zhu, Y. Zhao, X. Bian, F. Du, B. Liu, Y. Gao and G. Chen, *J. Power Sources*, 2017, **346**, 134–142.

134 L. Luo, K. Zhou, R. Lian, Y. Lu, Y. Zhen, J. Wang, S. Mathur and Z. Hong, *Nano Energy*, 2020, **72**, 104716.

135 W. Feng, R. Ruben and V. Etacheri, *ACS Appl. Mater. Interfaces*, 2020, **12**, 4443–4453.

136 C. Alex, M. Zhang, A. C. Macrae, H. Liu and Y. Shirley, *J. Electrochem. Soc.*, 2016, **163**,

A2368.

137 Y. Wang, X. Xue, P. Liu, C. Wang, X. Yi, Y. Hu, L. Ma, G. Zhu, R. Chen, T. Chen, J. Ma, J. Liu and Z. Jin, *ACS Nano*, 2018, **12**, 12492–12502.

138 M. E. Spahr, P. Novak, O. Haas and R. Nesper, *J. Power Sources*, 1995, **54**, 346–351.

139 J. T. Incorvati, L. F. Wan, B. Key, D. Zhou, C. Liao, L. Fuoco, M. Holland, H. Wang, D. Prendergast, K. R. Poeppelmeier and J. T. Vaughey, *Chem. Mater.*, 2016, **28**, 17–20.

140 L. F. Wan, J. T. Incorvati, K. R. Poeppelmeier and D. Prendergast, *Chem. Mater.*, 2016, **28**, 6900–6908.

141 G. Gershinsky, H. D. Yoo, Y. Gofer and D. Aurbach, *Langmuir*, 2013, **29**, 10964–10972.

142 Y. NuLi, J. Yang, J. Wang and Y. Li, *J. Phys. Chem. C*, 2009, **113**, 12594–12597.

143 Y. Nuli, J. Yang, Y. Li and J. Wang, *Chem. Commun.*, 2010, **46**, 3794–3796.

144 Y. Zheng, Y. Nuli, Q. Chen, Y. Wang, J. Yang and J. Wang, *Electrochim. Acta*, 2012, **66**, 75–81.

145 Y. Li, Y. N. Nuli, J. Yang, T. Yilinuer and J. L. Wang, *Chinese Sci. Bull.*, 2011, **56**, 386–390.

146 J. Z. Sun, *Monatshefte fur Chemie*, 2014, **145**, 103–106.

147 Z. Li, L. Han, Y. Wang, X. Li, J. Lu and X. Hu, *Small*, 2019, **15**, 1–16.

148 C. Ling, J. Chen and F. Mizuno, *J. Phys. Chem. C*, 2013, **117**, 21158–21165.

149 D. M. Kim, Y. Kim, D. Arumugam, S. W. Woo, Y. N. Jo, M. S. Park, Y. J. Kim, N. S. Choi and K. T. Lee, *ACS Appl. Mater. Interfaces*, 2016, **8**, 8554–8560.

150 R. Y. Wang, C. D. Wessells, R. A. Huggins and Y. Cui, *Nano Lett.*, 2013, **13**, 5748–5752.

151 Y. Mizuno, M. Okubo, E. Hosono, T. Kudo, K. Oh-Ishi, A. Okazawa, N. Kojima, R. Kurono, S. I. Nishimura and A. Yamada, *J. Mater. Chem. A*, 2013, **1**, 13055–13059.

152 H. Takahashi and H. Takamura, *Key Eng. Mater.*, 2012, **508**, 291–299.

153 P. Canepa, G. S. Gautam, D. C. Hannah, R. Malik, M. Liu, K. G. Gallagher, K. A. Persson and G. Ceder, 2017, **117**, 4287–4341.

154 C. Delmas, A. Nadiri and J. L. Soubeyroux, *Solid State Ionics*, 1988, **28**–**30**, 419–423.

155 J. J. Shi, G. Q. Yin, L. M. Jing, J. Guan, M. P. Wu, Y. L. Zhou, H. L. Lou and Z. Wang, *Int. J. Mod. Phys. B*, 2014, **28**, 1–9.

156 K. Makino, Y. Katayama, T. Miura and T. Kishi, *J. Power Sources*, 2001, **99**, 66–69.

157 Z. D. Huang, T. Masese, Y. Orikasa, T. Mori and K. Yamamoto, *RSC Adv.*, 2015, **5**, 8598–8603.

158 N. K. Anuar, S. B. R. S. Adnan and N. S. Mohamed, *Ceram. Int.*, 2014, **40**, 13719–13727.

159 N. N. Sinha and N. Munichandraiah, *Electrochem. Solid-State Lett.*, 2008, **11**, 3–6.

160 H. Kurihara, T. Yajima and S. Suzuki, *Chem. Lett.*, 2008, **37**, 376–377.

161 S. Okamoto, T. Ichitsubo, T. Kawaguchi, Y. Kumagai, F. Oba, S. Yagi, K. Shimokawa, N. Goto, T. Doi and E. Matsubara, *Adv. Sci.*, 2015, **2**, 1–9.

162 X. Sun, P. Bonnick, V. Duffort, M. Liu, Z. Rong, K. A. Persson, G. Ceder and L. F. Nazar, *Energy Environ. Sci.*, 2016, **9**, 2273–2277.

163 A. Robba, A. Vizintin, J. Bitenc, G. Mali, I. Arčon, M. Kavčič, M. Žitnik, K. Bučar, G. Aquilanti, C. Martineau-Corcos, A. Randon-Vitanova and R. Dominko, *Chem. Mater.*, 2017, **29**, 9555–9564.

164 H. S. Kim, T. S. Arthur, G. D. Allred, J. Zajicek, J. G. Newman, A. E. Rodnyansky, A. G. Oliver, W. C. Boggess and J. Muldoon, *Nat. Commun.*, 2011, **2**, 426–427.

165 H. Tian, T. Gao, X. Li, X. Wang, C. Luo, X. Fan, C. Yang, L. Suo, Z. Ma, W. Han and C. Wang, *Nat. Commun.*, 2017, **8**, 1–8.

166 Z. Zhang, Z. Cui, L. Qiao, J. Guan, H. Xu, X. Wang, P. Hu, H. Du, S. Li, X. Zhou, S. Dong, Z. Liu, G. Cui and L. Chen, *Adv. Energy Mater.*, 2017, **7**, 1–10.

167 J. Bitenc, K. Pirnat, T. Bančič, M. Gaberšček, B. Genorio, A. Randon-Vitanova and R. Dominko, *ChemSusChem*, 2015, **8**, 4128–4132.

168 R. Deivanayagam, B. J. Ingram and R. Shahbazian-Yassar, *Energy Storage Mater.*, 2019, **21**, 136–153.

169 D. Aurbach, H. Gizbar, A. Schechter, O. Chusid, H. E. Gottlieb, Y. Gofer and I. Goldberg, *J. Electrochem. Soc.*, 2002, **149**, A115.

170 W. Pan, X. Liu, X. Miao, J. Yang, J. Wang, Y. Nuli and S. ichi Hirano, *J. Solid State Electrochem.*, 2015, **19**, 3347–3353.

171 X. Fan, R. R. Gaddam, N. A. Kumar and X. S. Zhao, *Adv. Energy Mater.*, 2017, **7**, 2–11.

172 M. Rashad, M. Asif, Y. Wang, H. Zhen and I. Ahmed, *Energy Storage Mater.*, 2020, **25**, 342–375.

173 Y. Ju, Y. Meng, Y. Wei, X. Bian, Q. Pang, Y. Gao and F. Du, *Chem. A Eur. J.*, 2016, **22**, 18073–18079.

174 Y. Cheng, H. J. Chang, H. Dong, D. Choi, V. L. Sprenkle, J. Liu, Y. Yao and G. Li, *J. Mater. Res.*, 2016, **31**, 3125–3141.

175 Y. Cheng, D. Choi, K. S. Han, K. T. Mueller, J.-G. Zhang, V. L. Sprenkle, J. Liu and G. Li, *AIChE Annu. Meet. Conf. Proc.*, 2016, **52**, 5379–5382.

176 F. Liu, Y. Liu, X. Zhao, K. Liu, H. Yin and L. Fan, *small*, 2020, **16**, 1906076.

177 Y. Wang, C. Wang, X. Yi, Y. Hu, L. Wang, L. Ma, G. Zhu, T. Chen and Z. Jin, *Energy Storage Mater.*, 2019, **23**, 741–748.

178 J. H. Cho, M. Aykol, S. Kim, J. H. Ha, C. Wolverton, K. Y. Chung, K. B. Kim and B. W. Cho, *J. Am. Chem. Soc.*, 2014, **136**, 16116–16119.

179 T. Gao, F. Han, Y. Zhu, L. Suo, C. Luo, K. Xu and C. Wang, *Adv. Energy Mater.*, 2015, **5**, 1–5.

180 H. D. Yoo, Y. Liang, Y. Li and Y. Yao, *ACS Appl. Mater. Interfaces*, 2015, **7**, 7001–7007.

181 H. Tang, N. Xu, C. Pei, F. Xiong, S. Tan, W. Luo, Q. An and L. Mai, *ACS Appl. Mater. Interfaces*, 2017, **9**, 28667–28673.

182 Q. Chen, Q. Xia, Y. Xu, P. Wang and Q. Tan, *Mater. Lett.*, 2019, **247**, 178–181.

183 Y. Cen, S. Li, Y. Zhou, X. Cai, X. Wang, Q. Xiang, B. Hu, D. Yu, Y. Liu and C. Chen, *J. Electrochem. Soc.*, 2019, **166**, A1660–A1667.

184 M. Li, C. Pei, F. Xiong, S. Tan, Y. Yin, H. Tang, D. Huang, Q. An and L. Mai, *Electrochim. Acta*, 2019, **320**, 134556.

185 M. Rashad, X. Li and H. Zhang, *ACS Appl. Mater. Interfaces*, 2018, **10**, 21313–21320.

186 C. Zhu, Y. Tang, L. Liu, R. Sheng, X. Li, Y. Gao and Y. NuLi, *J. Colloid Interface Sci.*, 2021, **581**, 307–313.

187 J. Bitenc, M. Firm, A. Randon Vitanova and R. Dominko, *Electrochem. commun.*, 2017, **76**, 29–33.

188 Z. Zlatanova, D. Marinova, R. Kukeva, L. Mihaylov, D. Nihtianova and R. Stoyanova, *J. Alloys Compd.*, 2021, **851**, 156706.

189 J. Fan, S. Shen, Y. Chen, L. Wu, J. Peng and X. Peng, *Electrochem. commun.*, 2018, **90**, 16–20.

190 C. Peng, H. Lyu, L. Wu, T. Xiong, F. Xiong, Z. Liu, Q. An and L. Mai, *ACS Appl. Mater. Interfaces*, 2018, **10**, 36988–36995.

191 C. Zhang, L. Zhang, N. Li and X. Zhang, *Energies*, 2020, **13**, 2–11.

192 Y. Zhang, J. Xie, Y. Han and C. Li, *Adv. Funct. Mater.*, 2015, **25**, 7300–7308.

193 X. Chen, S. Wang and H. Wang, *Electrochim. Acta*, 2018, **265**, 175–183.

194 T. Li, A. Qin, H. Wang, M. Wu, Y. Zhang, Y. Zhang, D. Zhang and F. Xu, *Electrochim. Acta*, 2018, **263**, 168–175.

195 Y. Zhang, Y. Li, Y. Wang, R. Guo, W. Liu, H. Pei, G. Yin, D. Ye, S. Yu and J. Xie, *J. Colloid Interface Sci.*, 2019, **553**, 239–246.

196 Y. Meng, D. Wang, Y. Wei, K. Zhu, Y. Zhao, X. Bian, F. Du, B. Liu, Y. Gao and G. Chen, *J. Power Sources*, 2017, **346**, 134–142.

197 S. Su, Y. NuLi, Z. Huang, Q. Miao, J. Yang and J. Wang, *ACS Appl. Mater. Interfaces*, 2016, **8**, 7111–7117.

198 S. Maletti, D. Mikhailova, A. Herzog-Arbeitman, S. Oswald, A. Senyshyn and L. Giebeler, *J. Phys. Chem. C*, 2020, **124**, 25239–25248.

199 J. Sheng, C. Peng, S. Yan, G. Zhang, Y. Jiang, Q. An, Q. Wei, Q. Ru and L. Mai, *J. Mater. Chem. A*, 2018, **6**, 13901–13907.

200 Y. Cheng, Y. Shao, J.-G. Zhang, V. L. Sprenkle, J. Liu and G. Li, *Chem. Commun.*, 2014, **50**, 9644–9646.

201 Y. Shao, T. Liu, G. Li, M. Gu, Z. Nie, M. Engelhard, J. Xiao, D. Lv, C. Wang, J. G. Zhang and J. Liu, *Sci. Rep.*, 2013, **3**, 4–10.

202 X. Bian, Y. Gao, Q. Fu, S. Indris, Y. Ju, Y. Meng, F. Du, N. Bramnik, H. Ehrenberg and Y. Wei, *J. Mater. Chem. A*, 2017, **5**, 600–608.

203 J. Zeng, Z. Cao, Y. Yang, Y. Wang, Y. Peng, Y. Zhang and J. Wang, *Electrochim. Acta*, 2018, **284**, 1–9.

204 R. Zhang, O. Tutusaus, R. Mohtadi and C. Ling, *Front. Chem.*, 2018, **6**, 1–10.

205 S. Rubio, A. Medina, M. Cabello, P. Lavela, R. Alcántara, C. P. Vicente, G. F. Ortiz and J. L. Tirado, *J. Solid State Electrochem.*, 2020, **24**, 2565–2573.

206 M. Cabello, F. Nacimiento, R. Alcántara, P. Lavela, G. Ortiz and J. L. Tirado, *J. Electrochem. Soc.*, 2016, **163**, A2781–A2790.

207 P. Northwest, E. Materials and A. P. Source, *Chem. Commun.*, 1–12.

208 K. V Kravchyk, M. Walter and M. V Kovalenko, *Commun. Chem.*, 2019, **2**, 1–6.

209 J. Muldoon, C. B. Bucur, A. G. Oliver, T. Sugimoto, M. Matsui, H. S. Kim, G. D. Allred, J. Zajicek and Y. Kotani, *Energy Environ. Sci.*, 2012, **5**, 5941–5950.

210 J. Muldoon, C. B. Bucur and T. Gregory, *Angew. Chemie - Int. Ed.*, 2017, **56**, 12064–12084.

211 R. Davidson, A. Verma, D. Santos, F. Hao, C. Fincher, S. Xiang, J. Van Buskirk, K. Xie, M. Pharr, P. P. Mukherjee and S. Banerjee, *ACS Energy Lett.*, 2019, **4**, 375–376.

212 B. Babu, P. Simon and A. Balducci, *Adv. Energy Mater.*, 2020, **10**, 2001128.

213 C. Choi, D. S. Ashby, D. M. Butts, R. H. DeBlock, Q. Wei, J. Lau and B. Dunn, *Nat. Rev. Mater.*, 2020, **5**, 5–19.

214 M. R. Lukatskaya, B. Dunn and Y. Gogotsi, *Nat. Commun.*, 2016, **7**, 1–13.

215 H. Huang and M. Niederberger, *Nanoscale*, 2019, **11**, 19225–19240.

216 V. Augustyn, J. Come, M. A. Lowe, J. W. Kim, P. L. Taberna, S. H. Tolbert, H. D. Abruña, P. Simon and B. Dunn, *Nat. Mater.*, 2013, **12**, 518–522.

217 H. S. Kim, J. B. Cook, H. Lin, J. S. Ko, S. H. Tolbert, V. Ozolins and B. Dunn, *Nat. Mater.*, 2017, **16**, 454–462.

218 M. Zukalová, M. Kalbáč, L. Kavan, I. Exnar and M. Graetzel, *Chem. Mater.*, 2005, **17**, 1248–1255.

219 S. Lou, X. Cheng, L. Wang, J. Gao, Q. Li, Y. Ma, Y. Gao, P. Zuo, C. Du and G. Yin, *J. Power Sources*, 2017, **361**, 80–86.

220 T. Xiong, H. Su, F. Yang, Q. Tan, P. B. S. Appadurai, A. A. Afuwape, K. Guo, Y. Huang, Z. Wang and M. S. (Ji. T. Balogun, *Mater. Today Energy*, 2020, **17**, 1–10.

221 R. Zhang, X. Yang, S. Xu, D. Xu and F. Du, *Phys. Chem. Chem. Phys.*, 2019, **21**, 25940–25944.

222 C. Zhan, M. Naguib, M. Lukatskaya, P. R. C. Kent, Y. Gogotsi and D. E. Jiang, *J. Phys. Chem. Lett.*, 2018, **9**, 1223–1228.

223 M. Vincent, V. S. Avvaru, M. C. Rodríguez, M. Haranczyk and V. Etacheri, *J. Power Sources*, 2021, **506**, 230118.

224 V. S. Avvaru, I. J. Fernandez, W. Feng, S. J. Hinder, M. C. Rodríguez and V. Etacheri, *Carbon N. Y.*, 2021, **171**, 869–881.

225 F. Liu, T. Wang, X. Liu and L. Z. Fan, *Adv. Energy Mater.*, 2021, **11**, 1–28.

226 Z. Zhang, S. Dong, Z. Cui, A. Du, G. Li and G. Cui, *Small Methods*, 2018, **2**, 1–15.

227 Z. Zhao-Karger and M. Fichtner, *Front. Chem.*, 2019, **7**, 1–12.

228 M. M. Huie, D. C. Bock, E. S. Takeuchi, A. C. Marschillok and K. J. Takeuchi, *Coord. Chem. revieus*, 2015, 15–27.

229 Z. Ma, D. R. MacFarlane and M. Kar, *Batter. Supercaps*, 2019, **2**, 115–127.

230 C. Di Valentin, G. Pacchioni and A. Selloni, *Phys. Rev. Lett.*, 2006, **97**, 166803.

231 D. A. Links, *Nanoscale*, 2012, **4**, 6682–6691.

232 X. Cai, Y. Xu, Q. An, Y. Jiang, Z. Liu, F. Xiong, W. Zou, G. Zhang, Y. Dai, R. Yu and L. Mai, *Chem. Eng. J.*, 2021, 128491.

233 V. Etacheri, M. K. Seery, S. J. Hinder and S. C. Pillai, *Inorg. Chem.*, 2012, **51**, 7164−7173.

234 A. Ghobadi, T. G. Ulusoy, R. Garifullin, M. O. Guler and A. K. Okyay, *Nat. Publ. Gr.*, 2016, **6**, 30587.

235 J. Chen, W. Song, H. Hou, Y. Zhang, M. Jing and X. Jia, 2015, 6793–6801.

236 E. Baudrin, *Electrochem. commun.*, 2007, **9**, 337–342.

237 S. Lettieri, D. K. Pallotti, F. Gesuele and P. Maddalena, *Appl. Phys. Lett.*, 2016, **109**, 1–12.

238 M. Li, M. Wang, L. Zhu, Y. Li, Z. Yan, Z. Shen and X. Cao, *Appl. Catal. B Environ.*, 2018, **231**, 269–276.

239 X. Jiang, Y. Wang, T. Herricks and Y. Xia, *J. Mater. Chem.*, 2004, **14**, 695–703.

240 A. Kumar, A. R. Madaria and C. Zhou, *J. Phys. Chem. C*, 2010, **114**, 7787–7792.

241 V. Etacheri, J. E. Yourey and B. M. Bartlett, *ACS Nano*, 2014, **8**, 1491–1499.

242 G. Xiang, T. Li, J. Zhuang and X. Wang, *Chem. Commun.*, 2010, **46**, 6801–6803.

243 X. Chen, H. Li, H. Wu, Y. Wu, Y. Shang, J. Pan and X. Xiong, *Mater. Lett.*, 2016, **172**, 52–55.

244 S. Pearton, *Nanoscale*, 2010, **2**, 1057.

245 T. Beuvier, M. Richard-Plouet and L. Brohan, *J. Phys. Chem. C*, 2009, **113**, 13703–13706.

246 O. Frank, M. Zukalova, B. Laskova, J. Kürti, J. Koltai and L. Kavan, *Phys. Chem. Chem. Phys.*, 2012, **14**, 14567–14572.

247 M. Cargnello, T. R. Gordon and C. B. Murray, *Chem. Rev.*, , DOI:10.1021/cr500170p.

248 D. Hou, M. Dahl, B. Williford, Z. Chong, H. C. Xiong and J. M. C. A, *J. Mater. Chem. A*, , DOI:10.1039/C9TA12499C.

249 Q. Wu, J. Xu, X. Yang, F. Lu, S. He, J. Yang, H. J. Fan and M. Wu, *Adv. Energy Mater.*, 2015, **5**, 1–9.

250 J. Y. Hwang, H. L. Du, B. N. Yun, M. G. Jeong, J. S. Kim, H. Kim, H. G. Jung and Y. K. Sun, *ACS Energy Lett.*, 2019, **4**, 494–501.

251 Q. Fu, R. Azmi, A. Sarapulova, D. Mikhailova, S. Dsoke, A. Missiul, V. Trouillet, M. Knapp, N. Bramnik and H. Ehrenberg, *Electrochim. Acta*, 2018, **277**, 20–29.

252 H. Bin Wu, J. S. Chen, H. H. Hng and X. W. Lou, *Nanoscale*, 2012, **4**, 2526–2542.

253 S. Wang, B. Y. Guan, L. Yu, X. Wen and D. Lou, *Adv. Mater.*, 2017, **1702724**, 1–5.

254 X. Li, G. Wu, X. Liu, W. Li and M. Li, *Nano Energy*, 2017, **31**, 1–8.

255 R. R. Maça and V. Etacheri, *Batteries*, 2021, **7**, 1.

256 A. Byeon, M. Q. Zhao, C. E. Ren, J. Halim, S. Kota, P. Urbankowski, B. Anasori, M. W. Barsoum and Y. Gogotsi, *ACS Appl. Mater. Interfaces*, 2017, **9**, 4296–4300.

257 R. Mohtadi and F. Mizuno, *Beilstein J. Nanotechnol.*, 2014, **5**, 1291–1311.

258 X. Li, Y. Tang, L. Liu and Y. Gao, *J. Mater. Sci.*, , DOI:10.1007/s10853-020-05358-z.

259 X. Yu, S. Yun, J. S. Yeon, P. Bhattacharya, L. Wang, S. W. Lee, X. Hu and H. S. Park, *Adv. Energy Mater.*, 2018, **1702930**, 1–33.

260 S. Guo, J. Yi, Y. Sun and H. Zhou, *Energy Environ. Sci.*, 2016, **9**, 2978–3006.

261 C. Pei, F. Xiong, J. Sheng, Y. Yin, S. Tan, D. Wang, C. Han, Q. An and L. Mai, *ACS Appl. Mater. Interfaces*, 2017, **9**, 17060–17066.

262 A. R. Armstrong, G. Armstrong, J. Canales, R. García and P. G. Bruce, *Adv. Mater.*, 2005, **17**, 862–865.

263 W. Guo, D. X. Ji, Z. S. Yuan, P. Wang, Y. F. Nie, Z. B. Gu and X. Q. Pan, *AIP Adv.*, , DOI:10.1063/1.5089906.

264 M. Wang, C. Chen, J. Ma, X. Zheng, Q. Li, Y. Jin and J. Xu, *J. Mater. Chem.*, 2012, **22**, 11904–11907.

265 H. Feng, L. Liang, J. Ge, W. Wu, Z. Huang, Y. Liu and L. Li, *J. Alloys Compd.*, 2020, **820**, 153139.

266 T. Wang, X. Meng, G. Liu, K. Chang, P. Li, Q. Kang, L. Liu, M. Li, S. Ouyang and J. Ye, *J. Mater. Chem. A*, 2015, **3**, 9491–9501.

267 B. Hao, Y. Yan, X. Wang and G. Chen, *ACS Appl. Mater. Interfaces*, 2013, **5**, 6285–6291.

268 B. Choudhury, A. Choudhury, A. K. M. Maidul Islam, P. Alagarsamy and M. Mukherjee, *J. Magn. Magn. Mater.*, 2011, **323**, 440–446.

269 K. Karthik, S. K. Pandian, K. S. Kumar and N. V. Jaya, *Appl. Surf. Sci.*, 2010, **256**, 4757–4760.

270 A. El Mragui, Y. Logvina, O. Zegaoui and J. C. G. Esteves, *Materials (Basel).*, 2019, **12**, 3874.

271 B. Choudhury and A. Choudhury, *J. Lumin.*, 2012, **132**, 178–184.

272 F. Almomani, K. L. Al-Jaml and R. R. Bhosale, *Int. J. Hydrogen Energy*, 2021, **46**, 12068–12081.

273 V. Swamy, B. C. Muddle and Q. Dai, *Appl. Phys. Lett.*, , DOI:10.1063/1.2364123.

274 D. Banerjee, S. K. Gupta, N. Patra, S. W. Raja, N. Pathak, D. Bhattacharyya, P. K. Pujari, S.

V. Thakare and S. N. Jha, *Phys. Chem. Chem. Phys.*, 2018, **20**, 28699–28711.

275 W. Wen, J. Wu, Y. Jiang, S. Yu, J. Bai, M. Cao and J. Cui, *Sci. Rep.*, 2015, **5**, 1–10.

276 Y. Zhu, Y. Xu, Y. Liu, C. Luo and C. Wang, *Nanoscale*, 2013, **5**, 780–787.

277 C. Chen, Y. Wen, X. Hu, X. Ji, M. Yan, L. Mai, P. Hu, B. Shan and Y. Huang, *Nat. Commun.*, 2015, **6**, 1–8.

278 J. Zeng, Z. Cao, Y. Yang, Y. Wang, Y. Peng, Y. Zhang and J. Wang, *Electrochim. Acta*, 2018, **284**, 1–9.

279 S. Rubio, R. Liu, X. Liu, P. Lavela, J. L. Tirado, Q. L, Z. Liang, G. F. Ortiz and Y. Yang, *J. Mater. Chem. A*, 2019, **7**, 18081–18091.

280 K. V Kravchyk, M. Walter and M. V Kovalenko, *Commun. Chem.*, 2019, **2**, 1–6.

281 F. Legrain, O. Malyi and S. Manzhos, *J. Power Sources*, 2015, **278**, 197–202.

282 M. Fehse and E. Ventosa, *Chempluschem*, 2015, **80**, 785–795.

283 *ChemNanoMat*, 2016, **2**, 764–775.

284 D. P. Opra, S. V. Gnedenkov and S. L. Sinebryukhov, *J. Power Sources*, 2019, **442**, 227225.

285 W. Wang, Y. Liu, X. Wu, J. Wang, L. Fu, Y. Zhu and Y. Wu, *Adv. Mater. Technol.*, 2018, **1800004**, 1–20.

286 V. Etacheri and B. M. Bartlett, *J. Mater. Chem. A*, 2013, **1**, 12028–12032.

287 J. R. Jokisaari, D. Bayerl, K. Zhang, L. Xie, Y. Nie, D. G. Schlom, E. Kioupakis, G. W. Graham and X. Pan, *Chem. Mater.*, 2015, **2**, 7896–7902.

288 G. Xiang, Y. Wang, J. Li, J. Zhuang and X. Wang, *Sci. Rep.*, 2013, **2**, 1–6.

289 I. Moeez, H. G. Jung, H. D. Lim and K. Y. Chung, *ACS Appl. Mater. Interfaces*, 2019, **11**, 41394–41401.

290 V. Aravindan, Y. S. Lee, R. Yazami and S. Madhavi, *Mater. Today*, 2015, **18**, 345–351.

291 M. Cabello, F. Nacimiento, R. Alcantara, P. Lavela, G. Ortiz and J. L. Tirado, *Journl Electrochem. Soc.*, 2016, **136**, A2781–A2790.

292 M. Cabello, R. Alcántara, F. Nacimiento, P. Lavela, M. J. Aragón and J. L. Tirado, *Electrochem. acta*, 2017, **246**, 908–913.

293 Q. Duc, T. Son and T. H. Hoa, *Mater. Lett.*, 2019, **254**, 357–360.

294 M. Zhou, Y. Xu, C. Wang, Q. Li, J. Xiang, L. Liang, M. Wu, H. Zhao and Y. Lei, *Nano Energy*, 2017, **31**, 514–524.

Appendix

Appendix 1. The Different BET isotherms. (I) Microporous solids – pore size ≈ 1 nm (a), <≈2.5nm (b), (II) nonporous or macroporous, (III) weak adsorbent and adsorbate interaction, (IV) (a) size of width more than critical width and (b) mesopores of smaller widths, (V) molecular clustering at filling of pores and (VI) multilayer adsorption on a uniform nonporous surface.